A Receiver Function Study of Southern Costa Rica Indications of Steep Cocos Ridge Subduction

vorgelegt von
Yvonne Dzierma

ii

Abstract

Central America is characterized by the subduction of the oceanic Cocos Plate underneath the Caribbean Plate and Panama Microplate along the Middle America Trench, in a setting that is transitional between oceanic island arc and continental active margin subduction. In addition to providing an interesting comparison with purely oceanic or continental subduction zones, the Central American subduction zone is particularly fascinating owing to its pronounced lateral variability regarding the nature of the overriding plate, subducting plate, seismicity, volcanism and geochemistry.

To explore the deep structure of the subduction zone, a transect of broadband seismometers across the Talamanca Range (Southern Costa Rica) was operated from spring 2005 to spring 2007. This region is characterized by the subduction of the aseismic Cocos Ridge, which has been observed to dip at an angle of 18° down to depths of about 40 km. Based on this shallow subduction angle, it has been speculated that shallow underplating of the Cocos Ridge is responsible for the gap in active volcanism and strong uplift in the Cordillera de Talamanca region.

A receiver function analysis of 522 teleseismic earthquakes was performed, yielding 1777 receiver functions. The data from the Talamanca Transect stations was complemented by short-period data recorded at the Quepos network land-stations, adding another 100 receiver functions for 39 events.

The Moho of the overriding plate is imaged around 35 km depth, and an intracrustal discontinuity is observed at about 20 km depth, in good agreement with previous active seismic studies. Contrary to expectations, the migrated sections clearly show a steeply dipping ($\approx 60°$) conversion down to more than 150 km depth, interpreted as the subducting slab. 3d-representations based on the migrated profiles do not indicate significant shallowing of the subducting plate towards the Cordillera de Talamanca. These results indicate for the first time that the Cocos Ridge may be subducting beneath Southern Costa Rica at a considerably larger angle and to greater depths than previously thought, opening new questions about the mechanism causing the gap in active volcanism and strong uplift in the Cordillera de Talamanca. Possible explanations include a compressional regime hindering the ascent of magmas to the surface or an anhydrous part of the subducting slab, preventing fluid-induced melting in the mantle wedge. Alternatives may be combined subduction/underplating scenarios or a transitional regime.

Modelling studies confirm that the dipping feature observed in the migrated receiver functions can be caused by a slab dipping at approximately the same angle. Possible anisotropy scenarios, such as corner-flow and the resulting olivine lattice-preferred orientation, are also investigated. The results point to the existence of mantle-wedge corner-flow, with possible additional arc-parallel flow.

Zusammenfassung

Die tektonische Situation in Mittelamerika ist gekennzeichnet durch die Subduktion der ozeanischen Cocos-Platte unter der karibischen Platte und der Panama-Mikroplatte entlang des mittelamerikanischen Grabens. Dabei handelt es sich um eine Übergangssituation zwischen aktiven Kontinentalrändern und ozeanischen Vulkanbögen. Zusätzlich zu dem interessanten Vergleich mit rein ozeanischer oder kontinentaler Subduktion ist die mittelamerikanische Subduktionszone besonders interessant aufgrund ihrer starken lateralen Variabilität, was die Natur der subduzierenden und der darüberliegenden Platte, die Seismizität, den Vulkanismus und die geochemischen Signaturen betrifft.

Um die Tiefenstruktur dieser Subduktionszone zu erforschen, wurde ein Transect von Breitbandseismometern durch das Talamanca-Gebirge (Süd-Costa Rica) aufgebaut und von Frühling 2005 bis Frühling 2007 betrieben. Diese Region ist geprägt durch die Subduktion des aseismischen Cocos-Rücken, der mit einem Winkel von 18° bis zu etwa 40 km Tiefe abtaucht. Basierend auf diesem flachen Subduktionswinkel wurde spekuliert, dass die sehr flache Subduktion des Cocos-Rückens verantwortlich ist fuer die Unterbrechung des aktiven Vulkanismus und die Hebung des Talamanca-Gebirges.

Eine Receiver-Funktions-Analyse von 522 teleseismischen Erdbeben wurde durchgeführt und lieferte 1777 Receiver-Funktionen. Die Daten der Talamanca-Transect-Stationen wurden ergänzt durch kurzperiodische Daten, die von den Landstationen des Quepos-Netzwerks aufgenommen wurden. Dies ergab weitere 100 Receiver-Funktionen zu 39 Ereignissen.

Die Moho der oberen Platte wird bei etwa 35 km Tiefe beobachtet, und eine inner-krustale Diskontinuität liegt bei ca. 20 km Tiefe, in guter Übereinstimmung mit früheren aktiv-seismischen Studien. Entgegen den Erwartungen zeigen die migrierten Profilschnitte klar eine steil abtauchende (60°) Konversion bis zu mehr als 150 km Tiefe, die als die subduzierende Cocos-Platte interpretiert wird. 3d-Darstellungen basierend auf den Migrationsprofilen deuten nicht auf einen significanten Übergang zu flacheren Subduktionswinkeln in der Nähe des Talamanca-Gebirges hin. Diese Ergebnisse deuten zum ersten Mal darauf hin, dass der Cocos-Rücken unter Süd-Costa Rica mit erheblich steilerem Winkel und zu größeren Tiefen subduziert, als bisher angenommen wurde. Dies eröffnet neue Fragen über den Mechanismus, der die Unterbrechung des aktiven Vulkanismus und starke Hebung des Talamanca-Gebirges herbeiführt. Mögliche Erklärungen sind unter anderem ein Kompressionsregime, das den Aufstieg von Magmen an die Oberfläche verhindert oder ein Mangel an Fluiden in der subduzierenden Platte, so dass es nicht zu fluid-induziertem Schmelzen des Mantelkeils kommen kann. Alternativen könnten kombinierte Subduktions/Underplating-Modelle oder ein Übergangsregime zwischen zwei verschiedenen Subduktionsstilen sein.

Modellierungs-Studien bestätigen, dass das beobachtete, als abtauchende Platte interpretierte positive Signal durch eine im ähnlichen Winkel subduzierende Platte hervorgerufen werden kann. Mögliche Anisotropie-Scenarien, wie "corner-flow" und die daraus resultierende bevorzugte Gitter-Orientierung von Olivine, werden ebenso untersucht. Die Ergebnisse deuten auf die Existenz von corner-flow im Mantelkeil hin, evtl. mit zusätzlichem Mantelfluss parallel zum Vulkanbogen.

Sinopsis

América Central se caracteriza por la subducción de la placa oceánica del Coco debajo de la placa Caribe y la microplaca Panamá en la fosa mesoamericana, en un ambiente transicional entre la subducción oceánica y la subducción continental. Además de proporcionar una comparación interesante con la subducción puramente oceánica o continental, la zona de subducción centroamericana es particularmente fascinante en que muestra gran variabilidad lateral, en lo que concierne la naturaleza de la placa superior e inferior, la sismicidad, el volcanismo y la geoquímica.

Para investigar la estructura profunda de la zona de subducción, una transecta de sismómetros de banda ancha a través de la Cordillera de Talamanca (en el Sur de Costa Rica) se operó desde avril de 2005 hasta marzo de 2007. Esta región se caracteriza por la subducción de la dorsal oceánica del Coco, la cual se ha observado bajando hasta profundidades de unos 40 km con un ángulo de 18°. Basándose en este ángulo bajo, se ha hipotesiado que el levantamiento del Coco se emplaza a baja profundidad, sofocando el volcanismo activo y causando el levantamiento de esa región.

Un análisis de "funciones receptor" de 522 telesismos dio 1777 trazas. Los datos coleccionados por la Transecta de Talamanca se complementaron por datos de alta frecuencia de 39 sismos que se recordaron en las estaciones terrestres de la red de Quepos, lo que resultó en otras 100 trazas más.

La discontinuidad Moho de la placa superior se observa a una profundidad de approximadamente 35 km y una discontinuidad de la corteza a unos 20 km, en buen acuerdo con estudios de sísmica activa. Al contrario de lo que se esperaba, los perfiles a través del volumen de migración muestran una conversión bajando con un ángulo de unos 60° hasta más que 150 km de profundidad, la que se interpreta como la placa del Coco. Representaciones tridimensionales no indican una transición a un ángulo más bajo acercándose a la Cordillera de Talamanca. Estos resultados indican por primera vez que la dorsal del Coco se está subduciendo debajo de Costa Rica a un ángulo mayor y hasta profundidades mayores que se solía suponer. Esto abre nuevas cuestiones acerca del mecanismo que causa la interrupción del volcanismo activo y el levantamiento de la Cordillera de Talamanca. Una explicación posible sería un régimen de compresión que impide la subida de magmas a la superficie o una parte seca de la placa del Coco, lo que dificulta la formación de magmas en el manto. Escenarios que involucran una combinación de subducción y bajocabalgamiento o una fase transitoria entre diferentes estilos de subducción presentan alternativas posibles.

Modelos sintéticos corroban que la estructura que se observa bajando en los perfiles de migración se puede crear por una placa bajando a un ángulo parecido. Estos estudios también incluyen escenarios probables de anisotropía, como el modelo de "corner-flow" y la orientación preferida de olivino. Los resultados indican la existencia de un "corner-flow" en el manto, con un posible flujo adicional paralelo al arco volcánico.

Contents

"El terremoto me captó en el trabajo. Me echó hacia abajo, casi me mato con el machete. El Volio se abrió como un hueco. Todo el mundo se calló cuando empezó a mover, porque pensaban que se iba a hundir todo, que las montañas les iban a venir por encima.

Cuando pasan estas cosas [terremotos y huracanes], no se debe correr. Mejor uno se siente en algún lugar. Ni se debe gritar. Antes, la gente respetaba esa ley.

En tiempos de los antepasados, un sismo era una cosa significativa. Sibu le dijo al quien cuida la canasta que contiene todos los tribus, el llalya, que moviera la canasta. Así avisaba a la gente que iba a llegar una enfermedad, algún mal. Por eso, si había sismos, la gente se asusta, porque sabe que va a llegar una calamidad."

"The earthquake caught me at work. It threw me to the ground, I almost killed myself with the machete. El Volio opened up like a hole. Everybody was silent when it started to shake, because they thought that everything was going to sink into the ground, that the mountains would fall upon them.

When these things happen [earthquakes and hurricans], you mustn't run. You better sit still in some place. And you mustn't scream. In the old days, the people respected these laws.

In the time of our forefathers, an earthquake was significant. Sibu [the highest God in the Bribri culture] told the guardian of the basket, which contains all the tribes, the Llalya, to shake the basket. This is how he warned the people that some illness, some disease was on the way. Therefore, when there was an earthquake, the people where frightened, because they knew that a plague was coming."

Silverio Sergio Morales Morales (age 106),
former chief of the Bribri, father of the present chief Don Timoteo

Chapter 1

Introduction

It may seem surprising that while the Bribri Indians living in the Cordillera de Talamanca in southern Costa Rica and northern Panama have legends and stories telling them about earthquakes and hurricanes, linking them with their main God Sibu, their oral tradition appears to completely lack mention of volcanic eruptions. In fact, active volcanism in the Cordillera de Talamanca ceased some millions of years ago, although volcanism is still observed today all through most of Central America, including northern and central Costa Rica.

Central America is characterized by the subduction of the oceanic Cocos Plate underneath the Caribbean Plate and Panama Microplate along the Middle America Trench (MAT), in a setting that is transitional between oceanic island arc and continental active margin subduction. To explore the differences of subduction processes in this regime as compared with oceanic and continental endmembers of subduction zones, and to take advantage of the marked lateral variability of the subduction zone properties – regarding the nature of the overriding plate, subducting plate, seismicity, volcanism and geochemistry – this region was chosen to be the focus site of the Sonderforschungsbereich (SFB) 574 phase 1 and 2 investigations.

The goal of the SFB 574 "Volatiles, Fluids and Hazards – Climate Feedback and Trigger Mechanisms for Natural Disasters" is to build a composite picture of the processes acting in subduction zones, with a special emphasis on the volatile budget and its implications for natural disasters and the Earth's climate. The volatile input, subduction with the downgoing Cocos Plate, their release at depth and interaction with the overriding plate, and the release of at least part of them in the volcanic arc, are elucidated by combined geophysical, geochemical and modelling studies.

Within this framework, the seismology subproject is aiming to determine the structure of the subduction factory at depth. Past investigations focussed on the seismicity, seismic velocities and velocity ratios from tomography, and the hunt for non-volcanic tremors and their correlation with aseismic slip. This work presents the receiver function analysis of a transect of seismic stations cutting through the northern flank of the Talamanca Mountains.

Spatial gaps in active volcanic chains are not uncommon in subduction zones (e.g., there are several gaps in the Chilean volcanic arc), and have in several cases been associated with the subduction of buoyant oceanic ridges [McGeary et al., 1985]. Based on the disappearance of a clear-cut, dipping Wadati-Benioff-Zone beneath the Talamanca, it was speculated that volcanism was extinct due to near-horizontal underplating of the Cocos Ridge in this region. However, no detailed seismological investigations of this area at depth existed to prove this hypothesis. Receiver functions

allow the investigation of structural boundaries down to several hundred kilometers depth, limited mainly by the amount and quality of available data recordings.

This thesis presents the results from a receiver function analysis of the Talamanca Transect seismic stations, complemented by data from the Quepos network (see Chapter 3). It is organized along the following lines:

Chapter 2 introduces the main geological and tectonic characteristics of the region, which will provide a framework for the interpretation of the results obtained by the receiver function study. The chapter concludes with an overview of some of the most relevant seismic and seismological investigations performed in the study region to date.

Chapter 3 presents the two networks whose data was used in the analysis: the Talamanca Transect – a broadband network installed with the explicit aim of collecting data for the receiver function analysis – and the land stations of the Quepos network. This short-period amphibious network operated during the first phase of the SFB 574, and was used to complement the Talamanca Transect recordings to extend its coverage further towards central Costa Rica at crustal depths.

Chapter 4 provides an introduction into the theoretical background of the receiver function technique and explains the main data analysis steps. The receiver function analysis follows the standard procedure used, e.g., by Yuan [1999], Yuan et al. [2000], Budweg [2003], Wölbern [2003], Kind et al. [1995], Gossler et al. [1999], including rotation into the L,Q,T coordinate frame and frequency deconvolution. The resulting receiver functions are stacked, or alternatively pre-stack depth migration is performed, reducing the smearing caused by summing traces from different back-azimuth bins.

The results of the analysis are presented in Chapter 5. Contrary to expectations, the migrated sections clearly show a steeply dipping conversion down to more than 150 km depth, interpreted as the subducting slab. The latitudinal changes in dip and the structure of the overriding plate crust are visualized by 3d-imaging. These images show no significant shallowing of the subducting plate towards the Cordillera de Talamanca, hence calling for a new explanation for the cessation of active arc volcanism in this region. In addition to the Moho discontinuity at around 35 km depth, at least one inter-crustal discontinuity is imaged at 15-20 km. Significant azimuthal variation of the receiver function is observed, which argues for the presence of dipping features and anisotropy.

Chapter 6 corroborates the results by synthetic modelling. Since the receiver function technique was originally developed for plane layering or shallow dip, it must be confirmed that dipping features can indeed be imaged and the observed dip angles correspond to the real dip angles in the subsurface. After a brief look into the main effects of dipping features and anisotropy on the azimuthal behaviour of receiver functions, synthetic models are calculated for various simplified models including a two-layered overriding crust and dipping high-velocity slab with different anisotropy scenarios. They match the observations well within the limitations imposed by the simplicity of the model, and argue for the presence of anisotropy in the mantle wedge.

This study provides first indications for the existence of a steeply dipping slab underneath the Cordillera de Talamanca, thus necessitating a revised explanation for the extinction of arc volcanism in this region and the absence of intermediate and deep seismicity. Chapter 7 discusses possible interpretations and the consequences of this new finding and its implications for the subduction

setting in Costa Rica. It further explores possible different scenarios to explain the observations, putting them global context.

A short summary and outlook is given in Chapter 8.

Chapter 2

Tectonic Setting and Geology

The Central American Subduction Zone forms part of the Pacific "Ring of Fire", a seismically and volcanically active region of destructive plate margins surrounding the Pacific Ocean.

From Mexico to Costa Rica, the Cocos Plate subducts along the Middle American Trench (MAT) underneath the Caribbean Plate and Panama Microplate (Figure 2.1). The convergence velocity of the Cocos Plate with respect to south Costa Rica is approximately 8.1 cm/yr [DeMets et al., 1990] in NNE direction (31°), at near normal angle to the trench axis.

Southern Costa Rica and Panama are located on the Panama Microplate [Adamek et al., 1988]. The Caribbean Plate underthrusts beneath its northern boundary in the so-called North Panama Deformed Belt. The north-western boundary of the Panama block is unclear and has been speculated to be located along a fault system in Central Costa Rica (the Central Costa Rica Deformed Belt, [Marshall et al., 2000, Montero, 2001]) or else to occur as far north as the Hess Escarpment.

Underneath Panama and further into South America, the Nazca Plate subducts almost perpendicularly to the Middle and South American Trench with an eastward motion (88°) of 7 cm/yr relative to South America (the relative velocity of "North-Nazca" relative to Panama is of the order 3.5-6.5 cm/yr) [Johnston and Thorkelson, 1997]. It is separated from the Cocos Plate by the Cocos Nazca Spreading Centre and the Panama Fracture Zone.

2.1 Evolution of the Cocos Plate and Panama Basin

2.1.1 Development of the Southern Central American Landbridge

The Central American Landbridge today is made up of three major structural elements [Escalante, 1990] (Figure 2.2):

1. the **Chortis Block** in the north, bounded by the Santa Elena Suture in prolongation of the Hess Escarpment, near the Nicaragua-Costa Rican border,

2. the **Chorotega Block** comprising Costa Rica and northern Panama, limited by the MAT in the south-west and by the North Panama Deformed Belt in the north-east, and

3. the **Choco Block** connecting eastern Panama with western Colombia.
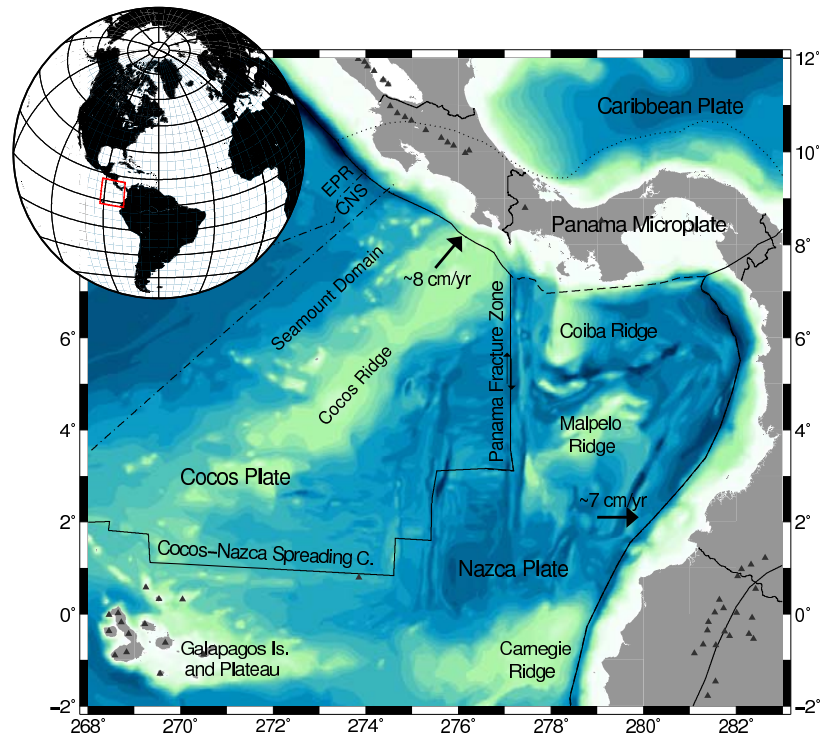
Figure 2.1: *Tectonic overview of southern Central America and the eastern Panama Basin. Volcanoes are indicated by dark triangles. The boundary between crust produced at the East Pacific Rise and at the Cocos-Nazca Spreading Centre is shown by the dashed-dotted line in the north-west (EPR-CNS). The dashed straight line below denotes the rough-smooth boundary, south of which lies the seamount segment. Plate boundaries are based on Bird [2003]. The boundaries of the Panama microplate (dotted lines) are not known precisely.*

While the Chortis Block existed already 165 Ma ago, before the opening of the proto-Caribbean Seaway at the start of the Cretaceous, the Chorotega and Choco Block are considerably younger and have hence often been grouped together [Burke, 1988].

Two competing models exist for the origin of the Caribbean crust:

1. The **"Pacific Models"** propose a formation of the present-day Caribbean crust in the Pacific region, with subsequent drift to its present position between North and South America [e.g., Pindell et al., 1988, Burke, 1988, Hoernle et al., 2002, Mann et al., 2007].

2. Alternative models argue for the formation of the Caribbean crust **between the two Americas**, though slightly to the west of its present location [Meschede, 1998, Meschede and Frisch, 1998].

Since geochemical studies point out a similarity of the Caribbean crust with Galápagos hotspot characteristics [Hoernle et al., 2002], the Pacific Model will be presented here (see Figure 2.3). From the beginning of the Cenozoic on, both models converge.
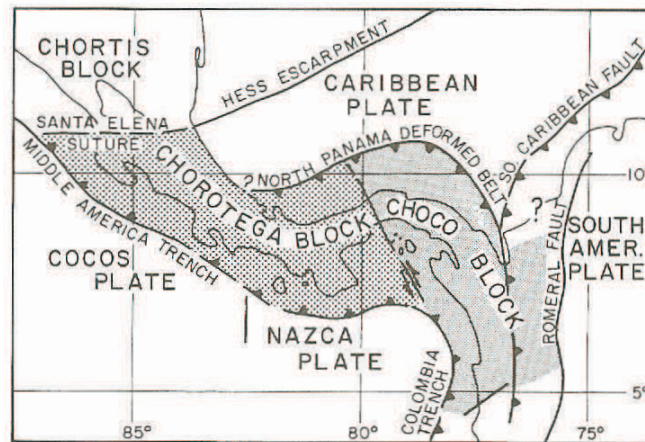
Figure 2.2: *Structural elements of Southern Central America [from Escalante, 1990].*
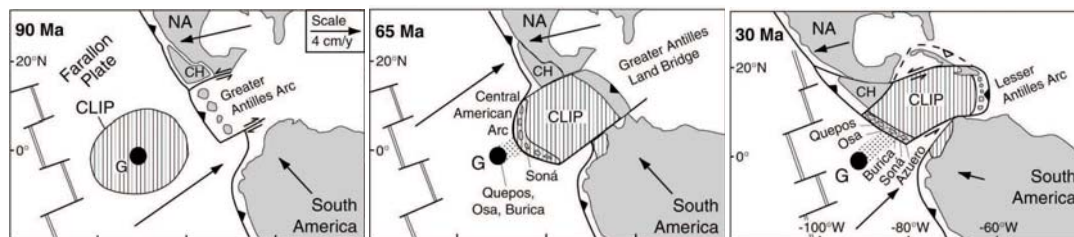
Figure 2.3: *Model for the tectonic evolution of the eastern Pacific and Caribbean over the past 90 Ma [from Hoernle et al., 2002].*

About 139 Ma ago, the Guerrero-Caribbean island arc overrode the Galápagos hotspot [Mann et al., 2007], causing a period of extreme volcanism and extrusive activity that formed the Caribbean Large Igneous Province (CLIP), which later developed into the Chorotega/Choco Block and Caribbean Plate. The period of strongest activity occurred between 72 and 95 Ma [Hoernle et al., 2002], with subsequent north-eastward drift of the plateau towards the Greater Antilles Arc.

The arrival of the young and buoyant plateau at the trench choked east-dipping subduction 70-75 Ma ago and caused uplift of the arc and a switch to west-dipping subduction along the Greater Antilles, which allowed the further eastward migration of the CLIP.

At the same time, east-dipping subduction occurred at the western edge of the CLIP, forming the Central American Arc on top of the oceanic plateau. By the combined action of uplift (partly caused by the collision of the CLIP edges with South America) and the accretion of large seamounts, islands and ridges to this margin over time, the final closure of the Central American landbridge was achieved in the early Pliocene. This led to a major change in ocean circulation and climate starting at 4.6 Ma and biotic interchange between the American continents starting about $3.7 - 3.1$ Ma ago.

2.1.2 Spreading Centre Evolution

The Cocos and Nazca Plates originated about 23 Ma ago in the break-up of the Farallon Plate [Hey, 1977, Lonsdale and Klitgord, 1978, Meschede and Barckhausen, 2000]. The crust of these plates is formed partly at the East Pacific Rise (EPR) in the west and partly at the Cocos-Nazca spreading centre (CNS) in the south. The boundary between the oceanic crust formed at the medium-spreading (3.1 cm/yr half-spreading rate) CNS and at the fast-spreading (5.5 cm/yr half-spreading rate) EPR is marked by the rough-smooth boundary.

The CNS experienced several changes in position and orientation over time, giving rise to a complicated magnetic anomaly pattern on the seafloor (Figure 2.4) [Hey, 1977, Meschede et al., 1998, Meschede and Barckhausen, 2000].
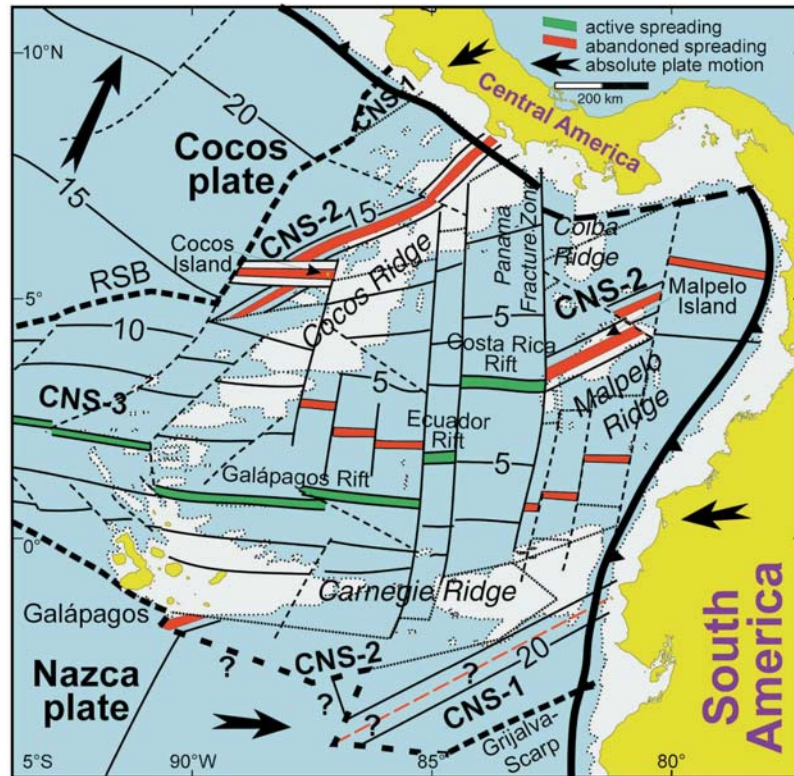
Figure 2.4: *Overview of the eastern Panama Basin [from Meschede and Barckhausen, 2000]. Numbers indicate the ages of oceanic crust.*

The first configuration, CNS-1, was active between 22.8-19.5 Ma and was oriented N50°E. Most of the crust produced by this spreading centre was later transferred to the Nazca Plate by spreading at CNS-2 and CNS-3; some remnants of CNS-1 oceanic crust remain off Nicoya Peninsula. At approx. 19.5 Ma, an abrupt change in orientation occurred, and spreading switched to the N70°E oriented CNS-2. About 14.7 Ma ago, spreading continued further to the south at CNS-3, which is still active today. The spreading axis is approximately east-west oriented and is offset by several

transform faults which dissect it into separate parts, most notably the Galápagos Rift, Ecuador Rift and Costa Rica Rift (from west to east). Its eastern boundary is given by the Panama Fracture Zone, a transform fault separating the Cocos Plate from the Nazca Plate and impinging on Central America in northern Panama, just south of the Cocos Ridge [Lonsdale and Klitgord, 1978]. The spreading axis is moving northwards with a velocity of 3.1 cm/yr, equal to the half-spreading rate [Meschede and Barckhausen, 2000].

2.1.3 Influence of the Galápagos Hotspot

A second mechanism creating a marked morphological segmentation of the Cocos Plate has been overprinting by the Galápagos hotspot. The interaction of the hotspot with the subsequent configurations of the Cocos-Nazca spreading centre has created the aseismic Cocos, Malpelo and Carnegie Ridges and possibly also the Coiba Ridge.

The **Cocos Ridge** is approximately 1000 km long and up to 200 km wide, attaining an elevation of less than 1000 m below sea level. At its crest the MAT is some 1400 m deep − compared with a depth of 3700 km at the ridge flank and 4000 m at Nicoya Peninsula [von Huene et al., 1995]. The Cocos Ridge trends N45°E, almost normal to the strike of the Middle America Trench. It collides with the Middle America Trench off southern Costa Rica, in the Cordillera de Talamanca region, producing strong uplift [Gardner et al., 1992, Collins et al., 1995].

The seamount domain adjacent to the northern ridge flank is equally caused by the influence of the Galápagos hotspot, as both are geochemically related [Werner et al., 2003], although some differences exist due to chemical zonation of the hotspot [Hoernle et al., 2008]. It consists of over 30 major (> 1000 m high) and many smaller seamounts.

The smaller **Malpelo Ridge**, located east of the Panama Fracture Zone, has been thought to have formed the continuation of the Cocos Ridge before having been cut off and displaced by the transform fault [Lonsdale and Klitgord, 1978, Meschede et al., 1998], although its origin at a second hotspot has been proposed [Meschede and Barckhausen, 2000, 2001], which may also have contributed to the Cocos Ridge formation.

Paleogeographic reconstructions based on this model suggest that a ridge length of about 250 km between the Cocos Ridge and the Malpelo Ridge is missing today and must have been subducted beneath Central America [Meschede et al., 1998, Meschede and Barckhausen, 2001]. This would correspond to a time of approx. 3-4 Ma since the onset of ridge subduction, using the present convergence rate of 8.1 mm/yr. The estimate of only 1 Ma by Lonsdale and Klitgord [1978] was based on a different paleogeographic reconstruction giving only about 40 km of subducted ridge length.

The interaction of the Galápagos plume with the CNS has furthermore created the **Carnegie Ridge**, a 1350 km long and up to 300 km wide E-W trending ridge on the northern Nazca Plate. The Galápagos archipelago at its western end concides with the present-day position of the hotspot. The relative motion of the CNS over time with respect to the hotspot and the jump from CNS-2 to CNS-3 have caused a partition of the Carnegie ridge into two elongated parts [Meschede and Barckhausen, 2000].

The origin of the **Coiba Ridge** is more elusive. While it has been proposed to have formed at the Galápagos hotspot [Meschede and Barckhausen, 2000], other scenarios have been proposed

(e.g., its similarity to the Mendocino Ridge – formed by minor underthrusting – as noted by Lonsdale and Klitgord [1978]).

Recent geochemical studies [Werner et al., 2003] suggest that all four ridges originated at the Galápagos plume, which is chemically zoned. Combining magnetic anomaly and geochemical data, they argue that the Malpelo Ridge rifted away from the Carnegie Ridge between 14.5 and 9.5 Ma, whereas it was the Coiba Ridge that was sheared away from the Cocos Ridge by a predecessor of the Panama Fracture Zone. The Coiba Ridge would be the earliest part of the Cocos Ridge track formed at the Galápagos hotspot, with an age between 20 and 23 Ma.

2.2 The Costa Rican Subduction Zone Today

2.2.1 Geology

The Central American landbridge can be divided geologically into two principal units recognized by Sapper, Schuchert and Stille [cited by Weyl, 1980]:

1. **The Northern Part**: North Nicaragua up to Guatemala
   Paleozoic or older metamorphic rocks and plutonites are overlain by upper Paleozoic, Mesozoic and Tertiary sediments. Deformation preceded violent continental volcanism in the Tertiary, during which large masses of ignimbrite were extruded. This unit can be regarded as continental crust.

2. **The Southern Part**: South Nicaragua, Costa Rica and Panama
   This unit is fundamentally different from northern Central America in that there is no Paleozoic crystalline basement nor any Paleozoic and Mesozoic deposits, but the oldest rocks are Jurassic-Cretaceous (200 Ma) in age and consists of basaltic rocks and oceanic sediments. Thick marine sediments and volcanics have deposited since the Tertiary, converting this region into the present-day so-called "tectonic crust" (MacDonald, 1972), which is transitional between purely oceanic and purely continental crust.

Costa Rica can be subdivided into three main morphological regions according to Weyl [1980]:

1. the central mountain range,

2. the Atlantic–Caribbean lowland,

3. the Pacific coastal region broken up by peninsulas and bays.

From the north-west to the south-east, the main regions were described as follows [Weyl, 1980] (compare with Figure 2.5):

- the **Cordillera de Guanacaste**, comprising the volcanoes of Rincón de la Vieja, Miravalles, Tenorio and Arenal,

- the **Cordillera de Tilarán**, made up of late Tertiary volcanic and plutonic rocks,

- the **Cordillera Central** with the volcanoes Poás, Barva, Irazú and Turrialba,

- the **Valle Central**, consisting of a slightly folded marine Oligocene and Miocene basement over which lavas, tuffs and ignimbrite sheets were deposited,

- the **Cordillera de Talamanca**, the largest and highest (Cerro Chiripó) mountain range in Costa Rica, built up of Tertiary marine sediments and intercalated volcanic and plutonic rocks from the Upper Miocene,

- the **Valle del General**, an intramountain basin with thick accumulations of Pliocene and Pleistocene gravels and volcanoclastic rocks,

- the **Fila Costeña** of marine Tertiary strata,

- the **Atlantic-Caribbean Lowland (Limón Basin)**, a large lowland region bounded by the volcanic chains, with sediment strata dating back to the Early Tertiary covered by alluvial fans and lahar deposits,

- the **Pacific Coastal Region** broken by peninsulas, bays and islands where uplift has exposed late Mesozoic ocean floor forming the Nicoya Complex.
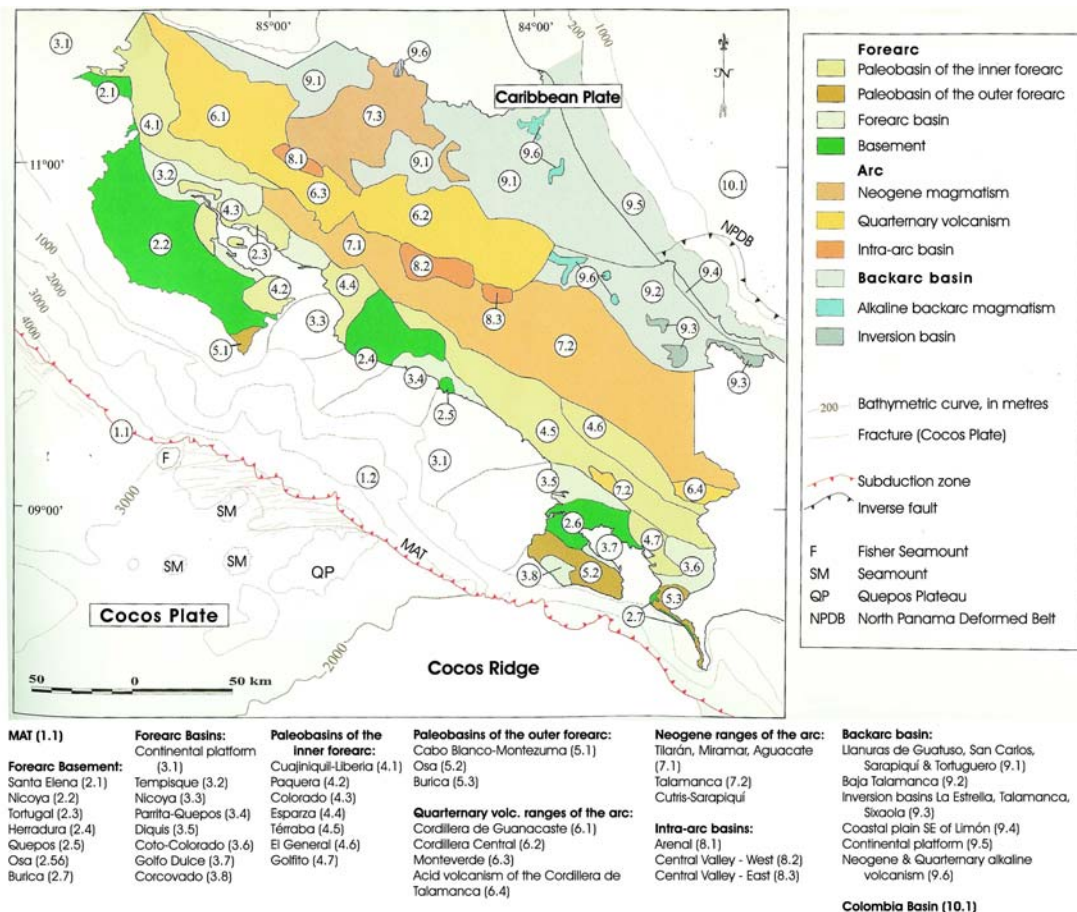

Figure 2.5: *Morphotectonic units [translated from Denyer et al., 2003]*

Jurassic-Cretaceous in age, the Nicoya Complex constitutes the oldest lithological unit which outcrops in the Nicoya and Santa Elena Peninsula, Turrubares and Osa Peninsula. This is overlain by late Cretaceous to Tertiary sedimentary rocks found in the Pacific and Caribbean basins. Large extrusions of volcanic rocks during the Miocene to Pliocene created part of the Talamanca and Tilarán Ranges and the Montes del Aguacate. The most important plutonic complex of Costa Rica are Miocene-age exhumed magma chambers found in the Cordillera de Talamanca. The mountain ranges were mostly created by Quarternary and recent volcanism.

2.2.2   Morphology of the Incoming Oceanic Plate and Continental Slope

The subducting Cocos Plate off Costa Rica can be divided into three morphologically distinct regions, which are linked to a corresponding tripartition of the upper plate [von Huene et al., 1995, 2000]. The morphological division is a consequence of the interaction of the spreading centres with the Galápagos hotspot, giving rise to:

- a **smooth segment** of igneous oceanic crust (20-25 Ma), covered by sediments,

- the **seamount domain** of 15-20 Ma oceanic crust covered 40% by seamounts, causing a highly disrupted continental margin,

- the **Cocos Ridge** subducting at a wide uplifted shelf.

The boundary between the smooth segment and the seamount domain is formed by the Fisher Seamount and the Fisher Ridge extending seaward from it. North of this morphological boundary, the smooth seafloor shows extensive bending-related faulting parallel to the MAT, where fluids are believed to enter the slab effectively.

Contrasting with the low local relief of the continental margin facing the smooth segment, the continental margin opposite the seamount segment is thinner and strongly disrupted, with furrows, uplifted blocks and slumps, fault and deformed sediments. Basal erosion is very active here, though it extends further North into the smooth segment [Ranero and von Huene, 2000, Vannucchi et al., 2001, 2003].

The southern boundary of the seamount segment is formed by the Quepos Plateau, standing some 2000 m above the surrounding ocean floor.

Owing to its convergence direction nearly normal to the MAT, the Cocos Ridge has been subducting in the same place since its collision with the MAT. Its crustal thickness midway between the crest and the Quepos Plateau is about 12 km [Stavenhagen et al., 1998, Stavenhagen, 1998], about twice as thick as the crust in the smooth and seamount segments, and reaches over 20 km thickness at its crest [Walther, 2003, Sallarès et al., 2003]. This causes resistance of the ridge to flexing as it enters the MAT and produces strong uplift of the Osa Peninsula and Talamanca Region.

2.2.3   The Central American Volcanic Arc

The volcanic arc in Costa Rica is part of the Central American Quarternary volcanic front, which extends along 1500 km length from the Mexico-Guatemala border into central Panama, with a pronounced gap of 200 km length between Irazú-Turrialba in Costa Rica and Barú in Panama [Leeman et al., 1994]. The volcanic front is located 165-190 km inland from the Middle America

Trench and is 10-15 km wide. The spacing between the volcanic centres is considerably narrower than at other subduction zones (25 km vs. 40-70 km) [Carr, 1984]. The most abundant volcanic products are basalts and andesites, with some alkaline lavas occurring in central Costa Rica.

The volcanic front can be divided into distinct segments of 100-300 km length, separated by changes in strike and offset. Along each segment, topography and structure are relatively uniform and the volcanic centres are aligned roughly in N60°W direction [Carr and Stoiber, 1990]. Offsets between segments of the volcanic front are often correlated with geologic transitions in the upper plate, such as the boundary between the Chortis and Chorotega blocks, which produces a step in the volcanic chain between Nicaragua and Costa Rica [Carr and Stoiber, 1990].

It was early recognized [Carr, 1984] that the crust is thinnest in Nicaragua, correlating both with the height of the volcanic edifices and with the silica content of the erupted lavas. Changes in isotopic composition, major and trace element ratios are also found to coincide with geological boundaries between different segments [Feigenson and Carr, 1993]. Carr et al. [1990] explained the geochemistry of Central American arc magmas by the mixing of four sources: depleted mantle, enriched mantle, metasomatized mantle and continental crust.

The volcanic gap in Costa Rica is bounded on both sides by two regions of anomalously high volcanic flux and lavas enriched in incompatible elements. Carr et al. [1990] hypothesized that enriched mantle melt was generated in the gap region, but diverted towards the sides of the gap. A signature of OIB-type mantle with Galápagos hotspot characteristics is found in these lavas.

Hoernle et al. [2008] suggested three source components based on lead isotope data: a normal EPR crust and sediment contribution found in Nicaragua, a Cocos/Coiba Ridge signal found in southern Costa Rica and Panama, and a marked influence of the subducting seamount province subducting beneath central Costa Rica.

2.3 The Cocos Ridge and the Cordillera de Talamanca – Past and Present

The absence of large Quarternary stratovolcanoes in the Talamanca region has been explained by Cocos Ridge collision/subduction, which also causes strong uplift of the region [McGeary et al., 1985]. Several studies have tried to link observations of volcanism and uplift with the subduction history of the Cocos Ridge and determine the onset of collision.

2.3.1 Timing of Ridge Collision from Uplift History

Based on stratigraphic records, Gardner et al. [1992] found rapid crustal uplift opposite the subducting Cocos Ridge, with a maximum of 6.5 m/ka on Osa Peninsula, decreasing towards the north (as compared with less than 1 m/ka for Nicoya Peninsula). They modelled their observation with subduction of the buoyant Cocos Ridge starting approximately 1 Ma ago [Lonsdale and Klitgord, 1978] and a subducted ridge length of approx. 50 km.

However, subsequent studies [Collins et al., 1995] argued for an earlier onset of ridge subduction (4 Ma) and greater subducted ridge length, needed to explain the later onset of uplift at the Caribbean margin as compared with the Pacific coast.

In agreement with these results, thermochronology and apatite fission track analyses suggest an onset of arc uplift at 4-6 Ma, contemporaneous with a thermal event seen in amphibole and biotite age spectra and with accelerated uplift [Gräfe, 1998].

2.3.2   History of Volcanism in the Talamanca Region

While Plio-Pleistocene and recent age stratovolcanoes are not observed in the Cordillera de Talamanca, de Boer et al. [1995] recognize that Miocene, Pliocene and Pleistocene volcanic rocks *do* occur in the region and argues that the absence of recent stratovolcanoes may be caused by the high elevation of the mountain range.

Adakites were emplaced in the Cordillera de Talamanca from 3.6 to 1.9 Ma [de Boer et al., 1995] and are believed to have originated in partial melting of the warm slab carrying the Cocos Ridge. The reduction in volcanism at this time may be caused both by low magma production and the inability of these magmas to rise through the thick and uplifted crust. From the maximum age of volcanic rocks related partial slab-melting, de Boer et al. [1995] argue that the subduction of Cocos Ridge crust must have started at least 5 Ma ago.

Johnston and Thorkelson [1997] rather propose the formation of a slab-window when the Panama Fracture Zone collided with the MAT. This would have allowed Pacific mantle to upwell and heat the slab edge, thus enabling the Cocos Ridge crust to melt [Abratis and Wörner, 2001].

2.3.3   The System at Depth – Seismic Studies

Wadati-Benioff-Zone (WBZ)

Local seismicity reflects the morphological tripartition of the incoming Cocos Plate: large ($M > 7$) earthquakes occur both in the smooth seafloor and Cocos Ridge segment of the subduction zone, but not in the segment dominated by seamounts, which may act as asperities [Protti et al., 1994, 1995].

A detailed study of the Wadati-Benioff Zone using local seismicity [Protti et al., 1994, 1995] imaged a well-defined WBZ under Costa Rica, with the maximum earthquake depth decreasing from 220 km under Nicaragua to 50 km south-east of Punta Uvita (on Osa Peninsula).

The prolongation of the rough-smooth boundary possibly concides with the Quesada Sharp Contortion (QSC), a hypothetical discontinuity seen below 70 km depth in central Costa Rica by Protti et al. [1994, 1995] (but not by Husen et al. [2003]). North of the QSC the slab dips at an angle of 80° with a maximum depth of seismicity of 135 km. To the south, seismicity occurs down to 125 km depth, dipping at an angle of 60°. The change in WBZ in this area may be explained by changes in the subducting plate physical parameters, since the rough-smooth boundary marks a jump in bathimetry, age and density of the subducting plate. At shallower depths, no discontinuity is seen crossing the QSC, instead the slab dips at a shallow angle angle of 20°.

The maximum depth of seismicity gradually shallows towards southern Costa Rica, related to the incoming plate age. Near Punta Uvita the WBZ terminates abruptly, suggesting shallow Cocos Ridge subduction. The hot subducted plate has therefore been believed to underplate the

upper plate and prevent the formation of an asthenospheric wedge, thereby causing the cessation of recent volcanism in this region.

Contrary to these studies (and largely unnoticed by literature), Arroyo H. [2001] observed local seismicity in south-eastern Costa Rica dipping at an angle of ca. 25° down to about 25 km depth and 60° between 25 and 65 km depth, interpreted as the subducting Cocos plate.

DeShon et al. [2003] performed a seismicity study focussing on the region between Quepos and Osa Peninsula, which imaged the dipping slab down to 30-40 km depth with an angle of 17° [DeShon et al., 2003].

Therefore we can conclude that while the shallow dip angle of 17-25° down to about 30 km has been confirmed by several studies, the geometry at greater depths still remains a matter of debate.

Active Seismic Studies

An onshore-offshore active seismic experiment along a transect from Dominical to Limón and its offshore south-westward extension [Stavenhagen, 1998, Stavenhagen et al., 1998] confirmed the dip angle of 17° at depth between 15 km and 35 km (Figure 2.6).

In the upper plate, high crustal velocities in excess of 6.0 m/s were observed beneath the sedimentary cover, and a Moho was proposed at 35-40 km depth. The identification of the Moho, however, was problematic, since the velocity structure underneath a strong intracrustal interface at 18 km depth could not be modelled satisfactorily.

The subducting plate has a thick crust with pronounced magmatic layering in the upper crust. Above the slab, a thick (> 5 km) low-velocity zone is seen, probably containing eroded margin wedge material.
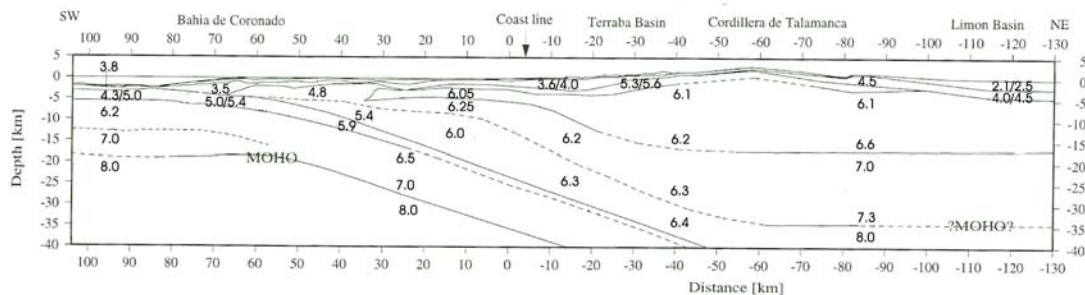

Figure 2.6: *Velocity model from active seismics [Stavenhagen, 1998]*

Local Earthquake Tomography

Observations of seismicity by Husen et al. [2003] confirm the pattern seen by Protti et al. [1994, 1995], with a decrease in maximum depth of seismicity to southern Costa Rica. A local earthquake tomography study based on their data could image the subducting Cocos Plate as a high-velocity

feature in northern and central Costa Rica down to 30 km and 70 km depth, respectively. The high-velocity slab is seen in good coincidence with the observed WBZ seismicity.

In southern Costa Rica, the subducting plate appears as a *low*-velocity feature, possibly due to its high temperature. It is limited by a high-velocity body which may be the Panama Block, possibly acting as a rigid back-stop. The tomographic resolution in this area is only reliable down to 30 km depth, and the WBZ is rather diffuse.

Husen et al. [2003] also imaged a low crustal velocity zone beneath the volcanoes Irazú and Turrialba, and a similar feature, though slightly displaced, beneath Poás.

Contrary to previous studies, Dinc et al. [2008] do not find a significant shallowing of the sub-duction dip towards southern Costa Rica. They see an increase in the dip angle of WBZ seismicity from 30° in northern Costa Rica to 40° south of Quepos, and a suite of linearly aligned events connecting the WBZ with the volcanic arc. The cold and dense Cocos Plate is imaged as a high-velocity anomaly down to ≈ 70 km, coincident with the WBZ seismicity, and overlain by a thin low-velocity layer.

Chapter 3

Analysed Data Sets

3.1 Talamanca Transect

As part of the SFB 574 phase 2 installations, 16 Güralp broad-band 3ESP and 3TD seismometers and four broad-band ocean bottom stations were installed in April 2005 along a transect through the Cordillera de Talamanca in southern Costa Rica, close to the seismic profile analyzed by Stavenhagen et al. [1998] (Figure 3.1).

Three additional land-stations were added in November 2005 to achieve a better coverage of the volcanic chain at the northern end of the transect. To further increase the resolution in this region, two stations were taken out of the southern part of the transect in November/December 2006 and placed north of Turrialba volcano. While the ocean-bottom seismometers were retrieved in December 2005, the land stations continued operation until the end of March 2007.

In addition to the data gathered by the SFB 574 seismological stations, data from three stations of the ETH Zürich were included in the analysis. The coordinates of all the stations included in the analysis are given in Table A.1 in Appendix A.

Several stations (crt-02, 07, 08, 13, 15, 21, 23, 25 and 32) had considerable timing errors of the order of up to a few hundred seconds. During each service visit to the stations, it was made sure that the time was synchronized with the correct GPS time, but between maintenance visits the internal clock of some stations experienced strong drift or, in other cases, a constant offset. This was either due to GPS malfunction, or the station could not adjust its internal clock to the GPS time (this was the case if the internal crystal was very old). A correction was therefore applied based on the observed arrival of known global events, with piecewise linear interpolation (shown in Appendix B for the relevant stations). After this correction, the station time errors are smaller than ± 10 s. This residual error was taken into account in the receiver function analysis. Since the receiver function analysis depends mainly on relative timing of the P wave and P-to-S converted waves, absolute timing errors of this size have no negative effects.
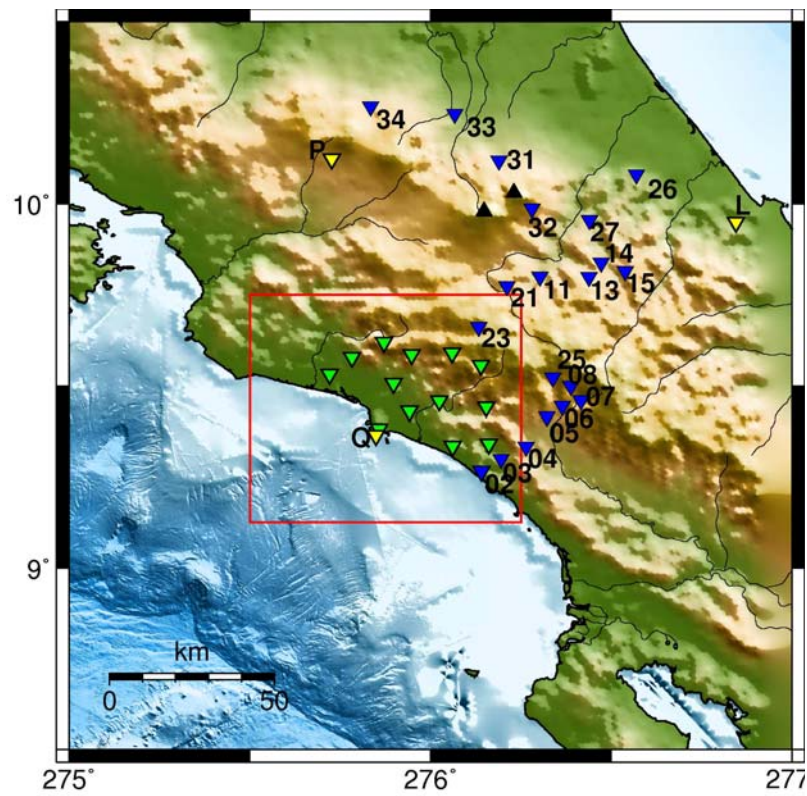
Figure 3.1: *Talamanca Transect stations (blue), Quepos stations (green) and ETH Zürich stations (yellow) included in the analysis. Black triangles denote the volcanoes Irazú and Turrialba that mark the end of the volcanic chain in Costa Rica. The station names are given next to the station symbol. The names of the Quepos stations are given in Figure 3.5, where the area inside the red box is enlarged.*

The time intervals at which data was recorded at each transect station, together with the quality of the recorded data, is shown in Figure 3.2. Severe data loss occurred between April 2005 and March 2006, particularly due to the failure of many SCSI disks. After the replacement of the disks, data recording was more stable, with only occasional data loss due to instrument malfunction, interruption in the power supply, water, lightning or damage by animals.
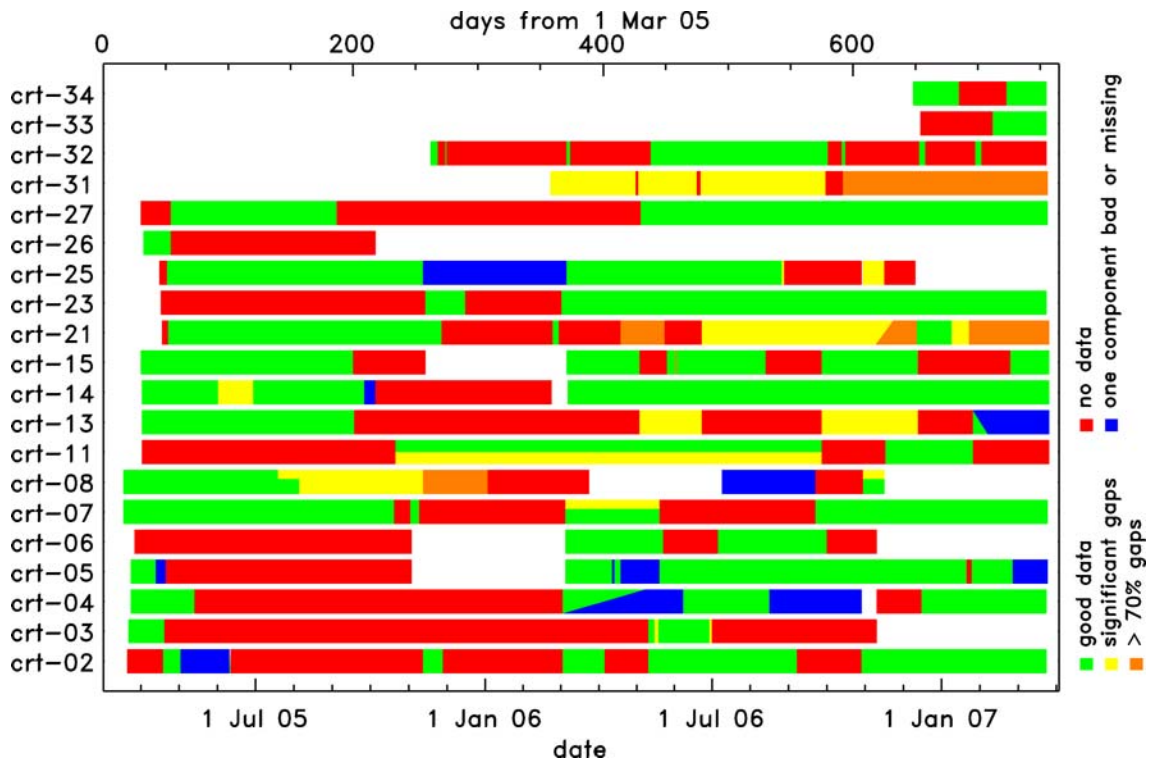

Figure 3.2: *Time intervals of data recordings at the Talamanca stations. The colour code represents the data quality, which was checked for all three components.*

A noise analysis is shown in Figure 3.3, which gives the average power spectral density observed at each station over five successive (and overlapping) intervals of 65536 samples (655.36 s), for a day with uninterrupted recordings of average quality. The noise spectra are contained between the expected low-noise model (LNM) and high-noise model (HNM) [Peterson, 1993], but generally show relatively high noise levels.
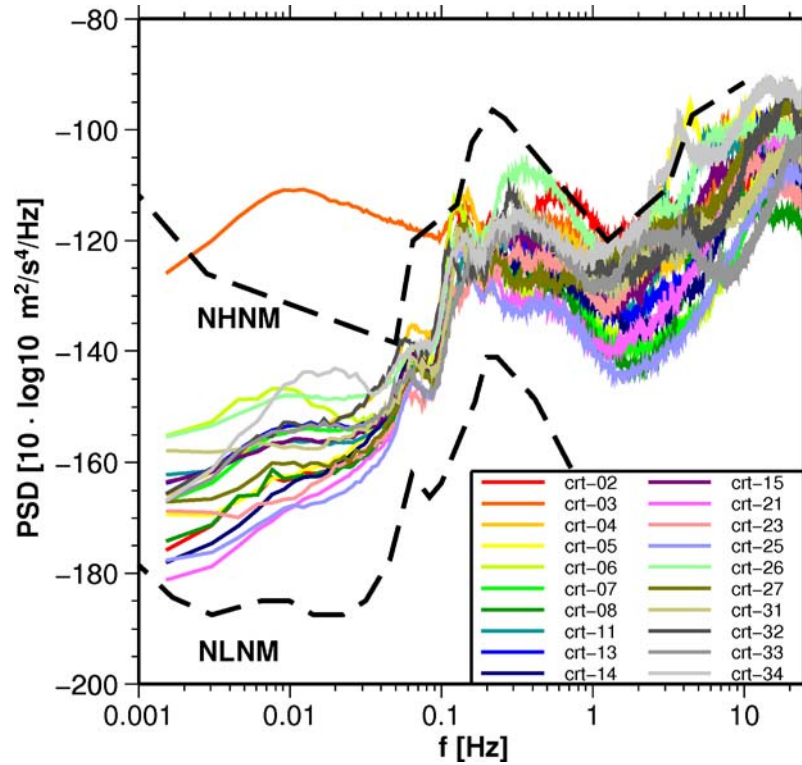

Figure 3.3: *Average power spectral density of the Talamanca Transect stations, compared with LNM and HNM [from Peterson, 1993]. Each spectrum is averaged over 5 partially overlapping intervals of 65536 samples, for all hours of a representative day of data recording.*

The main contribution of cultural noise is seen strongly at frequencies above 1 Hz, while the noise peak between 1 Hz and about 0.05 Hz is dominated by natural microseisms. Marine noise has dominant frequencies between 0.1 and 0.2 Hz, where a peak in noise level occurs for all stations and is particularly strong at those stations situated close to the coast.

A record section for a sample event recorded at the Talamanca Transect stations is shown in Figure 3.4. This event occurred on July 8, 2006, at 20:40:00.98 UTC, 51.21° N, 179, 310° W and had magnitude 6.6. In the plot, the stations are ordered by epicentral distance from the hypocentre. Since the event occurred to the north-west of the stations (back-azimuth approx. 320°, it was recorded first at station crt-31 (Guápiles, in the north-west) and last at station crt-02 (Dominical, in the south-east). The traces were integrated and filtered with a 0.05-5 s bandpass.
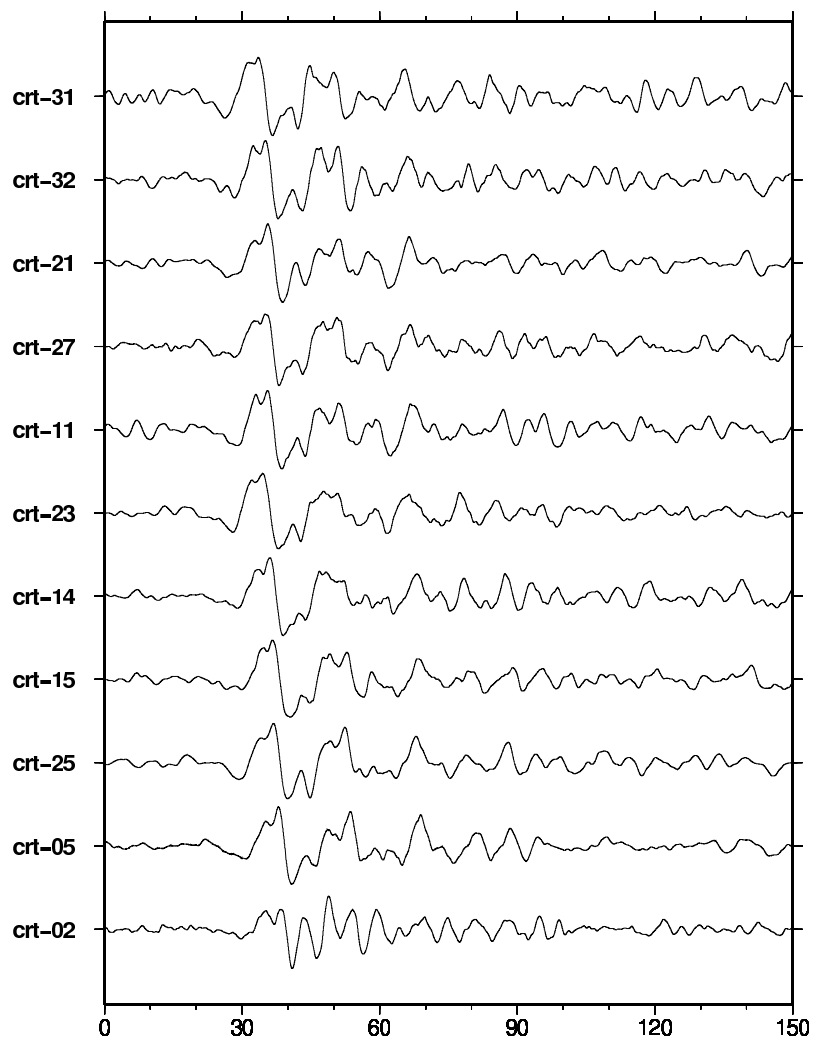

Figure 3.4: *Record section for the July 8, 2006 mag 6.6 event recorded at the Talamanca Transect stations. Stations are ordered by epicentral distance from the event, with the first arrival at the top (station crt-31, Guápiles). Only the z component seismograms are shown, after integration and filtering in the range 0.05-5 s.*

3.2   Quepos Network

The Quepos network (Figures 3.1, 3.5) consisted of 23 ocean bottom seismometers and 15 land stations deployed around the town of Quepos on the Pacific coast of central Costa Rica as part of the SFB 574 phase 1 seismic investigations. The stations were installed in October 2002 and the land stations were removed in March 2003, while the marine stations were recovered in July 2003.

In this work, only the land stations have been used (coordinates are given in Appendix A, Table A.2). Since the Quepos network consisted of short-period MARK L4 3-component 1 HZ seismometers, the main goal of the receiver function analysis of the data was to determine the crustal structure of the overriding plate. Deeper structure, such as the subducting slab, is seen more easily in low-frequency recordings, which were not possible with the Quepos network. Data recording times of the Quepos network were analyzed in the SFB 574 Progress Report (Phase 1) and are reproduced in Figure 3.6.

Since the Quepos network consistent of short-period Mark seismometers, the noise analysis was carried out in this narrower frequency range, shown in Figure 3.7. Again, the noise levels range between the high-noise model and low-noise model, closer to the high-noise scenario.

A record section for the Quepos stations is displayed in Figure 3.8, for a mag 6.6 event that occurred on November 15, 2002, at 56.05° S, 36.4° W. The seismograms were restituted and filtered between 0.4 and 10 Hz. Station MAN showed a timing deviation of the order of 1 min, which was manually corrected.
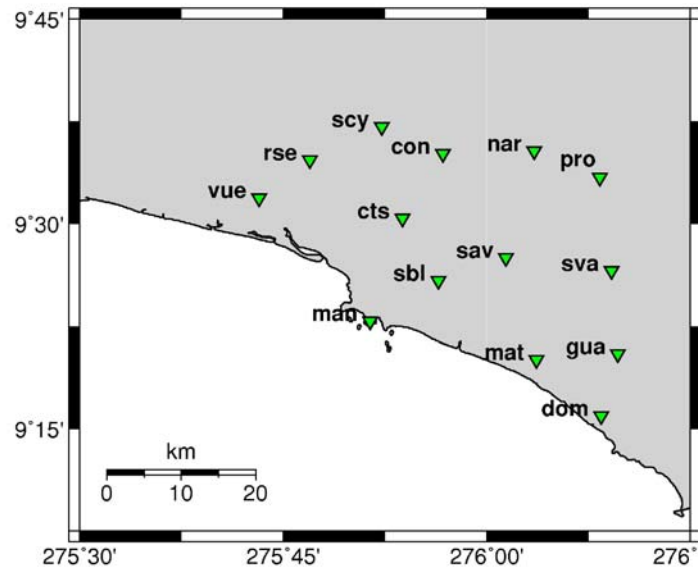

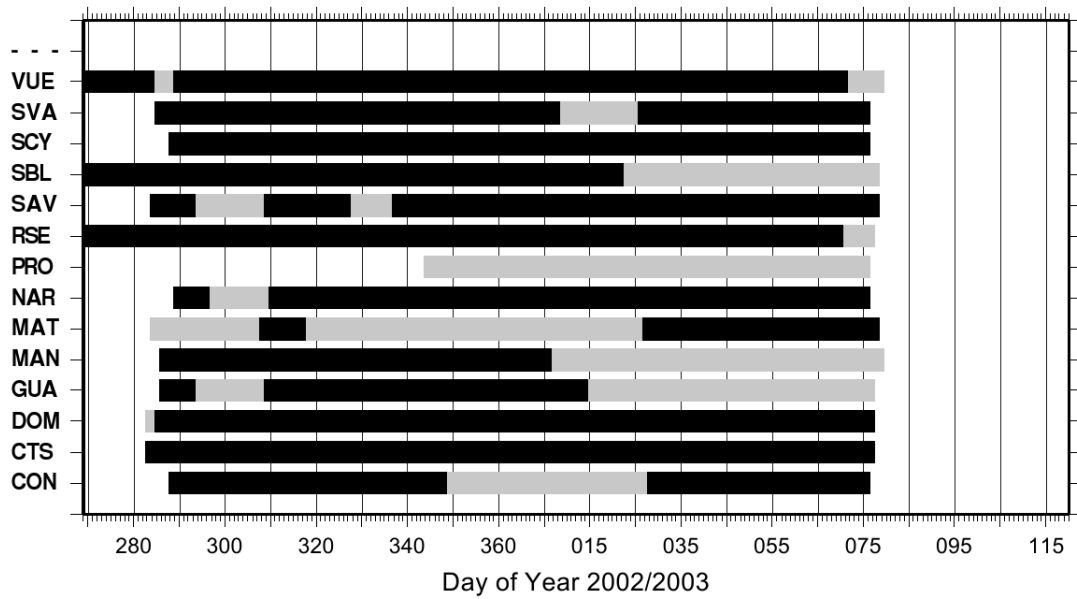Figure 3.5: *Quepos land-stations (enlarged from Figure 3.1)*

Figure 3.6: *Time intervals of data recordings at the Quepos stations [from the SFB 574 Progress Report (Phase 1)]. The days during which at least a portion of the data of the specified station can be used are marked black, while grey means that the station was deployed but the data (if any) cannot be used.*
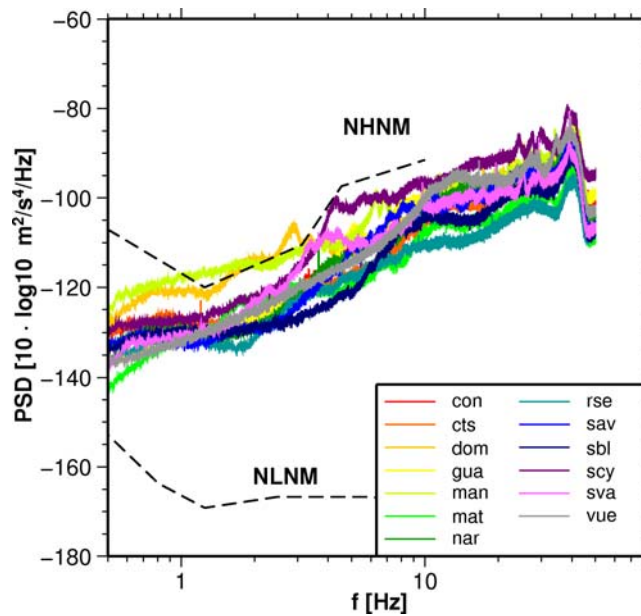

Figure 3.7: *Average noise spectra of the Quepos stations, compared with LNM and HNM [from Peterson, 1993]. Each spectrum is averaged over 5 partially overlapping intervals of 65536 samples, for all hours of a representative day of data recording.*
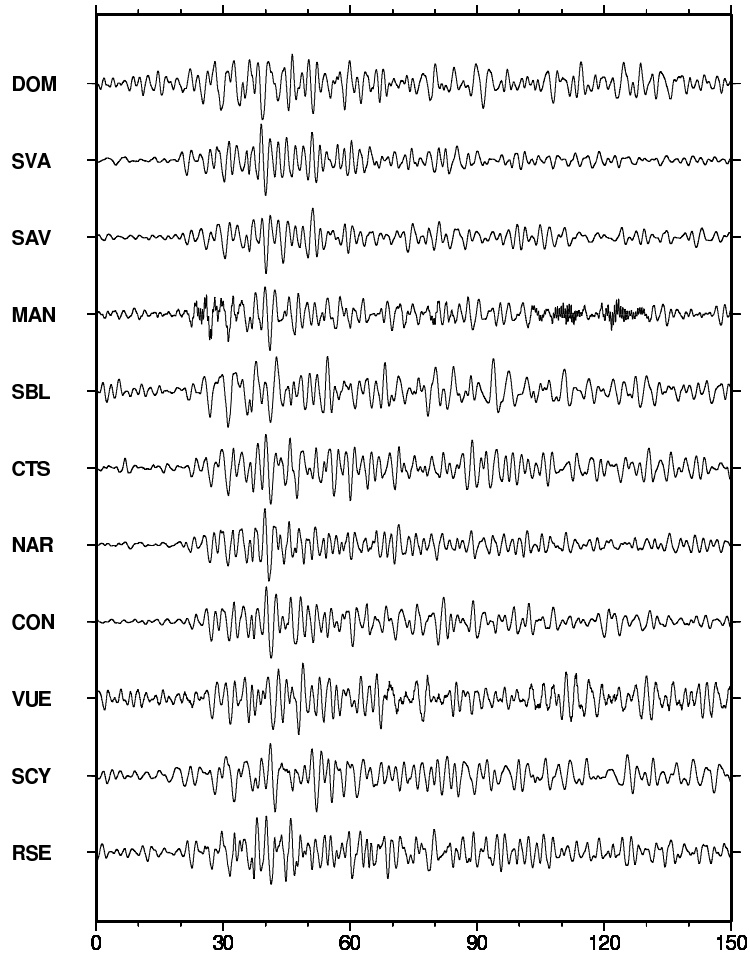
Figure 3.8: *Record section of the November 15, 2002 mag 6.6 event observed by the Quepos network stations, ordered by epicentral distance from the event. Only the z component seismograms are shown, after restitution and filtering in the range 0.4-10 Hz.*

Chapter 4

Receiver Function Method

Today the receiver function technique belongs to the standard seismological methods for the investigation of crustal and mantle structure. It is based on the fact that different types of seismic waves can be converted into each other at discontinuities along the wave path.

The first historic application of this principle was made in the 1950s in the Soviet Union and GDR under the name "Zemlja (Earth) Method" or "Converted Waves Method", respectively [Pomeranceva et al., 1970, Hoffmann et al., 1989]. Although considerable money and efford was invested into the development of this method, it was later on abandoned since the analogue data recordings could not be analysed effectively.

In the 1960s the technique was rediscovered in the USA by Phinney [1964], who used the spectra of digital datasets to calculate "crustal transfer functions", amplitude ratios of fourier spectrograms underneath single stations. The first time domain modelling was performed by Burdick and Langston [1977] and Langston [1977], and henceforth the method was continuously improved until reaching its "standardisation" by Owens et al. [1984], which coined the name "Receiver Functions" and is still used today.

Active seismic techniques were incorporated into the receiver function method over the following years, such as deconvolution, moveout-correction, stacking and inversion techniques [Vinnik, 1977, Owens and Zandt, 1985, Kind and Vinnik, 1988, Stammler et al., 1992, Kind et al., 1995, Yuan et al., 1997, Bostock and Sacchi, 1997, Bostock, 1997]. The final breakthrough of the method was also linked with the application to seismic arrays, which provided a deep look into the Earth's mantle [Yuan et al., 1997, Jones and Phinney, 1998, Bostock and Rondenay, 1999, Kosarev et al., 1999, Ryberg and Weber, 2000].

The present chapter will give an introduction to the theoretical background of the method; a concise introduction to the data analysis steps is given in Section 4.2 and 4.3.

4.1   Theoretical Background

4.1.1   P-S Conversions at Discontinuities

Seismic body waves can be classified as either P-waves (pressure waves, primary waves, longitudinal waves) or S-waves (shear waves, secondary waves, transverse waves), which propagate through the Earth at different velocities α and β, respectively:

$$\alpha = \sqrt{\frac{K + \frac{4}{3}\mu}{\rho}} \tag{4.1}$$

$$\beta = \sqrt{\frac{\mu}{\rho}}, \tag{4.2}$$

with K the bulk modulus, μ the shear modulus and ρ the density of the medium. From these formulae it follows that P-waves have higher velocity than S-waves; when the shear modulus becomes zero (e.g. in the liquid outer core), S-waves cannot propagate. When the waves strike an interface between two media, they are reflected and/or refracted according to Snell's Law

$$\frac{\sin i_1}{v_1} = \frac{\sin i_2}{v_2} = p, \tag{4.3}$$

with the angles before and after reflection/refraction i_1 and i_2 and the corresponding velocities v_1 and v_2. While Snell's Law holds true, its wording must be adjusted for a spherical Earth, so that in this case

$$p = \frac{r \cdot \sin i}{v} \tag{4.4}$$

is conserved, where i is the angle with respect to the local vertical. In a horizontally layered medium, the ray parameter p is conserved along a ray. In the case of dipping layers, the angle to the vertical i is no longer equal to the angle of incidence at the interface, so that p is not conserved (although of course Snell's Law remains locally valid).

In addition to refraction and reflection, conversion of P- into S-waves (and vice versa) at interfaces takes place to ensure the continuity of displacement and stress at the interface, as shown in Fig. 4.1.
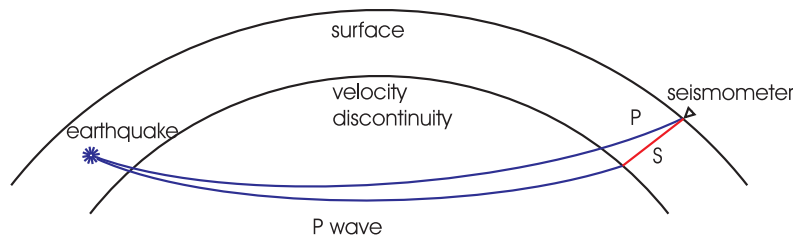

Figure 4.1: *Schematic illustration for P-S conversion of a P wave from a teleseismic event at a velocity discontinuity below the receiver [adapted from Yuan, 1999]*

In the case of plane interfaces in isotropic media, only conversions between P- and SV-waves (polarized in the plane of refraction/reflection) occur; at dipping interfaces or in anisotropic media SH-waves (polarized normal to the plane of refraction/reflection) can be created. The conversion coefficients for P-to-S conversions at an interface can be calculated from the continuity conditions [Aki and Richards, 2002] and are strongly dependent on the velocity and density contrast and the angle of incidence at the discontinuity (see Fig. 4.2).

Since S-waves propagate more slowly than P-waves, the converted phases arrive within the P wave coda following the direct P onset. The time difference between the onsets can be used to determine the depth where the conversion occurred, if a velocity model for the underground is assumed. The time difference between the P and S signals created at an interface at depth d is given by Kind and Vinnik [1988]

$$t_{Ps} = \int_0^d dz \left(\sqrt{\beta^{-2} - p^2} - \sqrt{\alpha^{-2} - p^2} \right) \tag{4.5}$$

Reverberations within the layers (multiples), shown in Figure 4.3, can be equally used to determine the depth of the discontinuity, using the relations

$$t_{PpPs} = \int_0^d dz \left(\sqrt{\beta^{-2} - p^2} + \sqrt{\alpha^{-2} - p^2} \right) \tag{4.6}$$

$$t_{PpSs} = 2 \int_0^d dz \sqrt{\beta^{-2} - p^2} \tag{4.7}$$

$$t_{PsSs} = \int_0^d dz \left(3\sqrt{\beta^{-2} - p^2} - \sqrt{\alpha^{-2} - p^2} \right) . \tag{4.8}$$
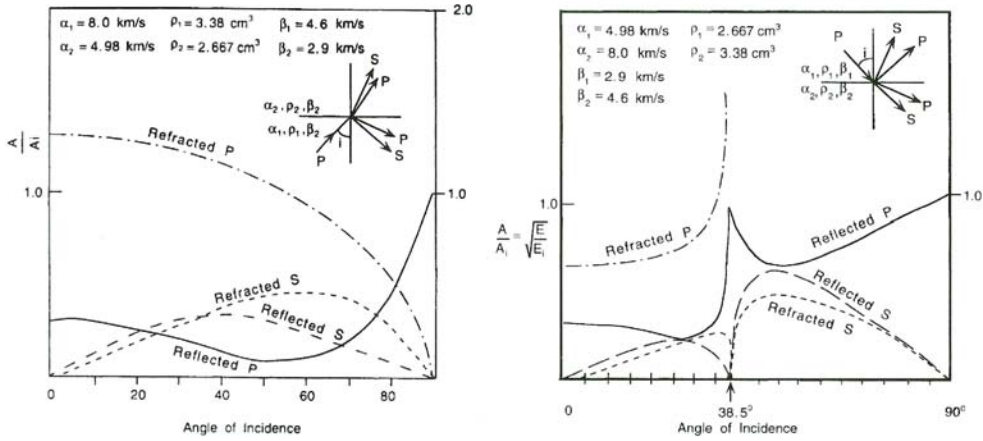

Figure 4.2: *Left: Reflection and refraction coefficients for a P wave incident on a boundary from a high-velocity region. Right: Reflection and refraction coefficients for a P wave incident on a boundary from a low-velocity region. [From Lay and Wallace, 1995]*
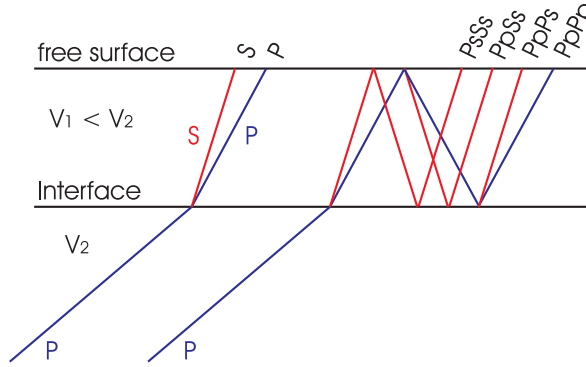
Figure 4.3: *Example for converted phases observed at a station. The left part shows the principle of P-to-S conversion, the right part of the figure illustrates the main multiple phases. Multiples are named according to the branches of the ray path. Upwards travelling waves are given capital letters in the nomenclature, downwards propagating waves are denoted by small letters. In the receiver function technique, all multiples observed at one station are deconvolved with the direct P wave arriving at the same station, although the conversion points for all phases differ slightly.*

4.2   Receiver Function Analysis

Receiver functions are time series, computed from three-component seismograms, which show the relative response of Earth structure near the receiver as observed by P-to-S conversions [Ammon, 1997]. The receiver function analysis is based on linear filter theory of seismic waveform modelling: In this approach, a seismogram $u(t)$ is represented by the convolution of different contributions representing the source signal $s(t)$, the propagation effects $p(t)$ and the seismometer response $i(t)$:

$$u(t) = s(t) * p(t) * i(t). \tag{4.9}$$

To apply this idea to the receiver function method, the propagation effect is broken down into a bulk-earth effect and the effect of the structure found close to the seismometers, i.e., where the conversions occur. Then the direct-P and P-to-S-converted wave seismograms are represented as

$$u_P(t) = s(t) * p_{far}(t) * p_P(t) * i(t) \tag{4.10}$$

$$u_S(t) = s(t) * p_{far}(t) * p_S(t) * i(t). \tag{4.11}$$

The "far-propagation" effect p_{far} is the same for both the P wave and the P-to-S converted wave, as the conversion occurs near the seismometer. Hence, the structure underneath the receiver can be obtained by deconvolving the S-wave signal from the P-wave signal:

$$RF := u_P^{-1} * u_S = p_P^{-1} * p_S \tag{4.12}$$

This definition of the receiver function makes it clear that it images *only* the structure close to the *receiver* − hence its name.

4.2.1 Resolution

The horizontal resolution is limited by the first Fresnel zone, defined as the region from which wave energy arrives with a phase difference of up to $\lambda/2$ for waves with the wavelength λ. All these waves interfere constructively. The radius of the Fresnel zone is given by

$$R_{F1} = \sqrt{\left(d + \frac{\lambda}{2}\right)^2 - d^2} \tag{4.13}$$

where d is the depth. Although this equation only holds true for the case of vertical incidence, it gives a measure of the maximum achievable resolution. Besides, this scenario is close to the realistic case because receiver function imaging is usually applied to nearly vertically incident rays.

Calculating with a maximum s-wave speed $v_s = 4.8$ km/s in the mantle and a typical frequency of about 1 s, we obtain a horizontal resolution of about 12 km at a depth of 30 km, which increases to 30 km at 200 km depth, where a low-frequency cut-off at 0.2 Hz is used.

Vertical resolution is good for discontinuities that are separated by more than $\frac{1}{4}$ of the S wavelength. For the example above, we can expect a vertical resolution of 1 km in the crust (for a typical period of 1 s) and 6 km in the mantle (where filtering is done to eliminate frequencies above 0.2 Hz).

4.3 Data Analysis Steps

For the receiver function analysis, the selection of events was made based on the following criteria:

- P phases:
  - $\Delta \geq 30°$ (corresponding to angles of incidence between about 27° and 14°, so that the waves penetrate deeply into the earth and the lateral distance between P-refraction and P-to-S conversion remains small) and
  - $\Delta \leq 95°$ (to avoid diffraction of the P wave at the core-mantle boundary)
  - $mag \geq 5.5$,
- PP phases:
  - $60° \leq \Delta \leq 180°$
  - $mag \geq 6.0$,
- PKP phases:
  - $\Delta \geq 145°$
  - $mag \geq 6.0$.

After preprocessing and signal-to-noise analysis (Section 4.3.3), 322 teleseismic events recorded at the transect stations were used, yielding 1777 receiver functions of P-to-S conversions. The location of events and the azimuthal distribution of receiver functions are shown in Figure 4.4. As can be seen in the figure, most events occurred in the north-west (Alaska-Aleutians) or in the south-east (Chilean subduction zone), producing a somewhat bimodal distribution in azimuth. Some Mid-Atlantic-Ridge events could also be included and the PP and PKP phases could be used to fill the azimuthal gap with events from the western and northern Pacific margin.
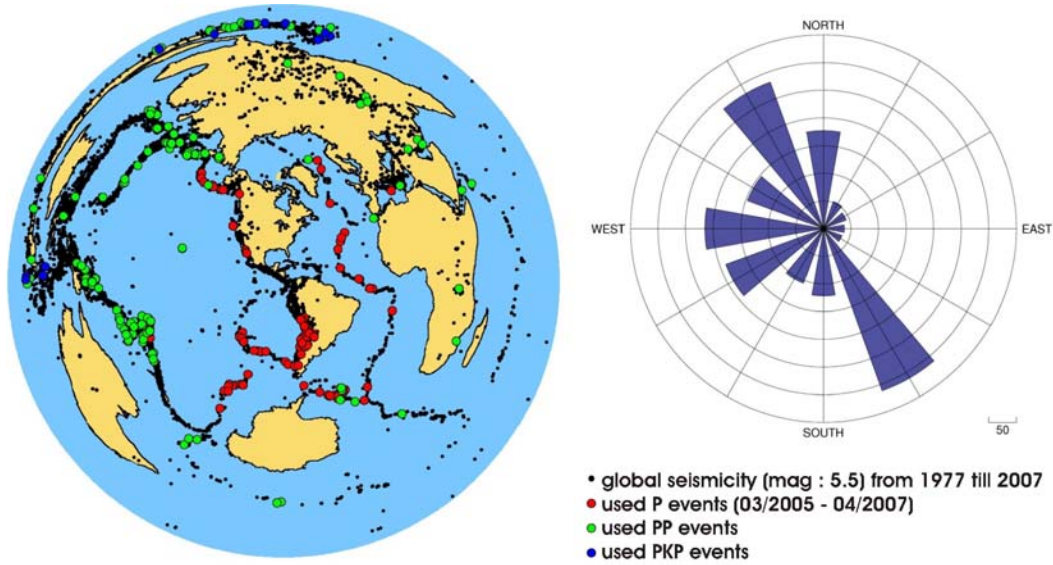
Figure 4.4: *Left: Events used in the receiver function analysis of the transect stations. P phases are displayed in red, PP phases in green, PKP phases in blue. For comparison, the global seismicity over a 30 year period is also plotted. Right: Azimuthal distribution of receiver function traces, plotted as a polar histogram.*

4.3.1   Restitution

The events used in the analysis were cut around the predicted onset and detrended. In general, the seismogram effect on the measured traces can be represented by a linear filter, the *instrument response*. Restitution is done applying the inverse filter to the observed seismogram and integrating the result to retrieve the "original" ground motion record. This eliminates the seismometer characteristics from the recordings and integrates the measured velocities to give ground displacement. In our case, this will make the data recorded on the Güralp and Mark 3 recordings comparable.

For the broad-band stations, restitution can be replaced by a simple integration to retrieve the displacement. This effectively enhances data quality as high-frequency signals (mostly noise) are suppressed. A data example is shown in Fig. 4.5. The traces were filtered with a 3rd-order Butterworth bandpass with corner frequencies 0.05 Hz and 5 Hz for the further analysis. All the filtering was done forward and backward to avoid phase shifts.

4.3.2   Rotation

The first receiver function studies assumed all the P-wave energy was concentrated on the vertical component, while the S-wave signal was found on the horizontal recordings. However, the results can be greatly improved by really separating the P- and S-wave signals, which requires rotation into a new coordinate system defined by the ray geometry.

In the first step, the horizontal components N and E are rotated by the backazimuth φ onto the new R and T coordinates. The radial coordinate R is aligned with the projection of the incident P wave onto the horizontal; the tangential coordinate T is normal to this. The second step rotates
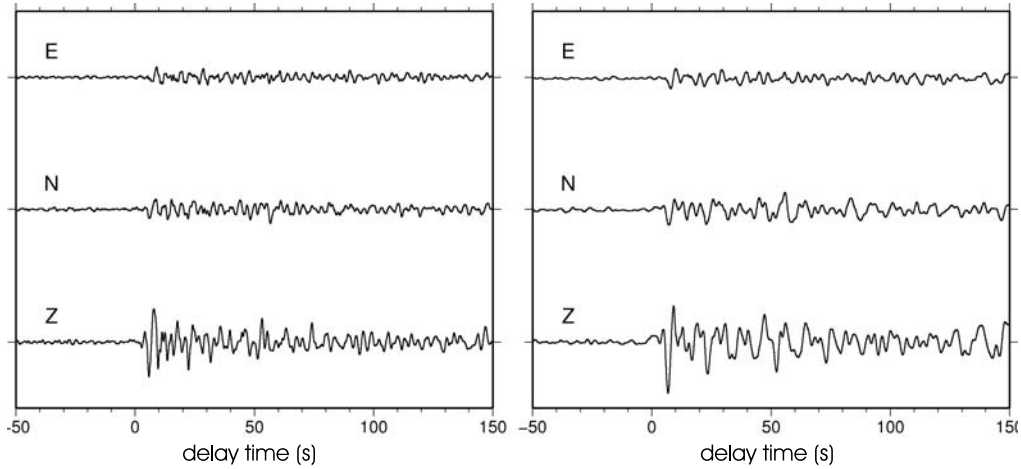
Figure 4.5: *Example of raw and restituted data for a single event on day 132, 2005, recorded at station crt-07 (Los Ángeles). The traces were filtered between* 0.05 Hz *and* 5 Hz.

the new system around the T component by the angle of incidence i, so that the new L component is parallel to the incoming P wave. The rotation is a linear transformation with the rotation matrix

$$
\left(\begin{array}{c} L \\ Q \\ T \end{array} \right) = \left(\begin{array}{ccc} \cos i & -\sin i \cos \varphi & -\sin i \sin \varphi \\ \sin i & \cos i \cos \varphi & \cos i \sin \varphi \\ 0 & \sin \varphi & -\cos \varphi \end{array} \right) \cdot \left(\begin{array}{c} Z \\ N \\ E \end{array} \right).
$$

After rotation, all P-wave energy is concentrated on the L component; the converted energy should be concentrated in the Q component, although anisotropy and dipping layers can produce converted signals on the T component. The geometry of the new coordinate system is shown in Figure 4.6; a data example is given in Figure 4.7.

The backazimuth and angle of incidence used for the rotation were determined in two ways:

1. by a polarization analysis of the measured wavefield [Kind et al., 1995]. To reduce the background noise level, the traces were filtered in the frequency range of 0.05-0.2 Hz before calculating the rotation angles. In the rotation and the following analysis steps, the original traces filtered over 0.05-5 Hz were again used.

2. Alternatively, the angles can be calculated theoretically based on the known location of the earthquake and seismometer and using a standard earth model, in this case AK135 [Kennett et al., 1995]. While this method can be applied without the problem of the noise level, it can give erroneous results if the underground is heterogeneous. There is also a slight deviation between the observed P-wave angle of incidence and the real angle, caused by reflection at the free surface.

Errors in backazimuth can project energy onto the T component, while deviations in the angle of incidence affect the Q component. Although the results of both methods often differ markedly, deviations less than 30° in angle of incidence and 45° in backazimuth do not significantly influence the energy partition [Li, 2001]. Where the theoretical and observed angles differed by more than

this, the theoretical angles were used in the rotation. The differences between the theoretical and observed angles are displayed in Figure 4.8. They resemble Gaussian distributions about 0°; in the case of the angle of incidence, the *Seismic Handler* routine in some cases calculated unrealistic angles above 90°, thereby producing the second peak in the deviation.
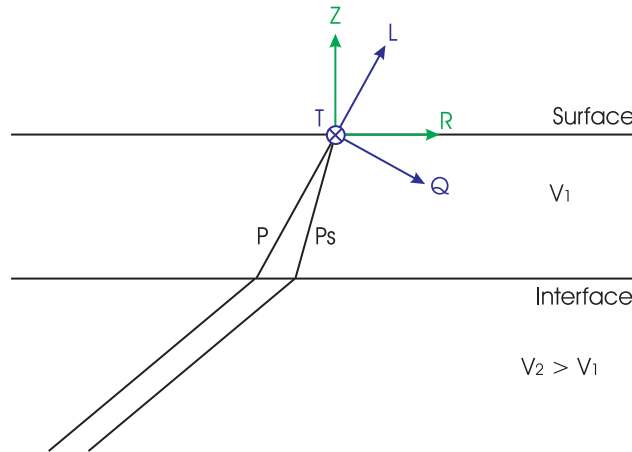

Figure 4.6: *Definition of coordinate systems used in the rotation. After rotation, the energy of the incoming P wave is confined to the L component, while the transverse SV-wave motion is primarily found on the Q component. If there is energy on the SH component, it shows up on the T component.*
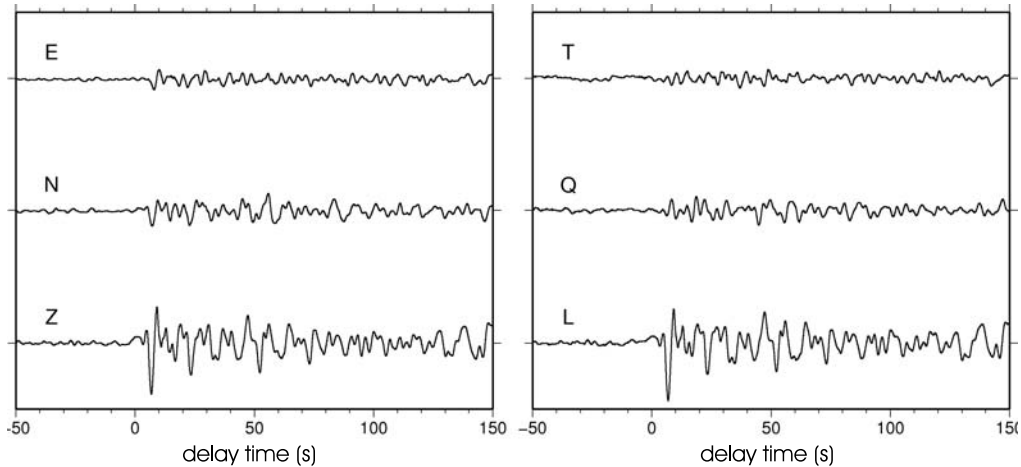

Figure 4.7: *Example of restituted (left panel) and rotated data (right panel) for the event on day 132, 2005, recorded at station crt-07 (Los Ángeles).*
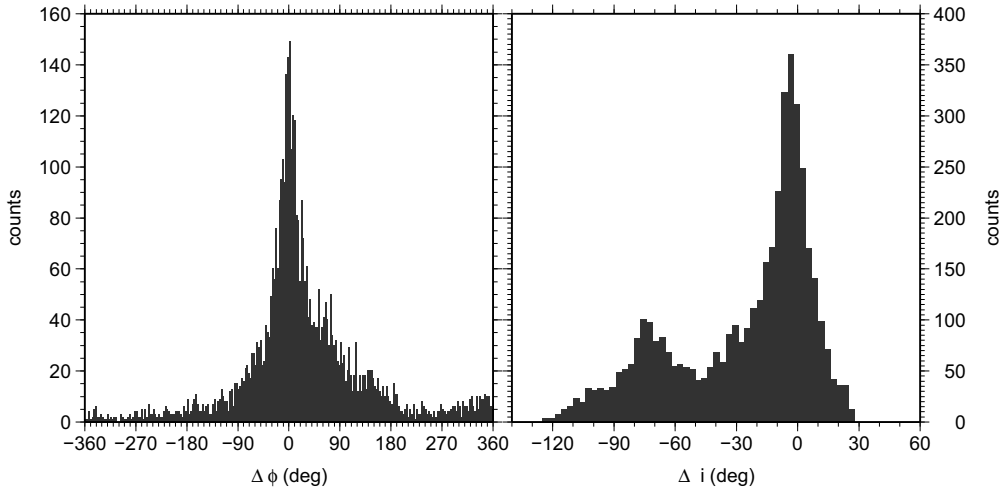
Figure 4.8: *Left panel: Histogram showing the deviation of theoretical and observed backazimuth ($\Delta\varphi$) for the Talamanca Transect stations. Right panel: Histogram showing the deviation of theoretical and observed angle of incidence (Δi) for the transect stations. Although the two diagrams have very different y-axis scales, the cumulative number of events is the same. The corresponding distribution for the Quepos network is similar in shape.*

4.3.3   Signal-to-Noise Analysis

Before proceeding with the analysis, a signal-to-noise test was carried out to improve the data quality. Since the P onset should be constrained to the L component, the signal-to-noise ratio (SNR) was calculated as the ratio of the maximum peak-to-peak amplitudes on the L trace in a 60 s-time window around and before the theoretical onset. It was checked whether the SNR could be improved if the traces were filtered with a Butterworth high-pass above 1 Hz or a band-stop was applied to reduce marine noise in the range 0.1-0.2 Hz. Events with SNR better than 2 were included in the analysis; events in the SNR range 1.4-2 were visually inspected and quality-checked. Out of 4414 traces, more than half had to be discarded. The signal-to-noise distribution is shown in Figure 4.9.

4.3.4   Deconvolution

By deconvolving the L component with the Q and T components, the source signal and propagation effect can be eliminated to retrieve the underground response in the vicinity of the receiver. This makes the receiver functions obtained from different events comparable with each other with respect to waveform and amplitudes. In the ideal case, the deconvolution compresses the P-wave to a delta function (spike), so that the S wave is reduced to a time series of reflection and conversion signals. Realistically, however, there remain a number of multiples that cannot be eliminated from the analysis; but they can be identified by their travel-times, move-out behaviour and modelling studies.
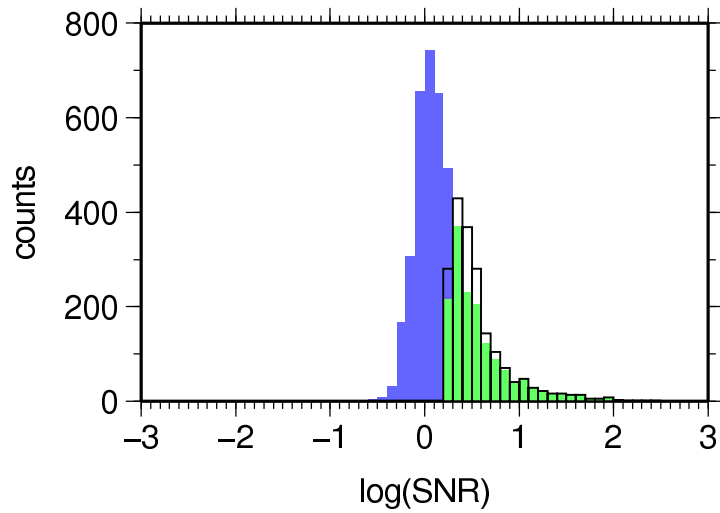
Figure 4.9: *Histogram giving the distribution of the signal-to-noise ratio of the 4414 traces entering the analysis of the transect stations. Events with $SNR > 1.8$ are shaded green, as this threshold normally provided clear p onsets. The box outlines events that had sufficient SNR after filtering with an addition high-pass or band-stop, as explained in the text. These amounted to about 360 additional events that could be included after further filtering. The SNR distribution of the Quepos stations is similar in shape.*
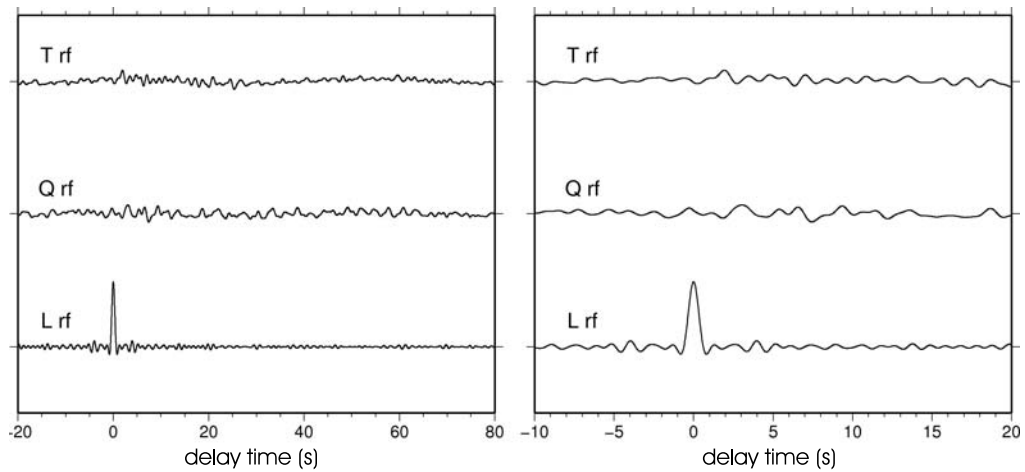

Figure 4.10: *Example of the deconvolved traces (averaging function and Q (radial), T (transverse) receiver functions for the same event on day 132, 2005, recorded at station crt-07 (Los Ángeles). The right panel zooms into the time series for a better view of the early conversions.*

In principle, the deconvolution can be calculated in the frequency domain by a simple spectral division:

$$RF_Q(\omega) = \frac{L^*(\omega)Q(\omega)}{L^*(\omega)L(\omega)}, \tag{4.14}$$

where $L(\omega)$ and $Q(\omega)$ are the Fourier transforms of the L and Q components of the seismogram and $L^*(\omega)$ is the complex conjugate of $L(\omega)$. The receiver function is then given as the inverse Fourier transformation of $RF_Q(\omega)$, $rf_q(t)$.

However, for small values of $L(\omega)$ the denominator becomes nearly zero, so a "water-level" is introduced to avoid dividing by zero in the calculation: In this algorithm, denominator values smaller than a given threshold value (water-level w_l times L^*L) are replaced by that threshold, thereby attenuating frequencies with a small vertical component. This is comparable to applying "pre-whitening" in deconvolution theory. Finally, one generally introduces an additional Gaussian filter, which produces neither phase distortion nor side-lobes, but makes the deconvolution more stable as compared with an ideal spike. The deconvolution is then performed according to the modified equation [Clayton and Wiggins, 1976, Owens et al., 1984, Ammon, 1991]

$$RF_Q(\omega) = \frac{L^*(\omega)Q(\omega)}{max(L^*(\omega)L(\omega), w_l \cdot L^*(\omega)L(\omega))}G(\omega), \tag{4.15}$$

where $G(\omega) = \exp\left(-\frac{\omega^2}{4\alpha^2}\right)$ is the Gaussian and w_l the water level. In this analysis, a water level of $w_l = 0.0001$ and a Gaussian filter of width 10 Hz was used.

The deconvolution of the L component with itself, called the averaging function, produces a spike that can be used to estimate the quality of the data both from the noise observed before the Gaussian and from the width of the Gaussian. An example of the averaging function, radial (Q) and transverse (T) receiver functions is shown in Figure 4.10.

4.3.5 Normal Moveout-Correction

The time difference between the P and converted S arrival at the surface depends on

- the depth of the discontinuity where conversion occurred

- the velocity difference between the P and S wave

- the angle of incidence of the ray at the surface, i.e., on the ray parameter p.

The last effect is independent of the characteristics of the underground and is referred to as *normal move-out (NMO)*. It is explained schematically in Figure 4.11.

Normal move-out is corrected to reduce all seismograms to what they would look like at a reference slowness. Normally 6.4 s/°, corresponding to an epicentral distance of 67°, is chosen, which gives a ray parameter approximately in between the 30° and 90° epicentral distance arrivals (the maximum and minimum epicentral distances used for the analysis of P phases). This amounts to a "compression" of seismograms with higher slowness and a dilatation of seismograms with smaller slowness than the chosen reference.

After compensating for normal move-out, conversions should be seen at the same time on rays with different ray paths (ray parameter). The correction is therefore necessary if traces with different ray paths shall be compared or stacked. An additional advantage of NMO-correction is that

while real conversions arrive simultaneously after correction, multiples do *not*; they can thus be identified and are attenuated by stacking.
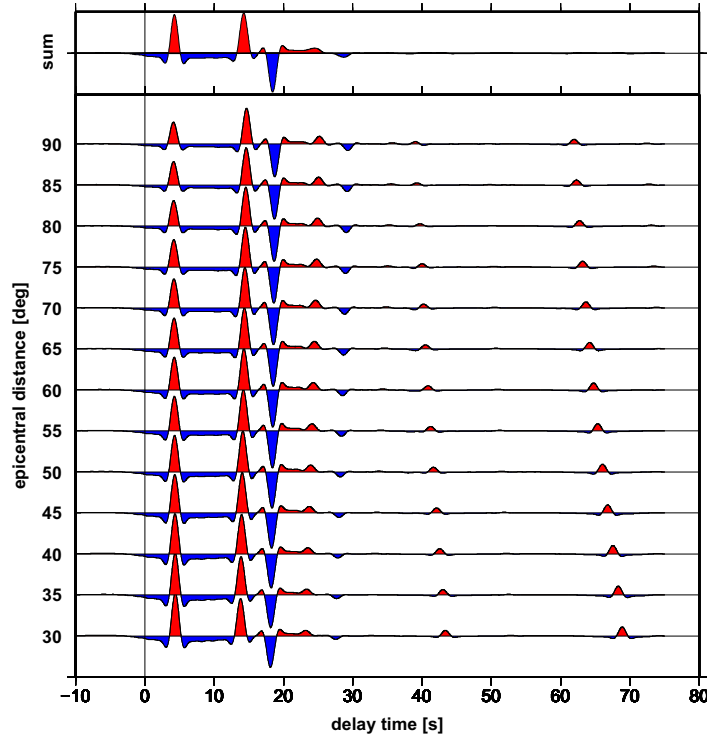

Figure 4.11: *Example for normal move-out effect. The traces were calculated for a model with a Moho at depth* 35 km *and mantle discontinuities at* 400 km *and* 660 km. *The largest move-out is observed for the deepest phases, which are so smeared out that they are lost by stacking.*

4.3.6   Stacking

The NMO-corrected traces can be stacked to improve the signal-to-noise ratio (SNR). This is due to the fact that the signal energy increases by a factor of n^2 if n traces are stacked, while the noise energy only grows with n [Morozov and Dueker, 2003]. Hence, an overall improvement by a factor of $\sqrt{n}$ in the amplitude SNR is achieved by stacking.

Stacking was done using a weighted average, where the weight for each trace was calculated as the peak-to-peak amplitude of the peak on the L-trace. In this way, traces with a good deconvolution resulting in a strong P-arrival are preferred in the sum.

Stacking does not give satisfactory results if additional effects like a dependence on back-azimuth come into play. In this case, the variations will be obscured and only the features that are common to all receiver functions reappear in the stacked trace.

4.3.7 Pre-stack Depth Migration

Depth migration is a technique used to transfer seismic traces recorded in the time domain into the depth domain and thereby image the subsurface structure. Migration can be performed on the stacked traces or on the individual, unstacked traces, both methods having their advantages and disadvantages. In this study, pre-stack depth migration was used to take azimuthal variations in the receiver functions into account. This method is significantly different from "typical" seismic migration where data are back-propagated to collapse diffraction hyperpolas etc., while remaining in the time domain.

The standard migration algorithm used in receiver function studies is based on ray-tracing. Each recorded event − with back-azimuth and ray-parameter given by the observation geometry or polarisation analysis − is traced back into the ground from the station using a 1-d velocity model. In this way, each time of recording can be associated with a given location (depth, latitude, longitude) in the subsurface, which is then assigned the conversion amplitude of the receiver function at this time.

A small error is introduced by using a 1-d velocity model; however, this technique has been routinely applied in many receiver function studies with good results [see, e.g., Kosarev et al., 1999, Gossler et al., 1999, Yuan et al., 2000, Ramesh et al., 2005]. Many studies rely on global Earth models, but since a 1-d velocity model for Costa Rica is available [Quintero and Kissling, 2001], this model (Table 4.3.7) has been used in the calculations presented here.

depth [km]	α [km/s]	β [km/s]
0 - 4	4.450	2.500
4 - 6	5.500	3.090
6 - 8	5.600	3.146
8 - 11	6.000	3.371
11 - 14	6.150	3.455
14 - 21	6.250	3.511
21 - 28	6.500	3.652
28 - 34	6.800	3.820
34 - 44	7.000	3.933
44 - 54	7.300	4.101
54 - 74	7.900	4.438
74 - 104	8.200	4.607
104 - 124	8.30	4.663
124 - 154	8.350	4.691
> 154	8.400	4.719

Table 4.1: *Velocity model used in the migration, [from Quintero and Kissling, 2001]. The P- to S-velocity ratio $\alpha/\beta = 1.78$ is assumed constant in this model.*

The subsurface volume traversed by the rays is divided into grid cells of $0.1° \times 0.1° \times 1$ km, with neighbouring grid cells overlapping by $0.01°$ and 0.1 km, respectively. The amplitudes of all rays crossing the grid cell are weighted with the peak-to-peak amplitude of the deconvolution spike on their L-trace and averaged. This creates a volume of conversion amplitudes that can be cut in different ways to provide migrated receiver function profiles.

4.3.8   Piercing Points

Closely related to the concept of migration and its implementation of tracing the rays back into the subsurface is the calculation of piercing points. Piercing points are the points in the subsurface at which the rays running towards a given station cross an imaginary surface placed at a given depth. They are where a conversion would occur if it occurred at that depth and therefore give a measure of the lateral spread of the rays underneath a station. To illustrate this idea, Figure 4.12 shows the calculated ray paths for all events recorded at stations crt-02 (Dominical), crt-08 (Río Blanco) and crt-14 (Guineal) and their piercing points at depths 100 km and 200 km. Due to the spread-out of the rays underneath each station, the latitudinal coverage of the network increases with depth.

In addition to providing a measure of the latitudinal coverage of the observed receiver functions, piercing points also show how well the area is covered. Overlap between piercing points of different events recorded at different stations indicates that the results are reliable in the sense that they are not derived from a single recording site, which might be influenced by local effects and errors. On the other hand, the density of piercing points is related to the resolution capability of the network at the given depth.
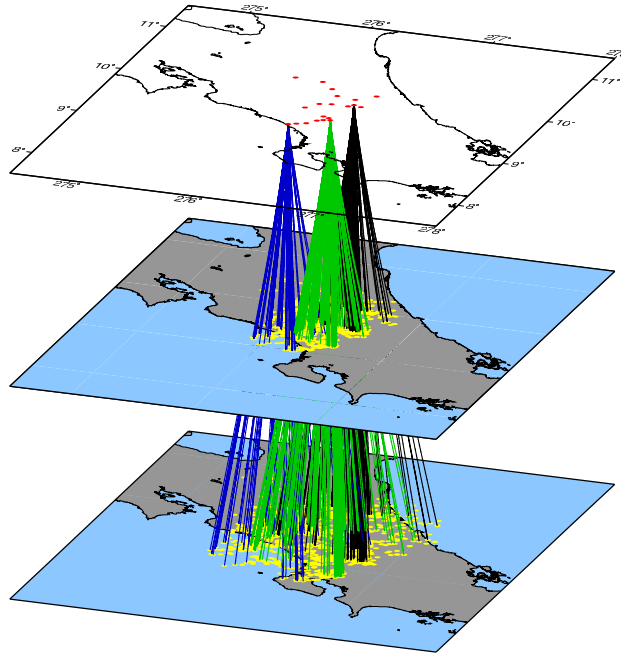

Figure 4.12: *The rays spreading out under the network are displayed for three stations (crt-02 in blue, crt-08 in green, crt-14 in black), together with their piercing points (yellow dots) at depths 100 km and 200 km.*

4.3.9 Bootstrap Method

The bootstrap method is a statistical test of the stability and accuracy of the observations [Efron and Tibshirani, 1986]. It is usually applied to receiver function studies by calculating the stacked trace for random sub-samples of the total observed receiver functions. If a signal is observed in all traces, it is a real conversion; if it only appears in some data subsets, it is probably produced by noise, very small heterogeneities or reverberations.

The discontinuities seen in the traces of the data subsets arrive at slightly different delay times, because the rays contributing to the conversions take different paths through the subsurface and hence probe a somewhat different region. Therefore, the variations in arrival time can be taken as an estimate of the uncertainties of the observed discontinuities.

In this study, the bootstrap method is applied to the migration algorithm. The data subsets are created by using only traces with even/odd running numbers. Hence there are two data sets half the size of the original data set, and with no overlap between each other.

For the stacked traces, an alternative test is presented that shows the results obtained by using *only* P, PP or PKP phases, respectively. This is different from the bootstrap test in that the number of traces stacked is different for all three cases, but what makes this test interesting is that it allows to see if the signals seen on the stacked traces are only produced in a given range of ray parameter and it shows if the results depend strongly on the number of traces stacked.

Chapter 5

Results

5.1 Talamanca Transect

5.1.1 Piercing Points

The piercing points for the Talamanca Transect are displayed for the expected Moho depth of 35 km and at 170 km depth in Figure 5.1. For depths in the crust and close to the Moho, there is a pronounced gap where the transect jumps northwards. This is closed at mantle depths, where the piercing points cover a much wider area from central Costa Rica to the edge of Osa Península.
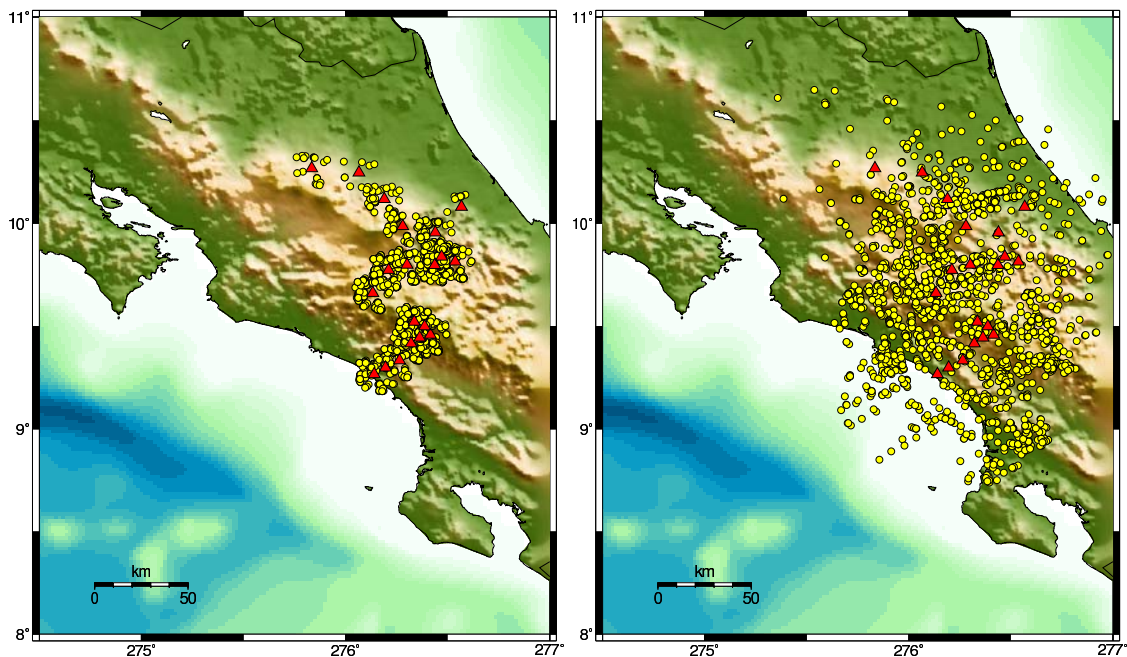

Figure 5.1: *Piercing points for Talamanca Transect stations at 35 (left) and 170 km (right) depth. Red triangles mark the transect stations.*

5.1.2 Stacked Section

For all Talamanca Transect stations, the receiver functions were weighted and stacked after filtering with a 2 s Butterworth low-pass. To give a better impression of the geometry of the observed structures, the stacked traces in Figure 5.2 were ordered by the station distance from the trench (crt-02 is at the Pacific coast, crt-26 is near Cimarrones, some 100 km further towards the Caribbean coast).
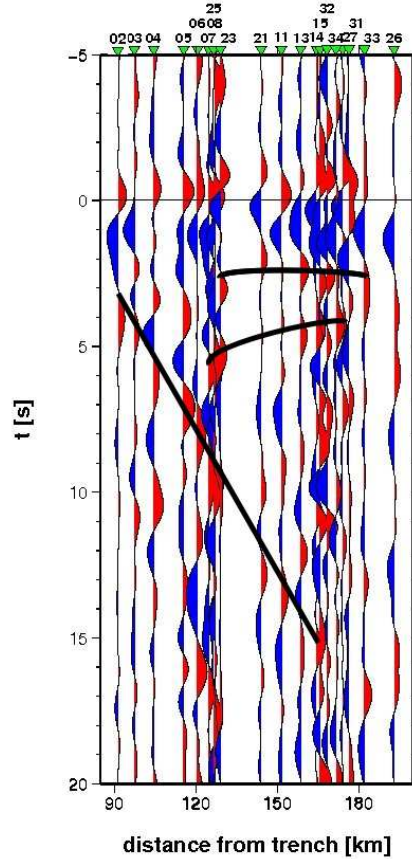

Figure 5.2: *Stacked radial receiver functions from the Talamanca Transect, ordered by distance from the trench. The black lines mark the most prominent features in the receiver functions*

The stacked traces show several prominent features. The coherent positive conversions corresponding to the main subsurface velocity contrasts are marked by black lines in Figure 5.2.

- All traces begin with a strong negative conversion shortly past 0 s delay time. This can be explained by a low-velocity layer in the uppermost crust.

- A strong positive conversion dipping steeply towards the East. This feature is clearly seen until station crt-13 (San Antonio Arriba), after which it seems to continue, but the depth cannot be determined without ambiguity. This positive conversion could represent the subducting Cocos Plate. The negative conversion that precedes the positive signal at some stations may be attributed to a low-velocity layer above the subducting Moho, possibly the

subducting oceanic crust itself or a sedimentary layer. Low-velocity layers above subducting slabs have been observed in various subduction zones (in receiver functions, this has been seen, e.g., by Yuan et al. [2000], Ferris et al. [2003], and has been more generally discussed by Abers [2005]). The negative signal may be explained by the crust of the subducting slab, the subduction channel or a hydrous mantle region. It becomes weaker with distance from the trench, until the subducting slab finally appears only as a positive velocity contrast.

- An inner-crustal discontinuity is seen as a band of positive conversions at around 2 s delay time.

- The Moho is imaged by a second band of positive conversions, following at 4-5 s delay time.

- For the stations very close to the trench, the subducting slab is still at shallow depth, disrupting the crustal signals. It is not clear in this region (stations crt-02 to crt-06) if the positive conversions belong to the inner-crustal discontinuity or to the Moho, or if the crust is disrupted in some way. It is also possible that the Moho appears as a negative conversion for those stations that have the subducting slab directly underneath the Moho (crt-05, crt-06 and possibly crt-04). A negative Moho signal has been observed in the Hellenic subduction zone [Li et al., 2003] and was explained by a velocity inversion in the mantle wedge, possibly due to serpentinization. Another possibility is that the lower-velocity subducting plate crust directly underlies the overriding plate lower crust, also creating a velocity inversion and making the Moho appear as a negative conversion in this setting (this effect was observed in the Aegean subduction zone by Sodoudi [2005]).

- Towards the Caribbean coast, the Moho seems to become slightly shallower and merges into the inner-crustal conversion at stations crt-31, crt-33 and crt-26. These data, however, should be handled with care, since all three stations only have few events and may not provide optimum resolution.

- The conversions seen underneath the Moho are hard to interprete and may be multiples. The Moho multiples are expected at around 10 s delay time; inner-crustal multiples would arrive before that, so the assumption is plausible. The strongly dipping features underneath the subducting slab are also multiples caused by the slab.

Figure 5.3 shows the result of the P, PP and PKP phases separately as a test of data quality: all these traces were combined to produce the image in Figure 5.2.

Although the combined stacked sections using all traces obviously produce the clearest image, the main features reappear in the data sub-sets. The PKP traces are very noisy, which is not surprising, given that there are only 43 PKP receiver functions in total; hence, some stations only have few traces or none at all. However, the PP traces already produce a rather good image as compared with the P traces (748 PP traces vs. 986 P traces). The dipping feature, Moho and crustal phase are all well imaged by the P and PP traces separately, and deviations in delay time between stacked traces at the same stations are always smaller than 1 s. The observed features are therefore stable and are taken to reflect real structures, with random errors in time smaller than 1 s and hence negligible in comparison with the low-pass filter width of 2 s.
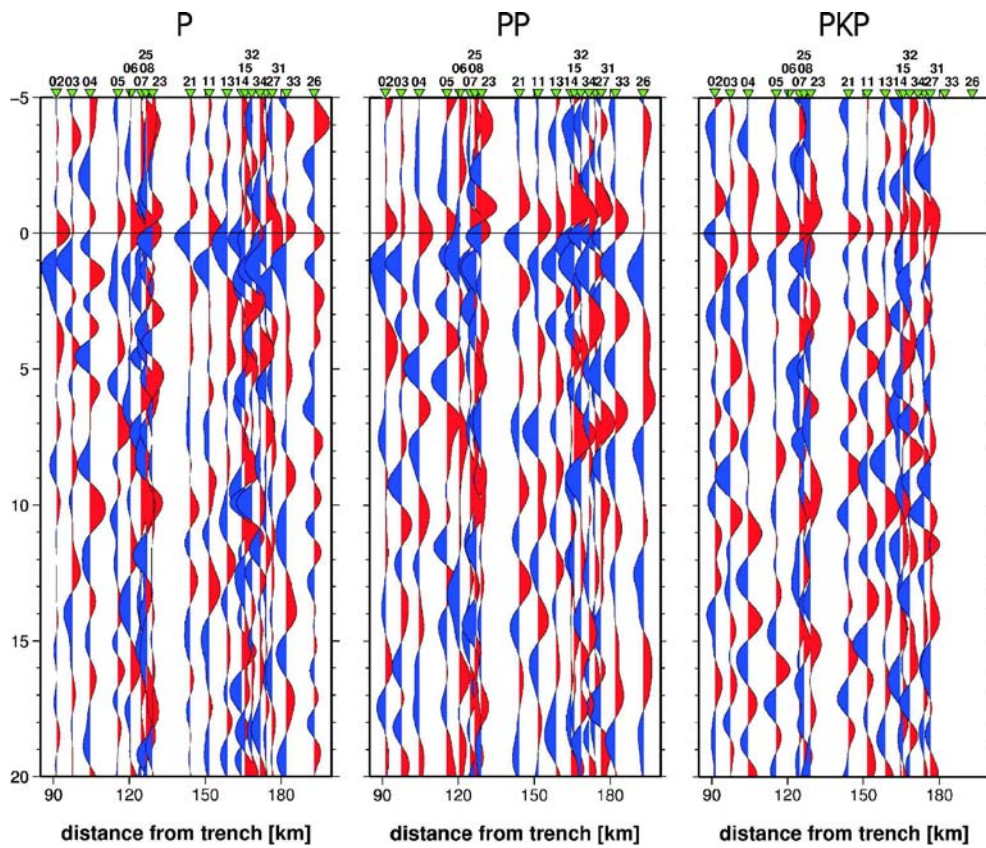
Figure 5.3: *Stacked radial receiver functions from the Talamanca Transect, ordered by distance from the trench. The representation follows Figure 5.2. Here, the stacked traces are shown separately for the P, PP and PKP phases, respectively.*

5.1.3 Migrated Images

The dipping feature in the stacked section suggests that the receiver functions should exhibit strong azimuthal variability, which in turn would be unsuitable for analysis by simple stacking. Therefore, a pre-stack depth migration was performed as explained in section 4.3.7. A migrated volume was created and gridded as explained; then several vertical slices were cut through the volume to be displayed as receiver function profiles through the area covered by the Talamanca Transect. For each profile, the values from grid cells within a thin layer around the profile plane were projected onto the surface and averaged with a moving-average weighted mean. In the migration, the data from three additional broad-band seismometers operated by the ETH Zürich was included. Figure 5.4 shows the receiver function profiles analysed.
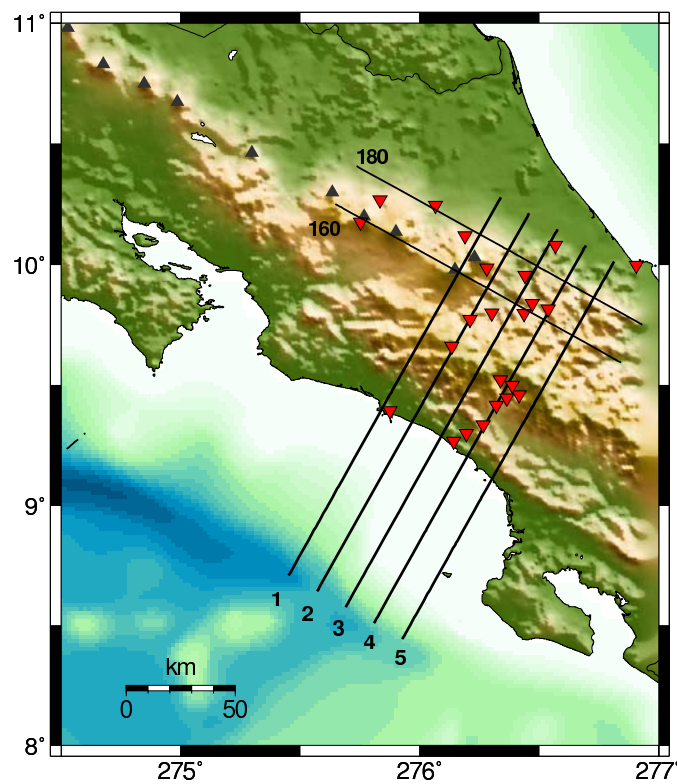
Figure 5.4: *Map of receiver function profiles through the migration volume. Profiles 1-5 start approximately at the trench and run normal to the trench (about N30°E) for* 200 km. *The spacing between these profiles is* 45 km. *Profiles 160 and 180 are approximately trench-parallel, at distances of* 160 km *and* 180 km *from the trench. Black triangles mark volcanoes, red inverted triangles the position of the Talamanca Transect stations and ETH Zürich broadband stations.*

It was found that deep structures were most easily seen when the receiver functions were low-pass filtered below 5 s, corresponding to about 25 km resolution. This smoothed over much of the noise that obscured the deeper parts of the migration amplitudes. To resolve crustal structure, a higher-frequency cut-off was needed. Therefore, the upper parts of the volume were calculated after 1 s low-pass filtering of the receiver function traces. Figure 5.5 shows the low-frequency results

for depths down to 200 km, Figure 5.6 the same migration applied to the 1 s filtered traces. In both cases, a Gaussian filter was applied to the final profile before plotting to remove any artefacts produced by cutting the smoothed cube along an inclined surface.

Radial receiver functions – Low-frequency profiles

A bootstrap-test was performed for all profiles; however, results are displayed only for profiles 2 and 5 in Figure 5.7. The centre profile evidently achieves best results in the bootstrap test, therefore profile 2 is shown as an example for the average data quality and profile 5 for the worst network coverage. The bootstrap test confirms the major features identified in the migrated profiles, and deviations in the depth of converted signals are smaller than the depth resolution that is achieved after filtering with a 20 km and 7 km running average, respectively.

In the low-frequency data, a strong positive conversion is seen dipping towards the East with a steep dip angle of about 60° relative to the horizontal. The velocity contrast that causes the dipping conversion is interpreted as the Moho of the subducting slab, where a positive velocity contrast occurs no matter what the seismic velocity of the dipping oceanic crust is in comparison with the overlying crust or mantle wedge. Therefore, the subducting Moho is thought to be positioned at the zero crossing from the negative to the positive conversion, which will not be shifted even when the signals are broadened by filtering.

The signal interpreted as the subducting plate (henceforth called the slab signal) is imaged dipping with an angle of approximately 60° down to a depth of 150-180 km, depending on the profile. In the bootstrap tests, this is unequivocally confirmed down to depths of at least 100 km even in the southern and northern profiles where coverage becomes poor. Even though some distortion in the slab signal is observed, linked probably to the occurrence of multiples, a continuation of the slab to depths in excess of 150 km is plausible.

A marked lateral change in slab dip angle cannot be seen. At its upper end close to the Costa Rican Pacific coast, a kind of "bump" is seen in the dipping conversion. This is most probably caused by smearing of the positive slab signal with the overlying crustal signals, which may be the Moho or inner-crustal discontinuities.

Between 100 and 150 km depth, the positive conversion is thinned and in some profiles interrupted, but reappears again about 10 km further down. This is probably due to the interference by crustal multiples, which can be expected to arrive around this time. They are observed around 100 km depth at the outer edges of the profiles.

The positive conversions dipping steeply around 150-200 km depth in the south-western edge of the profiles correspond to slab multiples. This will be made clear when modelling studies are performed (see Chapter 6).

The Moho of the overriding plate and crustal structures are all smeared together by the broad filter into a pronounced positive signal observed at 30-40 km depth. For the interpretation of crustal structure, it is preferable to consider the higher-frequency receiver functions displayed in Figure 5.6.
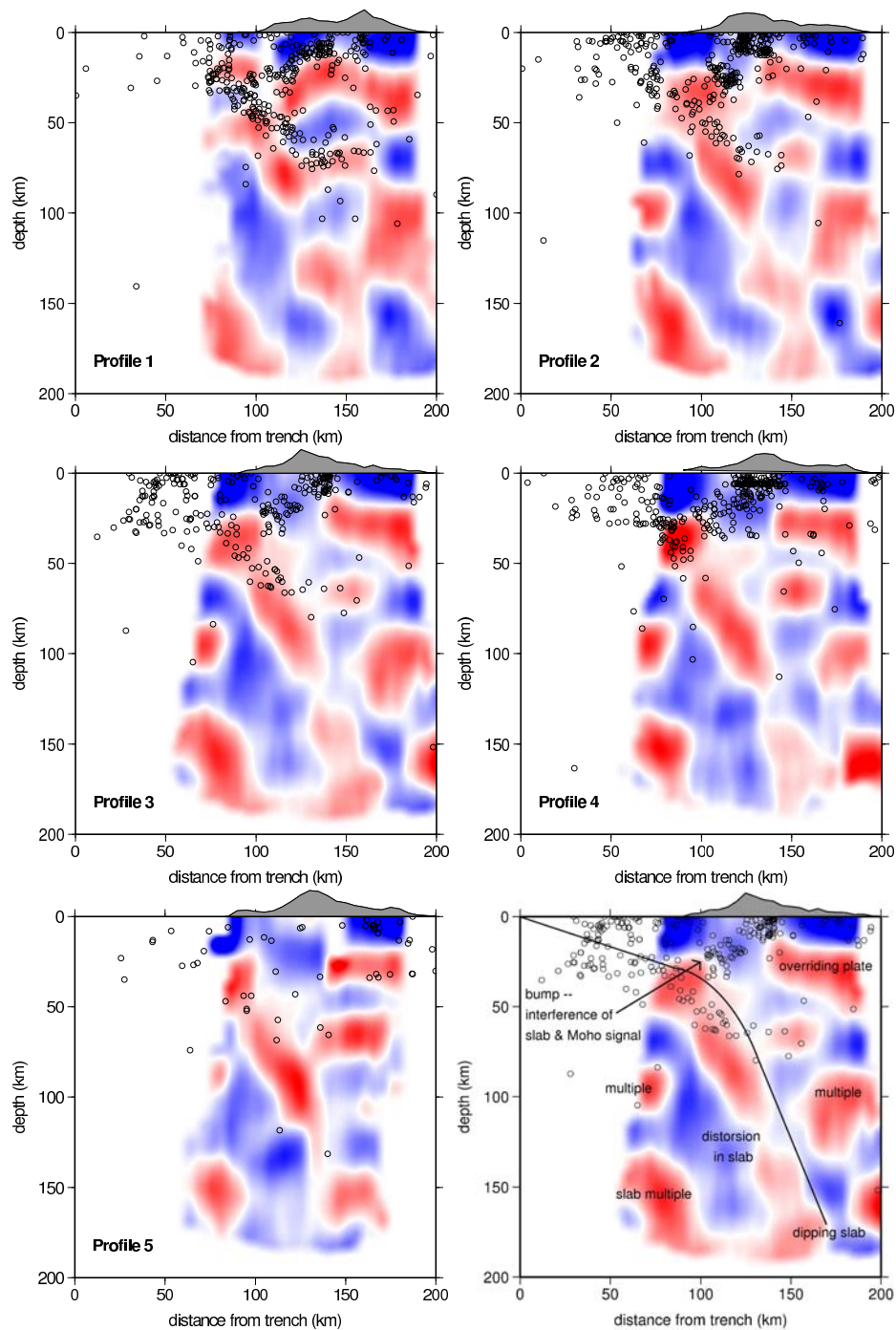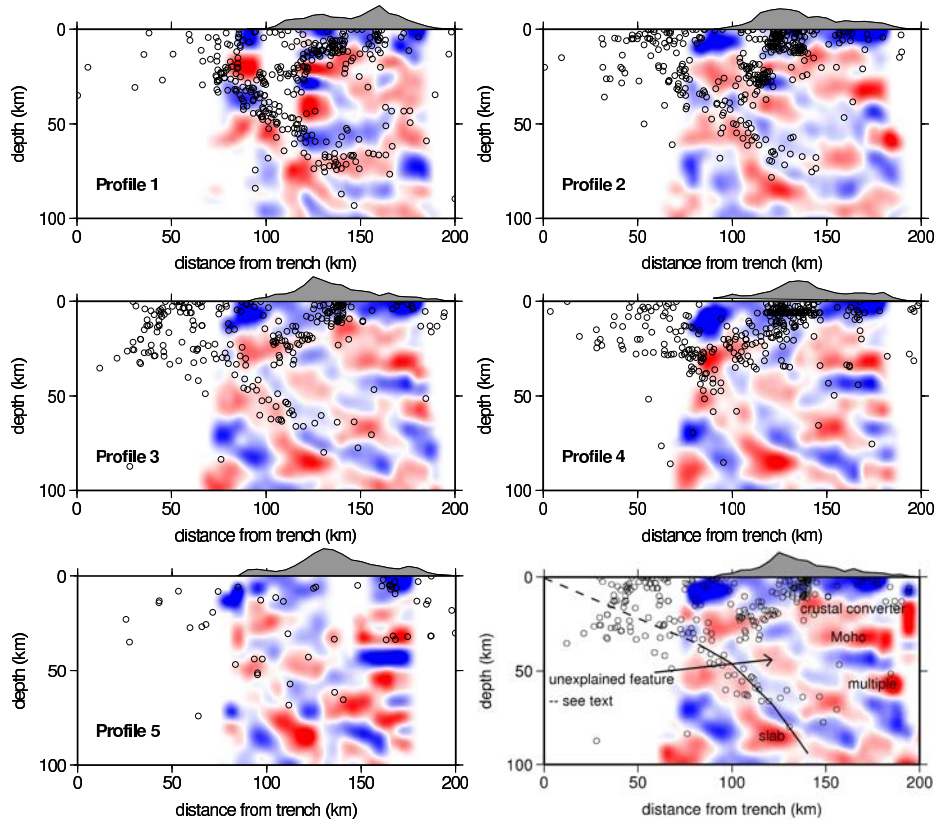
Figure 5.5: *Low-frequency receiver function profiles through the migration volume. Receiver functions were low-pass filtered below 5 s before migration. Red amplitudes denote positive conversions, blue amplitudes negative conversions. Upper left: profile 1 (in the north-west), lower left: profile 5 (in the south-east). The migrated sections were smoothed with a 20 km Gaussian filter before plotting. The topography is overlain in grey, with an amplification factor 4. Black circles indicate earthquake epicenters observed by the Quepos network. Lower right: annotated version of the central profile (profile 3), for easier interpretation.*

Figure 5.6: *High-frequency trench-normal receiver function profiles through the migration volume. Receiver functions were low-pass filtered below 1 s before migration. The migrated section was then smoothed with a 7 km Gaussian filter before plotting. Red amplitudes denote positive conversions, blue amplitudes negative conversions. Upper left: profile 1, lower left: profile 5. The topography is overlain in grey, with an amplification factor 4. Black circles indicate earthquake epicenters observed by the Quepos Network. Lower right: annotated version of the central profile (profile 3), for easier interpretation.*
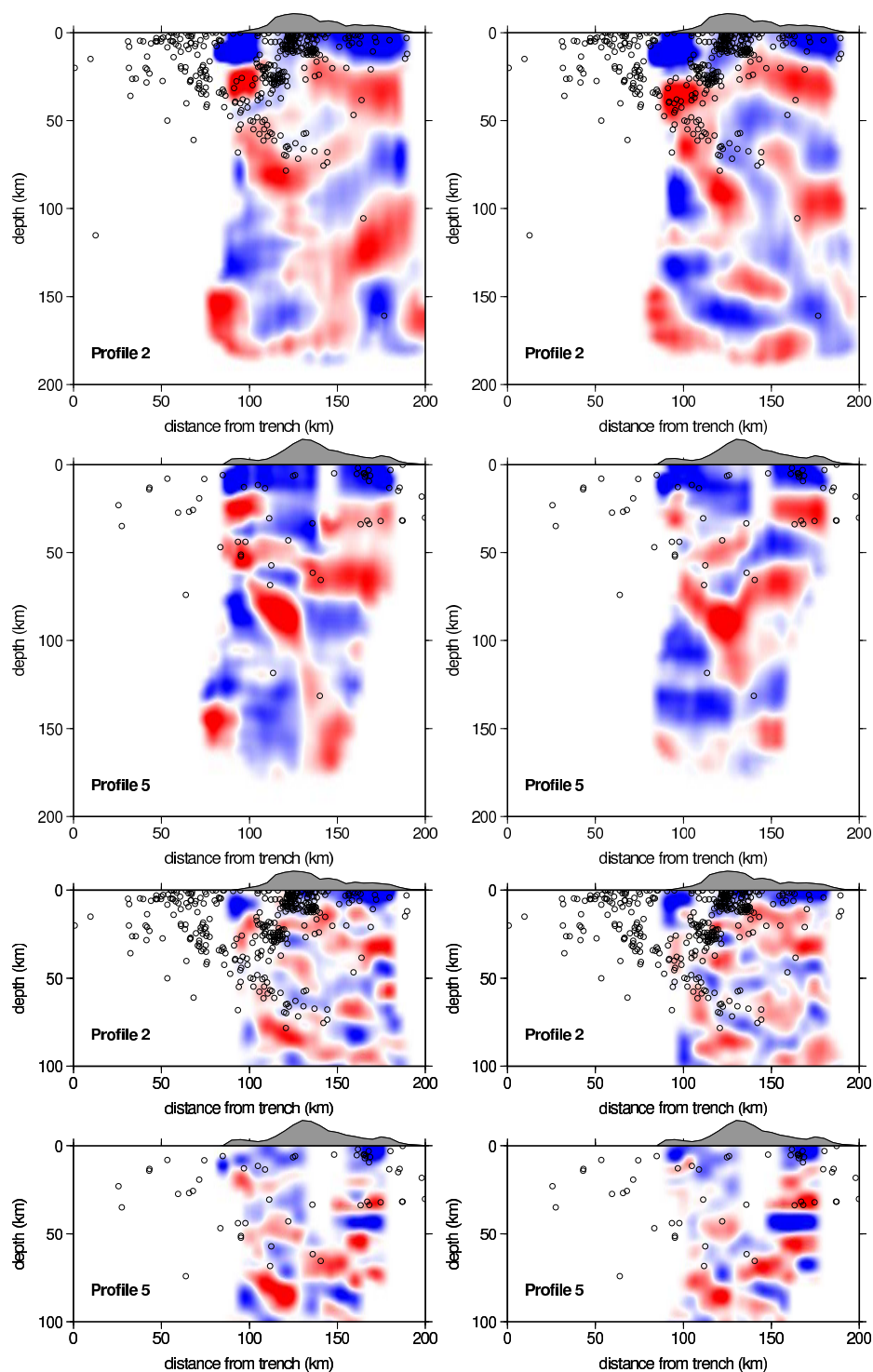
Figure 5.7: *Bootstrap-test for migrated receiver function profiles. Left panels: migration using odd-numbered traces; right panels: migration using even-numbered traces. Receiver functions were low-pass filtered below 5 s before migration. Red amplitudes denote positive conversions, blue amplitudes negative conversions. Upper panels: profile 2, receiver functions low-passed below 5 s, below: profile 5, same filtering. Lower panels: profiles 2 and 5, respectively, with a low-pass filter below 1 s. A Gaussian filter was applied before plotting like in Figures 5.5 and 5.6. The topography is overlain in grey, with an amplification factor 4. Black circles indicate earthquake epicenters observed by the Quepos network.*

Radial receiver functions – High-frequency profiles

In the high-frequency images, the Moho is seen as a prominent positive conversion at 35-40 km depth underneath the northern flank of the Talamanca Range. It appears at about the same depth in all the profiles and is nearly horizontal. Above, there is a second positive conversion at 15-20 km depth, which is identified with an inner-crustal velocity discontinuity. The two features are distinctly imaged in the north-eastern parts of the profiles, starting at about 150 km distance from the trench, and are confirmed by the bootstrap-test.

Closer to the trench, the signals are less clear. A positive discontinuity is imaged above the subducting slab in most profiles at around 25 km depth. This is then disrupted by a slightly deeper positive feature, while either a gap occurs in the overlying crustal and Moho conversion, or a small positive feature links the two-layered conversions in the east with the one positive conversion in the west. The interpretation of these features is difficult, and it may be that the subducting slab disrupts the overlying crust in a way to make the interpretation in terms of a simple model and scales of 10 km impossible.

While the features observed between 50 and 100 km depth are probably crustal and Moho multiples, the positive conversions between 100 and 150 km distance from the trench cannot be caused by overlying structure. Their appearance on several profiles and in the bootstrap-test show that they must be real. The explanation is unclear, the following hypotheses are suggested:

- The crust may be bent down towards the subducting slab, which drags it down to some degree.

- Crustal blocks may have been broken off, possibly rotated.

- There may be the ascent of melts or hydrated material, which would be seen as a low-velocity feature. (But the normal-velocity material around it would then again produce a positive conversion.)

- The geometry may be quite "simple", but the relative velocities may be changed by fluids or temperature, giving rise to complicated conversions.

In any case, it becomes clear from the high-frequency images that the "bump" in the subducting slab seen in the low-frequency images is just an effect of smearing the slab signals into the crustal conversions. The upper part of the subducting slab is therefore determined from the high-frequency images, by following the boundary between the high-velocity dipping signal and the overlying negative conversion. This part of the subducting slab dips less steeply, with an angle of about 50°. The slab seems to bend and give over to even shallower subduction at its upper end.

There appears to be a consistent negative conversion directly above the positive dipping slab conversion. This would indicate the presence of a low-velocity layer, as explained above.

Comparison with seismicity

The seismicity observed by the Quepos network is projected onto the profiles for events that occurred within 5 km to either side of the profiles. A similar distribution of seismicity was observed by the Talamanca Transect itself; however, the analysis of the seismicity recorded at the Talamanca stations has not been completed yet and many more events are available for the Quepos network. This is why the analysis of seismicity will concentrate on the Quepos observations, even though

the Quepos network was slightly to the north of the Transect and therefore some lateral change may be expected.

It can be seen that the slab reaches down to much greater depths than the seismicity. The seismicity is confined around the Moho of the subducting slab, with some events reaching upwards from the slab to the volcanic chain. Allowing for some uncertainty in the depth of the slab (the 1 s filtered traces will not allow for more than about 5 km depth resolution, and an additional error will be introduced by using a 1-d velocity model that was optimized for Costa Rica, not for the study region), the seismicity is in good agreement with the observed slab signal.

The shallowing of the slab close to the trench to dip angles of 50° or less corresponds well with the observed seismicity. Close to the trench, the seismicity follows approximately an 18° dipping line that meets with the dipping slab at the edge of the receiver function profile.

Interestingly, the disruption of the Moho and innercrustal signal in the receiver function profiles coincide with seismicity reaching upwards towards the volcanic chain at an angle of about 45°. It may be speculated that the negative signal observed in receiver functions in this area could be caused by the ascent of fluids or melt, characterized by a low-velocity zone and seismic activity.

Receiver function profiles parallel to the trench

Two trench-parallel sections through the migration volume were calculated in the same way as the trench-normal profiles for the high-frequency receiver functions (Figure 5.8). These profiles are at distances of 160 km and 180 km from the trench, respectively, because the north-westwards extension of the network provides good lateral coverage in this region.
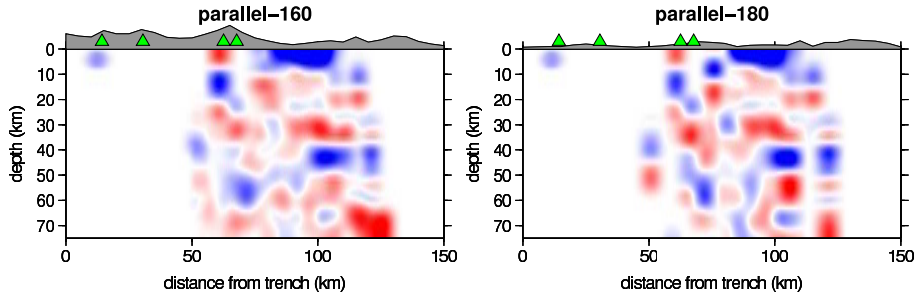

Figure 5.8: *Trench-parallel receiver function profiles through the migration volume. Receiver functions were low-pass filtered below* 1 s *before migration. Red amplitudes denote positive conversion, blue amplitudes negative conversions. The migrated section was then smoothed with a* 7 km *Gaussian filter before plotting. The topography (exagerated by a factor 4) is shown in grey, where green triangles mark active volcanoes. Left: profile 160, right: profile 180*

Like in the trench-normal profiles, the inner-crustal discontinuity at 15-20 km depth and the Moho at about 35 km depth are clearly imaged in the trench-parallel profiles. Unter the Talamanca mountain range, the Moho shows no significant variations in depth. Both the Moho and the crustal discontinuity have very uniform topography over several tens of kilometers into the Talamanca. This picture changes close to the end of the active volcanic chain, where both the Moho and crustal

discontinuity are disrupted. Underneath Irazú and Turrialba volcanoes, a strong negative conversion is observed at 10-20 km depth. This may indicate the presence of melt, possibly in a magma chamber or plumbing system.

To further analyse lateral changes in the structure of the subducting and overlying plate, a 3-d analysis was made to visualize the combined results from different profiles. The results from this study will be presented in Chapter 5.3.

Transverse receiver functions

The conversions seen on the transverse components are very complicated and will not be analyzed in detail here. Modelling results for the transverse components observed in very straightforward geometries will be shown in Chapter 6. Here, only the high-frequency migrated sections are shown for a comparison with the radial components. The long-period migrated sections are displayed in Appendix C, as their quality is very bad. These images are heavily impared by noise, and small-scale structures are blurred by filtering over low frequencies, so no interpretation is attempted.
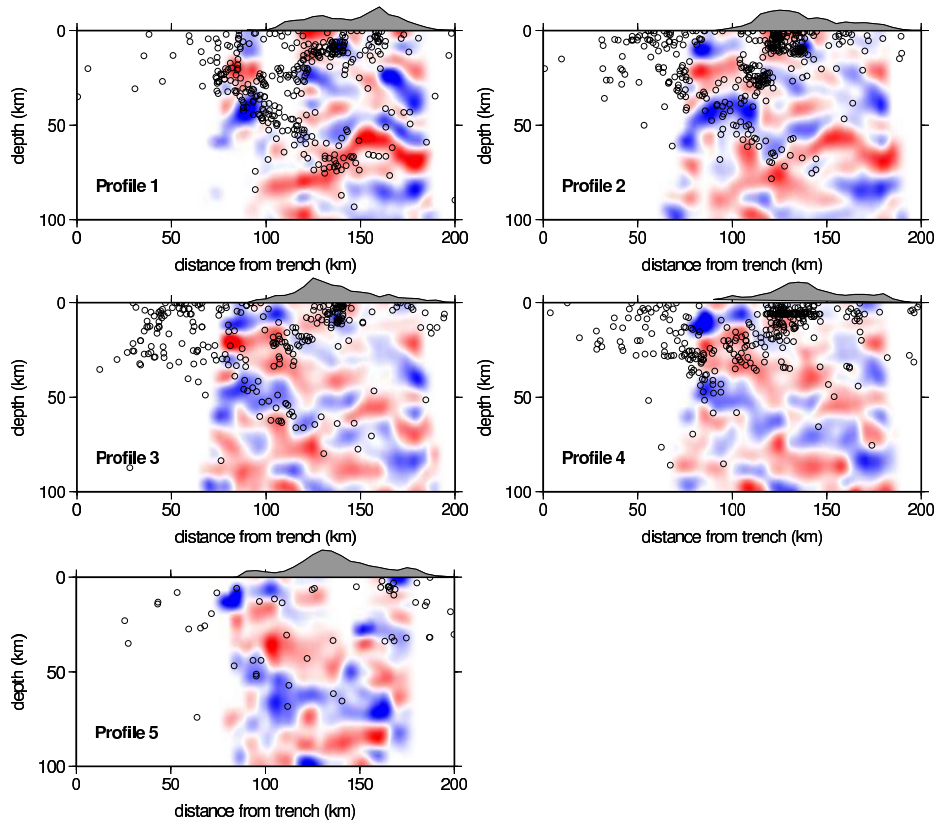
Figure 5.9: *Trench-normal transverse receiver function profiles through the migration volume. Quepos network seismicity is overlain, the topography is exaggerated by a factor 4.*

While the noise is generally high and no coherent large-scale conversions are seen in the transverse profiles, some general features are observed in the better resolved profiles. In profiles 2-4, a dipping feature appears at about $100 - 150$ km distance from the trench, collinear with seismicity. This corresponds to a similar feature observed in the radial receiver functions, though the signal is less clear on the transverse component. Hence it seems plausible that this conversion is due to the dipping oceanic slab.

Some crustal structure around 15 km depth is suggested by profiles 1-4, with a clear change in the crustal structure underneath the mountain range. A disrupted Moho conversion can also be seen in some plots, heavily relying on our expectations from the radial receiver function images. However, the crustal structure and Moho cannot be clearly identified and their topography remains elusive in these plots.

Even though the interpretation of the transverse migrated images relies heavily on our knowledge from the radial components and does not provide further independent insight into the subduction zone structure, the fact that there *is* energy on the transverse component proves that dipping structures and/or anisotropy must exists underneath the stations. The topic of dipping features and anisotropy and their influence on receiver function studies will be further analyzed in Chapter 6.

5.2   Quepos Network

From the Quepos network, a total of 100 receiver functions were obtained for 39 events with magnitude > 5 occurring at epicentral distances of 30-180° (P, PP and PKP phases). Since the Quepos stations do not provide long-period recordings, filtering over periods longer than 1 s is not sensible. We will therefore concentrate the following analyses on the relatively short-period recordings at frequencies around 1 Hz.

While the receiver functions obtained from the Quepos stations show the most notable subsurface features, their interpretation is less clear than for the Talamanca Transect stations, mainly because of the smaller number of available events (and hence, traces) and the resulting lower signal-to-noise ratio. Furthermore, the area sampled by the Quepos receiver functions is concentrated around Quepos, at the Pacific coast. The results from the Quepos stations will thus be presented jointly with the analogous results obtained from the Talamanca Transect, which will present the broader framework for the analyses of the Quepos observations. An example of an earthquake recorded by the Quepos station Dominical is compared with a similar event recorded by the Talamanca Transect station crt-02 (at the same location) in Appendix D.

5.2.1   Piercing Points
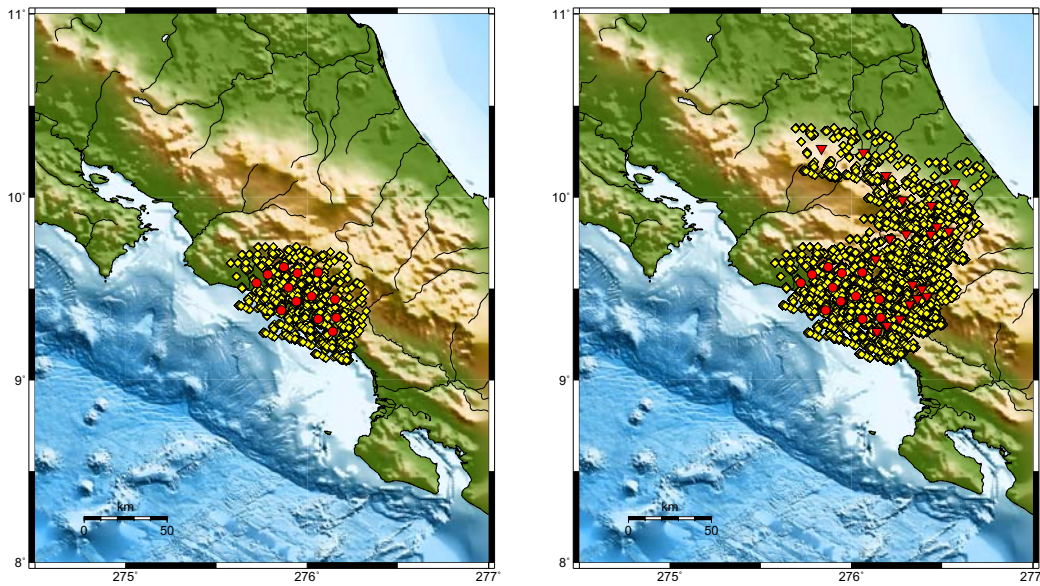
Figure 5.10: *Left: Piercing points for the Quepos stations at* 35 km *depth. Right: Combined piercing points for the Quepos stations (red circles) and Talamanca Transect stations (red inverted triangles) at* 35 km *depth.*

The piercing points for the Quepos stations are shown in Figure 5.10. As noted before, only the near-coastal region is sampled by the receiver functions of the Quepos network. Once the Quepos

data is combined with the recordings of the Talamanca Transect, however, the spatial coverage is greatly increased. The Quepos network fills the coverage gap produced by the north-westwards jump of the Talamanca Transect (compare Figure 5.1), thus providing good lateral coverage at crustal depths on the Pacific side of the mountain range.

5.2.2 Stacked Section

The radial receiver functions were filtered with a 1 s Butterworth low-pass and stacked like in the case of the Talamanca Transect stations (Section 5.1.2). Both the stacked Quepos and Talamanca Transect receiver functions are displayed in Figure 5.11, ordered by distance from the trench.
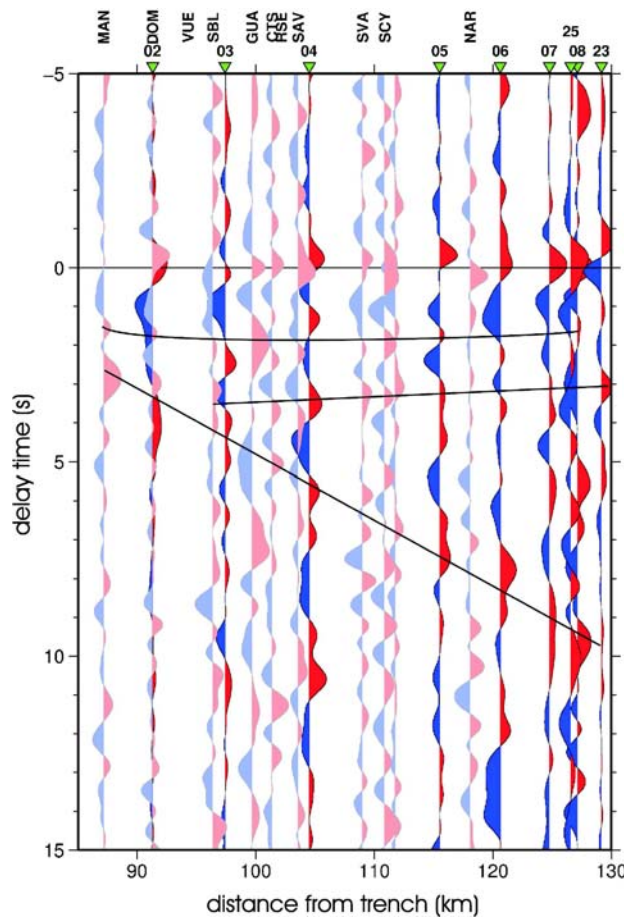
Figure 5.11: *Stacked radial receiver functions from the Quepos network (light colours) and southern section of the Talamanca Transect (intense colours), ordered by distance from the trench (in km). The black lines mark the most prominent features in the receiver functions. The vertical axis is the delay time (in s). The stations crt-02 and DOM were installed at the same place, in Dominical, and are therefore plotted at the same distance from the trench. See Appendix D for a comparison of the two sites.*

At crustal levels, the Quepos data show coherent positive conversions at 1.5-2 s and 3-4 s, interpreted as a crustal discontinuity and the Moho, respectively. These observations agree very well with the stacked receiver functions from the Talamanca Transect, which also show these two prominent features. Above the inner-crustal discontinuity, strong negative conversions are observed, confirming the hypothesis of a low-velocity upper crustal layer suggested based on the stacked receiver functions of the Talamanca Transect.

The dipping positive conversion observed at the Talamanca Transect stations is also present in the Quepos recordings, although it is somewhat obscured by the high noise level in the available frequency range. At these relatively high frequencies, the dipping slab is also seen less clearly on the Transect stations, as compared with the longer-period receiver function images. While the quality of the Quepos data is not sufficient to identify the dipping slab clearly on the basis of this dataset alone, it is consistent with the interpretation of the dipping slab seen by the Talamanca Transect.

The Quepos stations fill the gaps between the Talamanca Transect stations, providing better sampling at smaller scales (smaller steps in distance from the trench). The behaviour of the crustal structure and Moho closer to the trench is better resolved by the inclusion of the Quepos stations. The combined stacked section suggests that the innercrustal discontinuity at 1.5 s delay time persists all the way to the coast, while the Moho is observed at least until about 95 km distance from the trench, where the descending slab is close underneath the overriding plate, with a delay time difference of less than 1 s.

Taking into account the fact that the Quepos stations sample a region to the north of the Talamanca Transect, the good correspondence of the results from both networks suggest that no strong change in the principal subduction zone geometry occurs over a distance of $50 - 100$ km along the coast, concerning the crustal discontinuity and Moho in particular, but also the indication for the subducting oceanic slab.

5.2.3   Migrated Images

For the pre-stack depth migration, the receiver functions from the Quepos network and Talamanca Transect were combined into a single volume. The volume was then plotted in the same way as for the Talamanca Transect stations and cut along the same trench-normal profiles. Since only short-period recordings were available from the Quepos network, only the short-period profiles (smoothed over 7 km) are shown in Figure 5.12.

The consideration of the piercing points (Figure 5.10) makes it clear that the Quepos stations contribute most to the migration volume close to the coast, in the northern and central profiles. Towards the south, in the east, and at depth the Talamanca Transect stations dominate. Profile 5 contains almost no contribution from the Quepos stations and is therefore not shown in the figure – it shows the same results as the migrated profile based on the Talamanca Transect data only (Figure 5.6). On the other hand, the Quepos stations serve to fill the gap produced by the jump in the Transect, filling profiles 1-3 closer to the coast and generally improving coverage at shallow depth.

At distances of 130-150 km and more from the trench, the crustal discontinuity and Moho are again seen, with rather smooth topography. Underneath the mountain range, this picture changes: The Moho is disrupted and takes on a shallow dipping and somewhat blocky appearance. The
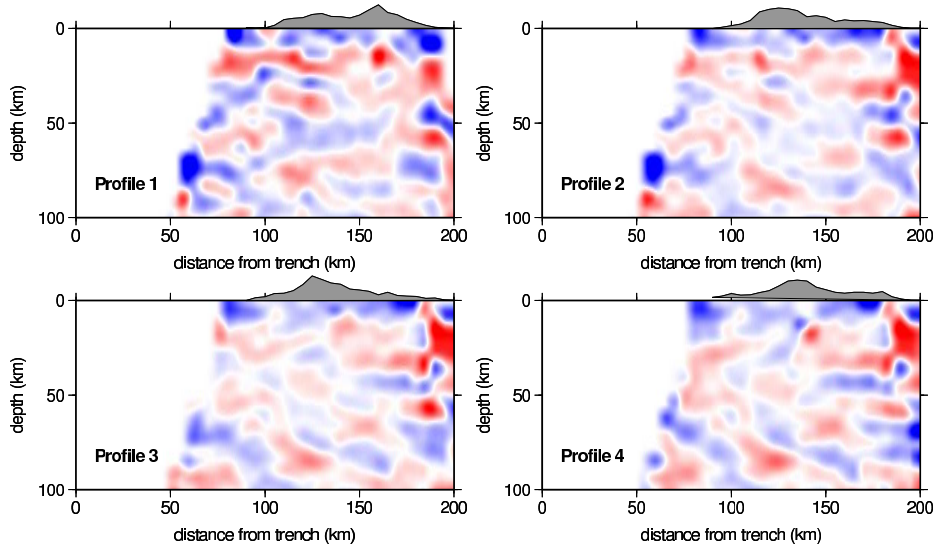
Figure 5.12: *High-frequency trench-normal receiver function profiles through the migration volume, combining Quepos and Talamanca Transect stations. Receiver functions were low-pass filtered below 1 s before migration. The migrated section was then smoothed with a 7 km Gaussian filter before plotting. Red amplitudes denote positive conversion, blue amplitudes negative conversions. Upper left: profile 1, lower left: profile 4. Profile 5 is not shown since the Quepos stations contribute little to the data volume in this region. The topography is overlain in grey, with an amplification factor of 4.*

crustal structure seems to continue throughout the observed volume for profiles 1-3, but is interrupted in the southern profile.

With the exception of profile 1, which almost completely relies on the Quepos data close to the trench and therefore has poor resolution at depth in this region, the profiles show a dipping positive conversion similar to the feature seen in the Talamanca Transect migrated profiles. This is again taken as evidence for the dipping slab.

Besides improving the coverage of the network further towards Central Costa Rica for shallow depth, the migrated profiles including the Quepos dataset do not provide new insight into the structure of the subduction zone. However, the enlarged area makes it worthwile to look for lateral changes in the subduction zone geometry. While the profiles show the most significant features of the system at depth, they are not well suited to analyse the lateral changes. A 3-d visualisation was therefore used to better image the observed structures and make the analysis of lateral changes and comparison with other results more intuitive.

5.3   3-d Visualisation of Results

To produce a 3-d image of the observed discontinuities, profiles across the migration cube were produced at distances of 5 km and loaded into the GoCad software. The Moho, crustal discontinuity and dipping slab were visually picked at distances of a few kilometers along each profile (shown schematically in Figure 5.13 for the short-period profiles).
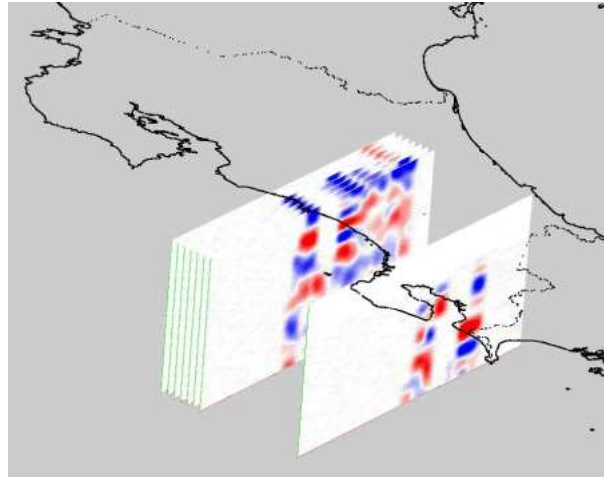
Figure 5.13: *Creation of 3-d surfaces based on* 5 km-*spaced profiles.*

The Moho and crustal discontinuity were picked approximately in the maximum of the positive conversion, the position of which should not be significantly affected by filtering. The descending slab was picked along the zero crossing above the positive dipping conversion, because the slab is expected to appear as a bipolar conversion, with a negative pulse corresponding to the low-velocity sediments and crust and a positive conversion produced at the oceanic Moho. When this signal is broadened by filtering, the zero crossing should remain at the same depth, while the negative and positive pulse spread out.

Surfaces were adjusted to the individual picks and smoothed slightly. The uncertainty of the results involves the following contributions:

- errors in the profile: the bootstrap test performed in Section 5.1.3 shows that the depth of the conversions is constrained within the errors produced by filtering with a 20 km and 7 km running average for the 5 s and 1 s traces, respectively. The crustal features were picked using the 1 s profiles, while the slab was picked along the 5 s profiles at depth below 100 km and along the 1 s profiles at shallower levels. At the edges of the profiles, errors may be greater, because the ray coverage becomes small and noise recorded by a few traces may appear as a strong signal. However, this effect is limited to the outer edges of the profiles and care was taken to supress grid cells with a low number or crossing rays.

- errors in the picks: visual picking includes some uncertainty in the decision at what depth to place the picks. In any case, these are significantly smaller than the width of the conversions seen in the profiles, i.e., smaller than the 7 km and 20 km filter width, respectively.

- smoothing of the surfaces: care was taken so that the smoothing process would not obliterate any structure observed in the individual picks. In particular, the position of the picks were not changed by more than the above noted uncertainty.

The overall error resulting from this procedure should therefore be within the original uncertainty introduced by the averaging process. However, systematic errors cannot be ruled out, e.g., the effects of the velocity model used in the migration.

Example views of the 3-d visualization are shown in Figure 5.14. The depths of the slab, the Moho and the crustal discontinuity are plotted in map view and "flying carpet" representation in Figures 5.15 to 5.17.
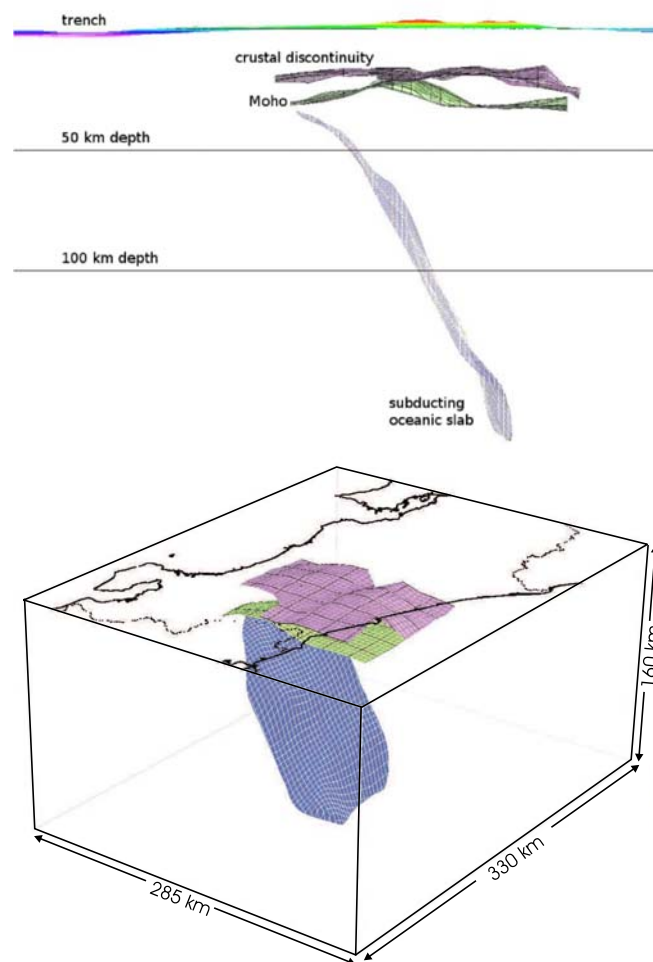
Figure 5.14: *Upper panel: Side view of the 3d-surfaces, looking northwestward parallel to the direction parallel to the trench. Surface topography is colour-coded. Lower panel: oblique view looking from the North. The coastline and frontiers between Costa Rica, Nicaragua and Panama are plotted for better orientation. No vertical exaggeration is applied in the plots.*
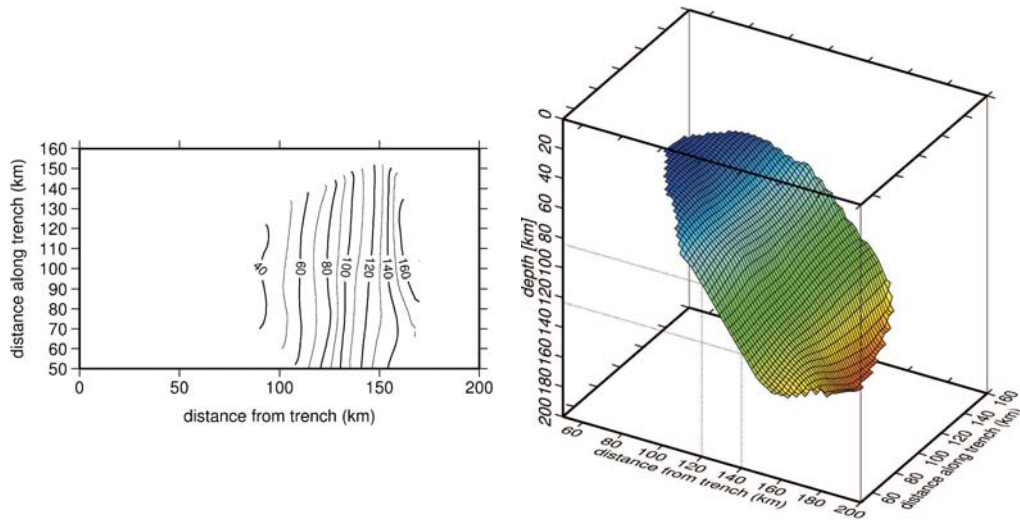
Figure 5.15: *Depth of subducting oceanic slab. Left: contour plot, right: "flying carpet" view. Distance along the trench is increasing southwards, like in the parallel migration profiles.*
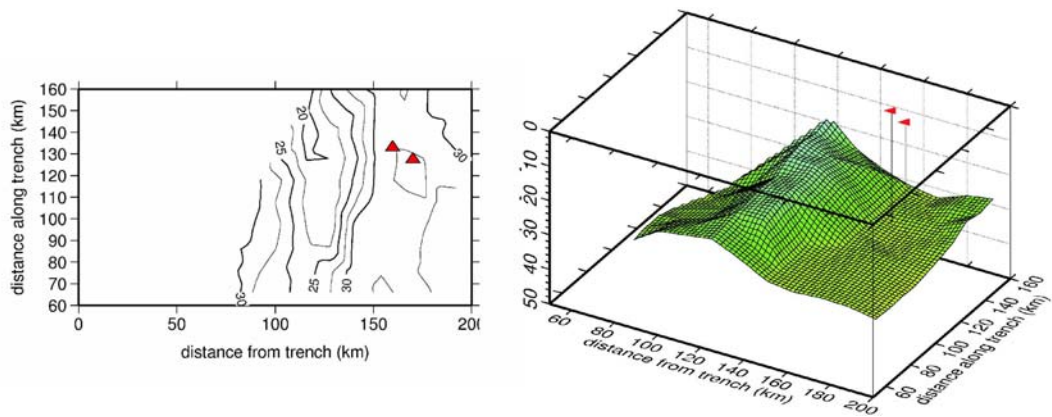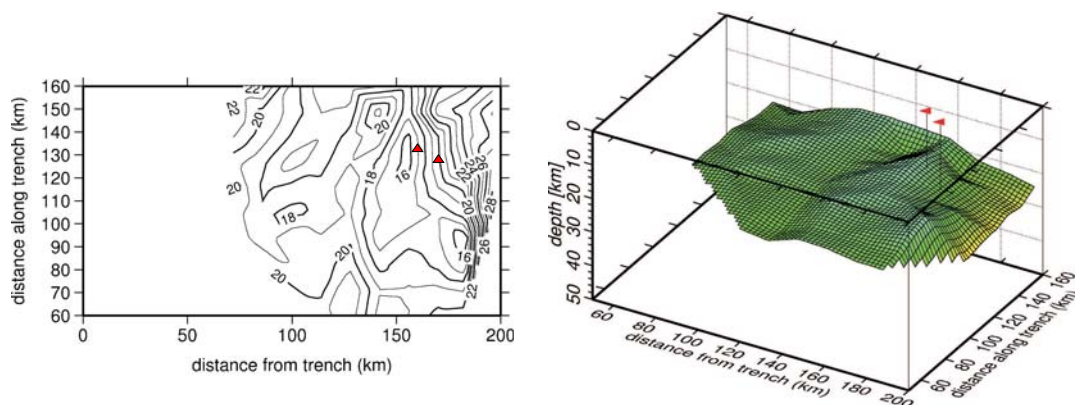

Figure 5.16: *Moho depth of the overriding plate. Left: contour plot, right: "flying carpet" view. Distance along the trench is increasing southwards, like in the parallel migration profiles. Red triangles mark the volcanoes Irazú and Turrialba.*

In the 3-d combined image from all the profiles, the slab is observed starting at a distance of 80 km from the trench, at a depth of 34 km, and reaches a depth of 170 km at 170 km distance from the trench. As Figure 5.15 shows, the dip angle of the slab is about 63°, remaining constant over the whole lateral extent of the region sampled by receiver functions (over 120 km). In particular, the slab shows no sign of shallowing towards the South.

The Moho depth obtained in this analysis (Figure 5.16) shows a strong variation normal to the trench, with shallow depths of around 20 km at about 130 km distance from the trench giving over to a "normal" Moho depth of about 35 km at larger distances. It is probable that the apparent shallowing at smaller distances is caused by interference of the Moho signal with the slab signal that is located at shallow depth; or the Moho is indeed distorted by the interaction with the subducting plate. Lateral variations in depth are small, but it appears that the Moho unterneath the volcanoes Irazú and Turrialba might be slightly depressed. However, a Moho depression of this order of magnitude (2 km) cannot be confidently resolved due to filtering over 7 km and errors caused by visual picking.

The depth of the crustal discontinuity is 19 km on average, with variations of about 5 km. The larger excursions at the edge are probably a boundary effect due to poor sampling in this region. The depression in this discontinuity at 120 km distance from the trench coincides roughly with the shallowing of the Moho, and may be caused by interference of these two signals with the slab and with each other, rather than by the real subsurface structure.

Figure 5.17: *Crustal interface in the overriding plate. Left: contour plot, right: "flying carpet" view. Distance along the trench is increasing southwards, like in the parallel migration profiles. Red triangles mark the volcanoes Irazú and Turrialba.*

While the lateral changes in the subduction zone geometry in the direction parallel to the trench are small, Figure 5.18 shows that some influence of the edge of the volcanic chain may exist. In this representation, it can be seen that the Moho curves slightly away from the volcanoes, while the crustal discontinuity appears bulging upwards. The changes are small and of comparable magnitude to the filter width and overall depth uncertainty of the interfaces, so this observation cannot be regarded as definite evidence, only as an indication of changing structure at the beginning of the volcanic chain.
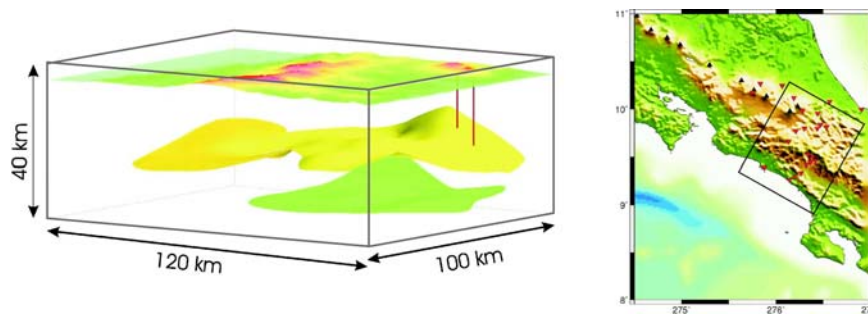
Figure 5.18: *Crustal discontinuity and Moho under the volcanoes Irazú and Turrialba. Yellow surface: crustal discontinuity, green surface: Moho. The red lines link the volcanoes Irazú and Turrialba with their respective projections onto the crustal discontinuity. The map inset shows the location of the 3-d image.*

5.4   Comparison with Previous Studies

5.4.1   Dipping Oceanic Slab

The 3-d visualisation allows an easier comparison with the results from previous studies. While seismicity studies by Protti et al. [1994, 1995] have been interpreted to indicate shallow under-plating of the Cocos plate underneath the Talamanca Range, the receiver function results clearly contain a steeply dipping slab signal. Though in contrast to the seismicity study, this result is consistent with the local and teleseismic earthquake tomography analysis of the Jaco and Quepos events performed by Dinc et al. [2008]. A comparison of the slab seen in the tomography study (defined based on the zero contour in the velocity perturbations) and the slab picked in the receiver function migration profiles is shown in Figure 5.19.

The slab seen in receiver functions fits the tomography results well at depths of 40-70 km. At shallower depths, the tomography results compare well with previous active and passive seismics results [Stavenhagen, 1998, DeShon et al., 2003], which imaged a 18° dipping slab. Figure 5.21 shows the perfect match of the slab from tomography to these results and the bending of the slab towards steeper dip below the depth range imaged by active seismics.

The tomography studies clearly show the transition from shallow dip (18°) to steep dip (60-65°) and hence link the receiver function image with active seismic studies. The receiver functions image the continuation of the steeply dipping regime of the slab down to far greater depths, until 170-180 km. Combining the three methods, the complete picture emerges and the subducting Cocos Plate is imaged from the trench down to 170-180 km depth.

The slab dip angle retrieved from the receiver function study and the tomography study by Dinc et al. [2008] were used to constrain gravimetric modelling of the Central American subduction zone perfomed by the A2/A6 subproject groups of the SFB 574. A slice through the modelled region in displayed in Figure 5.20. The model including a steeply dipping slab also in southern Costa Rica is consistent with gravimetric measurements and provides the optimum model for this region (H.-J. Götze, personal communication).
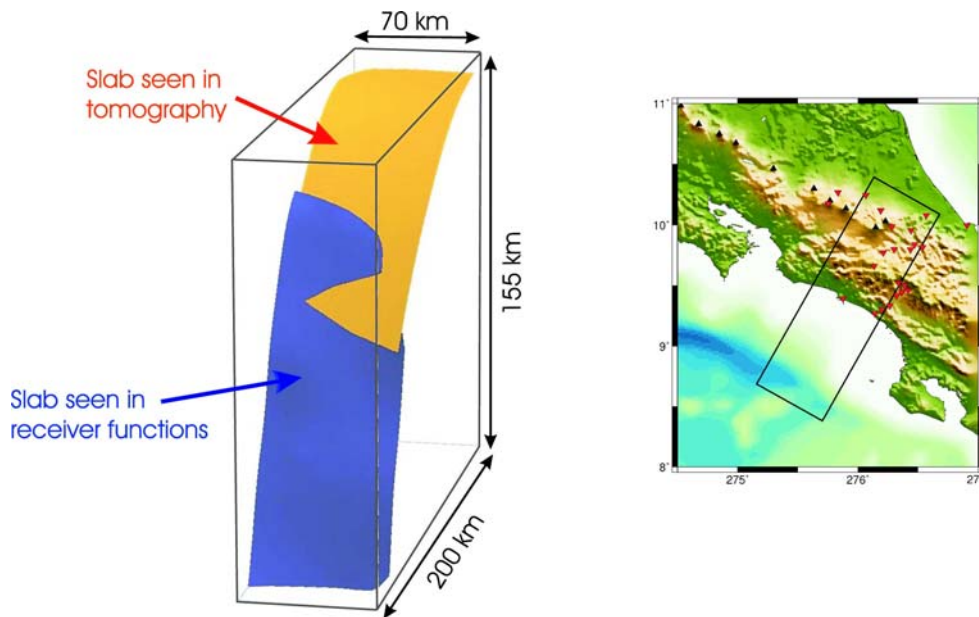
Figure 5.19: *Comparison of the subducting slab seen in receiver functions (blue) and the slab seen in tomography results (orange, from Dinc et al. [2008]). The map shows the location of the 3-d image. The slab seen in receiver functions can be followed further to the south, while the tomography results cover a region further to the north. In this figure, only the overlapping region covered by both studies was imaged. Lateral variations in slab dip, however, are minor even outside the lateral extension of this image.*
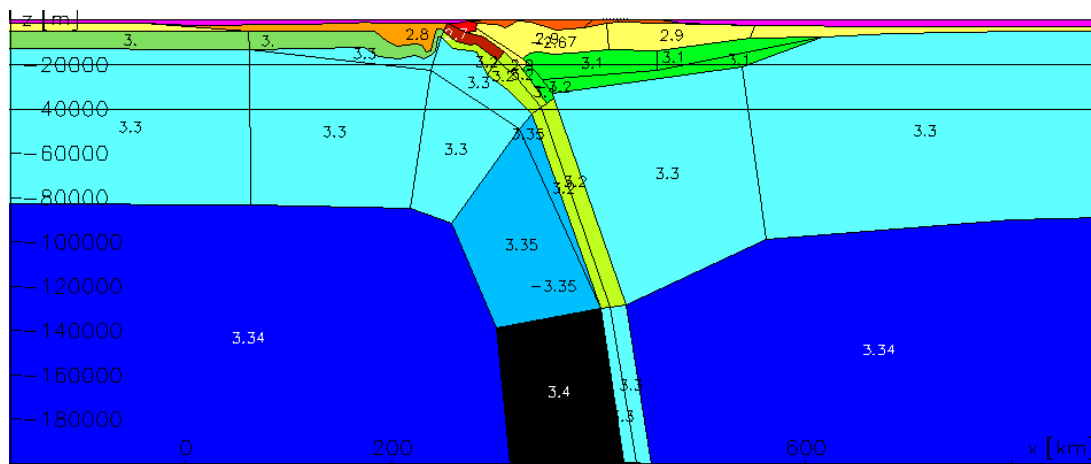
Figure 5.20: *Gravimetric model for Southern Costa Rica, from the A2/A6 subprojects of the SFB 574 (figure provided by V. Giszas). Densities are given in the model bodies (in kg/l). Depth is in metres, distance in kilometres (image not to scale).*

5.4.2   Moho and Crustal Structure

The crustal structure seen in receiver functions corresponds well to the structure observed by active seismics [Stavenhagen, 1998]. Both the Moho and the crustal discontinuity are imaged at the same depths where a velocity contrast is observed in active seismics (Figure 5.22).

Closer to the shoreline, the velocity model from active seismics could not clearly resolve these velocity discontinuities (dashed lines in the figure), so it is not surprising that the discontinuities in the receiver functions cut through the proposed lines of velocity discontinuities from the active seismic results in this region. Furthermore, the receiver functions in this region may be influenced by the shallow slab and several conversions may interfere. We have seen before (Section 5.1.2) that the Moho might be traced by a negative amplitude conversion where it directly overlies the subducting slab. If this is the case here, the continuation of the Moho towards the trench might be expected at lower depths than the "upward bulging" feature seen in the receiver functions, and possibly remain constantly at about 35 km depth, where it is observed at greater distance from the trench.

The receiver function results are consistent with both the observations from active seismics and tomography studies. Given the very different methods applied and hence different definitions of discontinuities – e.g., tomography looking at relative velocity perturbation contours vs. discrete velocity discontinuities in receiver functions – and the inherent uncertainties in all the methods, the quality of the fit from all three studies is amazing. Taking these results together, a much clearer picture of the structure of the subduction zone emerges over a markedly increased depth range (also compare the joint study by Damm and Götze).

5.4.3   Structure Related to the Volcanic Chain

The Moho and crustal interface observed by the receiver function method are slightly distorted in the vicinity of the edge of the volcanic chain (Figure 5.18). This distortion, while small and at the resolution limit of the technique, reappears in gravimetric studies [Lücke, 2008].

In particular, a low-density body interpreted as a joint magma reservoir beneath the volcanoes Irazú and Turrialba is observed at 1 km to 10 km depth (Figure 5.23). This may be the cause for the positive conversion at the 0-10 km depth interval observed in the trench-parallel receiver function profiles (Figure 5.8), which is located directly underneath the two volcanoes, and restricted to the immediate vicinity of the volcanoes. This feature indicates a low-velocity body at shallow depths. Low velocities concentrated in this body are also observed in seismic tomography [Arroyo, 2008], which is overlain on the gravimetry model.
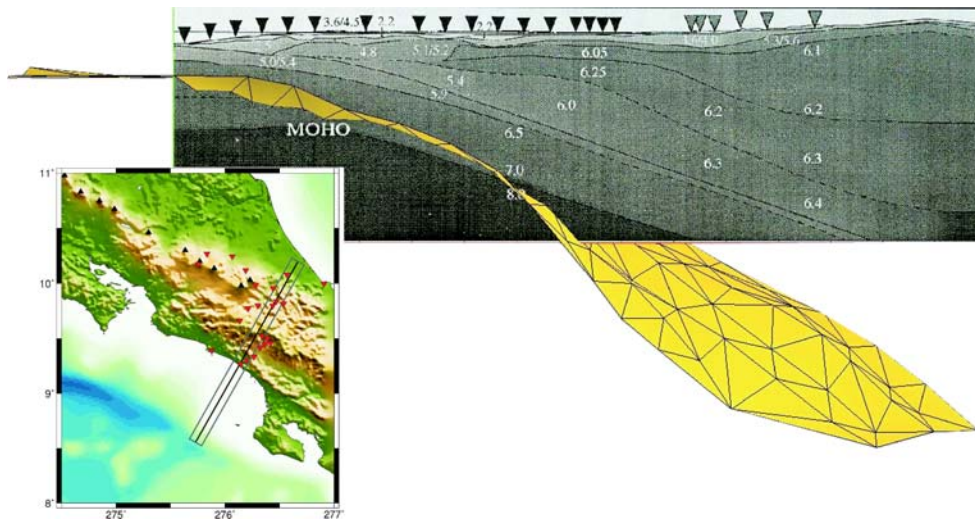
Figure 5.21: *Comparison of the slab seen in tomography studies (yellow, from Dinc et al. [2008]) with active seismics section from Stavenhagen [1998]. The map inset shows the location of the active seismic transect.*
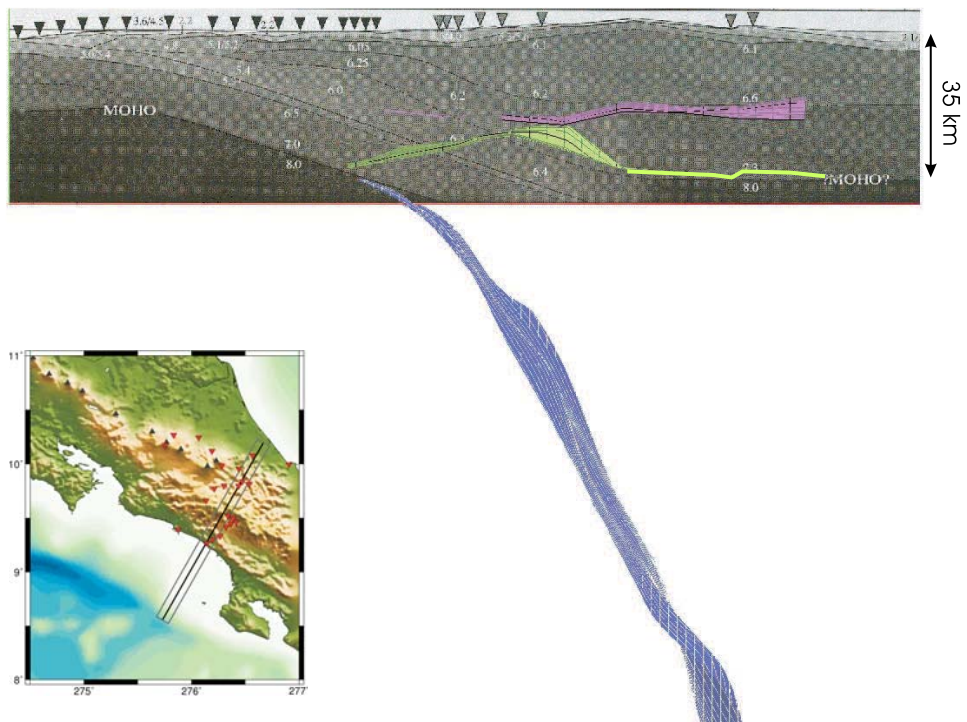

Figure 5.22: *Comparison of receiver function results with active seismic profile [Stavenhagen, 1998]. The map inset shows the position of the active seismic transect.*
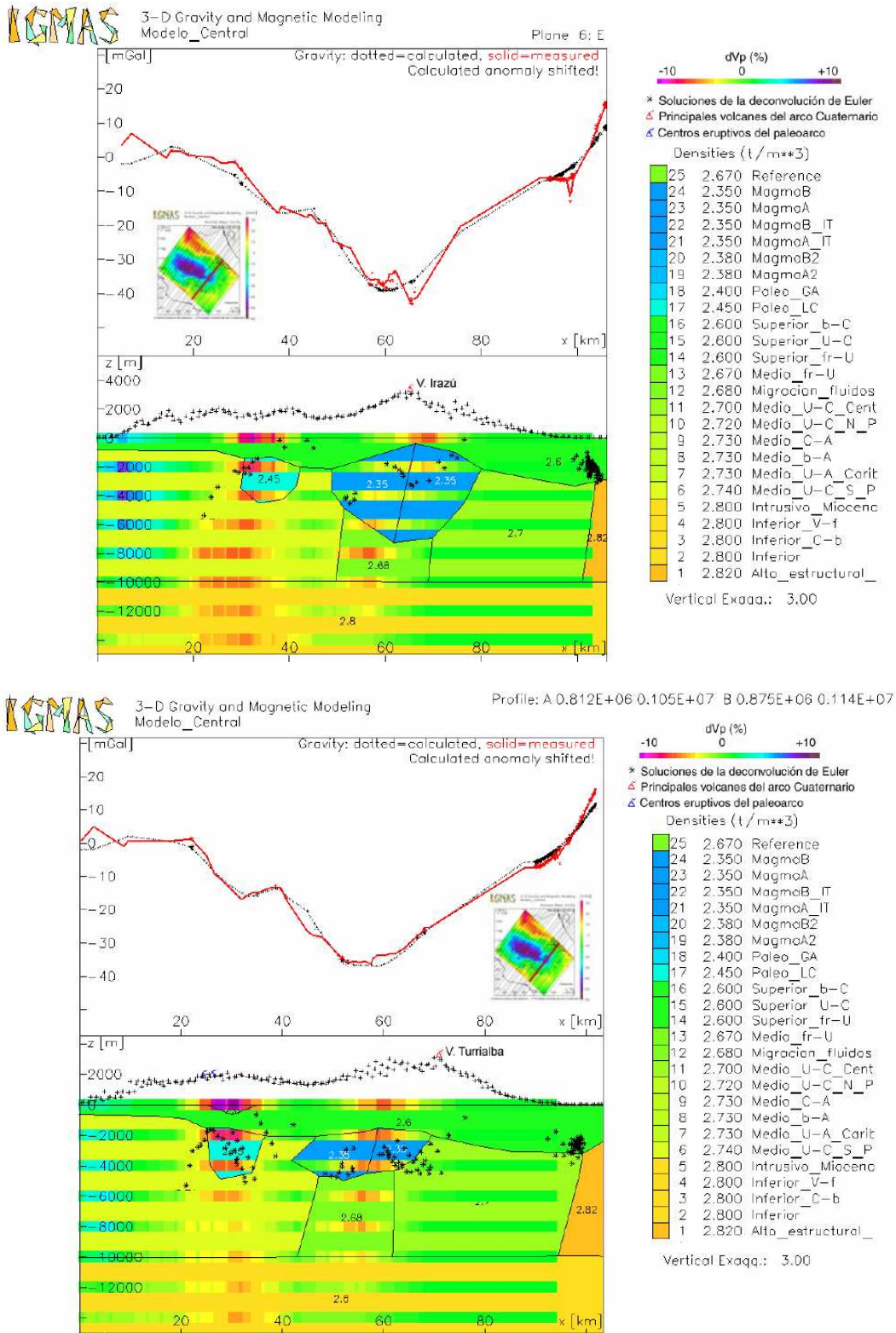
Figure 5.23: *Profile through the density model in the region of the volcanoes Irazú (upper panel) and Turrialba (lower panel). Seismic tomography results and seismicity are overlain, with dV$_p$ giving the relative velocity deviations in percentages [Arroyo, 2008]. Figures reproduced from Lücke [2008].*

5.5   Azimuthal Variation of Receiver Functions

5.5.1   Analysis of Several Example Stations

The receiver functions observed at each station vary strongly with back-azimuth. The radial and transverse receiver functions after normal move-out correction and filtering below 1 Hz are displayed in Figure 5.24 to 5.27 for the Talamanca Transect stations crt-02, crt-07, crt-21 and crt-32. Similar figures for the other Talamanca Transect stations can be found in Appendix E.

Two different kinds of representing azimuthal variability are used parallel in these figures: the upper panel shows all the receiver function traces, sorted by back-azimuth (and giving additional information about the ray parameter p and epicentral distance of the event). In the lower panel, all traces in an azimuth bin of $\pm 10°$ around the given back-azimuth (in steps of $5°$) are stacked.

The advantage of azimuth binning is that the stacked traces are equidistant in back-azimuth and make it easier to visually inspect the azimuthal variability. In particular, π and 2π-periodicity caused by dipping structure or anisotropy (Chapter 6) can be more clearly seen and a sine-dependency can be identified easily. On the other hand, the number of traces stacked is different for each bin, so the noise surpression is different for all stacked traces. In particular, sometimes only a few traces contribute to each bin, and it is not clear how to distinguish noise from real conversions.

To obtain a reasonable coverage of the azimuthal range, overlapping azimuth bins were used, which makes interpretation easier in the sense of providing a continuous coverage and smoothed stacks, but coherency cannot be seen in these data, because each bin contains traces that are also included in the neighbouring bins, so even incoherent traces will appear coherent. Another disagreable effect of this way of binning is that sometimes four neighbouring bins show nearly the same trace, if there are very few traces in just one or two of the bins, isolated from the other back-azimuth ranges.

When all traces are plotted (upper panel), coherent signals can be unambiguously identified from neighbouring traces. Furthermore, the signal seen in the receiver functions does not only depend on back-azimuth, but also on the ray parameter (more specifically, on the angle of incidence). Even though all traces are NMO-corrected, a different angle of incidence on the interfaces will result in a different conversion coefficient and thus influence the receiver functions. In the azimuth-binned stacks, all traces in the same azimuth bin are stacked regardless of the ray parameter. The individual traces (upper panels) allow to compare traces from similar back-azimuths, but different epicentral distances, resulting in different ray parameters.

To take advantage of the strenghts of both representations, both are used parallelly in this study. Some Talamanca Transect stations will be analysed in detail for their azimuthal variability here. These stations were chosen on the basis of the amount and quality of data recorded, and to be in some way representative for part of the transect. In the end, an overview of the main characteristics observed in the radial and transverse receiver functions will be given.

Station crt-02 (Dominical)

The station crt-02 (Dominical) is located closest to the trench, where the subducting slab is very shallow and cannot be distinguished from the Moho. Together they form a strong positive conversion at 4 s delay time, which is clearly observed in the stacked radial receiver function.
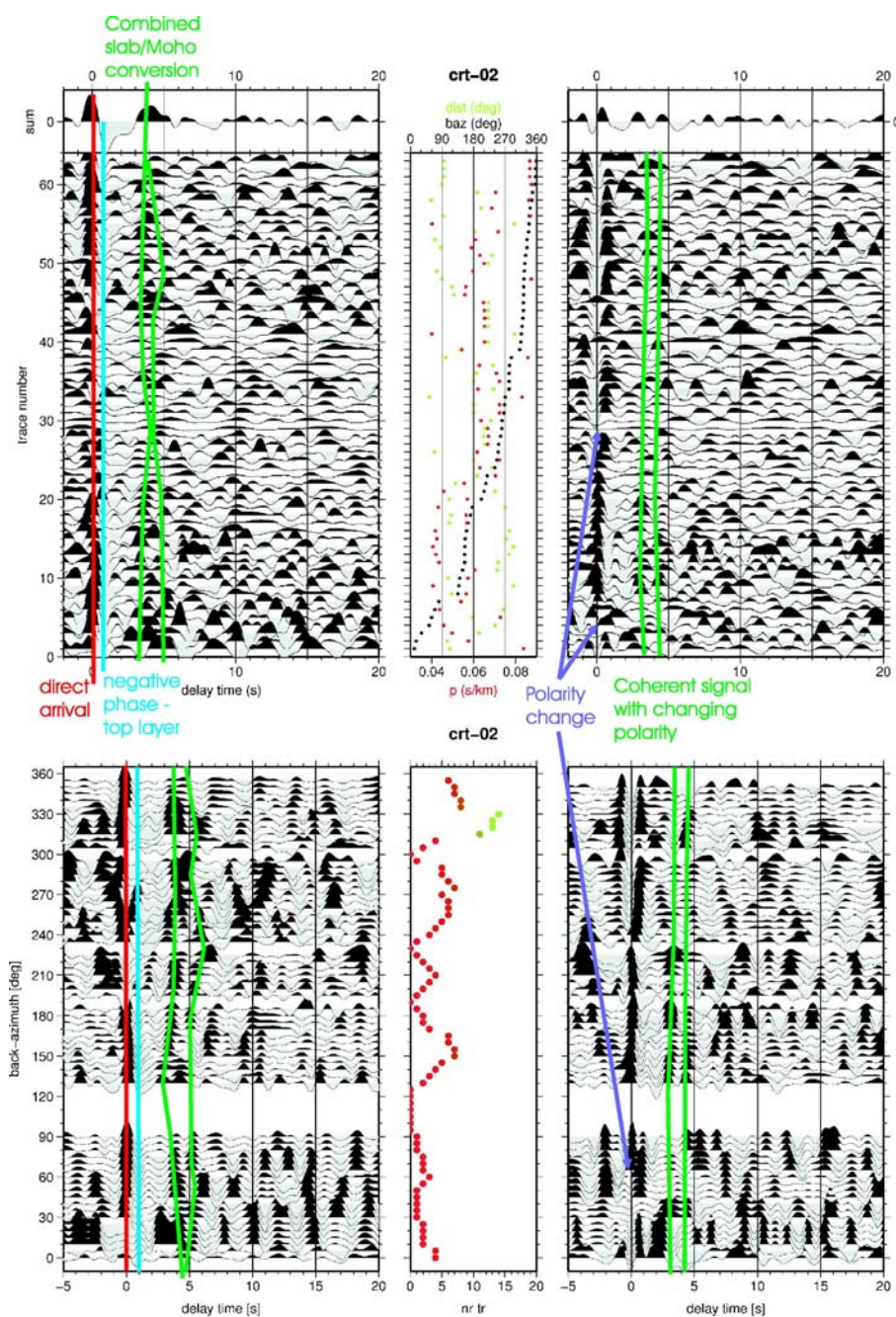
Figure 5.24: *Radial (left) and transverse (right) receiver functions for station crt-02 (Dominical). Upper panel: all traces, sorted by back-azimuth. The middle panel gives back-azimuth (in degrees, black), epicentral distance (in degrees, green) and ray parameter p (s/km, red). Lower panel: Receiver functions stacked in 10° bins. The middle panel gives the number of traces in each stack (also colour-coded). Receiver functions were corrected for normal move-out for p = 6.4 s/km and filtered with a 1 Hz low-pass.*

Some of the features observed at this station are:

- The radial receiver functions show a positive direct arrival directly followed by a negative conversion for all back-azimuths, indicating a low-velocity layer on the top of the crust.

- The merged Moho/slab positive conversion is observed in the whole back-azimuth range. This sometimes appears to consist of two separate positive conversions, and a slight time-variation may be present.

- All the above features (the direct arrival, the negative sediment conversion and the Moho/slab conversions) appear to decrease in strenght in a back-azimuth range of 240-270°. This may be caused by a close to normal incidence of these rays on the dipping slab, which will depress the conversion amplitudes.

- The transverse component experiences a polarity change at zero delay time between 240° and 250° and between 30° and 60°. This two-lobed symmetry pattern is indicative of a dipping structure (or dipping anisotropy in the uppermost layer). If this is caused by a dipping feature, it should strike approximately $N30°W$, as the synthetic tests (Chapter 6) show that the polarity change occurs in the updip and downdip directions.

- A coherent signal is observed in the transverse receiver functions at 3.5 s, which appears positive for back-azimuth of approximately 140-200° and negative for 290-360°.

- This conversion is followed by a second conversion about 1 s later, with similar polarity. It can be speculated that the transverse components allow the separation of the Moho and slab signal, which is obscured in the radial receiver functions.

Station crt-07 (Los Ángeles)

Station crt-07 is located at a distance of about 120 km from the trench, where the slab in the stacked section is observed around 9 s delay time. The radial and transverse receiver functions show the following azimuthal variations:

- While a negative conversion appears at about 0.5 s delay time in almost all radial traces, again indicating a low-velocity surface layer, this is followed by a positive conversion at 1.5 s only in the back-azimuth range 0-210°. In the stacked sections, it seems to disappear after 160° already, but the individual traces show it to be a coherent feature until about 210°. Some traces seem to suggest that this conversion continues with negative polarity at other back-azimuths, but this is unclear. Based on the arrival time, this conversion should correspond to the crustal discontinuity seen in the migrated images.

- The Moho is observed in the radial receiver functions as a positive conversion at 3-4 s, with slight variations in arrival time. At back-azimuth 150-210° it appears split into two successive positive conversions.

- A pronounced positive conversion occurs in the radial traces at 5-6 s delay time, which is interpreted as a crustal multiple phase.

- The dipping slab is identified clearly at 9-10 s delay time for back-azimuth 180-270°. Considering a slab dipping towards $N60°E$, it should arrive earliest at back-azimuth 240° and latest at 60°. A $\sin(baz)$ variation in arrival times may indeed be found, with an arrival at 11 or 12 s delay time at 60° back-azimuth, although the exact continuation of the sine-curve is not clear.
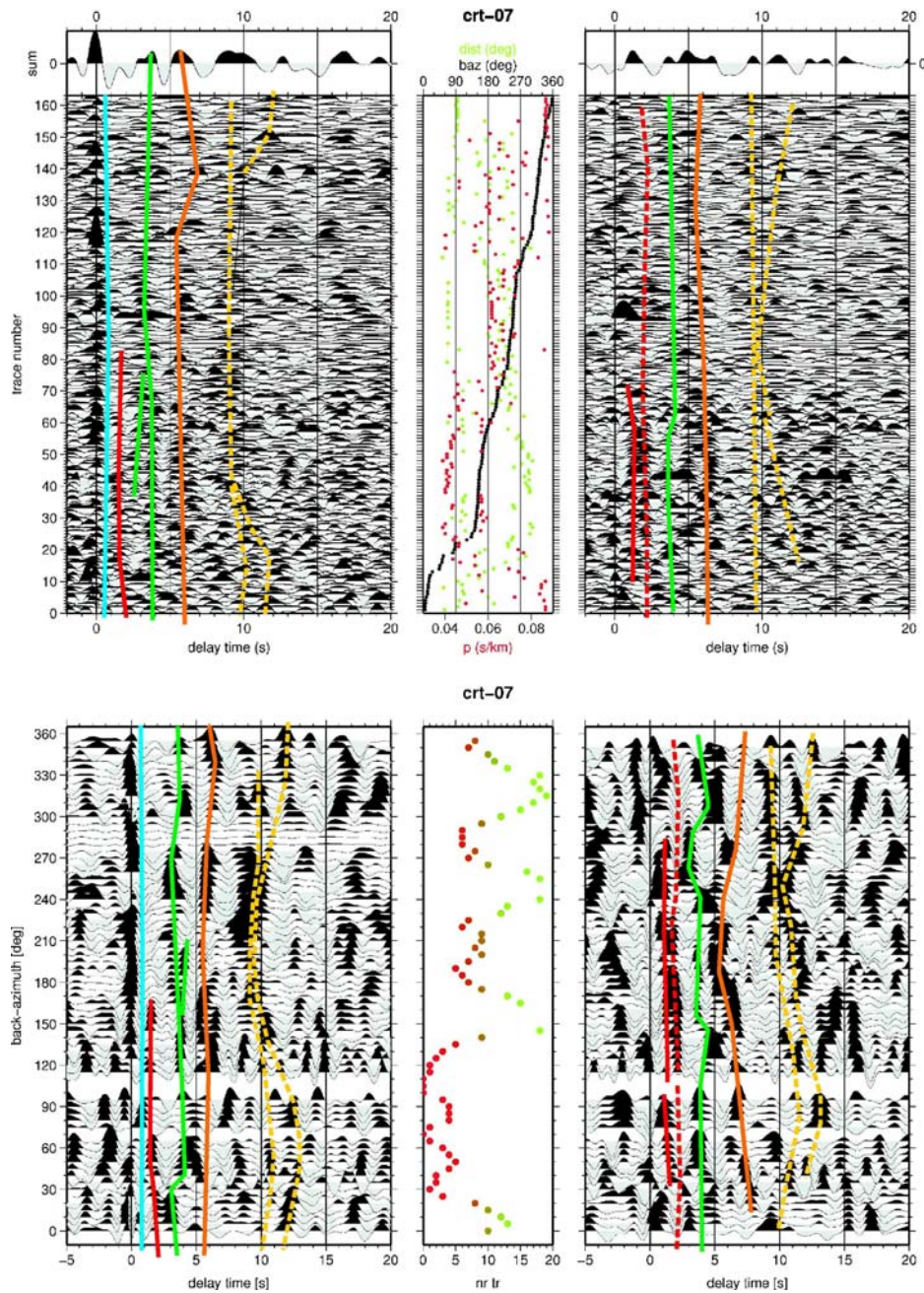
Figure 5.25: *Radial (left) and transverse (right) receiver functions for station crt-07 (Los Ángeles), plotted in the same way as figure 5.24.*

- In the transverse components, a double positive conversion at 1.5 s and 2 s stands out at back-azimuth 90-210°, which may reappear as a negative conversion at back-azimuth 270-340°. This is again interpreted as the inter-crustal discontinuity.

- The Moho is observed at 3-4 s as a positive conversion with a slight azimuthal variation in delay time, similar to the radial components.

- The crustal multiple at 6 s is also found on the transverse components, strongest for back-azimuth 120-220°.

- The dipping slab produces a positive conversion around 9 s for back-azimuth around 240°, deepening towards 360°. The continuation for lower back-azimuth may be followed along a sinusoidal curve between 9 and 12 s, but is not quite clear.

Station crt-21 (Río Orosi)

This station was placed at a distance of about 140 km from the trench, and is displaced laterally (i.e., parallel to the trench) by about 40 km to the north-west with respect to station crt-07. The following characteristics are observed here:

- The radial receiver functions show a negative direct arrival on many traces, which is particularly strong in the back-azimuth range between 90° and 270°, where it is followed by a positive conversion shortly before 1 s.

- The crustal interface at 1.5-2 s is imaged clearly as a positive conversion.

- The Moho appears as a positive conversion between 3.5 and 4.5 s delay time, but is not as strong as observed at other Talamanca Transect stations.

- The strong positive conversion at 10 s can probably be explained as a Moho multiple, which exhibits a slight variation in arrival time with back-azimuth.

- The subducting slab appears at 12-13 s in the stacked section, and is clearly seen as a positive, coherent signal at these times near 240° back-azimuth. Moving towards higher and lower back-azimuth, the delay times seem to increase, but unfortunately there are very few traces around 60° back-azimuth, so that the behaviour of the slab conversion is not constrained in the down-dip direction.

- The transverse receiver functions direct arrivals change polarity somewhere between 180° and 240°, again suggesting the presence of dipping structures and/or dipping anisotropy.

- A strong positive conversion at 1 s is observed between 240° and 330°, which seems to continue for back-azimuth outside this range, but with smaller amplitude.

- Although conversions occur in the transverse components around 3-4 s, the Moho cannot be identified clearly. Positive conversions at 5 s for back-azimuth 100-180°, 7.5 s for back-azimuth 270-300°, and 10 s for 150-270° and later times remain elusive.
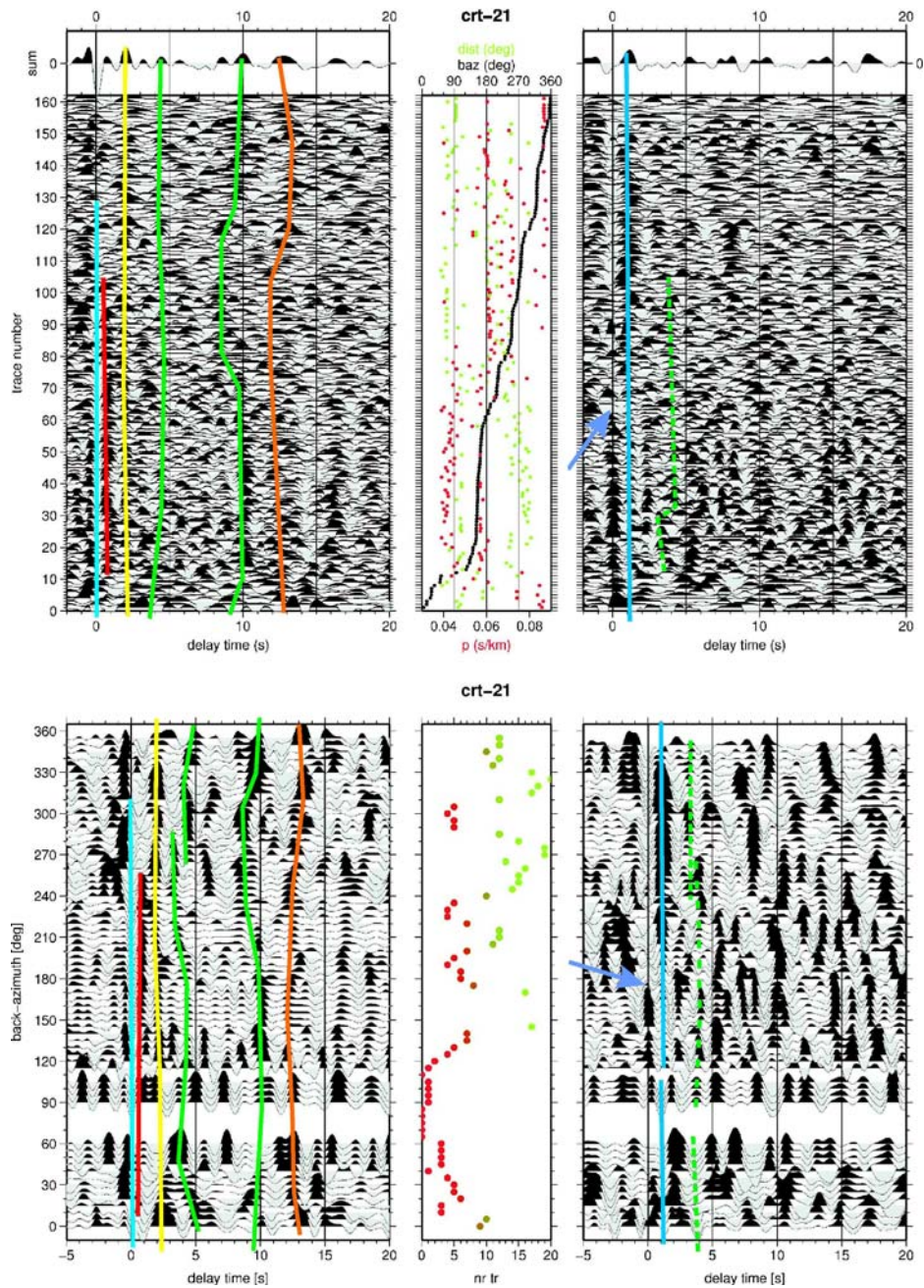
Figure 5.26: *Radial (left) and transverse (right) receiver functions for station crt-21 (Río Orosi), plotted in the same way as figure 5.24.*

Station crt-32 (Guayabo Arriba)

Guayabo Arriba is placed close to Turrialba volcano, at a distance of more than 160 km from the trench. The slab is expected after 15 s delay time and can hardly be distinguished in the short-period traces, but the following features related to crustal structure are observed:

- Shallow crustal structure is indicated in the radial receiver functions by a pronounced positive conversion at 0.5 s over the whole back-azimuth range.

- A second positive conversion occurs between 2 and 3 s, the delay time of which may vary slightly with back-azimuth. It cannot be identified clearly with either the crustal discontinuity or the Moho; however, a subsequent positive conversion at 4-5 s is a possible Moho candidate.

- A coherent positive conversion around 7 s can probably be identified as a multiple of the 2 s conversion.

- The positive conversion at 0.5 s in the radial receiver functions is reproduced by the transverse receiver functions in the back-azimuth range above 270° (and possibly for lower angles as well).

- The 2-3 s conversion also reappears in the transverse components. It is unclear if a phase shift occurs below 150° or the signal moves to slightly later arrival times (from 2 s to 3 s).

- A double-positive conversion at 4 s and 5 s occurs in the 90-180° range. For larger back-azimuth, these two conversions seem to merge together, getting weaker until they are lost around back-azimuth 330°.

- Positive conversions similar to those on the radial components exist at 12 s and 14 s, varying somewhat with back-azimuth. They are supposed to be multiples of the phases mentioned before.

General observations

The most prominent features observed in the radial receiver functions are those that also appear in the sum traces and were already shown and discussed in section 5.1.2. The inner-crustal conversion at 1.5-2 s is clearly seen at most stations, as well as the Moho conversion between 3 and 5 s delay time (at least visible for some back-azimuth ranges). Several stations show a negative conversion at very early times, suggesting a lower-velocity layer at the surface.

It is not easy to distinguish the slab signal from the multiples, particularly at larger depth, where broader filtering would enhance the visibility of the slab. The identification is further complicated by the strong azimuthal variability. In some cases, it is not clear if a conversion can be followed along back-azimuth with changing arrival times, or with changing polarity − hence the continuity of some features cannot be established easily. Given the marked variability in slab conversion arrival time and amplitude, it is surprising that the stacked sections were able to resolve the dipping slab (section 5.1.2).

Where the slab signal *can* be identified, it exhibits azimuthal variations similar to the expectations for a dipping feature striking $N30°W$: latest arrival times are observed in the down-dip direction (back-azimuth 60°), earliest arrivals occur up-dip (back-azimuth 240°), with sinusoidal variations in between.
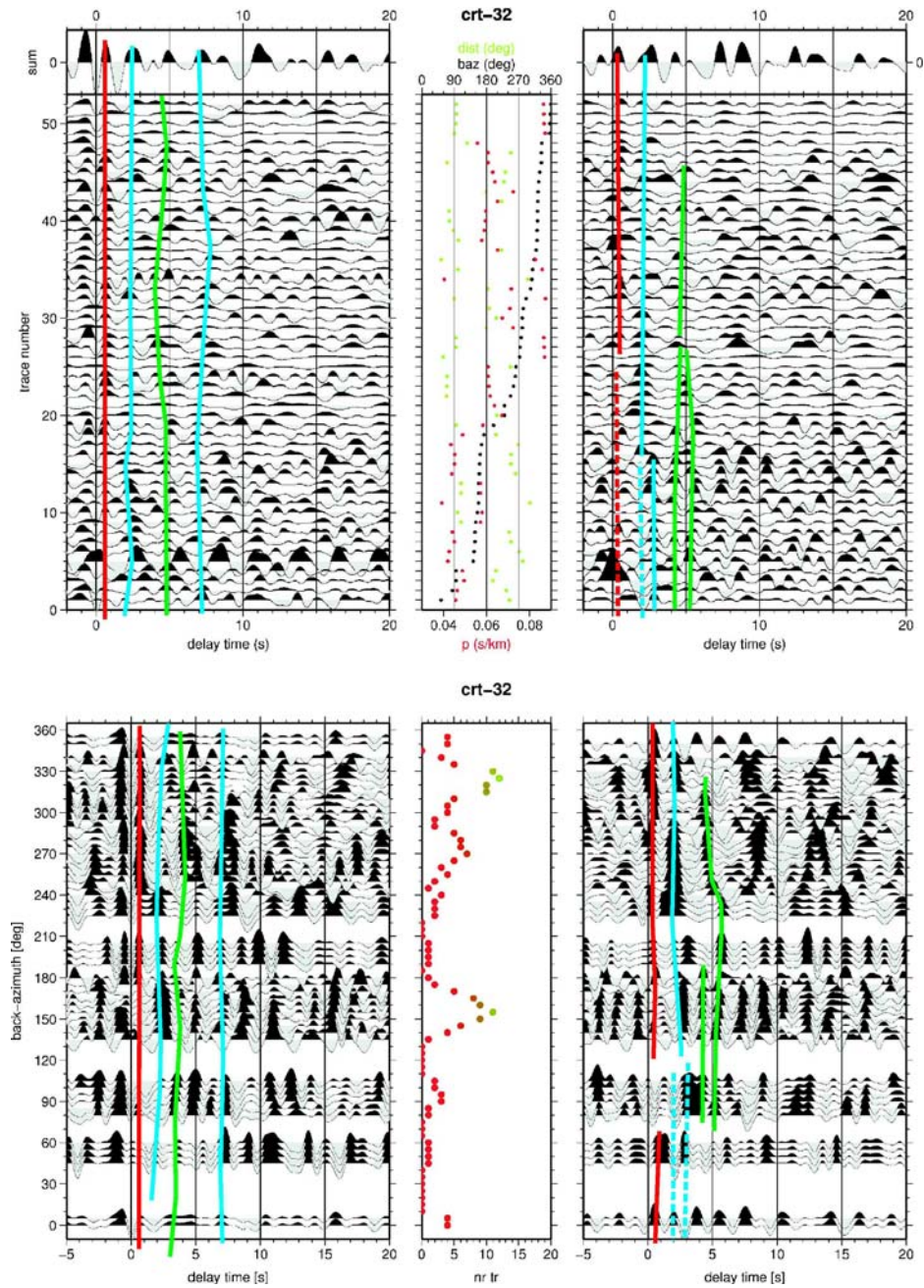
Figure 5.27: *Radial (left) and transverse (right) receiver functions for station crt-32 (Guayabo Arriba), plotted in the same way as figure 5.24.*

In the region around back-azimuth 150°, many high-frequency signals are observed, giving over to "quieter" traces at back-azimuth above 210° (e.g., stations crt-05, 14 and 15 in Appendix E). Here, many features are discontinued or broadened, but some of these truncated conversions continue up to back-azimuth ≈ 270° or higher. There are few events arriving with back-azimuth in the north-east quadrant, so this range is poorly sampled. A possible reason for the occurrence of high-frequency signals around back-azimuth 150° might be scattering by the Cocos Ridge, which is located in this direction.

The general division of the coherent signals into back-azimuth ranges $120 - 210°$, $210 - 300°$ $300 - 360°$ would be consistent with a subducting slab with dip direction to the $N30°E$. The rays impinging on the slab with almost normal incidence (updip arrivals from back-azimuth $≈ 210°$) would then expected to show lower signal levels, since they make a steep angle with the dipping slab, giving smaller conversion coefficients. Some symmetry of the receiver functions should be expected for arrivals from the SSE and the NNW, as is indeed observed in the higher-frequency content traces.

A polarity change in the transverse component direct arrival indicates dipping structure and/or dipping anisotropy underneath many stations. The polarity changes occur at approximately 60° and 240°. If we assume a slab dipping towards $N60°E$, the transverse receiver functions would vanish at back-azimuth 240° and 60° − this is also where polarity changes could occur. The overall patterns are therefore roughly consistent with the assumed subduction geometry, although these are only qualitative indications.

In total, polarity changes in the radial and transverse receiver functions are seen clearly at several stations and different times, making a case for the influence of dipping layers and/or anisotropy. In several cases, arrival time variations with back-azimuth are also observed, providing further indication of dipping layers. These strong variations with back-azimuth make it hard to follow all the conversions over the whole range in back-azimuth, since it is not always clear at a back-azimuth change if they invert polarity, change signal shape or just arrive at earlier/later times.

The azimuthal variability is hard to interprete with an intuitive view of what could be expected for a crust with several layers, mantle wedge and dipping oceanic slab. Modelling studies are clearly required for a more thorough analysis. However, what becomes clear from these plots is that the signals are largely coherent − at least while the back-azimuth is held nearly constant − and the features seen in the receiver functions are therefore real, not noise.

Example − expected delay times for a dipping slab signal at station crt-04

To give an example that a large part of the azimuthal variability can indeed be explained by a dipping slab a simple forward calculation was made based on the assumption of a slab at depth 55 km below station crt-04 (at a distance of 105 km from the trench), based on the slab depth observed both in local earthquake tomography [Dinc, 2008] and migrated receiver function sections. The slab was assumed to dip at an angle of 60°. For all rays recorded at station crt-04, the piercing points where the rays would intersect the slab were calculated based on backward ray-tracing in the same way as used in the migration algorithm, and the corresponding delay times are plotted in the azimuthally-sorted trace gather in Figure 5.28.

In addition to coherent arrivals from the Moho (at around 3.3 s) and from the crustal discontinuity (about 1.4 s), this figure shows a clear signal from the slab conversion. The delay times
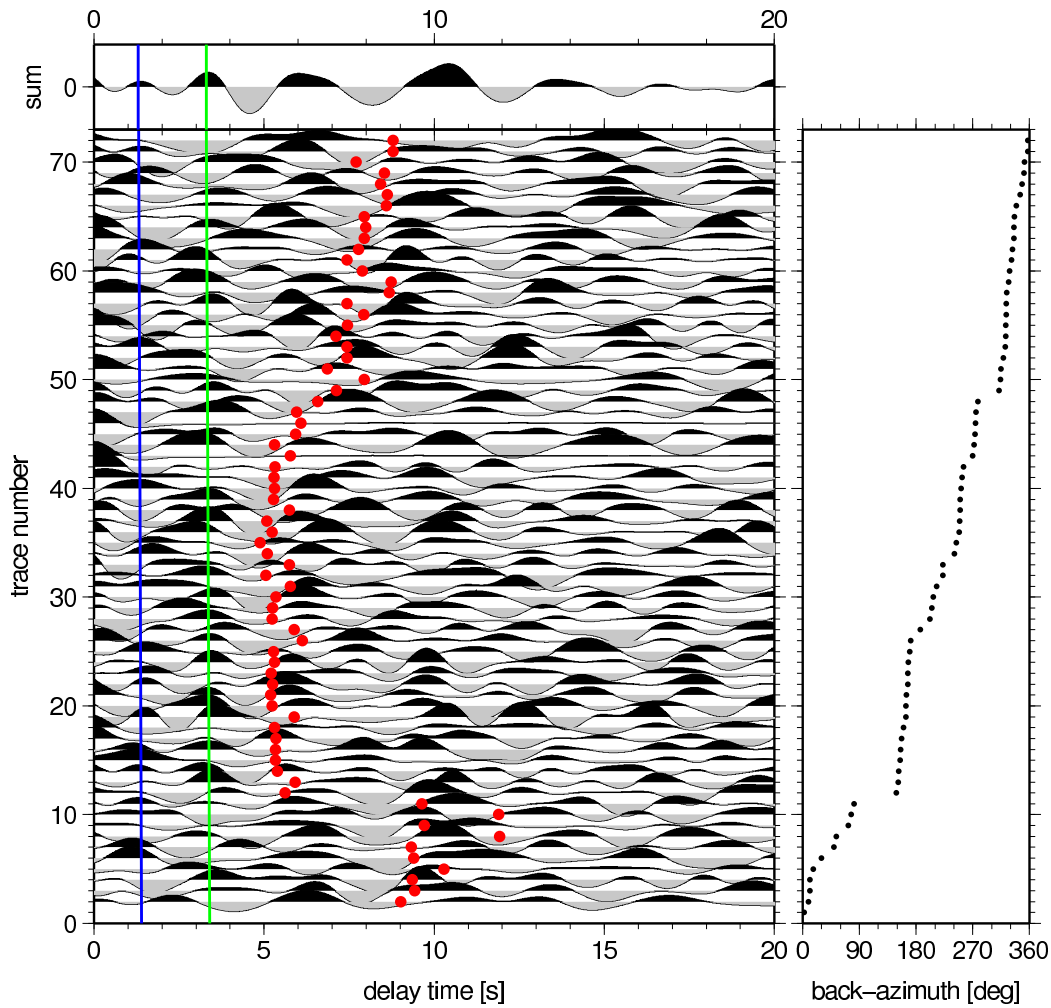
Figure 5.28: *Radial receiver functions for station crt-04 (Alto San Juan) (left panel), sorted by back-azimuth (right panel). The green line marks the Moho arrival, which is clear in the single traces and also well reflected in the stacked section. The blue line marks the preceding crustal discontinuity. Althouth this arrival is somewhat disrupted in some back-azimuth ranges, it is still sufficiently coherent to stand out as a clear conversion and also appear in the stacked trace. The red dots mark the expected delay times of a slab signal created by a 60° dipping slab at 55 km depth below the station. Some scatter in the times is caused by different epicentral distances; e.g., the two outlying points at 12 s delay time at about 90° back-azimuth move close to the 9-10 s points if an epicentral distance of 60° is assumed for all traces in the calculation.*

predicted for the dipping slab are almost all found close to a marked negative-positive conversion signal. This is the kind of signal expected for a subducting slab, because the low-velocity subducting crust will produce a negative conversion, followed by a positive conversion from the underlying fast slab mantle.

While this kind of signal can hardly be recognized in the single traces without synthetic calcula-

tions to guide the eye, the feature is very clear when compared to the expectations. Althouth there are also positive conversions at backazimuth 0-90° and 330-360° at 6-7 s, these are *not* preceded by a negative-polarity conversion and are therefore not identified as a slab conversion. The positive signal at this time is probably a multiple of the crustal structure. In the same way, the Moho multiple around 11 s delay time can also be distinguished from the slab signal.

While the simple forward calculation of expected slab arrivals gives good results for the stations close to the trench, the predictions are unreliable where the slab is very deep, because the simple geometric back-propagation of the rays breaks down. Therefore, the results are only shown for station crt-04, where correspondence with expectations is good and the slab is at shallow depth.

In the following, more sophisticated modelling studies are presented, which are much more reliable. At this point, the most important conclusion to be taken from the figure is that the azimuthal variability of the observed signals is too complicated to be intuitively understood by mere inspection of the traces; although it can be explained even by rather simple models. A further difficulty in the interpretation arises from the fact that the azimuthally variable conversions interfere with different multiples and are therefore hard to retrieve without clear expectations what to expect at a given time. Even so, the coherency among traces is better than might be expected for single traces and encourages more detailed synthetic modelling approaches.

Chapter 6

Synthetic Models

The azimuthal variability observed in the receiver functions, the dipping layer seen in the migrated profiles and the tectonic setting all suggest that dipping structures and possibly anisotropy may be expected. Therefore, a 1-d isotropic model cannot be hoped to reproduce the observed receiver functions. Indeed, it was attempted to invert restricted ranges in back-azimuth or the stacked traces by a simple 1-d isotropic model, but unsuccessfully. A 2-d model with dipping layers and anisotropy, developed by Frederiksen and Bostock [2000], is used in the following analyses. This routine makes use of the Diebold [1987] traveltime equation and does not require ray tracing. It is based on the assumptions that the layer boundaries are planar, the incoming wave is planar and ray theory is applicable. I will first consider the effects of dipping layers on the observed receiver functions and then extend the investigations to include anisotropy.

6.1 Dipping Interfaces

6.1.1 Basic Effects of Layer Dip in Receiver Functions

The influence of layer dip on receiver functions was first investigated in a modelling study. To understand the basic effect of dipping structures, a very simple model was chosen, consisting of a homogeneous, isotropic layer with velocities $\alpha_1 = 7.0$ km/s and $\beta_1 = 4.0$ km/s, underlain at 80 km depth by an eastward-dipping high-velocity wedge with $\alpha_2 = 8.0$ km/s and $\beta_2 = 4.57$ km/s. Simulations were carried out over the full backazimuth range for varying dip angle between $0°$ and $70°$. For dips steeper than $60°$, rays arriving from the downdip direction miss the dipping layer, causing failure of the modelling routine. Thus, only results for dips up to $60°$ are displayed in Figure 6.1. The seismograms were processed in the same way as the real data to obtain the corresponding receiver functions.

It is evident that the dipping layer has a marked effect on both the radial and transverse receiver function. Non-zero dip rotates part of the energy of the converted S-wave onto the transverse component, unless the plane of incidence is along the dip direction of the interface (in the model, this is for back-azimuth $90°$ and $270°$). Is is evident from the geometry of the incoming ray that a polarity change occurs on the transverse component at these back-azimuths.

SV   0 deg   SH

10 deg
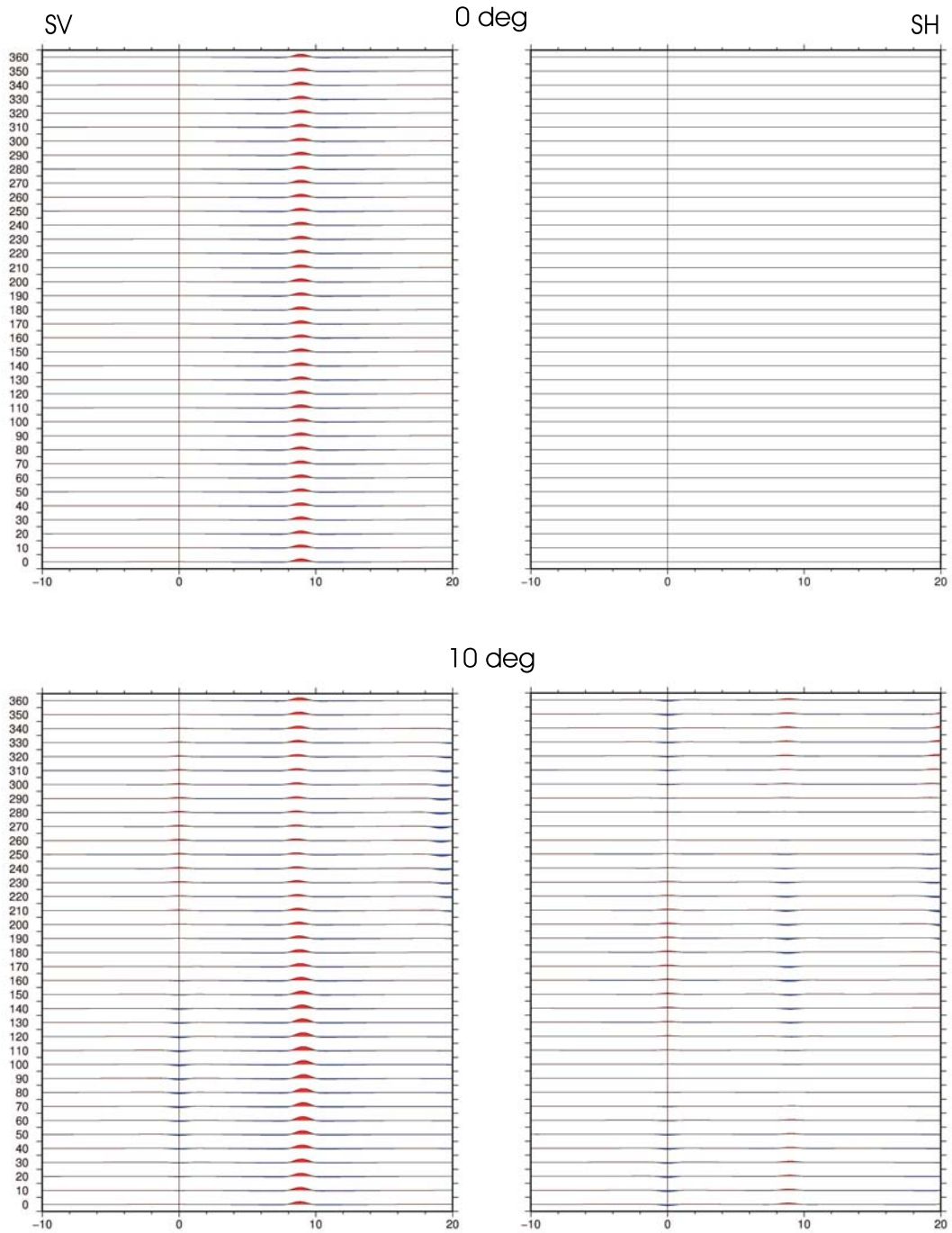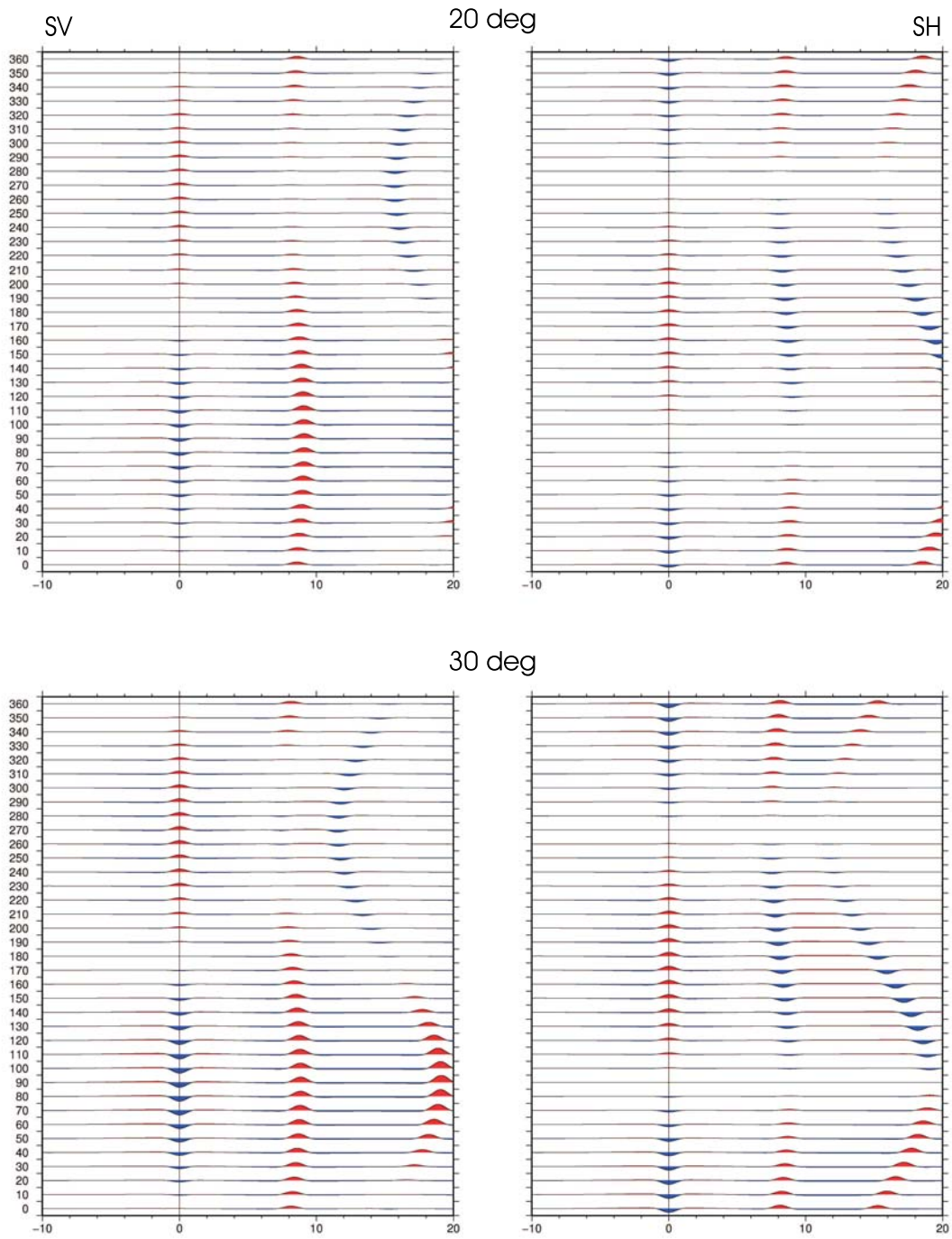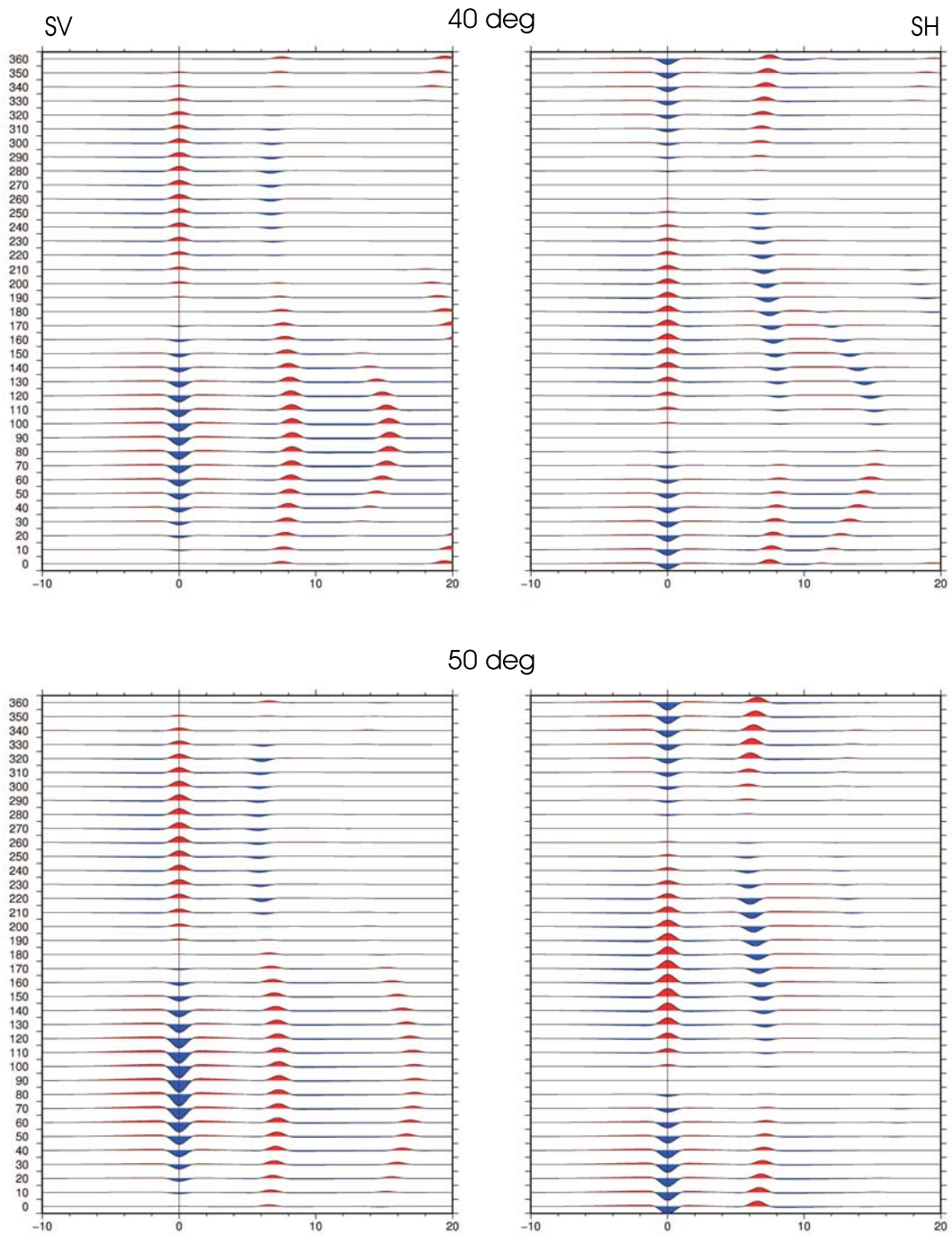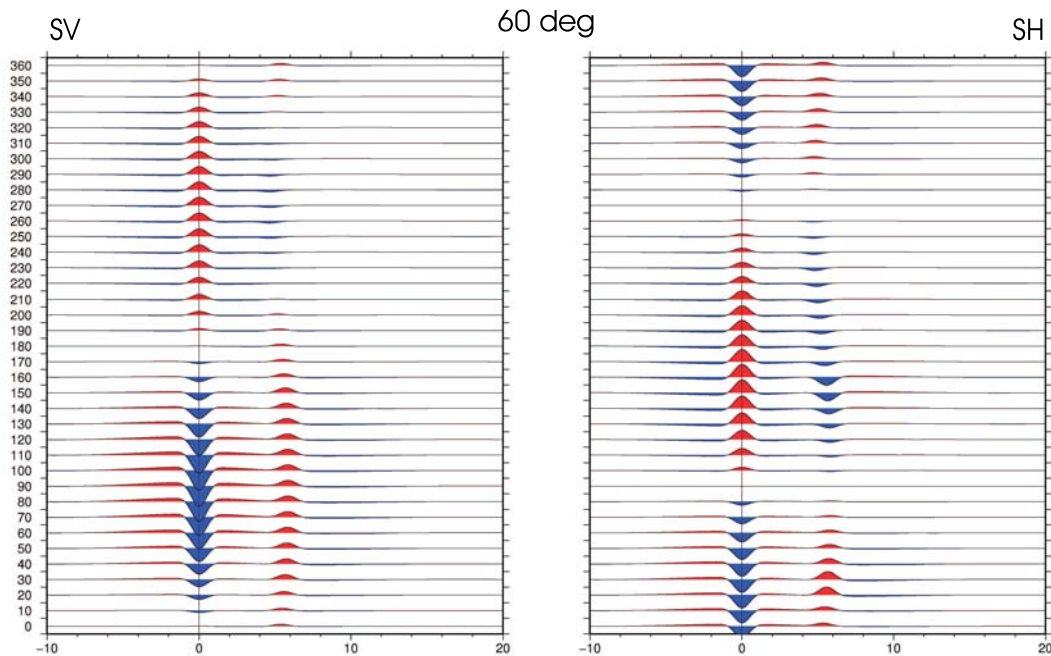
Figure 6.1: *Synthetic receiver functions for a dipping layer at 80 km depth. Left panels show radial receiver functions, right panels transverse receiver functions. Dip angles increase from 0° to 60° in steps of 10°. Back-azimuth increases from 0° to 360°, also in steps of 10°. The model is fully elastic.*

Both radial and transverse receiver functions show extremely variable delay times with changing backazimuth, which can be explained by the fact that conversions occurring updip travel a shorter path through the low-velocity surface layer than downdip conversions. The change in delay time with back-azimuth follows a sine-curve of backazimuth with 360° periodicity. Largest delay times are found for rays arriving from the east, where the dipping layer is deepest, and shortest delay times for rays coming from the west.

Multiples show an even stronger variation of delay time with back-azimuth, which makes clear identification of multiples in real data sets difficult, since their arrival can occur very shortly after the main conversion for updip arrivals and at more than twice the main conversion delay time for downdip arrivals.

Radial and transverse receiver functions for a given back-azimuth arrive with equal delay times, since the medium is taken to be isotropic, and conversion occurs at the same place.

Several main features seen in the synthetic receiver functions will be investigated in more detail, since they appear somewhat surprising at first sight:

1. It is intuitive that the amplitude of this sine-curve, i.e., the difference between the latest and earliest arriving conversion, should increase with increasing dip angle. However, while this behaviour is indeed observed for dip angles between 0° and 40°, the synthetic results show that the trend reverses somewhere between 40° and 50°.

2. The mean arrival time (independent of back-azimuth) decreases with increasing dip, although the depth of the dipping interface beneath the observing station is held constant.

3. For dip angles in excess of 20°, the radial receiver functions have negative polarity for updip arrivals. Although it is evident that variations in conversion amplitude with back-azimuth should be observed, given that the angle of incidence on the interface changes and gives rise to a variation in conversion coefficients, the polarity change is counter-intuitive and warrants further investigation.

To understand this behaviour, an analytical calculation for the delay times from the updip and downdip directions was performed, taking into account the fact that the ray geometry changes at certain angles. The different geometries of a P-to-S converted ray impinging on one dipping layer are displayed in Figure 6.2.

Updip case 1 is the "normal" case that also occurs for horizontal layers. For a moderately dipping layer, the P-to-S conversion is observed further downdip, i.e. at greater depth, than the travel path of the unconverted (refracted) P-wave. Only when the dip of the layer becomes so large that the rays arriving from the updip direction can strike the interface *below* the normal to the interface can case 2 occur, where the P-to-S conversion happens at shallower depth than the unconverted P-wave piercing point. The transition from updip case 1 to updip case 2 occurs when the incoming ray (P wave) impinges vertically on the interface, i.e., when the incoming ray angle with respect to the vertical ϕ_{in}^p equals the layer dip Δ. This translates into a condition for the steepness Δ for the second case:

$$\Delta \geq \phi_{in}^p = \arcsin\left(\alpha_{in} p\right) \tag{6.1}$$

For an incoming ray with ray parameter $p = 5.0 \cdot 10^{-2}$ s/km and velocity 8 km/s in the mantle, updip case 2 can only occur for dip angles in excess of 23.6°.

For downdip arrivals, three possible geometries exists, in all of which the P-to-S conversion occurs at shallower depth than the P-wave piercing point. The "normal" case (valid also for horizontal layers) has the expected ray geometry in the sense that rays coming from the downdip direction (to the right in the figure) are also seen to be coming from the downdip direction when looking back from the observing station. However, for larger dip angles there comes a point when the converted S-wave is going vertically upwards and henceforth appears to come from the updip direction, while the refracted P-wave is still seen to come from downdip (case 2). In this case, tracing the converted waves backwards from the station based on their theoretical back-azimuth places the conversions in the wrong direction and at wrong depth.

When the dip angle increases even further, eventually both the S-wave and the P-wave will be refracted back to the direction they came from, both now appearing to arrive from the updip direction. Downdip case 2 gives over to case 3 when the P-wave is refracted in a way to travel vertically upwards to the surface.
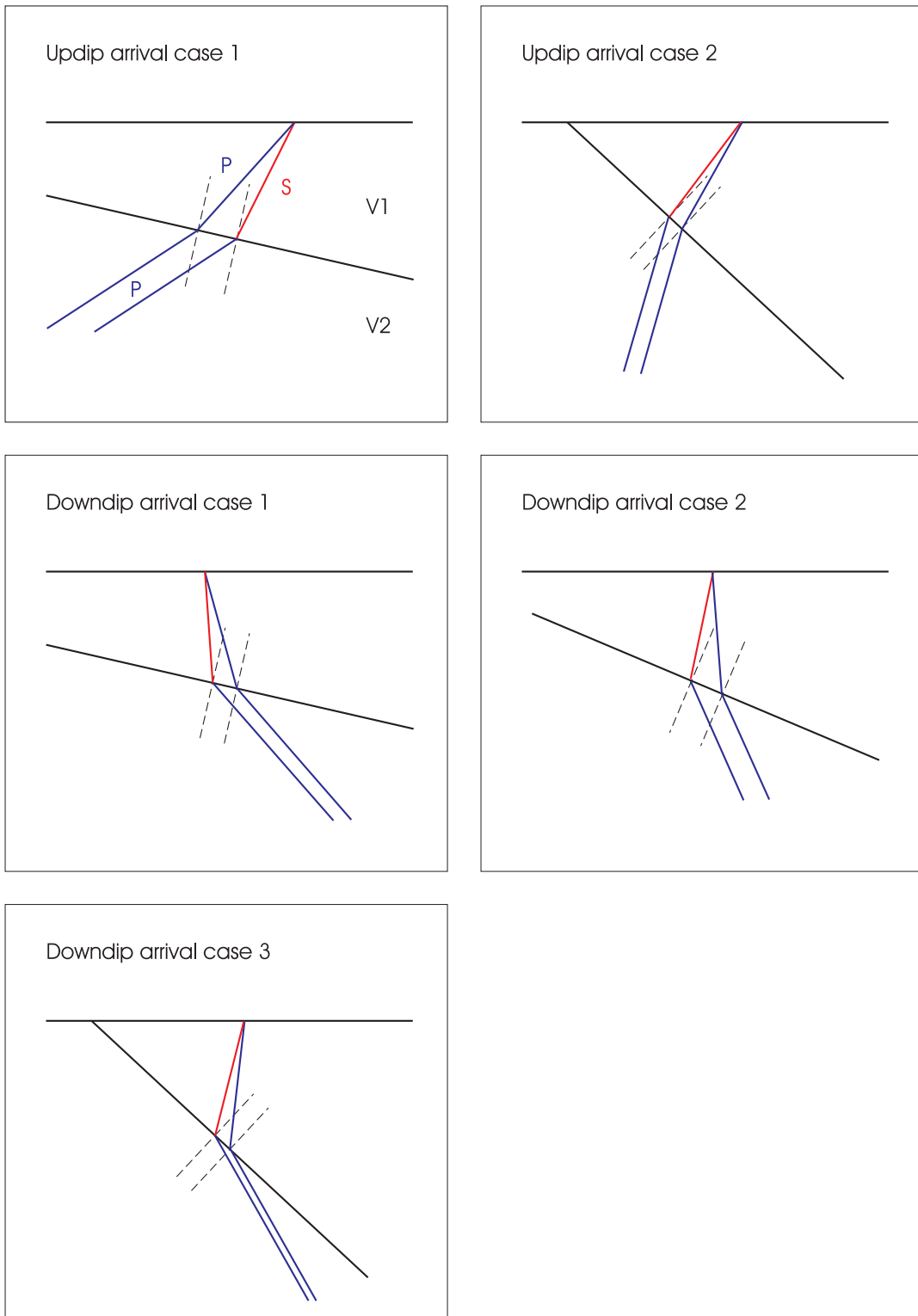
Figure 6.2: *Possible geometries of P-to-S converted rays at a dipping interface*

The different geometries are given by the conditions

downdip case 1: $\Delta < \arctan \frac{\beta_1 p}{1 - \sqrt{(\beta_1/\alpha_2)^2 - p^2}} = \Delta_{lim}^s$

downdip case 2: $\Delta_{lim}^s \leq \Delta < \Delta_{lim}^p$

downdip case 3: $\Delta < \arctan \frac{\alpha_1 p}{1 - \sqrt{(\alpha_1/\alpha_2)^2 - p^2}} = \Delta_{lim}^p$

For the above example and values of $\alpha_1 = 7.0$ km/s, $\alpha_2 = 8.0$ km/s and $\beta_1 = 4$ km/s, we find $\Delta_{lim}^s = 21.7°$ and $\Delta_{lim}^p = 70.1°$.

Taking the geometry changes into account, the P-S delay times can be calculated for any layer dip Δ. These calculations were performed with the same parameters used in the above examples. The delay times for updip and downdip arrivals were calculated separately and are shown in Figure 6.3.
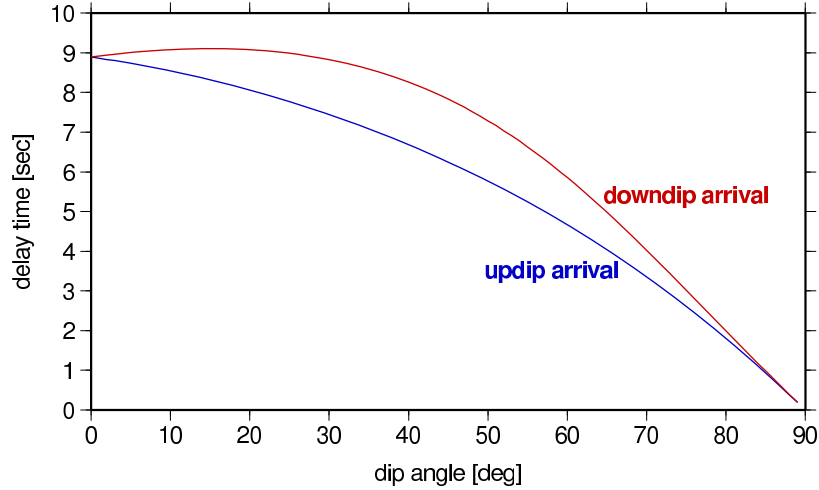
Figure 6.3: *Variation in delay time as a function of layer dip for updip and downdip arrivals, respectively. The delay time of the converted wave from a 80 km deep dipping interface was analytically calculated for the model given above ($\alpha_2 = 8$ km/s, $\alpha_1 = 7$ km/s, $\beta_1 = 4$ km/s).*

It becomes clear from the figure that while the updip arrival comes at earlier times for increasing layer dip, the downdip delay times first increase with dip till somewhere around $17°$ dip and then decrease again with increasing layer dip. Qualitatively, this somewhat surprising behaviour is caused by the fact that for small dip, the downdip converted S wave travels a longer path through the upper layer, where the velocities are lower, and hence arrives later for increasing dip. When the dip becomes steeper, though, the effect is compensated by the fact that the conversion occurs further updip, thereby decreasing the path in the lower-velocity medium.

We are now in a position to explain the changing amplitude of the sine-curve of delay times with back-azimuth. The amplitude is given by half the difference between maximum and minimum delay times, i.e. between the updip and downdip delay times, while the average arrival time is determined by the mean of the updip and downdip delay times, $\frac{1}{2}(t_{up} + t_{down})$. Both values are plotted as a function of layer dip in Figure 6.4.
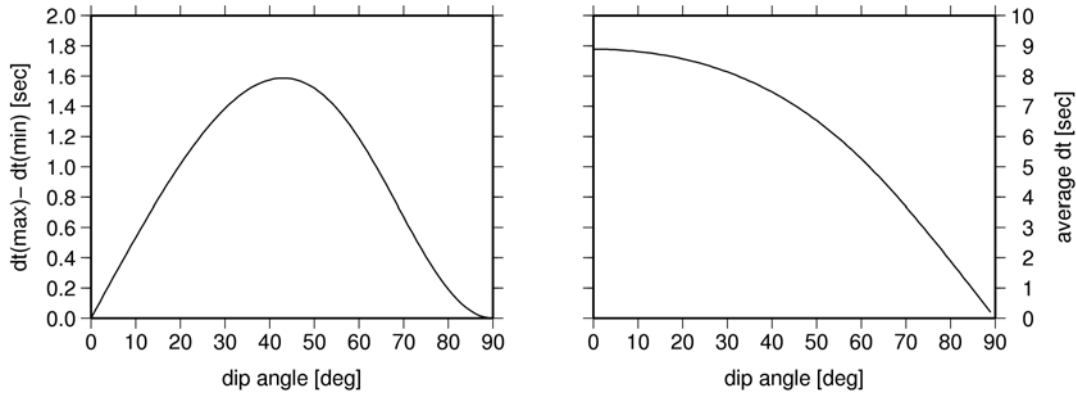
Figure 6.4: *Left panel: Variation between maximum and minimum delay time (downdip vs. updip arrivals) as a function of layer dip. Right panel: Mean delay time as a function of layer dip.*

These figures reflect the behaviour seen in the synthetic traces, the initial increase in the sine-curve amplitude with dip, which reverses at about 42.5° layer dip, and the fact that the mean arrival time is earlier with increasing dip. Intuitively, this follows directly from Fermat's Principle, stating that the seismic waves travel in a way to minimize (extremize, really) the travel time, and are thus "pulled" into the faster medium, with the conversions occurring farther updip for steeper dipping interfaces. However, this characteristic shows that care must be taken with a too "naive" interpretation of receiver function images, where arrival time is taken as a measure for the depth of the interface underneath the station: If all the traces are stacked and or the average delay time is chosen for the interpretation, the interface will appear shallower the steeper it dips.

Finally, the polarity change observed for updip arrivals and large dip angles can be understood by inspection of Figure 6.5. The direction of P- and S-wave movement is plotted along the rays, where the direction of S-wave movement is given by the condition of continuity of displacement at the interface. For all downdip arrivals, the direction of S-wave movement relative to the P-wave movement is in the same direction. Contrary to this, the S wave movement for updip arrivals clearly reverses its direction when the incoming ray passes below the normal of the interface, i.e. when the transition from updip case 1 to 2 occurs.

This last result can be generalized to the 3-d case by considering that to a ray arriving outside the plane defined by the normal to the dipping layer and the vertical, the slab will appear less steep than to a ray coming from the up-dip direction in this plane. For a given layer dip, the range in back-azimuth where negative polarity conversions are observed for given epicentral distances between 30° and 90° is shown in Figure 6.6. In these figures it was assumed that the dipping layer is deepest in the direction *N*60°*W*, as is probably the case for the subducting Cocos Plate. The figures therefore appear rotated by −30° with respect to the synthetic seismograms in Figure 6.1. The conversion from epicentral distance to angle of incidence was done using the *onset* routine of the *passcal* package.
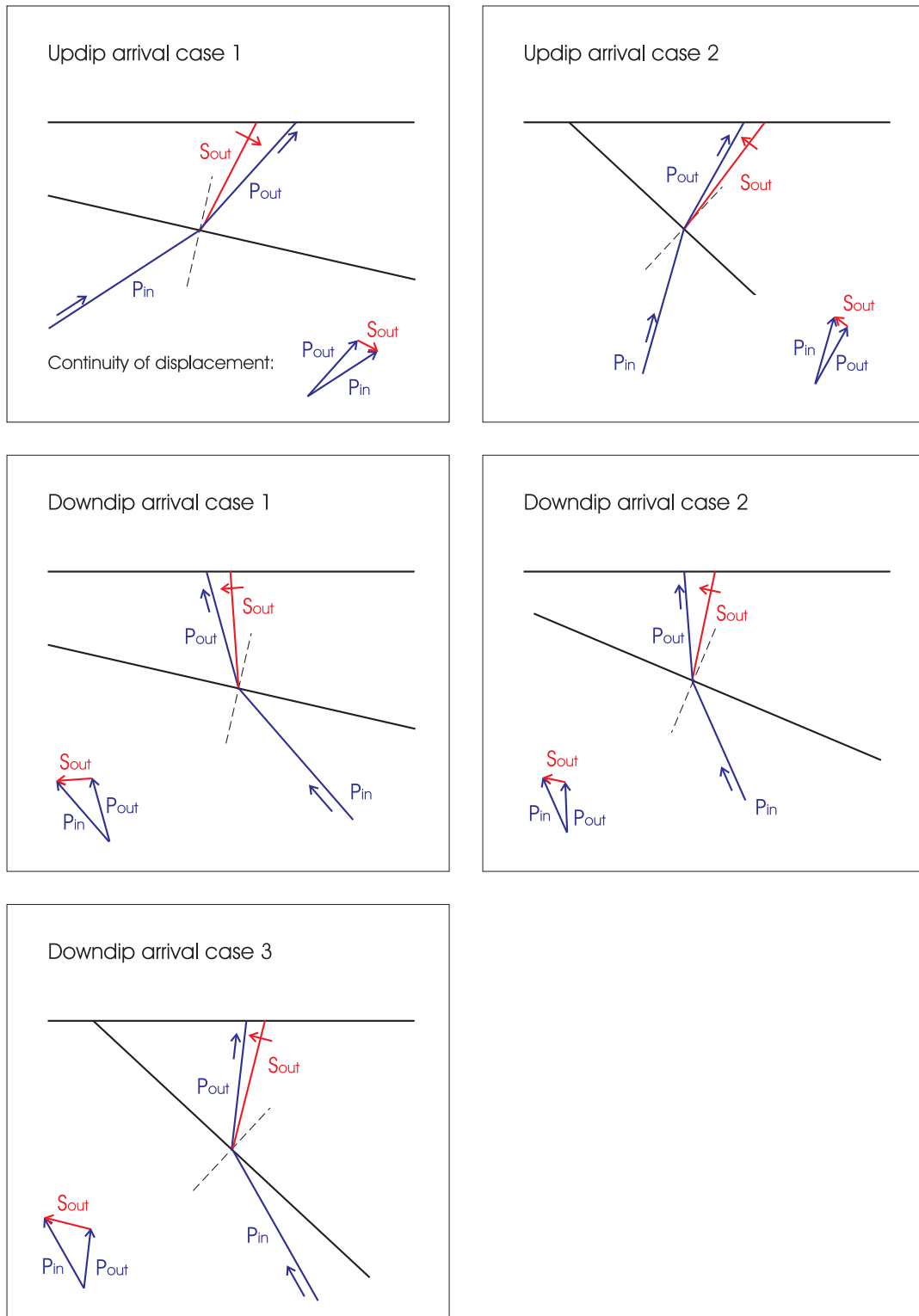
Figure 6.5: *Continuity of displacement for different ray paths and interface dip angles. The same cases of ray path geometry are displayed, with the direction of motion of the P and S waves. The continuity of displacement (shown in the vector addition in the corner of the boxes) fixes the direction of converted S wave movement.*
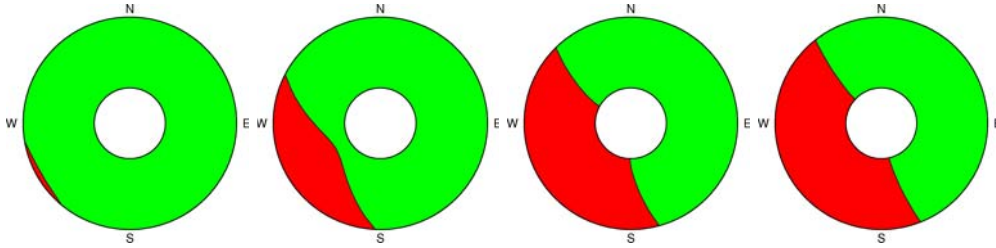
Figure 6.6: *Polarity of conversions from an interface dipping towards N60°W, as a function of back-azimuth and epicentral distance (30° in the inner ring of the torus, 90° at the outer rim.) The dip angle of the velocity discontinuity increases from 15° over 25° and 45° to 60° from left to right. Green: positive polarity, red: negative polarity.*

For small dip angles, only a very small range in back-azimuth and angle of incidence will show negative polarity conversion. Starting between 25° and 30° layer dip, negative polarity arrivals occur for all possible epicentral distances. In the case of the Cocos Plate subducting at a dip angle of about 60°, negative arrivals should occur for most rays arriving from the updip-direction. The fact that these are not clearly identified in the azimuthal variation of the receiver functions may be explained because they are obscured by multiples and noise, and the azimuthal coverage is poor in some back-azimuth intervals. For some stations, part of a negative-polarity sine-curve may be identified in the azimuthal plots, e.g. at crt-02 around 8 s delay time. However, the continuation between possible negative polarity conversions and the corresponding positive conversions at later times for down-dip arrivals is unclear. Later modelling (Section 6.4) will show that the negative/positive arrivals are often followed or preceded by a positive/negative conversion, so that a simple sine-variation in delay time with a clear polarity cannot be expected in the data.

6.1.2 Dipping Wedge Modelled for the Actual Observation Geometry

Several model calculations were carried out using the same processing technique and observation geometry as was given for the real data: For each station, all the events observed at this station were used to calculate synthetic traces for the given back-azimuth and ray-parameter. The synthetic seismograms were then deconvolved, filtered, migrated and visualized in the same way as the real data. This was done to check if the experimental settings allowed the observation of dipping structures, and whether the dip angles seen in the migrated images corresponded to the "real" dip angles in the underground (i.e., in the model).

Models were calculated for a 15°, 30°, 45° and 60° dipping wedge with strike $-30°$. The velocity of the wedge was taken to be $\alpha = 8$ km/s, $\beta = 4.57$ km/s, the layer above was assumed homogeneous with velocity $\alpha = 7$ km/s, $\beta = 4$ km/s. The dipping wedge velocity corresponds to upper mantle velocities, while the layer above was chosen to encompass both the crust and mantle wedge. More realistic models with a separate crust and mantle wedge will be considered in Section 6.1.3; at this point the main interest is to confirm that a dipping wedge structure can be resolved by the data set and will appear with the same or a similar angle in the migrated sections as the real dip angle. This is by no means trivial; receiver functions were developed for plane layering cases and have usually been applied to horizontal or low-angle dipping features. It must therefore be confirmed that the dipping feature observed in the migrated images is not an artefact. In particular, we have seen that a dipping feature causes both positive and negative polarity conversions,

depending on back-azimuth, so we must make sure that these do not cancel each other out or produce other unwanted effects in the migrated sections.

For this study, we are hence only interested in the overall features, such as the visibility and dip angle of the subducting slab, which is not notably influenced by the absolute velocities used in the model. Receiver functions are mainly sensitive to velocity contrasts, so simple values for the velocities were chosen for this modelling series, although they do not correspond to realistic expected velocities. The depth of the wedge was 50 km below station crt-02.

Figures 6.7 and 6.8 show the results obtained after migration of the synthetic traces on a grid identical to the one used for the real data, for a 15° and 30° dipping wedge, respectively. The left panel was obtained with a 1 s low-pass filter, the right panel with a 5 s filter. The wedge surface used in the model is shown as a line in the migrated sections.
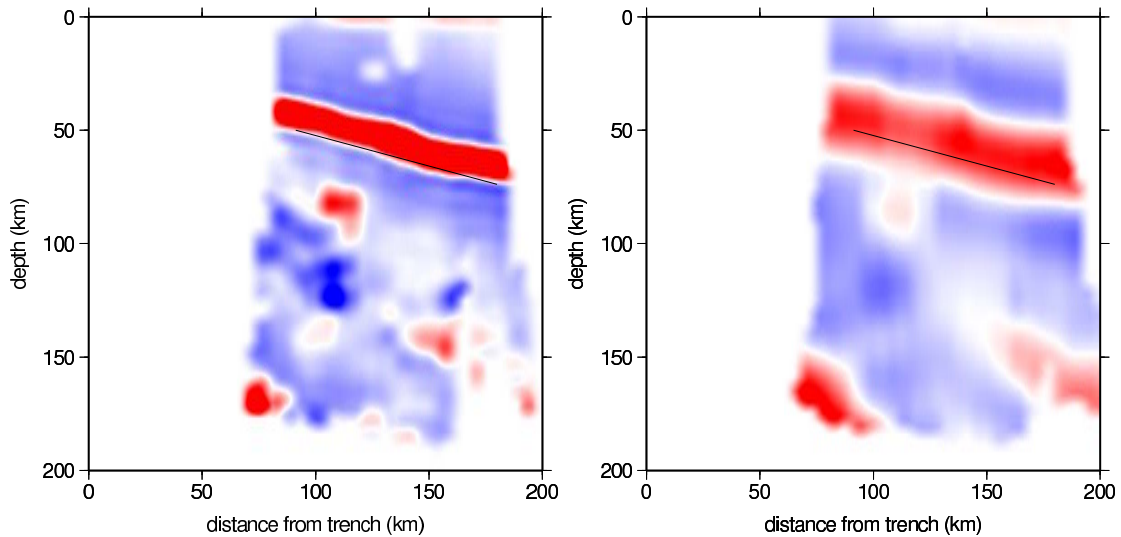
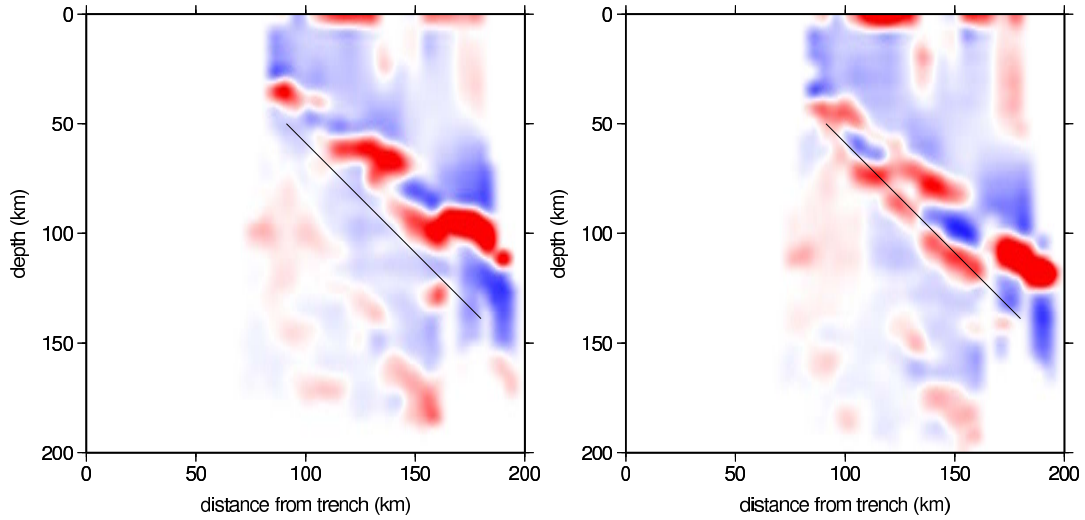Figure 6.7: *Synthetic receiver function results for a 15° dipping high-velocity wedge − migrated profile. Left: synthetic receiver functions low-pass filtered below 1 s, right: below 5 s.*

The results for the 1 s and 5 s filtered receiver functions are very similar, so henceforth we will consider only 1 s filtered traces. The dipping wedge is clearly imaged as a strong positive dipping anomaly in all profiles. Multiples are observed dipping steeply in the lower left corner of the profile, where a pronounced positive signal was also observed in the receiver function results.

The retrieved dip angles correspond closely to the input model, although the slab would be expected at slightly shallower depths than it really is. This is mainly due to the fact that the 1-d velocity model used in the migration cannot account for refraction of the rays at the dipping feature, therefore the slab is displaced somewhat to the north-east in the images. A secondary effect may be a trade-off between depth and velocity, since the 1-d Quintero and Kissling [2001] velocity model does not exactly reproduce the velocities in the subsurface.

To investigate further the effect of the 1-d velocity model used in the migration, the same cal-
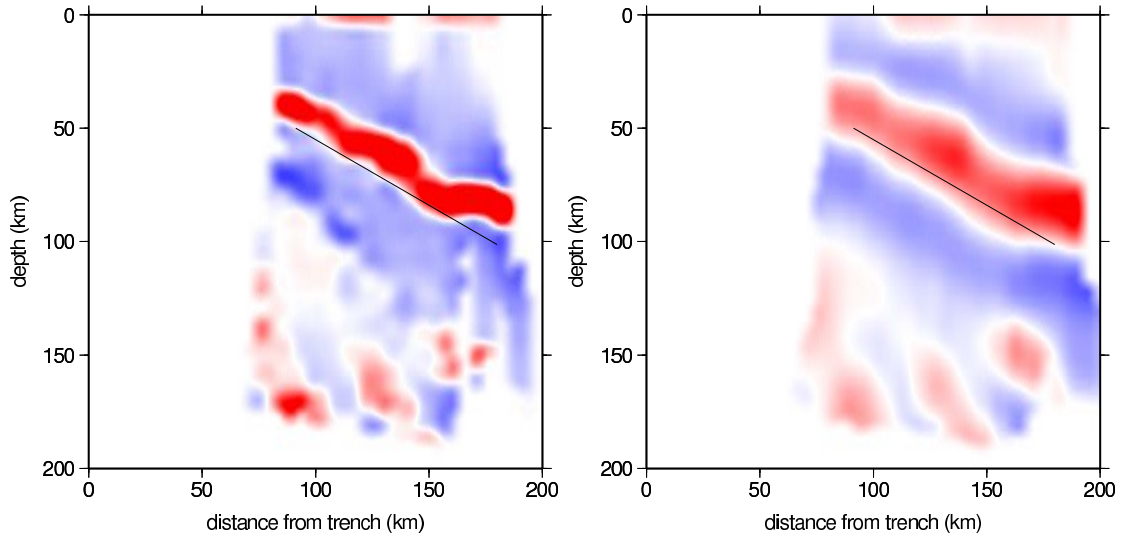
Figure 6.8: *Synthetic receiver function results for a 30° dipping high-velocity wedge − migrated profile. Left: synthetic receiver functions low-pass filtered below 1 s, right: below 5 s.*

culations were performed with a second, very simple 1-d model using the same velocities as given in the input model, but horizontal layering (i.e., $\alpha = 7.4$ km/s, $\beta = 4.229$ km/s above 35 km depth and $\alpha = 8.0$ km/s, $\beta = 4.571$ km/s below). The results are displayed for a 45° and 60° dipping wedge model in Figures 6.9 and 6.10 (left panel: migration using the Quintero and Kissling [2001] velocity model, right panel: migration using a 1-d velocity model with the velocities used in the input model).

Even though the migration is still performed with a 1-d velocity model and by ray-tracing using the theoretical back-azimuth and ray parameter, the results are improved when the 1-d velocity model is a better representation of the real velocities in the underground. In particular, the deviation of the retrieved wedge dip angle from the input dip angle is much smaller. The wedge signal is seen to split into two positive conversion "layers" when the dip is large, the steeper one of which giving an approximation of the real slab.

If the migration velocity model is chosen close enough to the input model, the dip of the slab can be determined from the migrated profile with good accuracy (deviations of a few degrees at most). For the Quintero and Kissling [2001] model, a good estimate of the dip angle can be obtained if care is taken to follow the lowermost conversions; however, there is a risk that these are smeared into the upper conversion signal and a significantly shallower dip is suggested. This effect is stronger the steeper the wedge dips: for a dip angle of 45°, the deviation is of some degrees only, while for a dip of 60° the retrieved dip may differ from the actual one by as much as 10-15°. In any case, these tests suggests that if a dipping conversion of 60-65° is observed in the receiver function profile, the real structure it is caused by will not be dipping any shallower than this.

The importance of this result is that an acceptable representation of the subsurface structure can be obtained even if very dissimilar velocity models are used in the migration. This is particularly essential since the Quintero and Kissling [2001] velocity model places the Moho at much

greater depth than the receiver functions indicate. It would be best to perform the migration with a model that corresponds to the structures seen in the receiver functions; but of course such a model is not known a priori. The above test indicates that the change in retrieved structure is small if a different velocity model is used, so it is permissible to perform the migration with the best known velocity model, even though this is not optimal.

Figure 6.9: *Synthetic receiver function results for a 45° dipping high-velocity wedge − migrated profile. Left: migration with the Quintero and Kissling [2001] velocity model; right: migration with the two-layer velocity model (see text).*
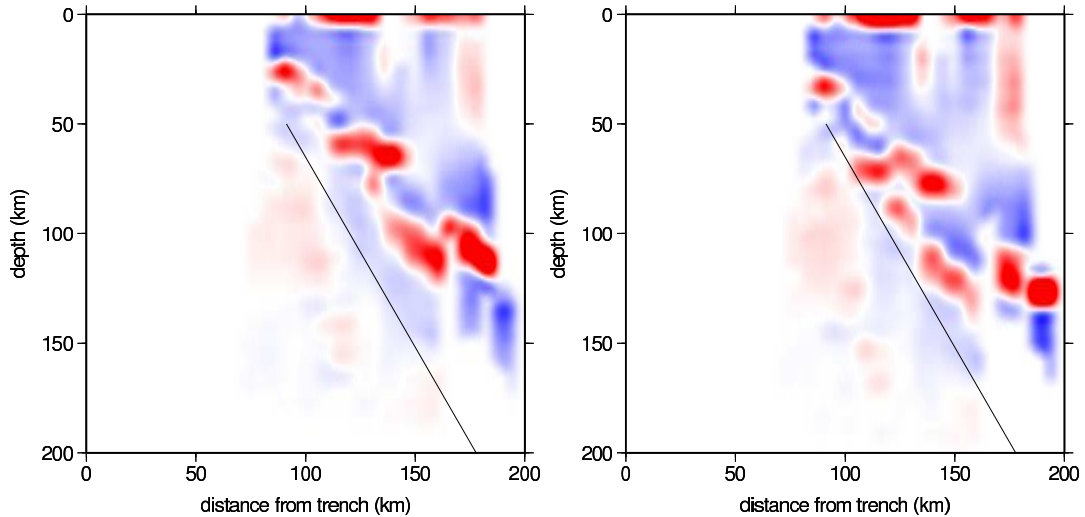
Figure 6.10: *Synthetic receiver function results for a 60° dipping high-velocity wedge − migrated profile. Left: migration with the Quintero and Kissling [2001] velocity model; right: migration with the two-layer velocity model (see text).*

The fact that the slab signal appears somewhat patchy, with positive conversions interrupted by negative signals in some places, can be speculated to be caused by the negative-polarity conversions that are observed on arrivals from the south-west. To test this hypothesis, only rays coming from back-azimuths between $-30°$ and $150°$ (corresponding approximately to the positive conversion range in Figure 6.6) were included in the migration. Results for the $60°$ dipping high-velocity wedge case are shown in Appendix F.1. The changes in the slab signal are slight − indeed the signal is rather more disrupted than before. The patchiness is hence not caused by interference and cancelling of negative and positive conversion signals migrated to the same position from different directions, but by the data coverage itself. Since the polarity change in the conversion signal coincides with changing delay times, the positive and negative signals appear at different depths and do not interfere destructively, justifying the "naïve" migration algorithm by simple back-tracing all rays.

The cause for the patchiness is probably in the fact that the migration algorithm is based on a 1-d velocity model. Therefore, refraction of the rays at the slab is not taken into account and the conversion signals are migrated to slightly shifted positions relative to their true origin, depending on the direction of the incoming rays.

A further attempt was made to improve the migration, taking into account the fact that the ray path geometries can become rather complicated, as seen above. Therefore, it is clear that simple backward ray-tracing in a 1-d velocity model based on the theoretical back-azimuth and ray-parameter will not in all cases migrate the receiver function signals to the real conversion points. An alternative migration algorithm was therefore implemented. In this approach, the observed receiver functions were back-projected into all possible back-azimuths for all values of $p = 0.03\text{-}1.0$ s/km.

Although this technique will "smear" the signal over a conical volume, it was hoped that the signals would add up at the real conversion points and cancel out everywhere else. However, the new migration algorithm does not give satisfactory results neither for the observed data nor for the dipping wedge models. As an example, the migrated section of profile 3 for the new migration algorithm is shown in Appendix F.2. Evidently, this migration method fails to produce a clear signal, because the amplitudes are very small and dominated by migration artefacts ("smiles") through a large part of the profile. This is probably due to the strong azimuthal variability of the signal and the steep dip of the structure. This test shows that while we can expect some error to be introduced in the simple backward ray-tracing migration, this technique is in any case superior to an indifferent back-projection of the conversion amplitudes onto a cone covering $360°$ in back-azimuth.

6.1.3 Models Including a Crust and Dipping Wedge

The encouraging results of the dipping wedge models suggest a refinement of the models to include the overlying crust. Although the model results using a migration based on the input velocity model (simplified to 1-d) give slightly better results, the plots presented in this sections used the Quintero and Kissling [2001] velocity model. This should provide better comparability with the real data, which were also processed in this way, as no better velocity model was given. Hence, any deviations from the real model should cause the same errors in the model results as in the real data.

The models considered in this chapter were designed to test simple scenarios that might be expected for a subduction zone. They were not chosen for the best possible fit to the individual traces, where the thickness of the crust, depth of the slab under the stations etc. should be deter-

mined with accuracy. Here, we are only trying to see the effects that a dipping slab would have in different settings, while the depth of the slab and other details are chosen arbitrarily within plausible boundaries.

The model includes an upper crust (15 km thick) and a lower crust (20 km thick) in addition to a high-velocity steeply dipping wedge. The geometry of the model is shown in Figure 6.11. Ray paths for two stations determined by back-ward propagating the rays with the Quintero and Kissling [2001] velocity model are displayed in Figure 6.12 to give an idea of the lateral spread of the rays.

The choice of velocities was made to represent average upper and lower crustal velocities, a serpentinized mantle wedge (15% serpentinization giving $v_p \approx 7.6$ km/s with the relations from Carlson and Miller [2003]) and a dipping wedge with mantle velocities. In later models, the velocity model will be refined based on results from active seismics [Stavenhagen, 1998] and tomography [Dinc, 2008]. Whatever the actual velocity values are, a velocity contrast of 6% of the slab relative to the mantle wedge corresponds to the generally observed values for subduction zones worldwide [compare, e.g., Helffrich, 1995]. v_p/v_s is taken to be 1.75 in the whole model. The calculations were performed for a case with and without multiples for a 45° and 60° dipping wedge and are compared in Figure 6.13.

The inclusion of multiples has a pronounced effect on the model results, with very broad and strong multiples showing up at a migrated depth of around 60 km and 120-150 km. Frederiksen and Bostock [2000] mention that their modelling routine may create unrealistically large multiples in some observation scenarios, explaining this by the fact that the model assumes perfectly smooth surfaces, whereas the real subsurface structure of, e.g., the Moho, may be rough and therefore have much smaller reflection coefficients. They propose to perform the modelling studies without the inclusion of multiples in this case.

To check if the strong multiples are only created by the given input model, several different models were calculated to compare the results with and without multiples, for various slab dip angles and different velocity contrasts at the Moho. In all cases the multiples were very strong, even when it was tried to forcedly suppress multiples by assuming the crust to consist of several layers with small velocity contrasts.
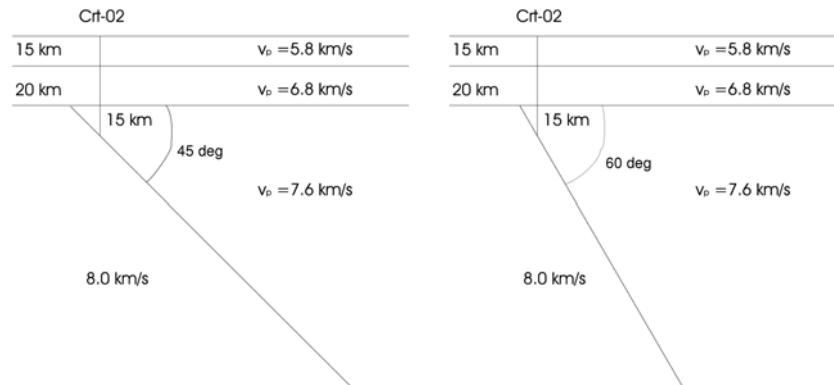
Figure 6.11: *Model geometry with homogeneous crust and 45° (left) vs. 60° (right) dipping mantle wedge*
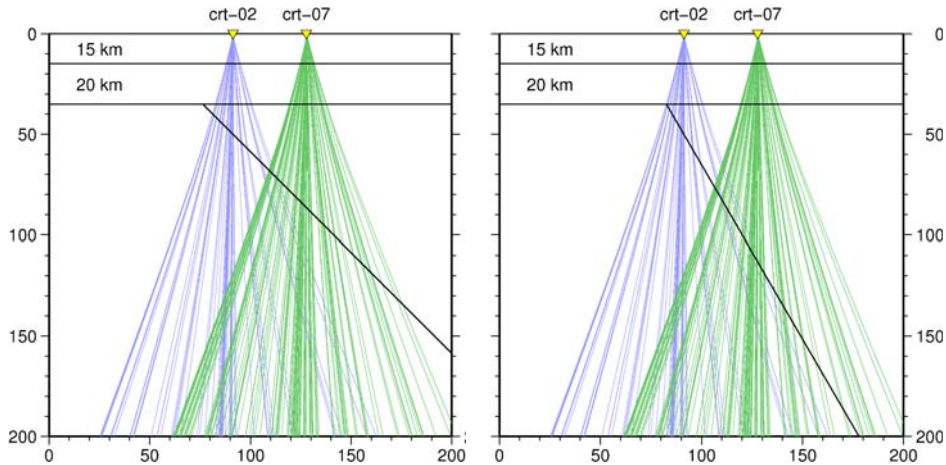
Figure 6.12: *Model geometry with homogeneous crust and dipping mantle wedge, with ray paths for two stations. Left: 45° dipping wedge; right: 60° dipping wedge. The rays are displayed for stations crt-02 (Dominical) and crt-07 (Los Ángeles). The model is not realistic close to the trench, because here the slab is observed to bend towards shallower angles. The ray paths were calculated in 3-d, but using the 1-d velocity model by Quintero and Kissling [2001]. Therefore, no refraction at the slab is taken into account.*
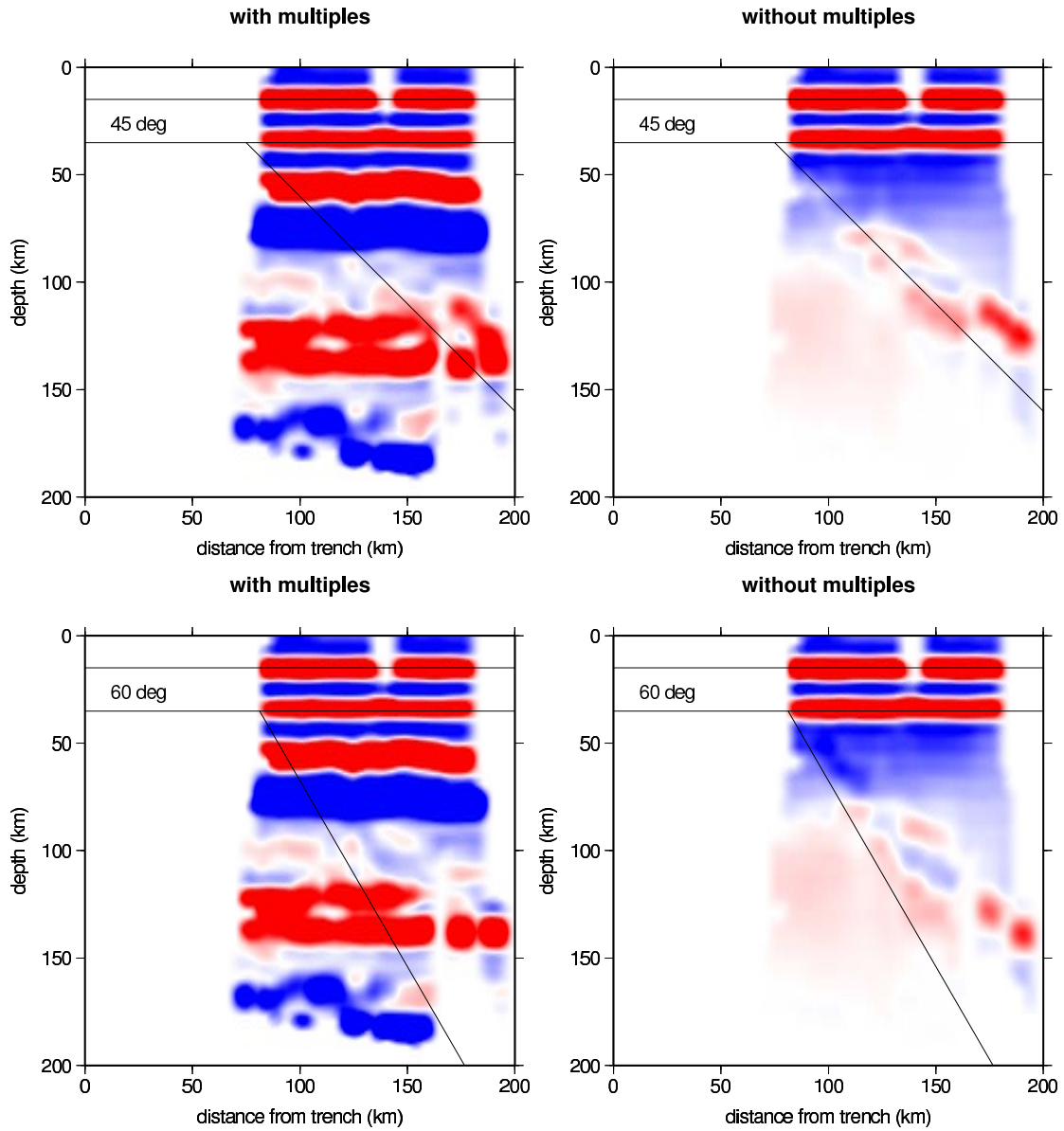
Figure 6.13: *Synthetic receiver function results for the model shown in Figure 6.11. Upper panel: 45° dipping wedge, lower panel: 60° dipping wedge. Migration was performed using the Quintero and Kissling [2001] 1-d velocity model. Left panel: model including multiples, right panel: model without multiples.*

6.2 Investigation of Multiple Strength by Finite-Difference Modelling

Finite-difference 2-d modelling was performed with the FDMPI program by Bohlen [2002] to compare the results with the modelling based on the Frederiksen and Bostock [2000] program. The same velocity model was used as in Figure 6.13, with a 60° dipping slab. Receivers were placed with a spacing of 10 km. The dipping wedge was at 70 km depth below the first receiver and at 190 km below the last receiver.

The first modelling series was done for different angles of incidence of a plane wave originating at 200 km depth, propagating upwards at an angle of 0°, ±10° and ±20° to the vertical. Positive angles denote a plane wave entering from the left in the model geometry, negative angles a wave entering from the right. The results are shown in Figure 6.14.

The modelling results for different angles of incidence show that the relative strength of the slab conversion as compared with the multiples depends strongly on the angle of incidence of the plane wave on the slab and Moho/crustal interfaces. This is a natural consequence of the angular dependence of the conversion coefficients. For moderate angles of the plane wave with respect to the vertical, the slab conversion can be easily discerned even where multiples are present. The Moho and crustal discontinuity are also readily seen in the synthetic data, although the Moho appears somewhat perturbed when the incoming wave comes from the down-dip direction. This may be explained if the wave is refracted at the slab in a way to impinge nearly vertically on the Moho, so that conversions would be very weak or absent. Conversely, at larger angles of incidence (20-30° inclined plane wave coming from the up-dip direction), the wave would strike the subducting slab almost vertically, depressing slab conversions.

6.2.1 Rough Moho Topography

Two different sets of models including a "rough" topography for the Moho and crustal discontinuity were calculated, with the following implementations of roughness:

1. The first set of models included a sinusoidal variation of the two discontinuities, with ±1 km amplitude and 5 km wavelength. This is below the resolution limit of the receiver functions, which was estimated to be about 12 km at a depth of 30 km (Chapter 4) and is about 9 km at 15 km depth.

2. In contrast to this smooth long-period variation in topography, a scenario with random fluctuations in depth of the Moho and crustal interface was investigated. This also included ±1 km variations in depth, which were randomly created at along the profile. Again, the variations are too small to be resolved at the wavelengths considered in the study, but create roughness of the interface.

While the roughness of the Moho and crustal structure was artificially created based on very simplistic models, the slab is intrinsically rough in the way that the dipping structure can only be represented as a "stair"-shape in the orthogonal grid. Therefore, while the topography of all discontinuities is probably far from smooth, the fact that the Moho and crustal interface – but not the slab – are explicitly roughed up does not stand in contrast to reality, but takes into account the treatment of the modelling routine of horizontal vs. dipping discontinuities.
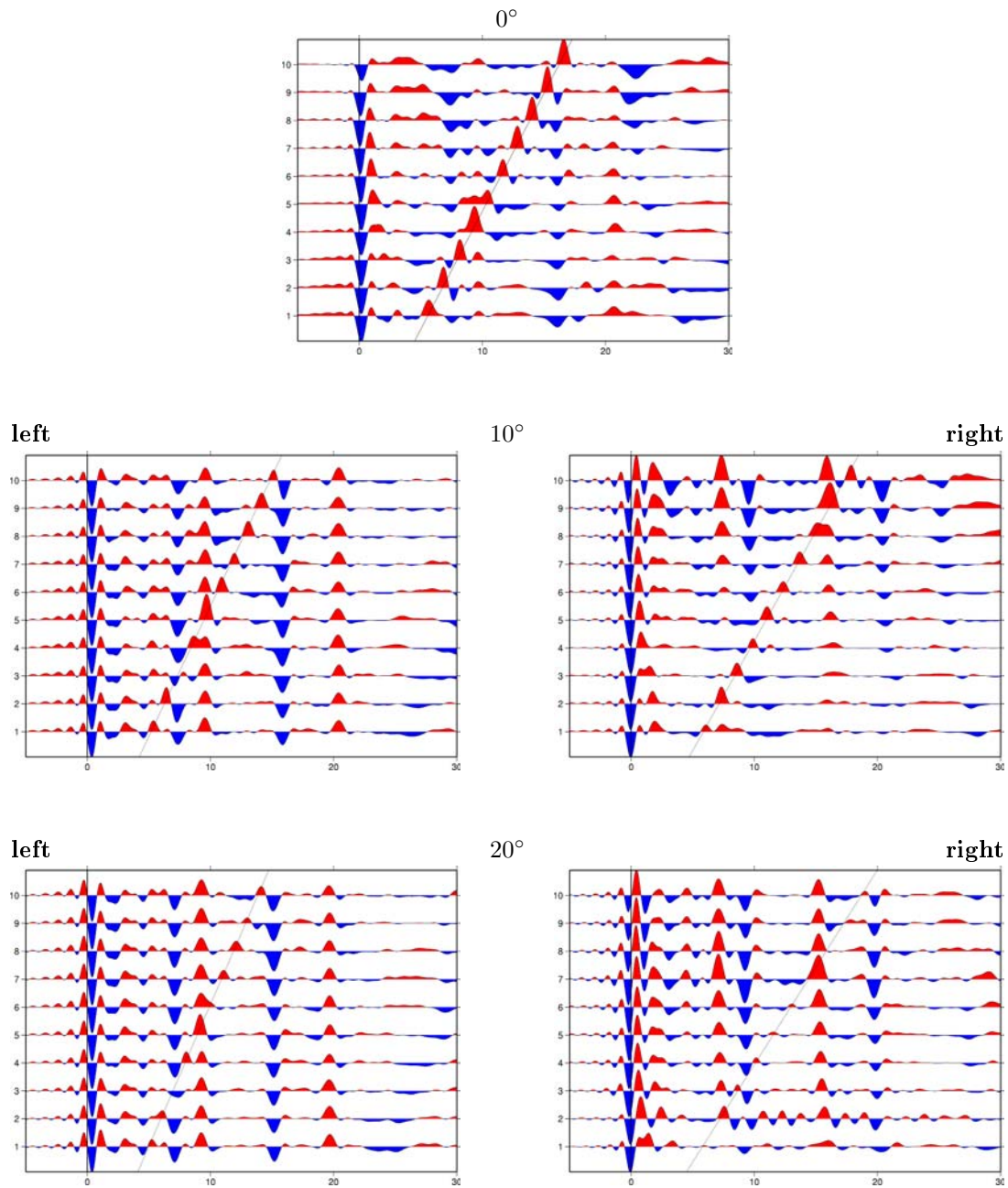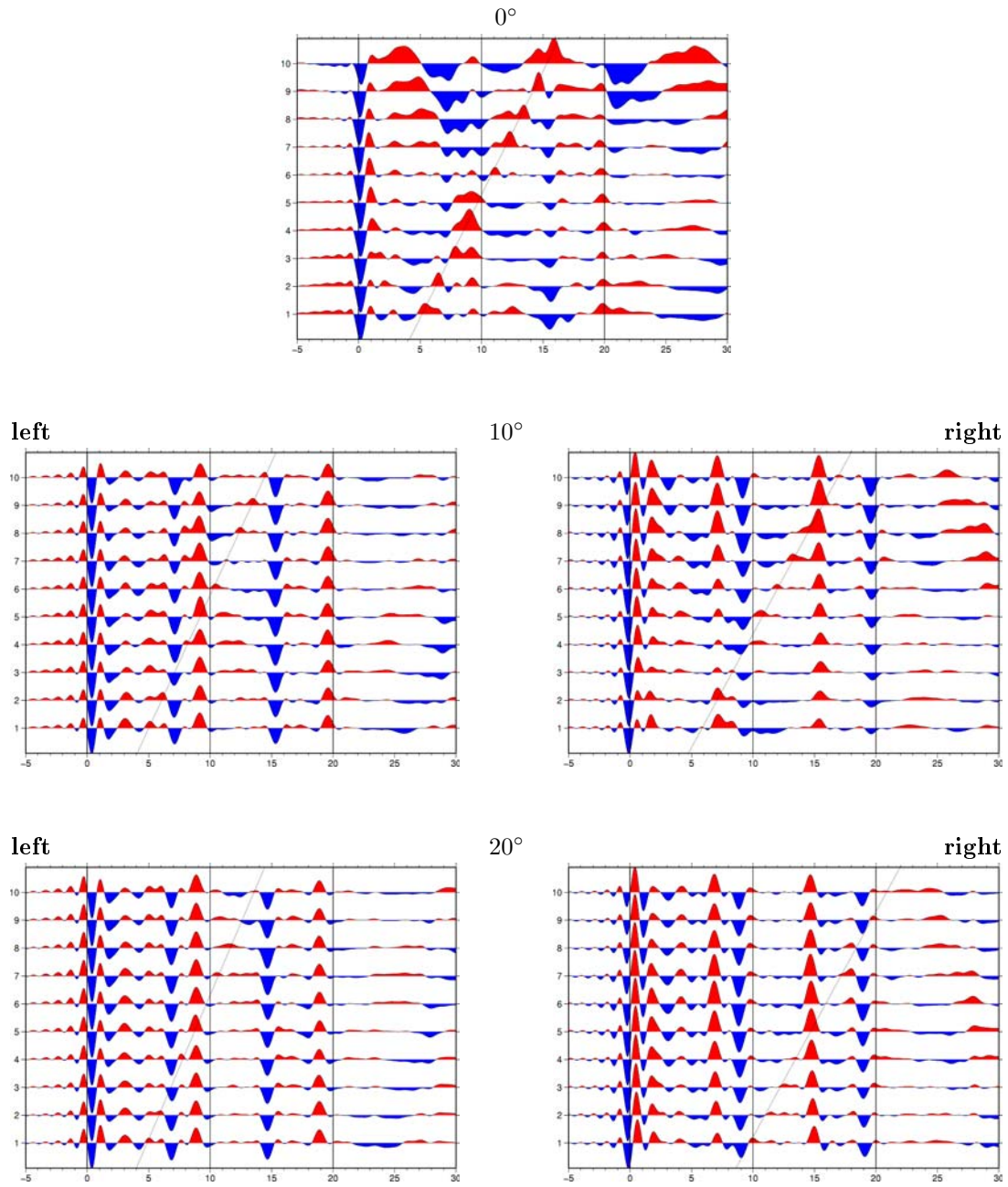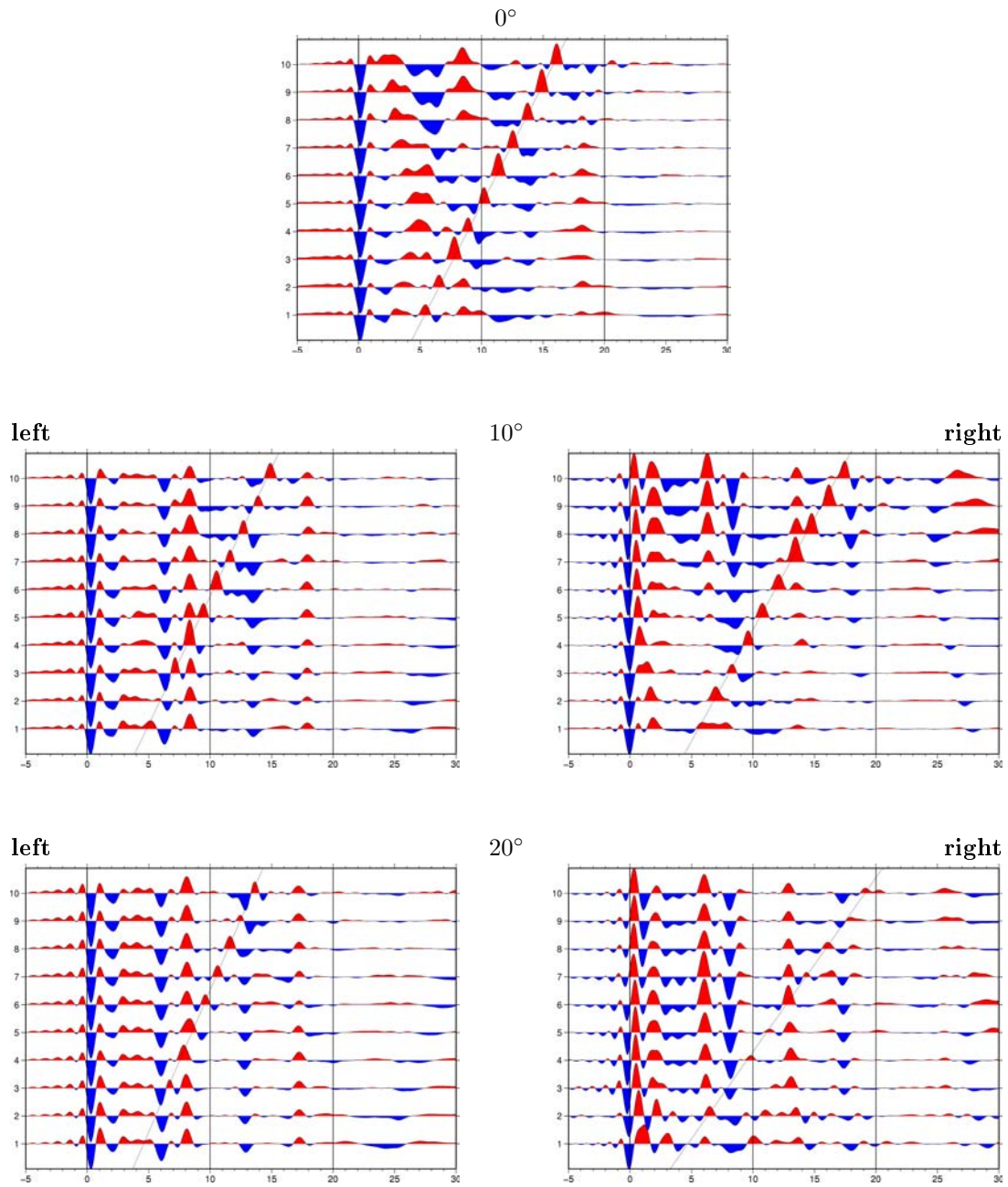
Figure 6.14: *Synthetic receiver function results for FD modelling of the scenario shown in Figure 6.11, but with a 60° dipping wedge. Trace 1 is 70 km above the dipping wedge, trace 10 190 km above. Traces were NMO-corrected and scaled relative to their maximum. Upper panel: vertically incident plane wave, middle: incident plane wave propagating 10° from the vertical, lower panel: incident plane wave propagating 20° from the vertical. Left: plane wave coming from the left (from the up-dip direction), right: plane wave coming from the right (from the down-dip direction in the model).*

Neither the long-wavelength sinusoidally varying Moho and crustal discontinuity nor shorter-period random fluctuations could significantly suppress multiples in comparison with the slab signal. The main effect of the introduction of sinusoidal variations is the creation of high-frequency reverberations in the receiver functions, which can be suppressed by low-pass filtering below 2 s. This somewhat obscures the slab signal very close to the trench (the same thing occurs for the first models with smooth Moho and crustal structure), but the main behaviour of the slab conversion remains unchanged. The results resemble the model run with smooth interfaces (see Figure G.1 in Appendix G).

The random fluctuations in Moho and crustal interface depth also introduced some fluctuations, but to a much smaller degree. By low-pass filtering with a corner frequency of 1 Hz, these fluctuations could be eliminated. The results (shown in Appendix G, Figure G.2) are very similar to the smooth model results, with only slight changes of the slab conversion-multiple ratio at distinct angles.

In spite of the simple nature of the roughness models, we can conclude that the strength of the multiples does not depend strongly on the interface topography. The slab conversions can be clearly distinguished for steep incidence of the plane wave, but become weaker for larger angles of incidence.

6.2.2   Absorption in the Crust and Mantle Wedge

In order to check a different mechanism affecting the strength of the slab conversions, attenuation is introduced in the model, while again assuming smooth surfaces. If attenuation plays a role in the crust and/or mantle wedge, it would affect multiples more strongly than conversions, because multiples have longer ray-paths in the crust. However, since the quality factor Q for P-waves in the Earth is generally larger than for S-waves [Lay and Wallace, 1995], the attenuation of the first crustal/intercrustal multiple (PPPS) is not as marked as that of later (PPSS and PSSS) multiples.

Two kinds of models were investigated:

- absorption in the crust and mantle wedge, $Q_P = 90$, $Q_S = 50$ with 2 relaxation mechanisms,

- absorption confined to the crust, $Q_P = 50$, $Q_S = 30$ with 7 relaxation mechanisms.

These quality factors are very low, though these values can occur in extreme settings such as subduction zone mantle wedges. Here, the values were chosen so low to investigate if absorption *can* account for the multiple strength. If these absorption values do not produce a marked effect on the multiples, we can be sure that absorption is not responsible for the weakness of the multiples. Modelling results are displayed in Figures 6.15 and 6.16, respectively. The frequency behaviour of Q is shown in Figure 6.17.

If absorption is assumed both in the crust and mantle wedge, the multiples are attenuated slightly, but the effect on the slab conversion is more significant. This can be understood because the S-wave created by conversion at the subducting slab travels a long way through the attenuating medium, while the multiples remain P-waves (with weaker attenuation) until their final conversion at the Moho, and then just traverse the crust as S-waves. This scenario cannot hence explain the relative strength of the observed slab signal in the receiver functions.

0°

left   10°   right

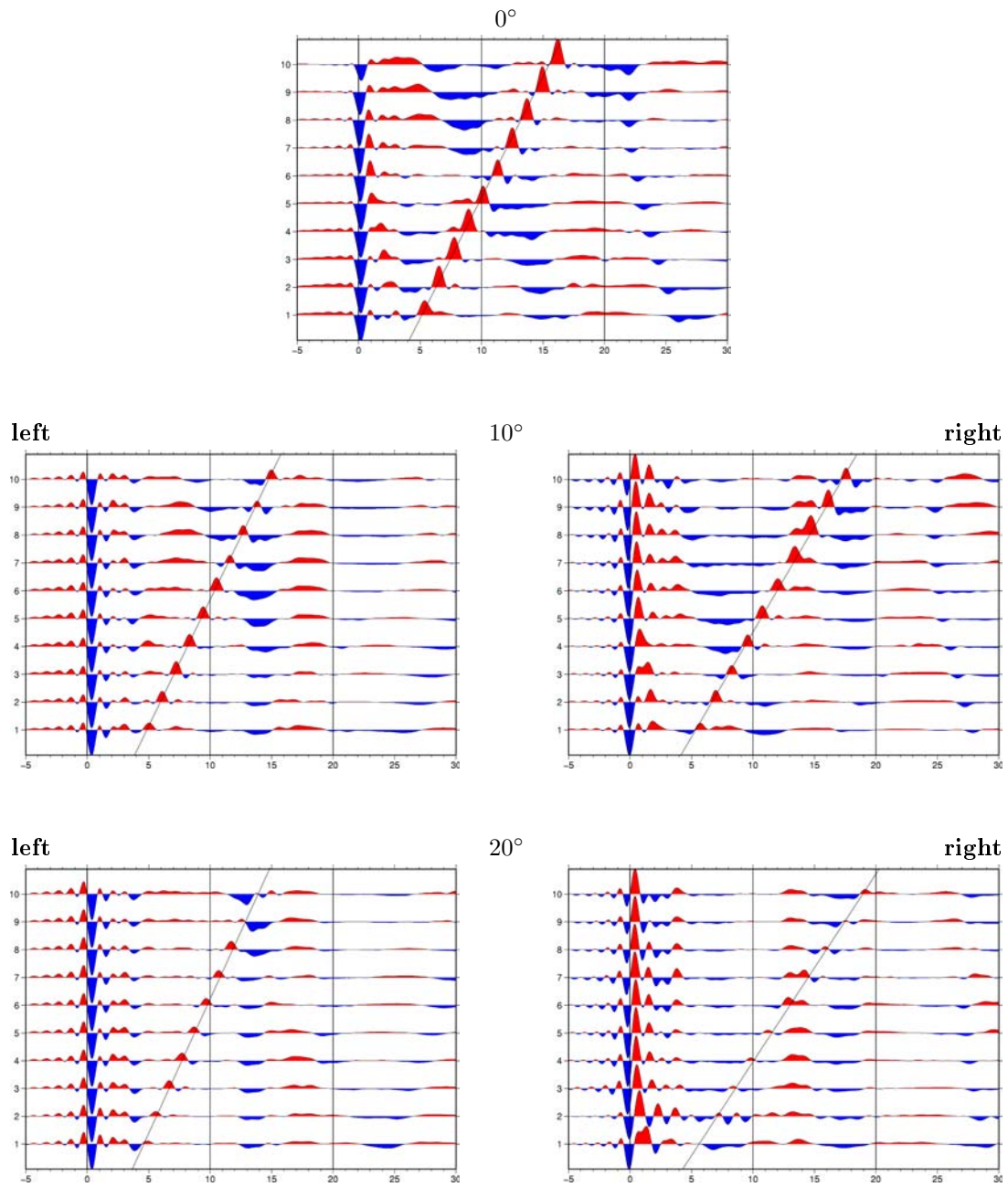left   20°   right

Figure 6.15: *Synthetic receiver function results for FD modelling of the scenario shown in Figure 6.11, but with a 60° dipping wedge and absorption in the crust and mantle wedge (absorption model 1). Traces were processed like in Figure 6.14.*

Figure 6.16: *Synthetic receiver function results for FD modelling of the scenario shown in Figure 6.11, but with a 60° dipping wedge and absorption in the crust only (absorption model 2). Traces were processed like in Figure 6.14.*
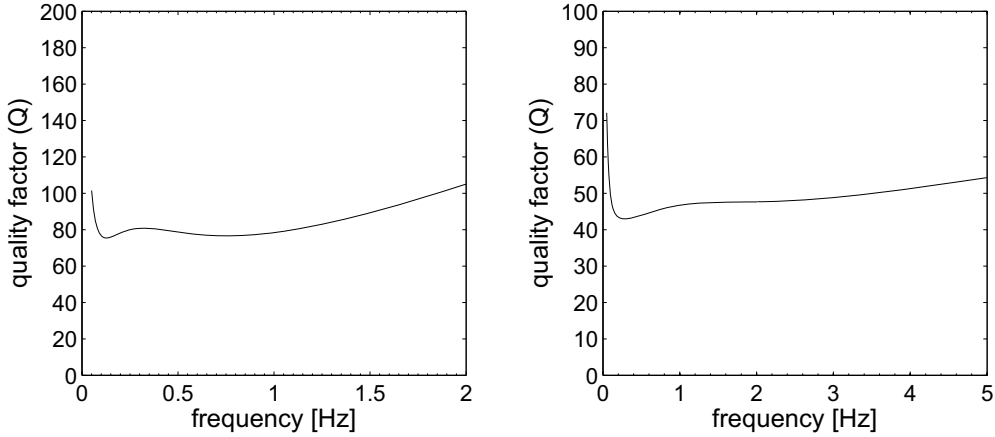
Figure 6.17: *Frequency behaviour of Q_P used in FD-modelling. Left panel: model with 2 relaxation mechanisms, absorption in the crust and mantle wedge; right panel: model using 7 relaxation mechanisms, absorption in the crust only.*

In the case of crustal attenuation only, the slab signal is not significantly influenced, while the later multiples (after about 10 s) are weakened. Even so, the effect on the first multiples is very slight. While attenuation in the crust cannot be excluded, it does not provide a mechanism for enhancing the strength of the slab signal in comparison with the crustal and Moho multiples.

It is certainly possible to enhance the slab signal over the multiples by introducing absorption with $Q_P < Q_S$; however, the above results show that a simple model of absorption cannot easily explain the observed multiple strength without considerable fine-tuning of the Q-values to match our expectations. It cannot be excluded that such a very carefully selected parameter set is indeed realistic, but it does not inspire confidence in the mechanism if the parameters need to be chosen within such a fine range, and without a good reason why extraordinary conditions like $Q_P < Q_S$ should be found here. I will therefore explore a final scenario that might be expected to influence the relative strength of multiples vs. primary conversions.

6.2.3   Effect of velocity gradients

If the velocity discontinuity is not as abrupt as assumed, but takes the form of a velocity gradient, multiples as well as primary conversions are significantly weakened. The present model assumes that the upper crust (0-15 km depth) presents a velocity gradient between $\alpha = 5.8$ km/s and $\alpha = 6.8$ km/s, $\beta = 3.2$ km/s and $\beta = 3.9$ km/s, while the lower crust has constant velocities $\alpha = 6.8$ km/s and $\beta = 3.9$ km/s. The Moho is again formed by a 5 km thick velocity gradient (between 30 and 35 km depth) from lower crustal velocities to the mantle wedge velocities of $\alpha = 7.6$ km/s, $\beta = 4.3$ km/s. These are the same velocities that were used throughout the FD-modelling studies, but with gradients smoothing the transition between different layers.

The results are shown in Figure 6.18. This model successfully produces clear slab conversions at all angles of incidence, while the multiples are significantly depressed. Still, the Moho and crustal conversions can be discerned in the receiver functions. In total, these results agree much better

with the observations.

Figure 6.18: *Synthetic receiver function results for FD modelling of the scenario shown in Figure 6.11, but with velocity gradients in the crust and at the Moho. Traces were processed like in Figure 6.14.*

Although the actual thickness of the velocity gradient layers may be different from the scenario assumed in this model, this shows that velocity gradients can provide an explanation for the observed slab signal and multiple strength. The upper crust will probably not be a single velocity-gradient layer, but rather consist of fine layers with increasing velocities; but the velocity gradient model appears to provide a better representation of the real crust than the two-layered model with abrupt velocity discontinuities.

Several further effects may come into play to determine the relative strength of multiples and primary conversions, which have not been analyzed in detail here. One is the NMO-correction, which can severely influence the multiples, depending on the velocity model used in the analysis. Even though the migration was performed for the not NMO-corrected traces, the migration velocity model will also influence the position of multiples and their strength in the migrated image. The topography of the study region is also far from the flat-surface case that was considered in the model, and may also influence the results.

In any case, in the velocity gradient models we have found a reasonable mechanism to explain why the observed multiples can be much weaker than those predicted in the Frederiksen and Bostock [2000] model. Since the Frederiksen and Bostock [2000] program cannot model velocity gradients, and seems to produce unrealistically strong multiples, further modelling studies with this code will be performed in the following without multiples. We know that we expect multiples between 8 s and 10 s, and 15 s and 20 s delay time, depending on the angle of incidence. Slab multiples occur as steeply dipping features at 15-25 s time, also seen at the left end of the migrated profiles (see Figures 6.7 to 6.10). The following studies will therefore concentrate on the primary conversions, taking into account an additional property into the modelling: anisotropy.

6.3 Anisotropy

6.3.1 Overview of Seismic Anisotropy

Wave propagation in an anisotropic medium

In the general case of anisotropic (but still linearly elastic) media, the elastic (stiffness) tensor C_{ijkl} relates stress σ_{ij} and strain ϵ_{ij} by Hooke's Law

$$\sigma_{ij} = C_{ijkl}\epsilon_{kl} \tag{6.2}$$

The equation of motion for seismic waves in such a medium is given by

$$\rho\frac{\partial^2 u_i}{\partial t^2} - C_{ijkl}\frac{\partial^2 u_k}{\partial x_j \partial x_l} = 0 \tag{6.3}$$

where ρ is the density of the medium and u_i is the displacement. For a plane wave

$$\mathbf{u}(\mathbf{x}, t) = \mathbf{A}(\omega)\exp\left[-i\omega(t - \hat{\mathbf{n}}\mathbf{x}/V)\right] \tag{6.4}$$

with unit vector $\hat{\mathbf{n}}$ in the direction of slowness $\mathbf{s} = \hat{\mathbf{n}}/V$ and the polarization vector $\mathbf{A}$ giving the direction of particle motion, the plane wave equation can be brought into the form of an eigenvector problem (Christoffel equation)

$$(C_{ijkl}n_i n_k - \rho V^2 \delta_{jl})A_l = 0 \tag{6.5}$$

The eigenvalues correspond to three separate types of body waves, which propagate with the polarization direction given by the eigenvectors.

For isotropic media, symmetry conditions imposed on the stiffness tensor allow its reduction to just two *Lamé parameters* λ and μ, and the solutions to the Christoffel equation give a longitudinally polarized P-wave and two transversely polarized S-waves propagating with the velocities

$$\alpha = \sqrt{(\lambda + 2\mu)/\rho} \quad \text{and} \quad \beta = \sqrt{\mu/\rho}$$

Such a distinction between P- and S-waves is not possible in a general anisotropic medium; however, in the case of weak anisotropy the three body waves are in practice similar to the isotropic body waves, in the way that there exist a quasi-P wave with almost longitudinal polarization and two quasi-S waves with different velocities and almost transverse polarization. There exist hence two kinds of observable anisotropy in an elastic medium:

1. azimuthal anisotropy, i.e., the variation in elastic wave speed with the direction of wave propagation, and

2. polarization anisotropy, i.e., the variation in wave speed with the polarization direction, which occurs for S-waves only.

Symmetry classes of anisotropy

If certain symmetries are satisfied in the elastic medium, the number of elastic constants decreases. Important special cases of anisotropy are

- orthorhombic anisotropy – characterized by three mutually orthogonal axes of symmetry,

- hexagonal anisotropy – characterized by a single plane of isotropy, i.e., by rotational symmetry around an axis normal to this plane, and

- isotropy − with the highest possible symmetry.

Hexagonal anisotropy (Figure 6.19) can be created either by periodic layering of materials with different elastic properties, oriented fracture sets, or aligned inclusions (so-called *extrinsic anisotropy*), with layer tickness small in comparison with the seismic wavelength, or by *intrinsic* mineral properties of such minerals as mica, clay or serpentine.
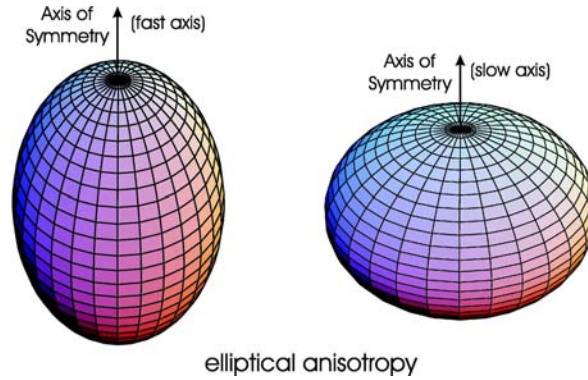
Figure 6.19: *Elliptical anisotropy (special case of hexagonal anisotropy): schematic representation of the velocity ellipse. Left: the symmetry axis has faster velocity than the two axes perpendicular to it, right: the symmetry axis has slower velocity.*

The dominant upper mantle material olivine has orthorhombic symmetry (Figure 6.20). However, the olivine-rich peridotites can be represented approximately by hexagonal anisotropy [Christensen, 1984, Park and Yu, 1992], which can be characterised by three anistropy parameters: the P-wave anisotropy, the S-wave anisotropy and the direction of the fast/slow axis.

In olivine, the [100] axis (a-axis) exhibits fastest P-wave velocities, and is the direction of polarization of the fastest S-wave; minimum P-velocities are parallel to the [010] axis (b-axis) [Mainprice et al., 2000]. The single-crystal P-wave anisotropy for olivine is

$$A_p := \frac{2(V_{p,fast} - V_{p,slow})}{V_{p,fast} + V_{p,slow}} = 22\% \tag{6.6}$$

Generation of macroscopic anisotropy

Single-crystal anisotropy can give rise to macroscopic anisotropy of the rock if the crystallographic axes show preferential alignment. This *lattice-preferred orientation* (LPO), produced by strain or viscous flow, is thought to be the main cause of anisotropy in the upper mantle.

Lattice-preferred orientation develops by a combination of two microscopic mechanisms [Karato, 2008, Chapter 14]:

- When deformation is due to dislocation glide, deformation-induced lattice rotation occurs, i.e. a rotation of the crystallographic orientation of the individual crystals, controlled by their slip systems. If microscopic deformation does not have a rotational component, as is the case for diffusional creep or dislocation climb, no LPO is created.
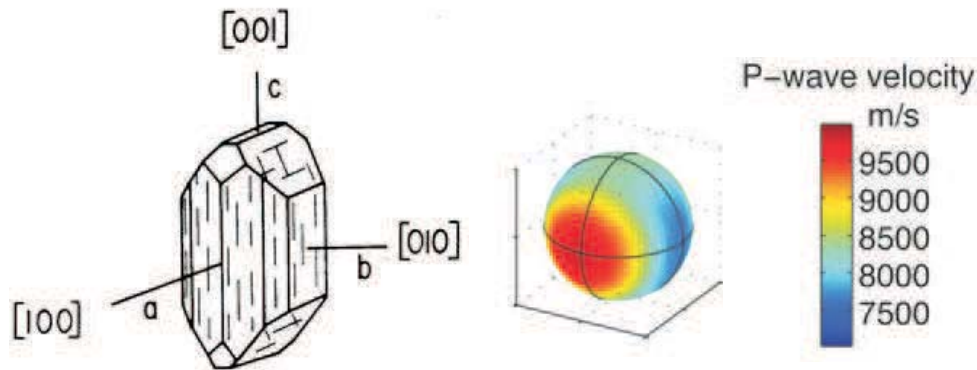
Figure 6.20: *Single crystal properties of olivine [adapted from Blackman, 2007]. Left: crystal structure, right: azimuthal variation in P-wave velocity.*

- Recrystallization, i.e. preferential growth of grains with one orientation and grain-boundary migration, also results in the creation of LPO.

Olivine can assume different kinds of LPO as a function of the physical and chemical conditions, shown in Figures 6.21 and 6.22.

The different olivine LPO fabrics generate different kinds of seismic anisotropy in olivine, which are simplified in the following overview:

A-type	fast axis parallel to flow	$A_p = 6\%$
	fast S-wave pol. parallel to flow	$A_{s,max} = 5\%$ orthogonal to flow
B-type	fast axis orthogonal to flow	$A_p = 5\%$
	fast S-wave pol. orthogonal to flow	$A_{s,max} = 5\%$ parallel to flow
C-type	fast axis approx. 30° to flow	$A_p = 11\%$
	fast S-wave pol. approx. 30° to flow	$A_{s,max} = 7\%$ orthogonal to flow plane
D-type	fast axis parallel to flow	$A_p = 15\%$
	fast S-wave pol. parallel to flow	$A_{s,max} = 0.5\%$ nearly orthog. to flow plane
E-type	fast axis parallel to flow	$A_p = 17\%$
	fast S-wave pol. parallel to flow	$A_{s,max} = 12\%$ orthogonal to flow plane

This overview can only be taken as a very coarse approximation of the real mantle fabric. Among other things, it should be kept in mind that the degree of alignment of the olivine a-axis depends on strain and temperature. Zhang and Karato [1995] and Zhang et al. [2000] show that at lower temperatures (1473°C) the olivine a-axis aligns to within 15° with the long axis of the strain ellipse for strains of about 1.1; alignment becomes nearly parallel for higher temperatures and/or higher strains.

The existence of olivine B-type fabric in high-stress environments with high water content is particularly interesting for anisotropy investigations of the mantle, because this fabric shows orthogonal alignment of the fast axis to the flow direction, while the other fabrics all orient the fast axis parallel to the flow.
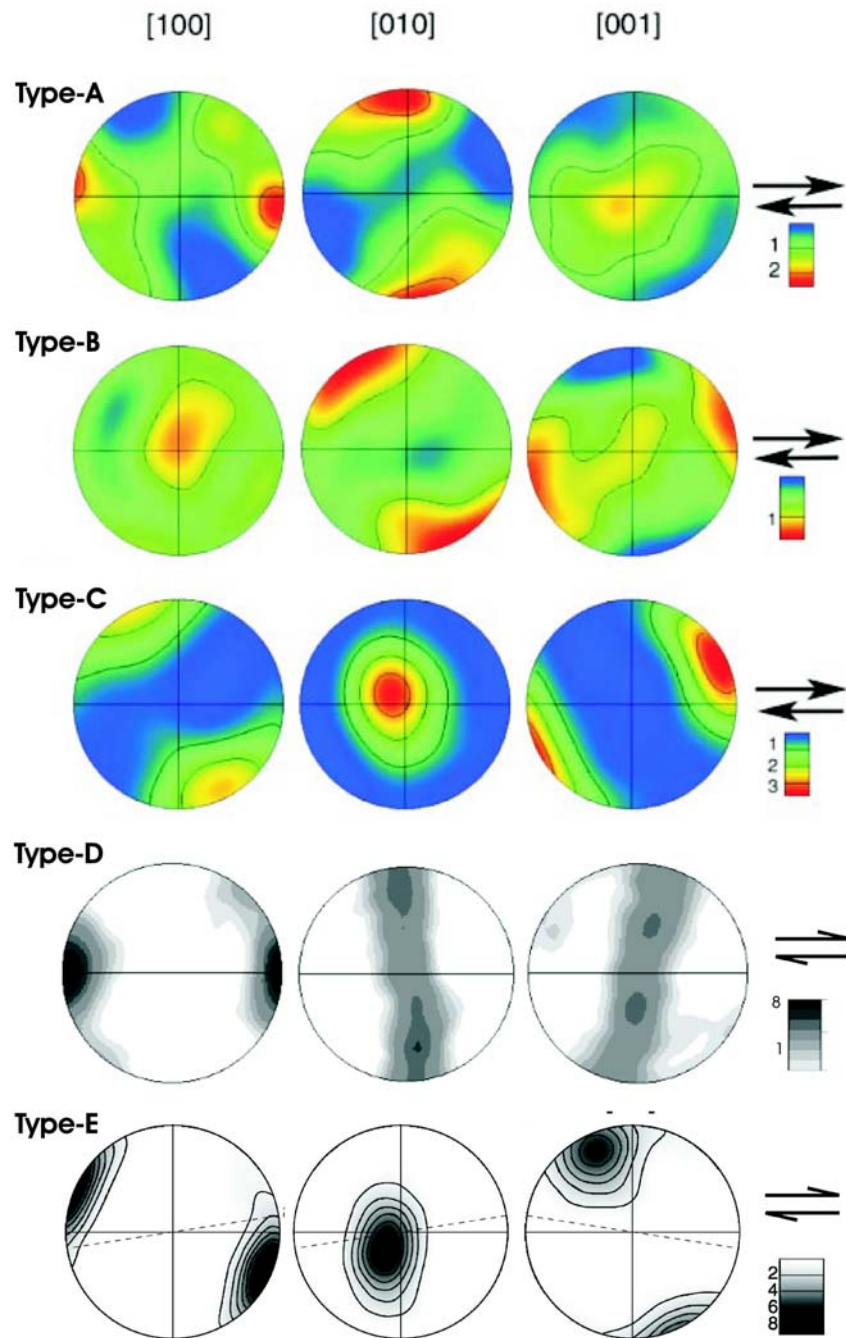
Figure 6.21: *Pole figures of deformed olivine crystallographic fabrics. The east-west direction corresponds to the shear direction. Equal area projection of the lower hemisphere. The colour coding refers to the density of data points. Type-A to C from Jung and Karato [2001], type-D from Bystricky et al. [2000], type-E from Katayama et al. [2004].*
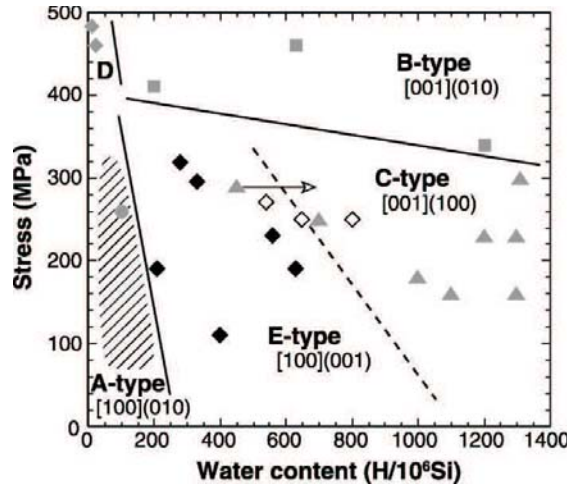
Figure 6.22: *Olivine fabric diagram as a function of stress (MPa) and water content (*H/10^8Si*) at high temperatures (1470 − 1570 K) [from Jung and Karato, 2001]. Katayama and Karato [2006] show that the B- to C-type transition occurs for lower stress if the temperature is lowered under water-saturated conditions.*

In addition to LPO, the presence of melt can produce anisotropy in the upper mantle. Anhydrous, partially molten mantle rocks exhibit a fabric with the a- and c- axis forming a girdle in the shear plane and the b-axis oriented normal to the plane. When the melt segregates into bands, the configuration switches, with the a-axis now normal to the shear plane and the c-axis nearly parallel to the direction of shear [Holtzmann et al., 2003].

In the uppermost crust, cracks and fine layering are the most important mechanisms causing anisotropy, while in the lower crust, both effects from aligned cracks and intrinsic crystal anisotropy (LPO) combine to create anisotropy.

Relevance of anisotropy for the study region

The classical view of a subduction zone predicts that mantle wedge material is entailed by the subducting slab and hence pulled to greater depth. While the mantle directly above the slab is flowing downwards parallel to the slab, a surface-parallel flow of back-arc mantle into the corner ensues. This is the corner-flow model, which predicts trench-normal anisotropy in the case that the olivine a-axis is oriented parallel to the flow (see Figure 6.23).

Contrary to the expectations based on the corner-flow model, shear-wave splitting observations from subduction zones all over the world have observed trench-parallel polarization directions of the fast S-waves, in particular in the fore-arc and back-arc [Russo and Silver, 1994, Fouch and Fisher, 1996, Fisher et al., 1998, Audoine et al., 2004, Nakajima and Hasegawa, 2004, Long and van der Hilst, 2005, Kneller and van Keken, 2007]. This may be due to olivine B-type fabrics, which have been predicted to occur in the mantle corner of the fore-arc. In the arc and back-arc, however, a different explanation is needed, as A-, C- or E-type fabrics (all with olivine fast axis approximately parallel to the flow direction) are predicted in this regime [Kneller et al., 2005]. The presence of melt is a possible alternative. Finally, it is possible that the observed arc-parallel

anisotropy directly reflects the mantle flow pattern (Figure 6.24), which would then include an oblique [Nakajima et al., 2006] or arc-parallel flow component [Long and Silver, 2008]. This last hypothesis is corroborated by geochemical studies [Hoernle et al., 2008] arguing for trench-parallel transport of geochemical tracers.
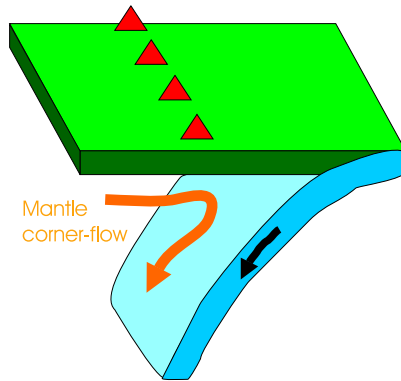
Figure 6.23: *Schematic representation of corner flow in the mantle in subduction zones*

In Central Costa Rica, arc-parallel flow is suggested on the basis of geochemical observations [Hoernle et al., 2008], and is also reflected in shear-wave-splitting analyses; however, these studies did not consider olivine fabric variations and possible occurrence of B-type fabric. Tomography studies observed a shift from trench-normal anisotropy in the fore-arc to trench-parallel anisotropy under the active volcanic arc in both Central Costa Rica and Southern Nicaragua. All these studies, however, have very limited resolution and provide only a picture of the integrated anisotropy between the source depth and the surface. The tomographic determination of the anisotropy direction is furthermore confined to horizontal anisotropy, which may in fact only be a projection of a dipping anisotropy axis onto the horizontal.

We will therefore explore three end-member scenarios of anisotropy in the mantle wedge:

- trench-normal anisotropy dipping parallel to the surface of the subducting slab (which would be caused by corner flow),

- trench-normal horizontal anisotropy underneath the Moho (also caused by corner flow),

- trench-parallel anisotropy in the mantle wedge (caused by olivine B-type fabric, melts or arc-parallel flow).

Oceanic crust and lithospheric mantle usually exhibit anisotropy "frozen in" after their formation at a mid-oceanic spreading centre. This *fossil fabric* is characterized by the alignment of the fast axis parallel to the spreading direction [Savage, 1999], i.e. orthogonal to the magnetic anomaly pattern. The region close to the Cocos Ridge shows a prominent change in magnetic anomaly patterns (Figure 6.25), with magnetic anomalies oblique to the trench north of the Cocos Ridge. The corresponding anisotropy should therefore be oriented approximately 20-30° sub-parallel to the trench. The Cocos Ridge itself, however, is liable to show more complicated − and a priori unknown − anisotropy.
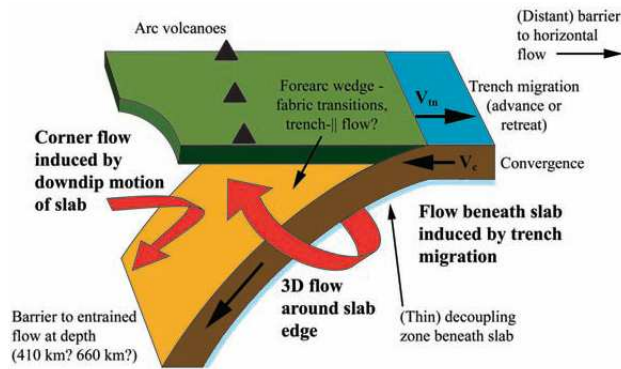
Figure 6.24: *Schematic representation of 3d mantle flow in subduction zones [from Long and Silver, 2008]*
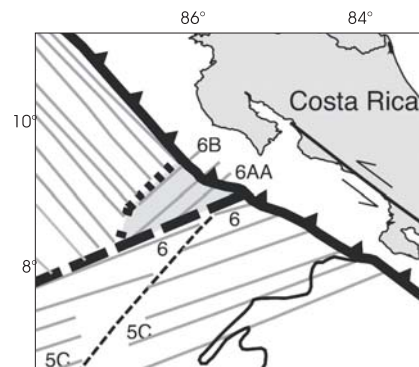
Figure 6.25: *Magnetic anomaly pattern off-shore Costa Rica [enlarged detail from MacMillan et al., 2004].*

Anisotropy caused by fine layering or aligned cracks is often observed in continental crust and may be present in the transitional crust of the overriding plate. However, since no prior information/hypothesis exists about the amount and direction of anisotropy in the overriding plate crust, it will not be considered in the modelling studies. The models are therefore compared with the observed migrated profiles for depths below the Moho, while a good fit at crustal depths is not attempted.

6.3.2   Basic Effects of Anisotropy in Receiver Functions

In the Frederiksen and Bostock [2000] modelling routine, hexagonal anisotropy is implemented. To give an overview of the effects of anisotropy on receiver functions, a very simple case of anisotropy has been calculated and is plotted in Figures 6.26 and 6.27. The model consists of a 30 km thick crust with velocities $\alpha = 7.0$ km/s and $\beta = 4.0$ km/s and a mantle with velocities $\alpha = 8.0$ km/s, $\beta = 4.571$ km/s. The upper 20 km in the mantle are modelled with 10% P-wave anisotropy with variable northwards dip. For the S-wave anisotropy, three runs were made for either zero, positive or negative (10%) anisotropy.

Figure 6.26 shows the results for positive S-wave anisotropy. Although this model is only very elemental, it shows several important characteristics of anisotropy effects in receiver functions. Like dipping layers, anisotropy can cause signals on the transverse receiver functions. For horizontal anisotropy, the amplitudes on both the radial and transverse component are periodic with 180°; they become 360° periodic when the anisotropy dips. The amplitude on the transverse component is zero in the direction of anisotropy (i.e., for waves arriving from the north and south in this model). In this direction, the radial amplitudes have local maxima. If the anisotropy has non-zero dip relative to the vertical, the radial components have a local and a larger global maximum, the latter one coinciding with the dip direction of the anisotropy.

Moho multiples are absent from the transverse receiver functions and are independent of both back-azimuth and anisotropy dip in the radial receiver functions. While the primary Moho conversion may have different polarity in some intervals of back-azimuth for steeply dipping anisotropy, the multiples always have the "correct" polarity for the positive velocity contrast and therefore help to interpret the radial components correctly.

The model simulations including negative S-wave anisotropy are similar in principle to the positive anisotropy case, therefore only examples are shown in Figure 6.27. The transverse components show approximately the same behaviour for both positive and negative S-wave anisotropy, while the radial components show slight differences. For horizontal anisotropy, the maxima of the primary conversions are shifted by 90° in back-azimuth for negative relative to positive anisotropy. However, for dipping anisotropy, the negative S-wave anisotropy case quickly changes to 360° periodicity, while the transition is more gradual for the positive S-wave anisotropy case. The differences in polarity and amplitude behaviour with back-azimuth are clearest for very shallow or very steep anisotropy (compare synthetics for 20° and for 80°, respectively).

Modelling results for zero S-wave anisotropy are not shown here; they look like the average of the negative and positive S-wave anisotropy results. The main characteristics of the receiver functions depend much more strongly on P-wave anisotropy than on the strength and polarity of S-wave anisotropy. We will therefore just consider positive P- and S-wave anisotropy, which is the most plausible scenario. The S-wave anisotropy would have to be very large in comparison with the P-wave anisotropy to significantly bias the results.

SV 0 deg SH

20 deg

SV   40 deg   SH

60 deg
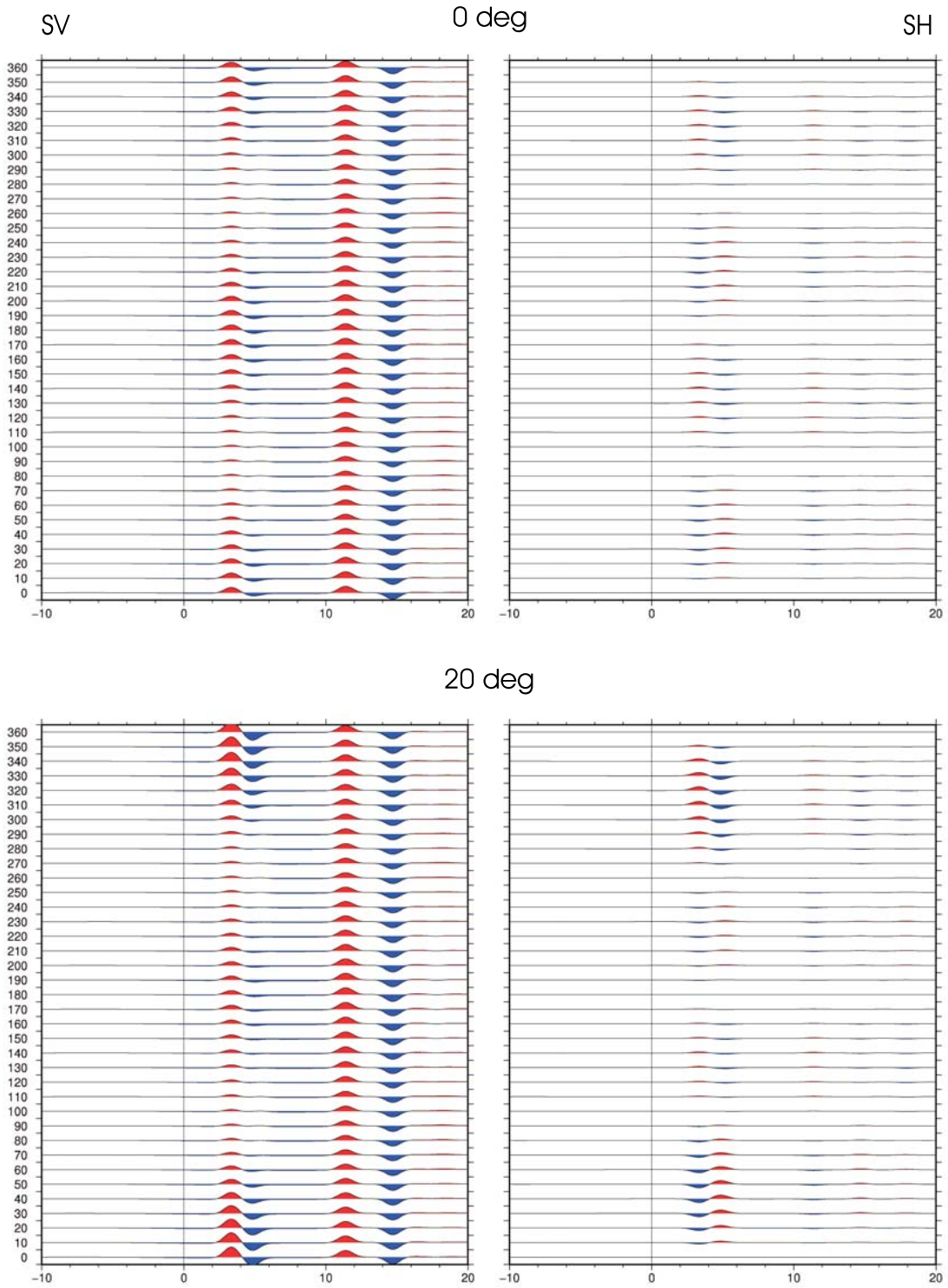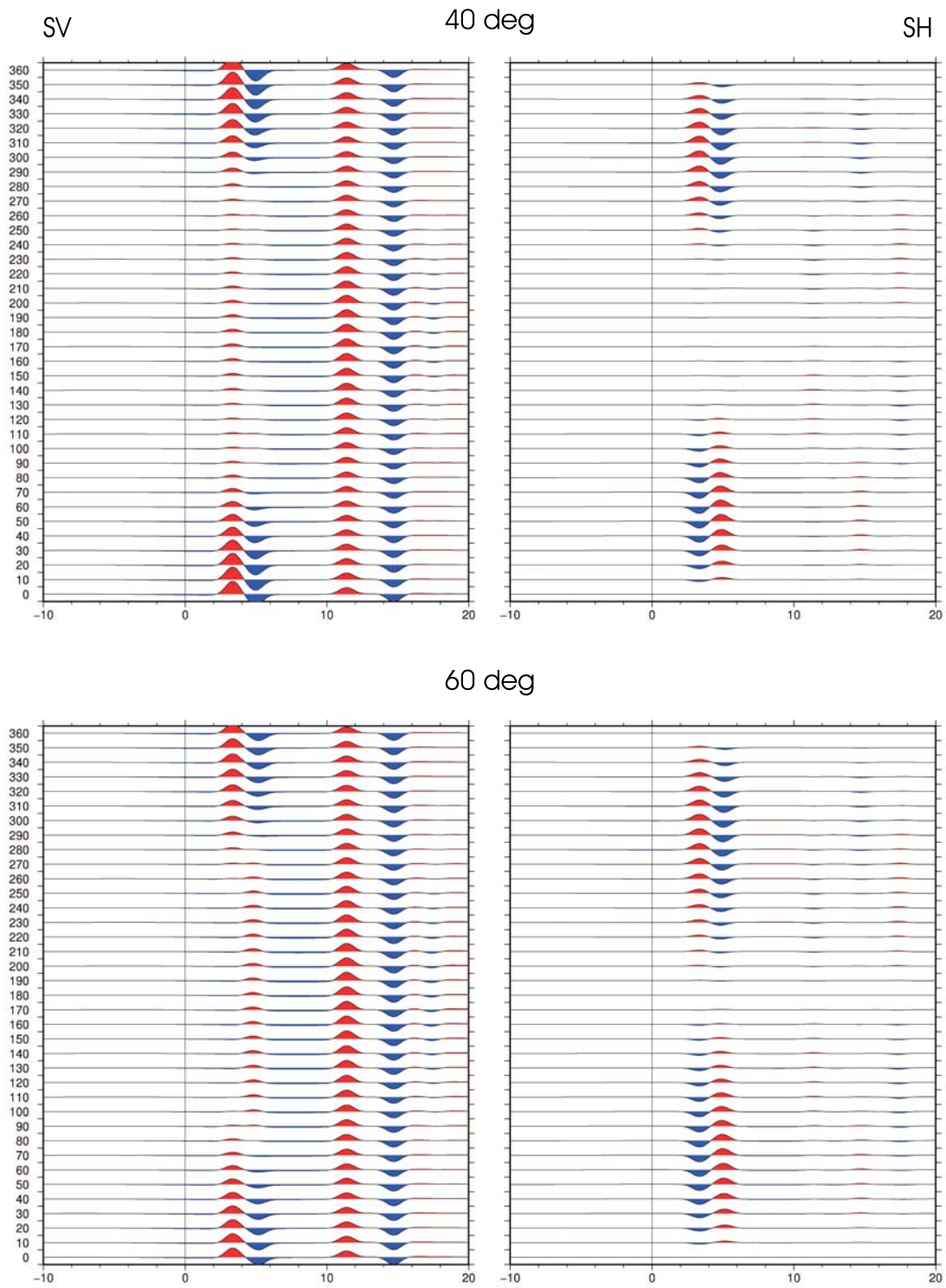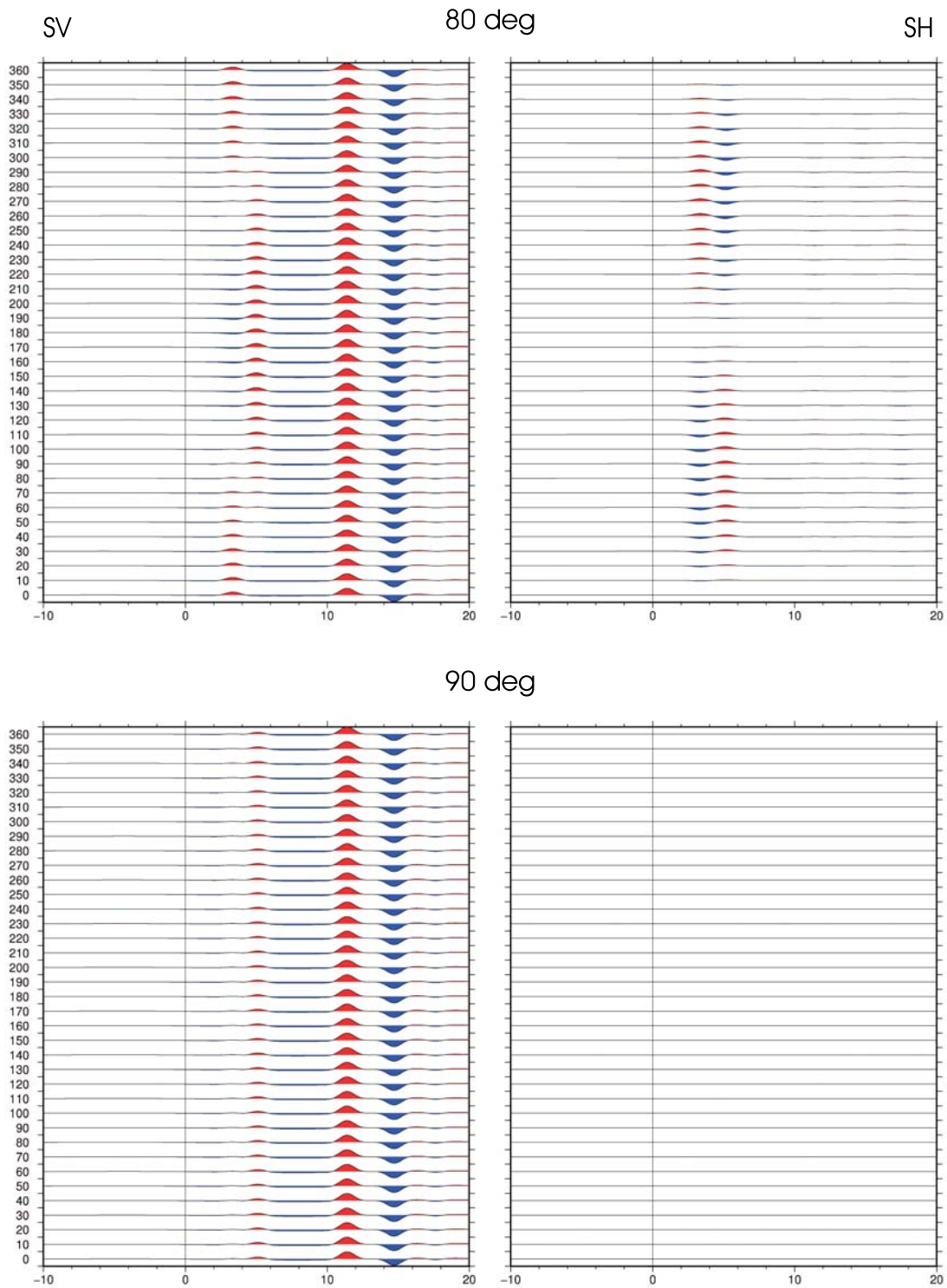
Figure 6.26: *Synthetic receiver functions for an anisotropic layer (10% P- and positive S-anisotropy) between two isotropic layers. Left panels show radial receiver functions, right panels transverse receiver functions. The dip of the anisotropy with respect to the horizontal is given in the headline. Back-azimuth increases from 0° to 360° in steps of 10°.*
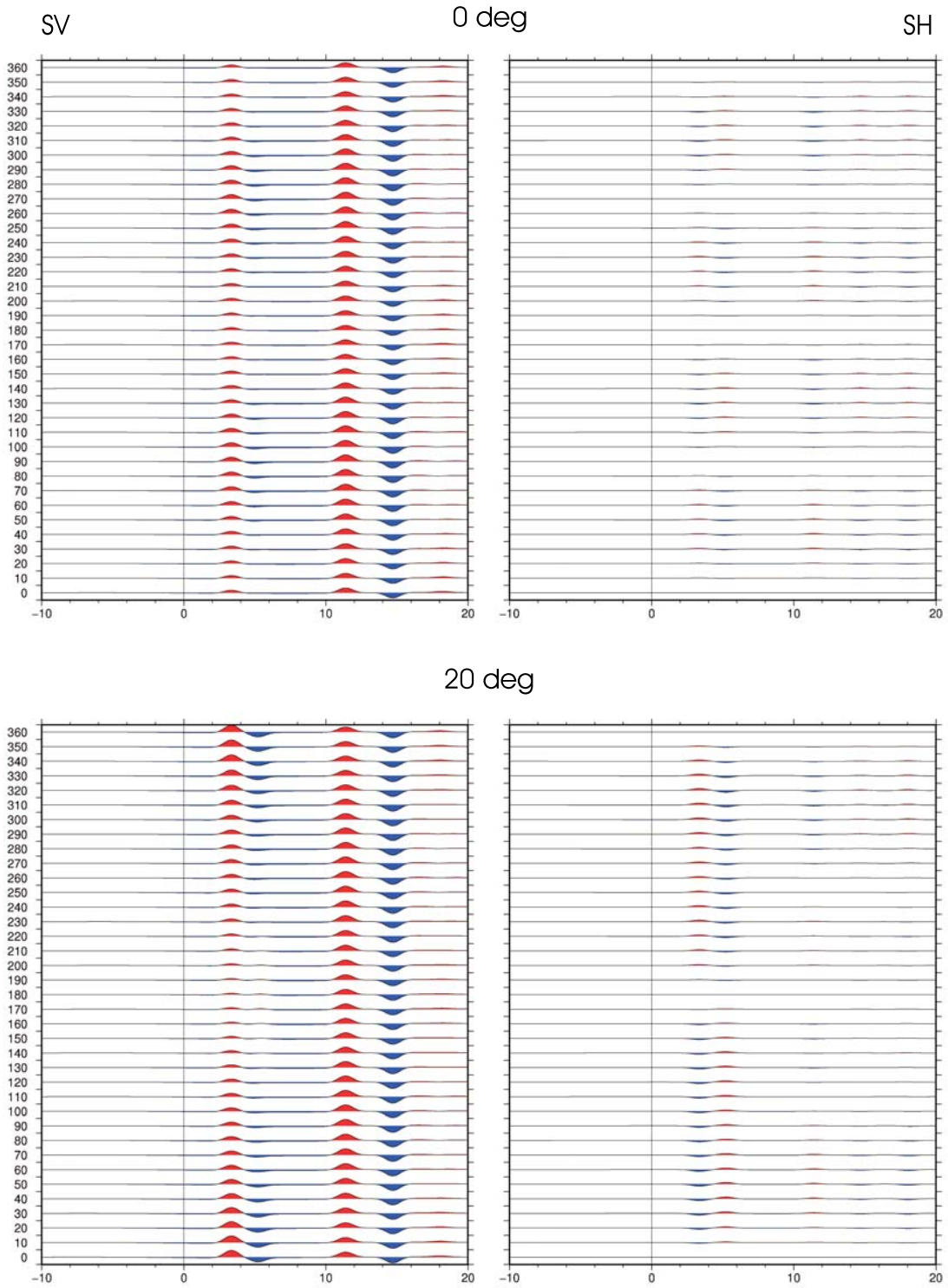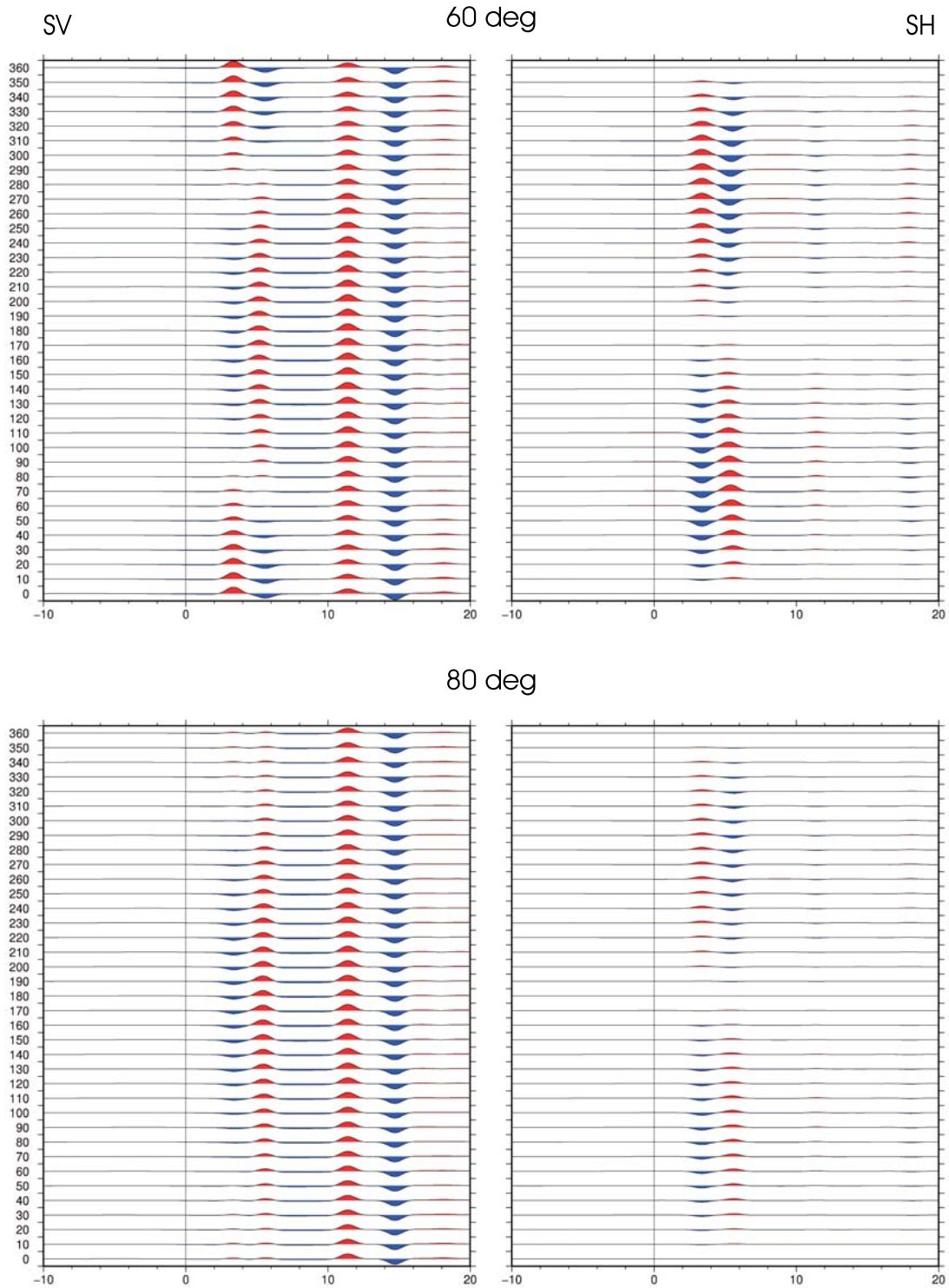
Figure 6.27: *Synthetic receiver functions for an anisotropic layer (10% P- and negative S-anisotropy) between two isotropic layers. Left panels show radial receiver functions, right panels transverse receiver functions. The dip of the anisotropy with respect to the horizontal is given in the headline. Back-azimuth increases from 0° to 360° in steps of 10°.*

In their classic treatment of anisotropy in receiver functions, Levin and Park [1998] perform a more systematic investigation of different anisotropy scenarios. Some important general conclusions that can be drawn from their work are:

- Only if the uppermost layer is anisotropic is the direct P wave observed on the transverse component. Therefore, a back-azimuth-dependent conversion at delay time 0 on the transverse component must either be caused by a dipping layer or by upper crustal anisotropy.

- The same holds for azimuthal variability of the direct P arrival on the radial component: significant variability is only observed in the case of dipping structures or anisotropy in the uppermost layer.

- Anisotropy can produce both 2-lobed and 4-lobed azimuthal patterns, depending on what kind of anisotropy is present (P- or S-wave or both) and its dip. In addition to variations in the conversion amplitudes, the delay times can also change with back-azimuth. In any case, *only* anisotropy can cause 4-lobed patterns, while dipping layers always give rise to 2-lobed patterns.

6.3.3   Dipping Wedge and Anisotropy – End-Member Case Studies

Several models were calculated for a 60° dipping slab (strike −30°) without multiples to explore different gerneral scenarios, all based on the same velocity model and different anisotropy scenarios. Model parameters are given in Tables 6.1 and 6.2. The results are displayed in Figure 6.28.

layer	α [km/s]	β [km/s]	thickness
upper crust	5.80	3.20	15 km
lower crust	6.80	3.90	20 km
mantle wedge	7.60	4.34	30 km thick under crt-02
slab	8.40	4.80	80 km
mantle	8.00	4.57	half-space

Table 6.1: *Model velocities*

Model a	isotropic
Model b	10% P- and S-wave anisotropy in the mantle wedge, horizontal and normal to the trench
Model c	10% P- and S-wave anisotropy in the mantle wedge, horizontal and parallel to the trench
Model d	10% P- and S-wave anisotropy in the mantle wedge, normal to the trench and dipping 60° (parallel to subducting slab)
Model e	10% P- and S-wave anisotropy in the subducting slab, 20° subparallel to the trench

Table 6.2: *Type of anisotropy considered in models*
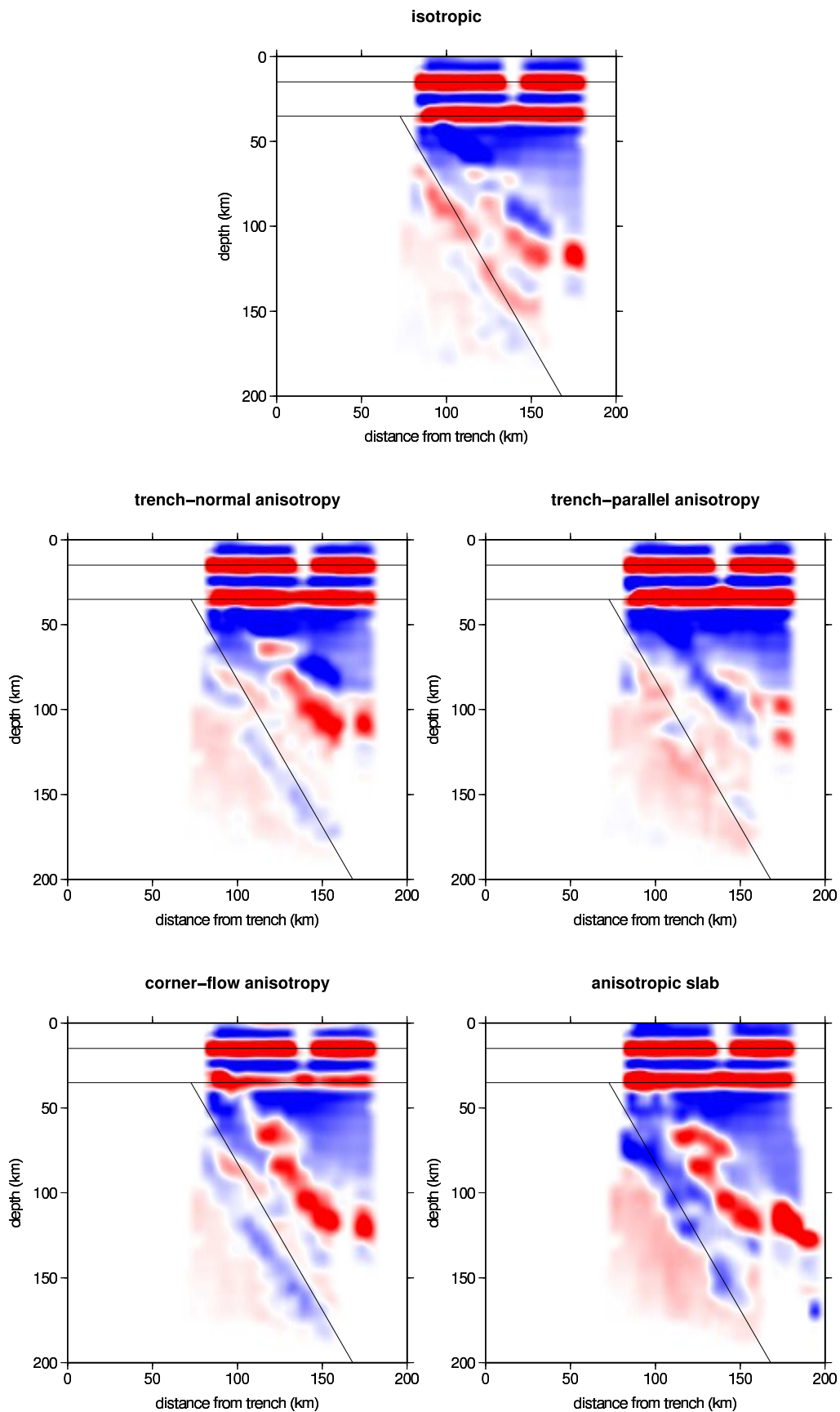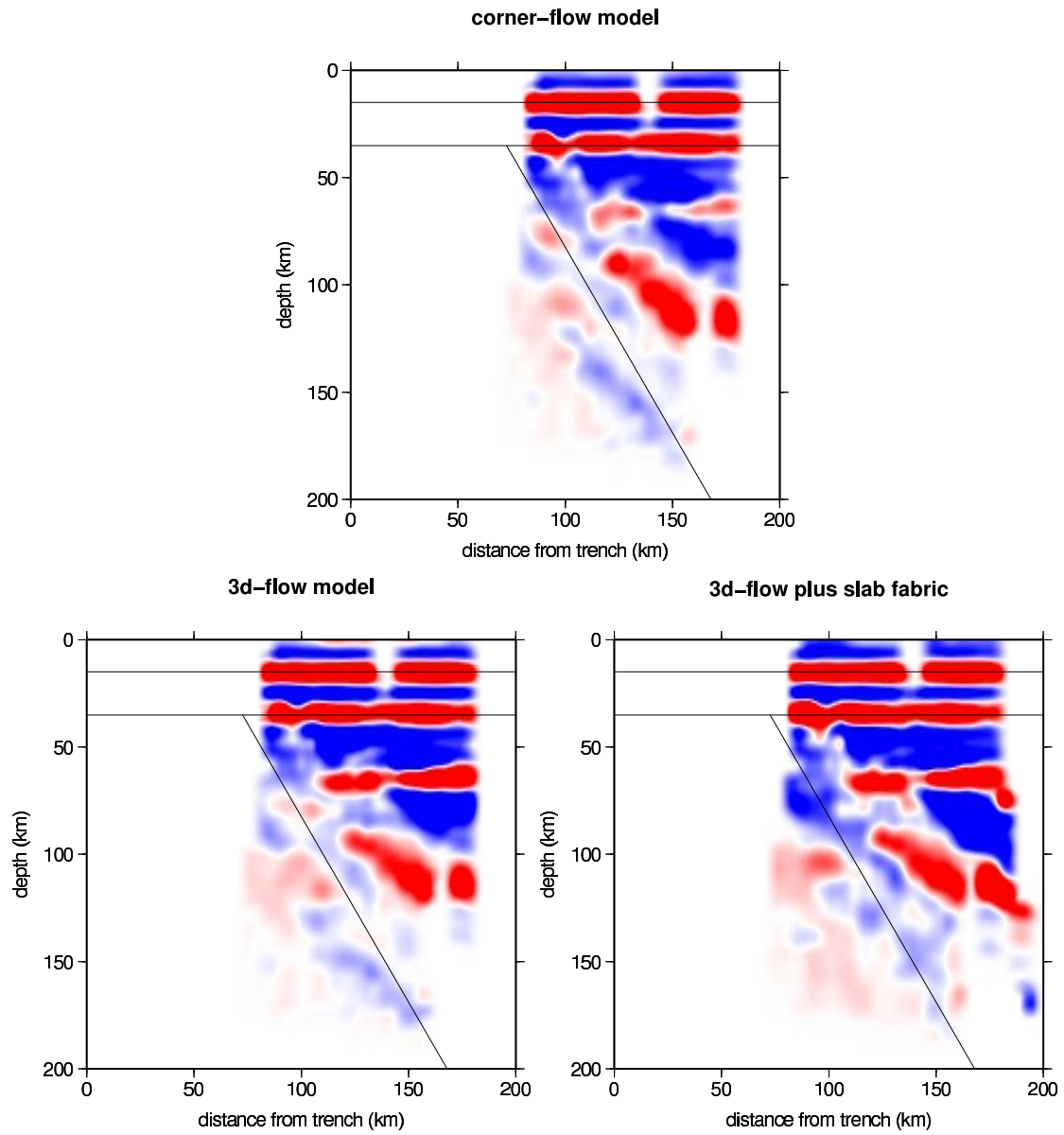
Figure 6.28: *Synthetic radial receiver function results for a 60° dipping slab and different kinds of anisotropy. Upper panel: model a (isotropic), centre left to lower right: models b to e.*

Model a assumes isotropy. It differs from the 60° dipping wedge model in Section 6.1.3 in considering a fast subducting slab, whereas the models considered before only included a dipping wedge, i.e., they made no difference between the subducting lithosphere and underlying mantle. The slab was modelled as a high-velocity feature of 80 km thickness, similar to what is usually seen in tomography studies.

Models b to e use the same geometry and velocity structure as model a to explore end-member cases of the probable anisotropy scenarios. Trench-normal horizontal and dipping anisotropy (model b and d, respectively) are predicted by the corner-flow model. Trench-parallel (horizontal) anisotropy (model c), though not predicted by the classical corner-flow model, was suggested by local earthquake tomography studies in central and northern Costa Rica [Dinc, 2008] and was argued to be an indication of arc-parallel mantle flow also consistent with geochemical studies [Hoernle et al., 2008]. In addition to these scenarios of possible mantle-wedge anisotropy, the influence of frozen-in slab anisotropy is explored (model e). In all cases, 10% P-wave and S-wave anisotropy were chosen, because the observations by Dinc [2008] suggested P-anisotropy of the order of 10%. The S-anisotropy has less influence on the results and is therefore taken to be consistent with the P-anisotropy.

While the subducting slab is observed in both the subducting wedge and fast subducting slab models with sufficient clarity, and with a dip close to the input dip of 60°, it is seen more clearly if the slab is truely simulated as a higher-velocity feature. The slight velocity reduction under the subducting slab appears as a weak negative conversion parallel beneath the high-velocity dipping feature. Indeed, such a signal is observed in the real data, arguing for a high-velocity subducting slab.

The isotropic model (model a) already provides a decent approximation of the observed receiver functions. The main features, i.e., the Moho, inner-crustal discontinuity and dipping high-velocity feature are clearly seen in all four anisotropy models.

The assumption of purely trench-parallel anisotropy in the mantle wedge gives least similarity with the actual observations. In this model, the dipping slab is only weakly seen, while spurious structures in the mantle wedge are created. This result indicates that trench-parallel anisotropy is not the main characteristic of the mantle wedge in the Cordillera de Talamanca region.

The only model that can reproduce the link between the Moho conversion and the dipping feature, which is also seen in the real data, involves anisotropy dipping at the same angle as the subducting slab. This model also clearly shows the lateral change in the strength of the Moho conversion, which may explain why the Moho is not seen clearly everywhere in the real data, or appears to change depth (this may be due to smearing with crustal discontinuities). In a qualitative view, the dipping anisotropy therefore appears most similar to the actual receiver function image.

Obviously, these models can only give some feeling of what general features could be expected for several simple scenarios. They can by no means be compared to an inversion, but should be taken as examples of what could be seen. Their aim is therefore to make plausible that we have a right to interpret the dipping positive feature seen in the data as a subducting slab, because a slab would indeed cause such a feature. This is, however, a qualitative similarity − the model was not designed to reproduce the slab depth and velocities correctly.

The details seen in the receiver function image may be related to some degree to the effects of anisotropy, and a case may be made for dipping anisotropy in the mantle wedge, in line with the usual corner-flow model. However, more likely there will be different kinds of anisotropy present, since the corner-flow would involve dipping anisotropy close to the surface of the subducting slab, but horizontal, trench-normal anisotropy below the Moho. In addition to this, trench-parallel 3-d flow may be present, possibly above the dipping anisotropy.

Finally, it should be noted that it is possible to create a velocity model in a way that a slab signal is seen even if multiples are included in the Frederiksen and Bostock [2000] code. Figure 6.29 (left panel) shows the results for the following model:

- homogeneous isotropic crust, $\alpha = 7.3$ km/s, $\beta = 4.171$ km/s,

- anisotropic partially serpentinized mantle wedge, $\alpha = 7.8$ km/s, $\beta = 4.457$ km/s, with $60°$ dipping trench-normal anisotropy (10%),

- dipping isotropic high-velocity half-space, $\alpha = 8.8$ km/s, $\beta = 5.028$ km/s.

The high crustal velocity was chosen to represent the velocity at the lower base of the crust to give a realistic velocity contrast towards the underlying mantle. Upper crustal velocities – and hence the receiver function profile above the Moho – can be expected to deviate from the model. A velocity gradient may exist in the crust, which cannot be implemented in the Frederiksen and Bostock [2000] routine, but would allow for lower velocities near the surface while preserving the undisrupted slab signal without crustal mutliples.
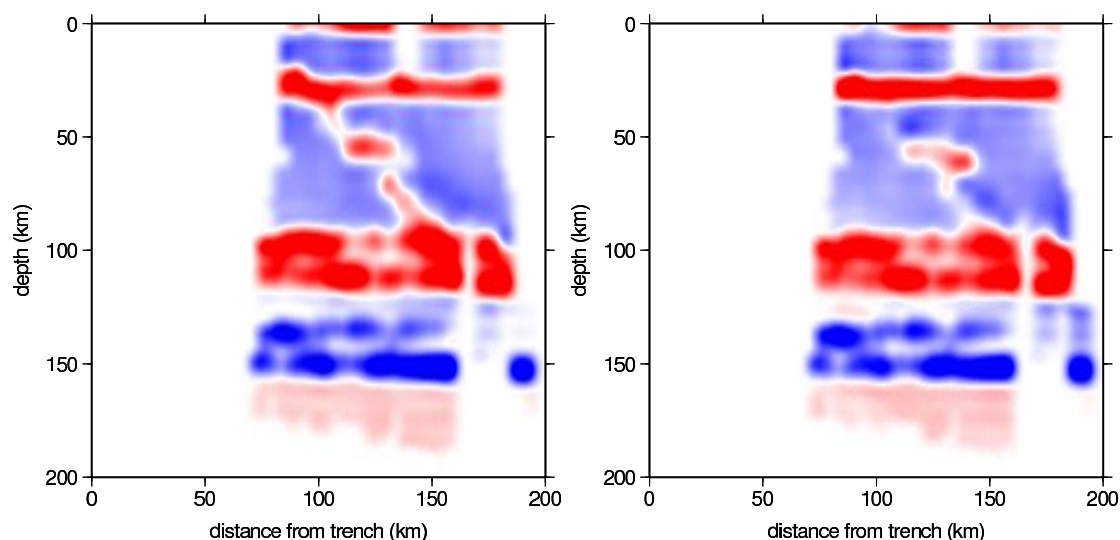
Figure 6.29: *Synthetic radial receiver function results for a 60° dipping slab – modified model to reduce multipes (see text). Left panel: model including 60° dipping trench-normal anisotropy in the mantle wedge; right panel: isotropic model.*

While it must be admitted that the model parameters need to be chosen carefully to obtain a good slab signal inspite of the multiples, this example suggests that it *may* be possible to adjust the velocities (and insert velocity gradients) in a way to match the results. In fact, the velocities can

be varied over a wider range, if the mantle-slab velocity contrast is sufficiently strong – although this is not shown here, several such models could be created. However, some kind of anisotropy *must* be included: if the above model is calculated for the isotropic case, hardly any slab signal appears, as shown in the right panel in Figure 6.29.

6.3.4   Dipping Wedge and Anisotropy – Combined Models

Three final, more realistic models were constructed to combine several kinds of plausible anisotropy scenarios. All models are based on the same velocity structure as before, but including the following kinds of anisotropy (10% P- and S-wave anisotropy):

- **corner-flow model**:

  – a 30 km thick mantle layer with horizontal, trench-normal anisotropy directly below the Moho,
  – and a 50 km thick mantle layer with 60° dipping, trench normal-anisotropy directly above the subducting slab surface,

- **3d-flow model**:

  – all of the above, plus
  – trench-parallel anisotropy in the remaining part of the mantle wedge,

- **3d-flow and slab fossil fabric**:

  – all of the above, plus
  – frozen-in anisotropy in the dipping slab (like in model e).

Results are shown in Figure 6.30. The dipping slab is still visible in all scenarios, but the inclusion of a layer of trench-normal horizontal anisotropy below the Moho creates a positive near-horizontal conversion at around 65 km depth. This is strenghtened if trench-parallel anisotropy is introduced in the mantle wedge between the corner-flow channels of trench-normal anisotropy. In the real data, this feature would be extremely hard to distinguish from the multiples arriving at around the same time.

The addition of frozen-in anisotropy in the subducting slab has hardly any influence on the resulting receiver function profiles and cannot be well resolved by this analysis.

These three models cannot reproduce the observed receiver function images any better than the simple models with a dipping slab and, possibly, trench-normal dipping or horizontal anisotropy. Since the amount of anisotropy was taken to be large in these models, the real case should be somewhere in between the anisotropic and isotropic model scenarios, and we cannot exclude the corner-flow or 3d-flow hypotheses or the presence of frozen-in anisotropy in the slab.

Figure 6.30: *Synthetic transverse receiver function results for a 60° dipping slab and different combinations of anisotropy. Upper panel: "corner-flow" model, lower left: "3d-flow" model, lower right: "3d-flow plus slab fossil fabric".*

6.3.5   Conclusions from radial receiver function modelling

All together, the radial receiver function modelling study can be summarized to conclude the following:

- A dipping wedge/slab structure can be clearly seen in the migrated receiver function profiles for the given observation geometry, i.e., using the real station and event locations, with the theoretical ray paths.

- The dip of the subducting slab is reproduced to within several degrees in the migrated profiles.

- While the multiples are overestimated in the Frederiksen and Bostock [2000] modelling routine, the Moho and crustal interface can be clearly identified based on the comparison of the modelling results with the actual observations. The observed dipping positive conversion can be explained by a steeply dipping slab. Velocity gradients in the crust may provide a realistic explanation for observing weaker multiples than predicted with the Frederiksen and Bostock [2000] model.

- Trench-normal anisotropy – probably dipping parallel to the slab – is a plausible scenario and most consistent with the observations.

- Trench-parallel anisotropy cannot be completely ruled out, but does not seem to account for the main direction of anisotropy in the mantle wedge.

6.3.6   Modelling Results for Transverse Receiver Functions

The transverse receiver functions for models a-e and for the "3d-flow" model are shown in Figure 6.31. While the dipping slab can be clearly seen in most models, it is blurred in the presence of trench-normal anisotropy and becomes very hard to recognize for trench-normal dipping anisotropy. Accordingly, it cannot be discerned clearly in the 3d-flow model, either. This may explain why it was nearly impossible to interpret the observed migrated transverse receiver function sections, particularly at depth.

Anisotropy also influences the appearance of the crustal and mantle wedge region, creating a complicated pattern of positive and negative conversions. The patchiness of the resulting image makes it difficult to interpret the transverse profiles for the real data, where many more effects (more velocity discontinuities, more complicated distribution of anisotropy, and multiples) play a role. Therefore, a good synthetic model of the transverse profiles is not attempted.
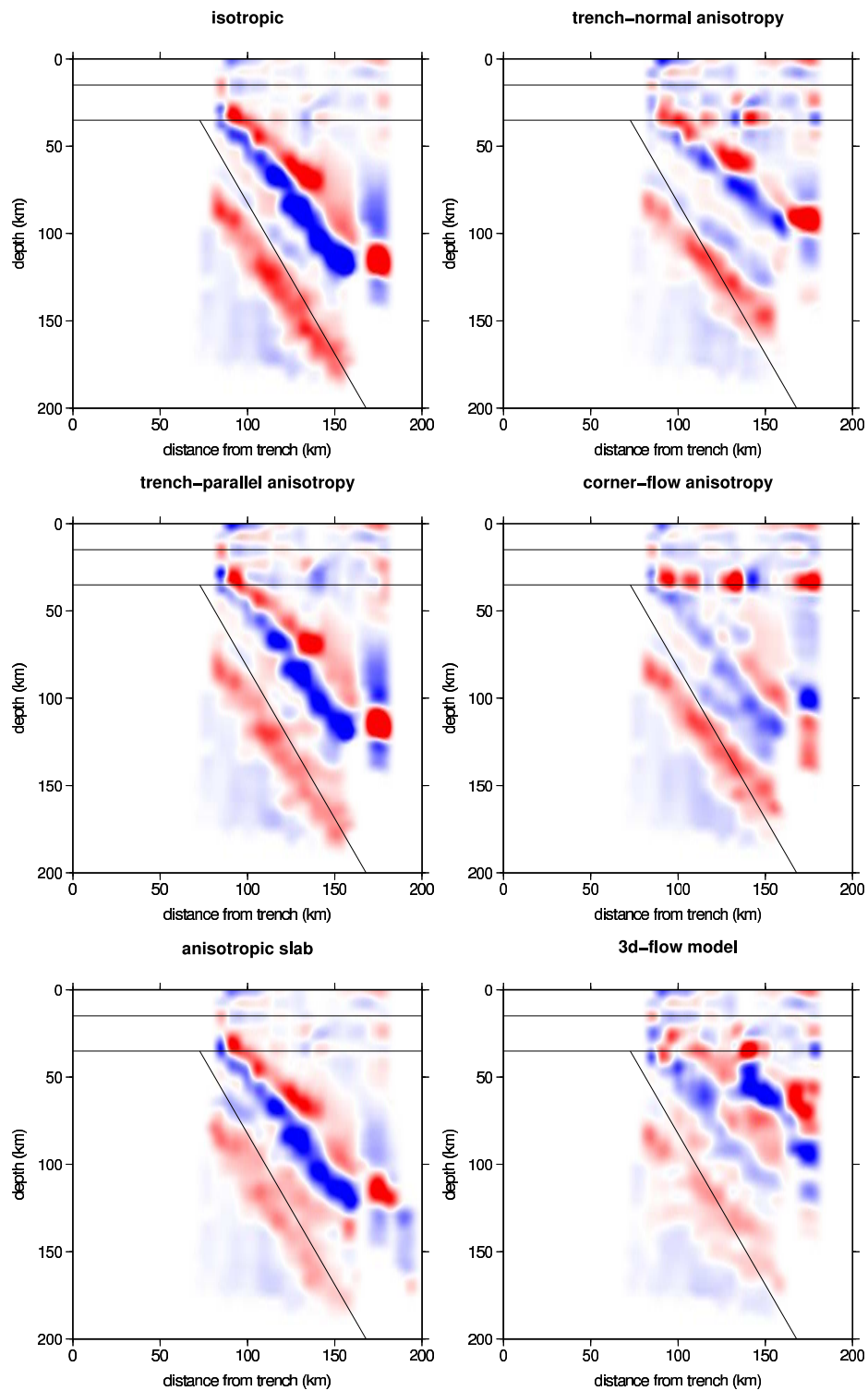
Figure 6.31: *Synthetic transverse receiver function results for a* 60° *dipping slab and different kinds of anisotropy. Upper panel: models a (isotropic) and b (trench-normal horizontal anisotropy), centre: models c (trench-parallel anisotropy) and d (dipping anisotropy), lower panel: model e (slab anisotropy) and 3d-flow model*

6.4 Azimuthal variation

The azimuthal variation of radial and transverse receiver functions was plotted for the different models to study the relevant features produced in the receiver functions. They are displayed in Figures 6.32 to 6.36 for station crt-21[1], which has good azimuthal coverage. The receiver functions observed at this station were shown in Chapter 5 and are reproduced here for comparison. Modelling was again performed for model a (with and without multiples), models b to e and the corner-flow and 3d-flow (with and without slab anisotropy) models.

The following general features are seen:

- The radial stacked traces of the different models are very similar, whereas the transverse stacked traces differ markedly between the models. This is probably due to the fact that the strongest conversions observed in the radial traces are the inner-crustal discontinuity and the Moho, which do not show marked azimuthal variability and are caused by isotropic, horizontal layers (in the models). The delay time of the Moho conversion varies by as much as 2 s on the radial components, but always appears as a clear conversion. Only in the case of 3-d flow is a second strong conversion observed some 5 s *before* the slab conversion, which is created at the transition between horizontal trench-normal anisotropy and horizontal trench-parallel anisotropy in the models. The much stronger variability of the transverse component stacked traces can be understood from the fact that the transverse components trace dipping structures and anisotropy, but are not sensitive to the isotropic, horizontal crustal layers. Therefore, the changes in anisotropy scenario influence the transverse component stacked traces more strongly.

- Both the radial and transverse components contain energy at zero delay time for some ranges in back-azimuth, with the same azimuthal behaviour for almost all anisotropy models.

- All isotropic models show the Moho of the overriding plate as a positive conversion around 4 s in the radial components. The positive conversion shortly before 2 s delay time reflects the inner-crustal discontinuity, which is more pronounced than the Moho signal. Indeed, if anisotropy is present in the mantle wedge below the Moho, the Moho signal is altered and depends on backazimuth: depending on the orientation of the anisotropy, the Moho signal nearly disappears at some back-azimuths and changes position slightly.

- The time between 5 and 10 s is dominated by crustal and Moho multiples. Since the slab signal moves into the time range between 6 and 10 s for back-azimuths around 270°, the multiples interfere with the slab signal and make interpretation of the real data set difficult.

- Around 10 s, the dipping fast wedge (or surface of the dipping slab) is seen. The delay times vary strongly with back-azimuth, by as much as 2-3 s. The lower boundary of the slab follows as a second, inverted polarity conversion about 10 s after the slab surface signal, at about the same time as the multiples around 14 s. The slab signal arrives earlier for earthquakes in the south-western sector, where the negative polarity arrival coincides with and is obscured by the negative Moho multiple. The amplitude and polarity changes with back-azimuth are strongly dependent on the kind of anisotropy assumed in the model.

---

[1]It should be kept in mind that the models were constructed to reproduce a 60° dipping slab, but *not* the real depth of the slab under each station. Therefore, the modelling results for "station crt-21" are not necessarily identical in timing to what is actually observed at this station, but may correspond to stations further updip or downdip as to the slab depth; in any case, they give the same slab dip and crustal structure, and are based on the events observed at station crt-21. The difference in slab depth only influences the delay times of the slab conversions, which may occur earlier or later than in the observations, but their azimuthal behaviour should remain unchanged.
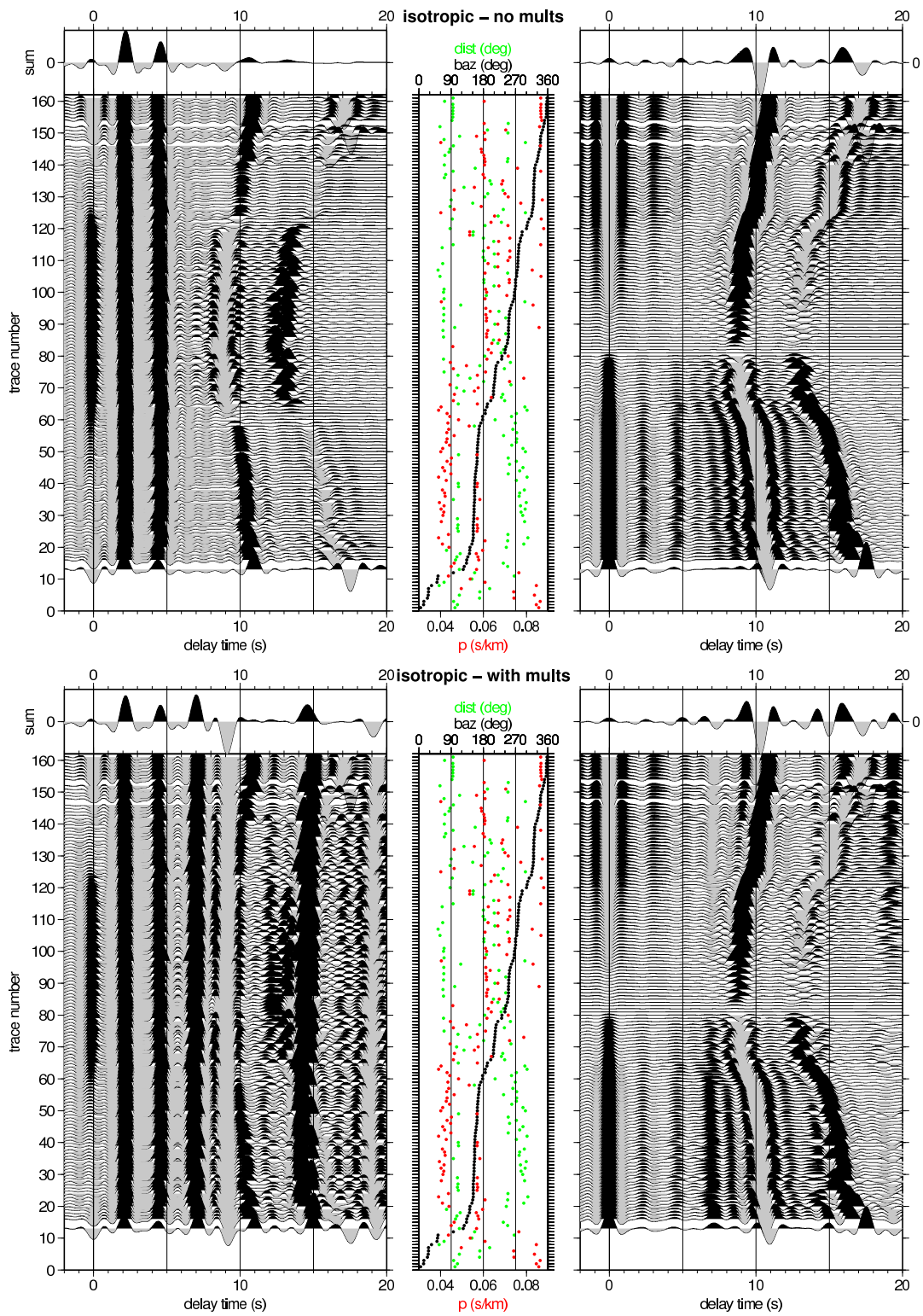
Figure 6.32: *Synthetic radial and transverse receiver functions for station crt-21, sorted by back-azimuth. Isotropic fast-slab model (model a) without (above) and with (below) multiples.*
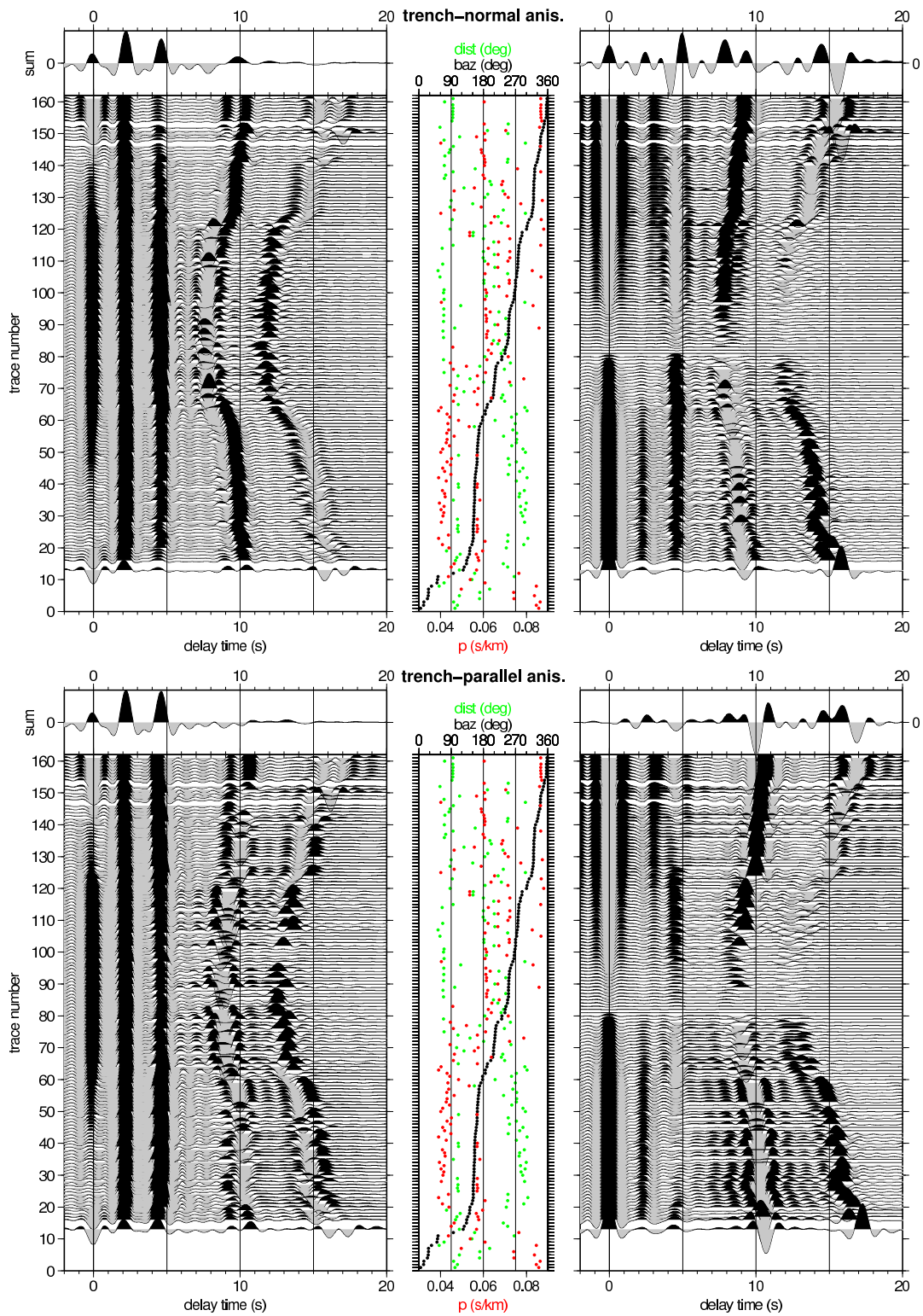
Figure 6.33: *Synthetic radial and transverse receiver functions for station crt-21, sorted by back-azimuth. Fast-slab model with trench-normal (model b, above) and trech-parallel (model-c, below) anisotropy in the mantle wedge, respectively.*
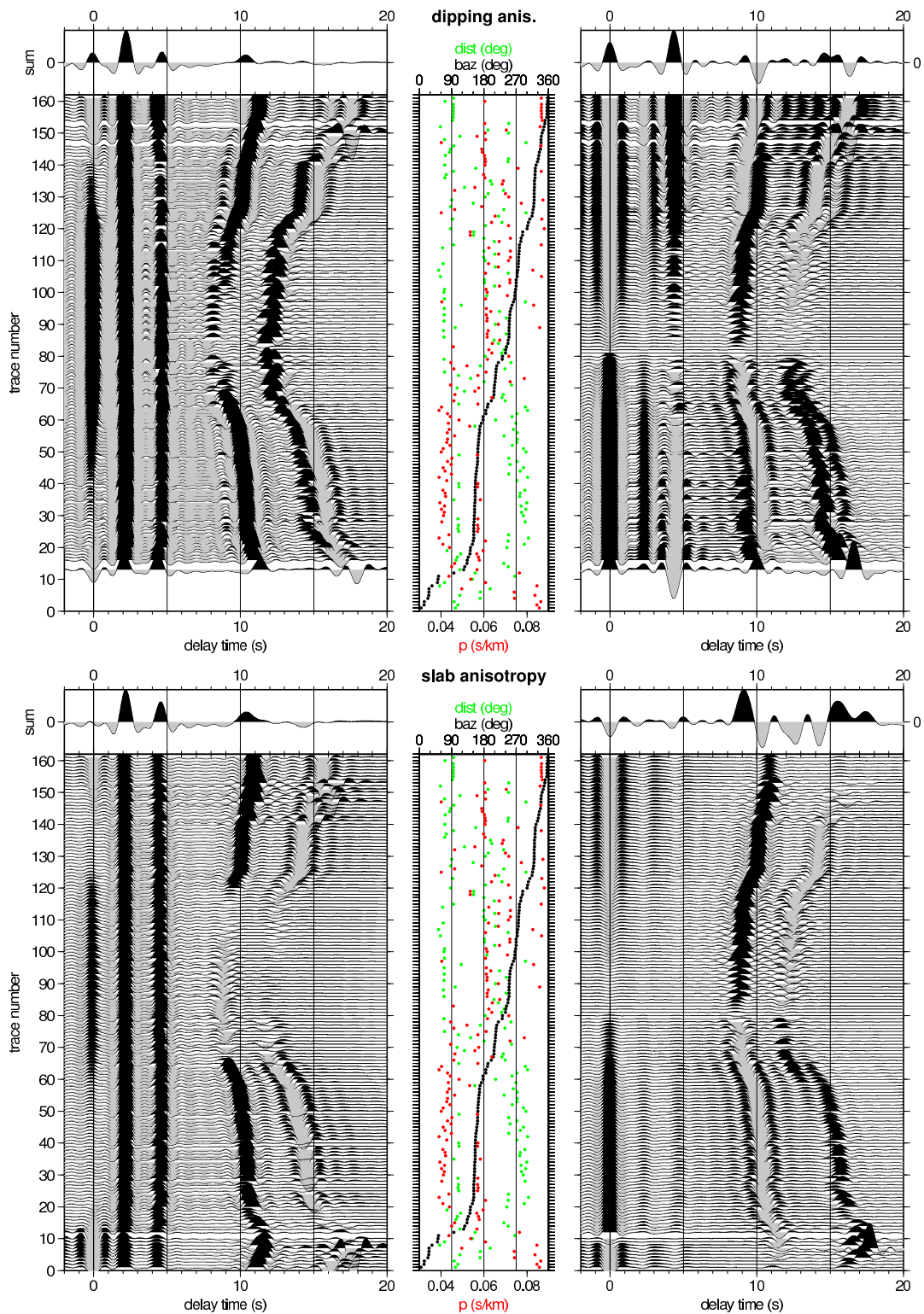
Figure 6.34: *Synthetic radial and transverse receiver functions for station crt-21, sorted by back-azimuth. Fast-slab model with dipping anisotropy (model d, above) and anisotropic slab model (model e, below), respectively.*
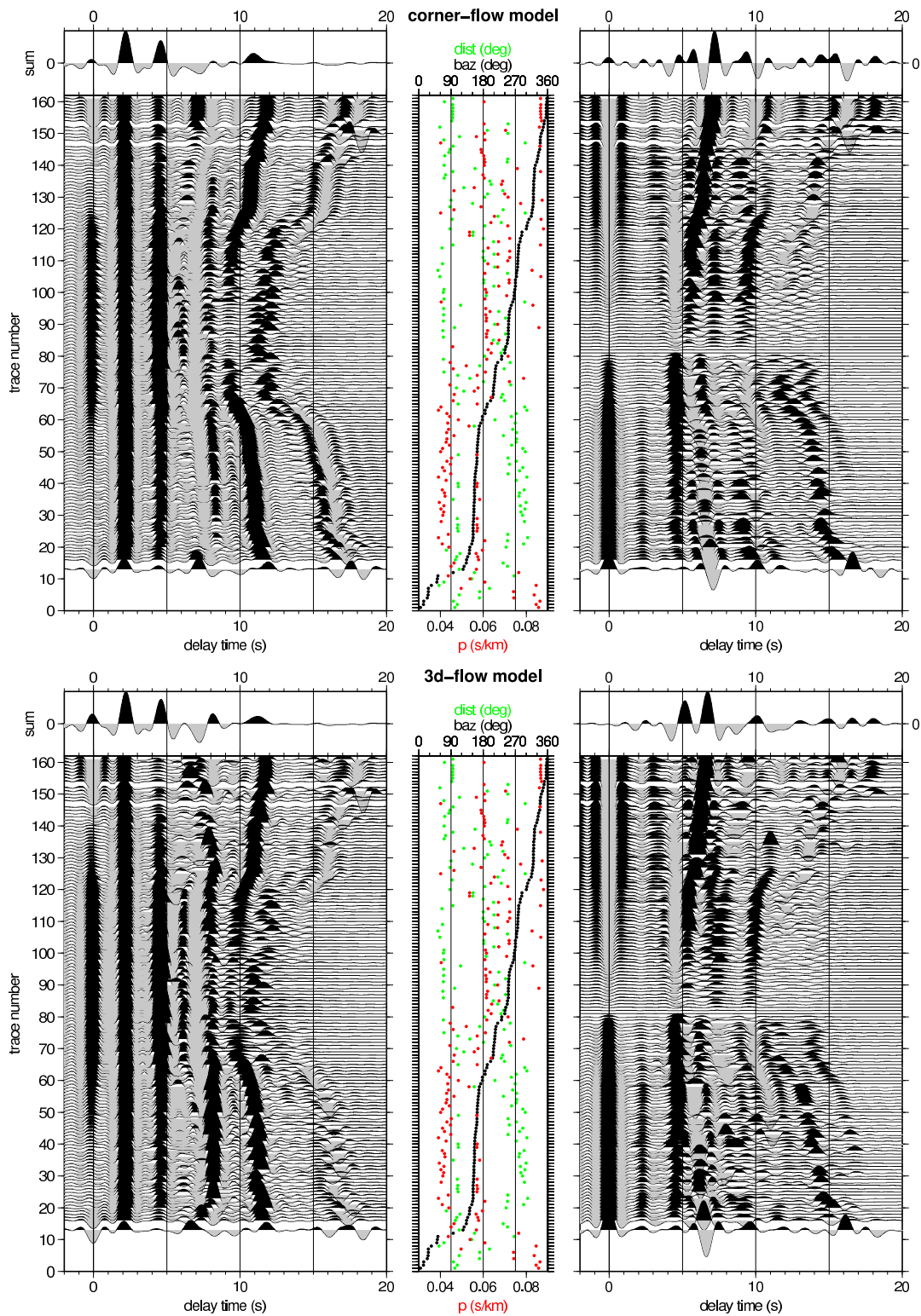
Figure 6.35: *Synthetic radial and transverse receiver functions for station crt-21, sorted by back-azimuth. Fast-slab model with corner flow (above) and 3d-flow (below), respectively.*
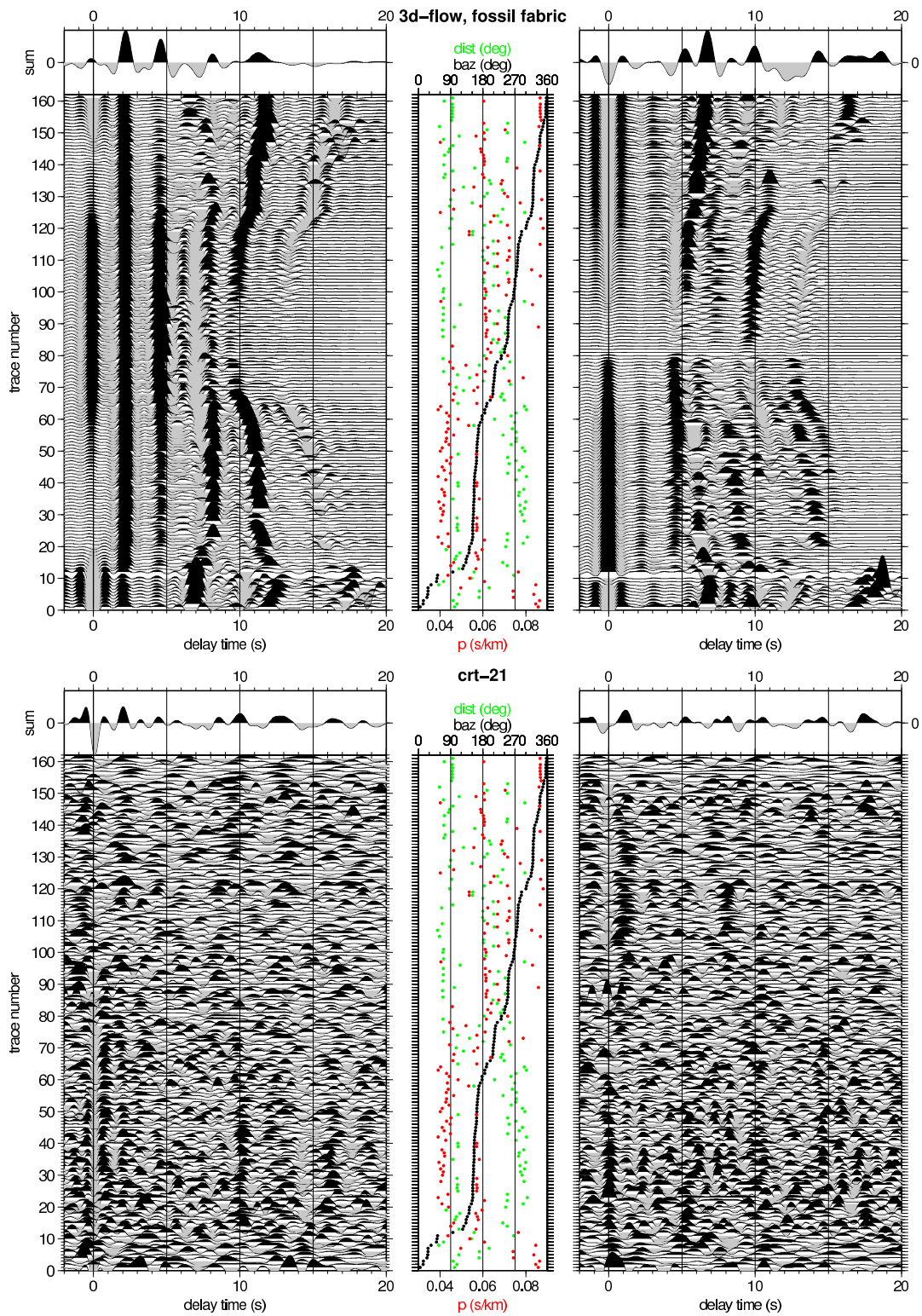
Figure 6.36: *Synthetic radial and transverse receiver functions for station crt-21, sorted by back-azimuth. Fast-slab model with 3d-flow and slab anisotropy (above), and observed receiver functions (below), respectively.*

- In the transverse receiver functions some energy is found before the arrival of the dipping conversions even where no anisotropy is present. In the presence of anisotropy, signals at 3-5 s are generated by the transition from the isotropic crust to anisotropic mantle wedge, with complicated back-azimuthal patterns and strong dependence on the anisotropy model.

- The dipping wedge/slab signal is observed in the transverse components at similar times as on the radial component, with an equally strong dependence of the amplitude and polarity changes on the orientation of the anisotropy considered.

The observed receiver functions share many of the features observed in the synthetic data. On the radial traces, the inner-crustal signal can be seen at 1.5-2 s, and the Moho signal appears weakly around 4.5 s with marked variations with back-azimuth, indicating the presence of − probably dipping − anisotropy in the mantle wedge. The dipping wedge signal is seen in the back-azimuth ranges around 150° and 330−360° most clearly as a positive conversion around 10 s. Outside this range, multiples and noise make the clear identification of this conversion difficult. The best comparison with the real data is achieved for the trench-normal horizontal or dipping anisotropy or possibly the corner-flow scenario. In contrast, the 3-d flow models (with or without slab anisotropy) do not match the observations well, most notably because the strong positive conversion between 7 and 8 s is absent in the observed receiver functions.

On the transverse component, the pronounced conversion at 0 s with polarity change around 240° is the same as observed in the modelled traces. The dipping slab feature cannot be seen clearly, probably because it merges into the multiples where it arrives early, but appears similar to that predicted for the case of trench-normal horizontal or dipping anisotropy or for the corner-flow model. While trench-parallel anisotropy compares well with the real data for the radial components, it does not match the observed transverse components well, in particular before 5 s delay time. Finally, fossil fabric causing slab anisotropy cannot alone explain the observations, because it fails to produce a realistic slab signal on the radial components between 70-120° back-azimuth and because it has no conversions on the transverse components before about 9 s.

In conclusion, these studies cannot hope to model the observed receiver functions satisfactorily; they were performed to point out the general features that can be produced even by these simple models. Strong variations in delay time as well as polarity changes and complicated amplitudal variations with back-azimuth can all be reproduced with very simple means. The fact that the Moho signal, though clearly seen in the migrated images, disappears in some back-azimuthal intervals seems well explained in the synthetic studies including anisotropy, while it does not seem possible to produce this effect in a purely isotropic model.

The anisotropy models indicate that slab anisotropy is not sufficient to explain the observations, strongly suggesting an anisotropic mantle wedge. The prevailing anisotropy scenario seems to be trench-normal horizontal or dipping anisotropy, or a combination of both such as proposed by the corner flow model. A scenario with trench-parallel anisotropy, especially a combination of corner flow with trench-parallel flow, does not seem likely; however, trench-parallel flow with small anisotropy in the flow channel cannot be ruled out.

The present studies have focussed on anisotropy scenarios in the mantle and subducting slab, leaving out possible crustal anisotropy in the overriding plate. Indeed, the azimuthal variability of the radial receiver functions before 2 s delay time and throughout the crust suggest that crustal anisotropy may be present, possibly caused by aligned cracks or thin layers.

Chapter 7

Discussion: Subduction vs. Underplating

7.1 The Receiver Function Results in the Context of Previous Geophysical Investigations

Former studies [Protti et al., 1994, 1995] suggested that the Cocos Ridge resists subduction and is instead underplated beneath the Panama Microplate in southern Costa Rica. This hypothesis was based on the shallow dipping plate observed down to about 40 km depth [Stavenhagen, 1998, DeShon et al., 2003, Husen et al., 2003], the lack of deep seismicity [Protti et al., 1994, 1995], the gap in the volcanic arc [Leeman et al., 1994, de Boer et al., 1995] and recent uplift of the region [Gardner et al., 1992, Collins et al., 1995, Gräfe, 1998].

Although the results by Arroyo H. [2001] indicated deeper and more steeply dipping seismicity, this study was not widely noticed; besides, the shallow underplating concept readily explained all different kinds of observations by one plausible mechanism, the buoyant ridge crust, which is both young (less than 15 Ma) and thick (reaching almost 20 km [Sallarès et al., 2003]).

While studies of local earthquake tomography [Husen et al., 2003, DeShon et al., 2003] and the active seismics profile by Stavenhagen [1998] could not resolve the structure at greater depths, it was assumed that the shallow dip angle of 19° observed down to about 40 km would continue to greater depths or possibly even give over to horizontal underplating. This conjecture was, however, not backed up by observations.

We have seen that the receiver function results indicate the presence of a steeply dipping slab down to about 170 km. Since this study cannot resolve the shallow part of the slab close to the trench, these results are not in contrast to previous observations – indeed the deep prolongation of the shallow slab, e.g. the 19° dipping WBZ, coincide with the beginning of the slab signal observed in the receiver function study – but they *are* in contrast to the shallow underplating scenario and the *expected* shallow continuation of the slab.

Deep seismicity (120 km) has now also been observed by the Quepos network. Consistently

with out study, Dinc et al. [2008] also do not find a significant shallowing of the subduction angle from central to southern Costa Rica. On the contrary, they observe an increase in the dip angle of the Wadati-Benioff zone seismicity from 30° in northern-central Costa Rica to 40° south of Quepos; the cold and dense Cocos Plate is imaged as a high-velocity anomaly down to 70 km, coincident with the WBZ seismicity, and overlain by a thin low-velocity layer.

Taking these new results into account, the deep slab imaged by receiver functions coincides well with the lower part of the tomography image, which in turn is well consistent with active seismic results (see comparison in Section 5.4). The present study hence expands the observations to greater depths; here, it is in disagreement with the hypothesis of shallow underplating.

The rest of this chapter will look into the following topics:

- Shallow underplating of the Cocos Ridge was not only expected based on local observations in Costa Rica, but was integrated into the general hypothesis that aseismic oceanic ridges cannot subduct steeply. Therefore, a short review on aseismic ridge subduction will be presented in Section 7.2. This includes observations of aseismic ridges/plateaus impinging on the South American subduction zone and scenarios commonly used to explain the behaviour of aseismic ridges in subduction zones. In general, the good spatial correlation of flat-slab subduction and volcanic gaps with aseismic ridges suggests a causal relationship between the two, which is corroborated by theory and modelling. However, the theory is far from complete and several open questions remain. It is therefore not excluded that exceptions exists in which aseismic ridges can indeed subduct.

- If we follow the general assumption that aseismic ridges do not subduct, we must reconsider the migrated receiver function profiles in the light of the underplating hypothesis (Section 7.3).

- On the other hand, if the Cocos Ridge is indeed an exception to the general rule and does subduct, as indicated by the migrated receiver functions, the cessation of arc volcanism and the absence of intermediate depth seismicity need to be explained. Possible models are discussed in Section 7.4. They include the presence of a strong compressional regime in the region, which does not allow melts to reach the surface. Alternatively, it is possible that the subducting Cocos Ridge crust and mantle are nearly anhydrous, therefore preventing flux melting in the mantle wedge.

- The actual scenario may be more complicated than the simple "end-member models" of underplating vs. normal subduction. Hybrid models and possible subduction scenarios will be presented and discussed in Section 7.5.

7.2   Global Observations of Aseismic Ridge Subduction

It has been speculated since the 1970s that the subduction of aseismic ridges, seamount chains and oceanic plateaus is generally associated with the development of flat-slab segments and the cessation of arc volcanism [Vogt, 1973, Pilger, 1981, Nur and Ben-Avraham, 1983]. While this observation presumably applies to subduction-zones world-wide, some of the best-documented examples are located along the South American subduction zone. This region is characterized by the eastward subduction of the Nazca Plate beneath the South American Plate with a convergence rate of about 8 cm/yr (central Chile) [DeMets et al., 1990, Kellogg and Vega, 1995] (Figure 7.1).
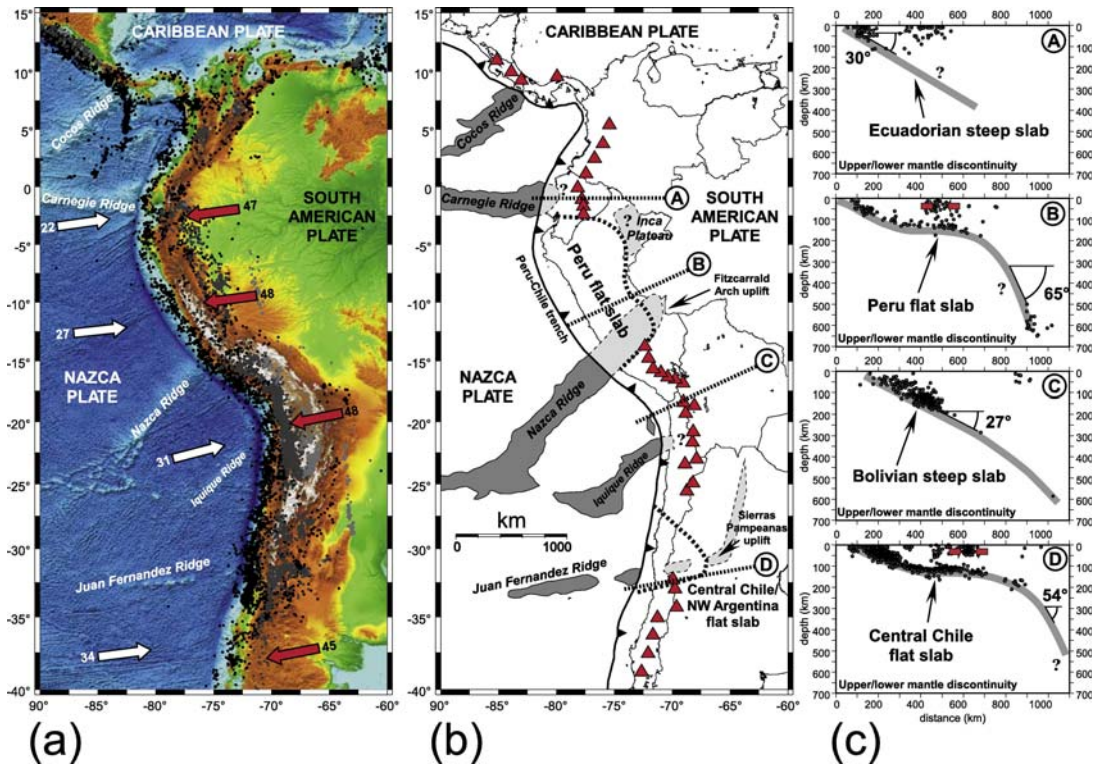
Figure 7.1: *Geodynamic setting of the Nazca-South America convergence system [from Espurt et al., 2008]. (a) Map of the eastern Pacific Ocean and South America. Earthquake epicentres are plotted: 0-99 km in black; 100-199 km in dark gray, 200-700 km in light gray. (b) The Nazca plate bears many topographic anomalies (aseismic ridges or oceanic plateaus marked by gray areas) where the crust is anomalously thick and buoyant. The estimated subducted lengths of these anomalies beneath South America are shown in light gray. Red triangles mark andesitic volcanism. (c) Profiles of the Nazca slab beneath the South American plate from earthquake epicentres [Gutscher et al., 2000b]. Red arrows show the locus of maximum shortening within the South American plate above the Peruvian and central Chile/NW Argentina flat slab segments.*

Two pronounced bathymetric highs subducting with the Nazca plate, the aseismic Nazca Ridge/Inca Plateau and Juan Fernandez Ridge, are spatially correlated with the Peru flat-slab (3-15°S) and Central Chile/NW Argentina flat-slab segment (27-33°S), respectively, and the associated gaps in the volcanic arc [Gutscher et al., 2000b, Yañez et al., 2001, Pardo et al., 2002]. In these two zones, the subducting slab as imaged by the Wadati-Benioff zone seismicity and tomography dips down to 100-120 km depth and then extends several hundreds of kilometers horizontally below the South American plate before resuming the downward plunge at a steep angle.

Several consequences of flat-slab subduction scenarios are generally observed:

1. **Arc volcanism**

   The onset of flat subduction can often be correlated with a broadening of the volcanic arc and arc migration away from the trench together with the extension of the flat-slab [Mahlburg

Kay et al., 1988, Kay and Abbruzzi, 1996, Mahlburg Kay and Mpodozis, 2002].

In several cases, a change of magmatism to adakitic signatures is observed [Gutscher et al., 2000a, Mahlburg Kay and Mpodozis, 2002], which has been argued to indicate slab melting. Whether slab melting is a natural cause of the thermal regime characteristic for flat-slab subduction [Gutscher et al., 2000a] or indicative of break-off of the deeper part of the slab [Yañez et al., 2002] is unclear.

After a few million years, active volcanism shuts off completely, which can be explained by the absence of an asthenospheric mantle wedge between the subducting slab and overriding plate, so no melting can take place [Nur and Ben-Avraham, 1983, McGeary et al., 1985, Gutscher et al., 2000a, Mahlburg Kay and Mpodozis, 2002, Ramos et al., 2002].

2. **Seismicity**

   Several authors note that the energy released by shallow seismicity in the overriding plate is larger than above steeply dipping slab segments, maybe due to the larger area of plate contact. It is argued that flat subduction cools both plates, increasing the lithospheric strength and therefore causing stronger viscous interplate coupling [Gutscher et al., 2000b].

3. **Shortening and uplift of the overriding plate**

   Uplift extends the whole way from the coastal region, through the mountain range and into the back-arc [Yañez et al., 2001, McNulty and Farber, 2002, Ramos et al., 2002]. Shortening has been observed above the flat-slab segments, and some authors suggested that shortening migrated eastwards with the underriding flat-slab [Pardo et al., 2002, Ramos et al., 2002, Siame et al., 2005]. On the other hand, uplift has also been argued to cause extension in the overriding plate [Cloos, 1993, McNulty and Farber, 2002], so the development of shortening/extension probably depends on a variety of factors interacting with each other, or may be related to the time since the onset of ridge subduction.

4. **Subduction erosion**

   Subduction of bathymetric highs with rough topography causes subduction erosion [von Huene and Scholl, 1991, Hampel et al., 2004] and has also been associated with the formation of forearc-basins [Laursen et al., 2002].

5. **Thermal regime**

   The initial migration of arc volcanism is associated with thermal weakening of the overriding plate [Ramos et al., 2002], causing uplift. During the initiation of flat subduction, the undersliding slab may be heated to the point of slab melting [Gutscher et al., 2000a], while prolonged flat subduction cools both the overriding and underplating slab. This strengthening of the slab facilitates the transfer of deformation even far from the trench.

7.2.1   Aseismic Ridge Subduction/Underplating – Mechanisms

The main mechanism invoked to explain the creation of flat subduction regimes has been the buoyancy effect of the subducting aseismic ridges (or oceanic plateaus, seamounts, etc.). The thicker-than-average oceanic crust would reduce the net density of the subducting slab, making it positively buoyant with respect to the mantle. While this holds true at shallow depths, the basalt/eclogite transformation should erase the buoyancy effect, making the crust negatively buoyant no matter what thickness it has. Therefore, the buoyancy argument only applies if some

mechanism delays the gabbro/eclogite transition to depths below 100 km.

Including such a mechanism, Cloos [1993] calculates that for an oceanic plate age of 80 Ma, oceanic plateaus need to exceed 17 km crustal thickness before they become "unsubductable". Similar analyses were carried out by Gutscher et al. [2000b], conluding that 18 km thick plateaus on a 50 Ma slab would be positively buoyant and resist subduction. While these calculations show that the buoyancy effect is indeed able to account for flat subduction, it should be kept in mind that the mechanism depends on the plate age and crustal thickness, and it is *"simply incorrect to assume that the subduction of most bathymetric highs is going to cause a widespread 'collisional orogenesis'."* [Cloos, 1993]

Several other mechanisms for the formation of flat-slab regions have also been proposed, most notably the influence of the overriding plate absolute velocity [for a review of other proposed mechanisms, see, e.g., Gutscher et al., 2000b, Pérez-Gussinyé et al., 2008]. If the overriding plate moved towards the subducting plate faster than this plate can sink, a flat slab would form. However, since the South American plate moves westwards at an approximately constant rate of 3-4 cm/yr, but flat subduction *only* occurs in discrete segments related to the subduction of aseismic ridges, this mechanism cannot be the sole cause of flat-slab subduction.

Further insight into the formation of flat-slab subduction regions comes from analogue and numerical modelling experiments. Martinod et al. [2005] model the subduction of a 200 km wide buoyant plateau, but without inclusion of the overriding plate. They do not reproduce a flat slab; the oceanic ridge is pulled down by the rest of the slab, with a subduction angle of about 60°, similar to their trial run for normal oceanic crust subduction. van Hunen et al. [2002, 2004] find that flat-slab subduction can be achieved, but depends critically on a combination of overriding plate motion, oceanic plateau subduction and possibly also slab suction forces.

An example of steep subduction of an aseismic ridge occurring in nature is the Iquique Ridge, which subducts below Southern Chile with a steep angle [Tassara et al., 2006], and does not appear to be associated with a volcanic gap.

Espurt et al. [2008] make a case that only the combination of aseismic ridge/plateau subduction *and* trenchward motion of the overriding plate lead to flat subduction. They furthermore analyse the temporal development of flat-slab subduction: At the initiation of plateau/ridge subduction, the subduction geometry remains unchanged, with a steep subduction angle corresponding to normal oceanic crust subduction. After about 360 km of the plateau have been subducted, the upper part shallows while the lower part steepens (reaching a dip angle of about 57° in the experiment), until finally flat subduction is attained with a delay of about 10 Ma after the ridge/plateau first reached the trench.

This observation is in agreement with the delay between the beginning of subduction and the cessation of volcanism in the case of the Nazca Ridge (11.2 Ma [Hampel, 2002] vs. 4 Ma ago [Rosenbaum et al., 2005], respectively) and the Juan Fernández Ridge (12 Ma [Yañez et al., 2001] vs. 5 Ma ago [Ramos et al., 2002], respectively). During plateau/ridge subduction, overriding plate shortening occurs above the termination of the flat slab, and uplift migrates away from the trench with the tip of the flat slab. The predicted uplift and shortening processes, and the lag between plateau subduction and the cessation of volcanism agree well with observations, making this analogue model a plausible representation of real processes, even though Espurt et al. [2008] admit that natural cases may furthermore involve slab break-off [see, e.g., Conrad et al., 2004].

Open questions

While the presently accepted scenario for aseismic ridge subduction leading to the development of a flat-slab subduction zone segment is in good agreement with most observations of the global occurrence of flat-slab segments, some open questions remain unanswered, two of which are briefly mentioned below.

- **Is Carnegie Ridge subduction steep or flat?**

  Whether or not the Carnegie Ridge causes flat-slab subduction beneath Ecuador is debated. While some authors argue for a flat subduction [e.g., Gutscher et al., 1999], a study by Guillier et al. [2001] suggests a moderately steep subduction angle (25-40°) similar to the angle observed in the "normal" subduction zone settings in South America, down to 200 km depth. The volcanic arc in the area of Carnegie Ridge subduction is still active, but particularly broad and exhibits adakitic signatures. This could be interpreted as the onset of flat-slab subduction, with slab flattening still ongoing [Espurt et al., 2008]. Lonsdale and Klitgord [1978] propose that Carnegie Ridge subduction began only 1 Ma ago, and even if they were wrong by a few million years, flat subduction might still be developing.

  The fate of the Carnegie Ridge and its influence on the Ecuadorian margin are particularly interesting because the Carnegie Ridge represents the "mirror image" of the Cocos Ridge on the Nazca Plate (Section 2.1.3). The two ridges (and their underlying ocean floor) were created at around the same time, and are subducting at similar velocities. Therefore, if indeed the Carnegie Ridge does subduct, it may be possible that so does the Cocos Ridge.

- **Why does the Juan Fernández Ridge cause flat subduction?**

  While it is very clear that the Juan Fernández Ridge *does* cause flat subduction, its crustal thickness cannot account for the positive buoyancy [Kopp et al., 2004]. The pervasive faulting observed along the hot-spot track may permit strong hydration of the ridge lithosphere, which is also indicated by reduced velocities. The reduction of density by hydration may be responsible for the buoyancy of the Juan Fernández Ridge and the resulting flat subduction. This would have to be a limiting case where flat subduction is only just possible due to the combined effect of hydration and slightly increased crustal thickness, because it is unlikely that hydration alone can cause flat subduction in normal oceanic crust (e.g., the strongly hydrated slab subducting in Nicaragua dips at a steep angle, causing active volcanism). The overriding plate velocity may, of course, also play a role in this setting.

The above examples show that while flat-slab subduction can generally be explained by the buoyancy effect of subducting aseismic ridges/plateaus, situations exist when ridges underplate in spite of only thin crustal roots, and conversely, ridges might subduct steeply even if their crust is sufficiently thick to suggest underplating. Not every occurrence of flat-slab subduction has been related clearly to the subduction of an aseismic ridge/plateau. For example, a flat-slab period of subduction in Central Chile before 14 Ma occurred before the Juan Fernández Ridge collided with the trench [von Huene et al., 1997, Mahlburg Kay and Mpodozis, 2002]. This suggests that for a given tectonic setting that allows for flat subduction, the arrival of a buoyant feature at the trench may in many cases just act as a trigger to change the subduction regime, while other tectonic regimes may cause stable steep subduction.

7.3   Flat Subduction of the Cocos Ridge?

Given the fact that shallow subduction is regarded as the normal mode of subduction of aseismic ridges, let us reconsider the migrated receiver function images in the light of the flat-slab hypothesis. Figure 7.2 presents the scenario expected for flat-slab subduction. The slab subducts down to 60-70 km depth, then bends towards the horizontal. This scenario seems plausible by comparison with the seismicity, which also shallows at this depth underneath the Talamanca mountain range, and with the positive conversion observed at similar depth.

However, the continuation of the slab towards the shallow small positive conversion shown in the figure is much less clear than the dipping feature, which is smooth and well-defined. The positive conversion at 60 km depth can be explained as a multiple of the innercrustal structure at 1-2 s, whereas the dipping feature cannot be a multiple of overlying structure. The seismicity observed here is not conclusive, since it occurs outside the Quepos network, where the localization is less well constrained.

If we expect the same underplating behaviour for the Cocos Ridge as is observed for the flat-slab segments in South America, indeed the bend towards horizontal subduction should occur below 100 km depth. This is the depth domain which cannot be imaged well by the receiver function method, because the Moho multiples are expected at the same time as the conversion signals of a hypothetical underplating slab at this depth. Therefore, receiver functions cannot rule out the existence of an underplating slab between 70 and 100 km depth, although the steeply dipping feature observed in the images appears more likely.
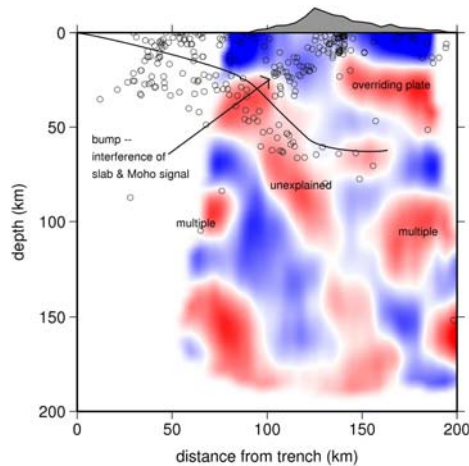
Figure 7.2: *Low-frequency receiver function profile 3 (centre profile), annotated for alternative underplating scenario.*

7.4   Steep Subduction of the Cocos Ridge?

The interpretation of the dipping positive conversion as the subducting slab is based on several facts:

- The dipping feature is clearly seen in receiver functions, and it cannot be explained as a multiple of the overlying structure.

- Both the bootstrap test and the inspection of individual traces show good coherence among the traces, and neighbouring profiles through the migration volume are very similar, so we can be confident that the observed feature is not noise but real.

- The migrated profiles do not change if only rays arriving from the NNW or from the SSE are used, arguing against a lateral change in slab configuration towards flat subduction in the SSE.

- The receiver function technique was originally meant for application to plane layering. Since this is not the case here, modelling studies were performed to test whether a steeply dipping feature can be imaged by the method. While mere forward modelling cannot prove that the dipping feature seen in the images is really caused by a dipping structure at depth, they do prove that a dipping structure would reappear as a similarly dipping conversion in the receiver function image. Thus modelling shows that the proposed model is possible.

- The dipping feature starts at the same place where the subducting slab imaged in active seismics ends (Figure 5.22).

- In the northern part of the studied volume, the dipping structure coincides extremely well with the slab observed in local earthquake tomography (Figure 5.19).

- If we accept that the northern profiles show the subducting Cocos slab in agreement with tomography, the closely-spaced migrated profiles and 3d-results show that the change from one profile to the next is very slight. If the dipping structure is interpreted as a slab in the north, there is no reason to interprete it as something different in the south, unless based on our expectations to find underplating in this region.

The simplest model including a steeply dipping structure is the "normal" steep subduction of the Cocos Plate that has been presented in previous chapters of this study (repeated in Figure 7.3). Steep Cocos Ridge subduction, while unexpected, might be possible if we keep in mind that its twin, the Carnegie Ridge, is believed to be subducting at a normal angle. Furthermore, the absolute velocity of the Panama Microplate is very slow, so if the overriding plate motion plays an important role in the development of flat subduction, this might not be sufficient for the formation of a flat slab underneath the Cordillera de Talamanca.

7.4.1   Thickness of the Subducting Crust

Receiver functions cannot distinguish whether the slab imaged at depth is the Cocos Ridge, thickened oceanic crust or normal oceanic crust. It is possible that the shallow dipping reflector seen by Stavenhagen [1998] could represent the subducted Cocos Ridge of ca. 100 km length (corresponding to an onset of ridge subduction approx. 1.1 Ma ago, in accordance with Collins et al. [1995]), which could give over further from the trench to more steeply dipping, older normal oceanic crust.
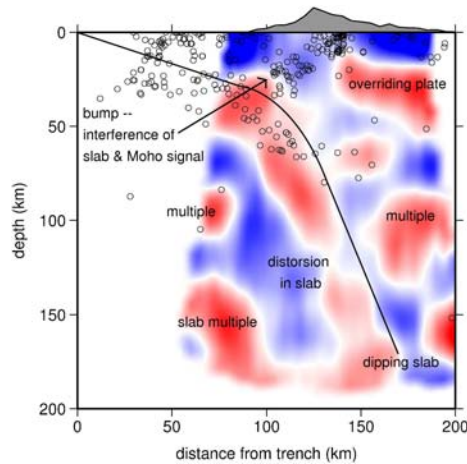
Figure 7.3: *Low-frequency receiver function profile 3 (centre profile), annotated for original steep subduction scenario presented in Chapter 5.*

Contrary to this, Meschede and Barckhausen [2000] estimate the length of the "missing part" of the Cocos Ridge to 200-250 km (corresponding to ridge subduction since 2.2-2.7 Ma). Their estimate is based on the assumption that the Cocos Ridge was cut off by the Panama Fracture Zone, so the distance between the northern end of the present-day Cocos Ridge and the prolongation of the fracture zone should give the length of the Cocos Ridge that has been subducted until the present day. A subducted ridge length of 200-250 km compares well with the length of the subducting slab seen in our study, which is about 270 km, indicating that the whole Cocos Ridge is imaged.

The trenchward prolongation of the southern profile cuts the MAT on the northern flank of the Cocos Ridge. The crustal thickness of the Cocos Ridge at this point is at least 12 km [Walther, 2003, Stavenhagen, 1998, Sallarès et al., 2003], well above the normal thickness of oceanic crust. Although it cannot be excluded that the ridge crest resists subduction, as suggested by earlier studies, the receiver function study shows that the northern side of the ridge is subducting. If the ridge crest does not subduct, the ridge must tear within the already thickened ridge crust to the south of the receiver function profiles. This would seen perplexing, given that we can expect the thickened crust to be more stable. Based on this argument and the estimate by Meschede and Barckhausen [2000], we believe it is indeed the northern flank of the Cocos Ridge that is seen subducting to about 170 km depth.

7.4.2   Cessation of Arc Volcanism and Intermediate/Deep Seismicity

If the Cocos Ridge subducts, this result has a major impact on our understanding of the tectonic settings in the region. The steep subduction geometry opens new questions regarding the thickness and buoyancy of the crust of the dipping slab and requires a different explanation for the cessation of active volcanism in the Talamanca Range and the uplift history.

Hypothesis 1: Compressional regime

It can be argued that the existence of a compressional regime in the region is responsible for quenching active volcanism. This compressional setting is evidenced, for instance, by the North

Panama Deformed Belt [Suárez et al., 1995]; Dinc et al. [2008] also interprete the 40° upwards trending seismicity unterneath the volcanic belt as an indication of compressional tectonics. The compressional regime may be caused either by the underthrusting of the Caribbean Plate under the Panama Microplate or by the the thickened crust of the Cocos Ridge, which may resist subduction more than average oceanic crust, or by the interaction of both processes.

As a consequence of this compressional regime, even though melts might be produced in the mantle wedge – possibly at shallower depths because of the younger, hotter subducting slab – their ascent to the surface might be hindered by the stress regime and altitude of the mountain range [de Boer et al., 1995]. They might rise some way to the surface and form melt intrusions and adakites, indications for slab melting of hot subducting lithosphere [de Boer et al., 1995, Abratis and Wörner, 2001].

Hypothesis 2: Fluid budget

A different possible explanation may be that the subducted Cocos Ridge carries less fluids than the faulted oceanic seafloor further north: Without sufficient fluid input into the mantle wedge, melting may not take place.

Even if the uppermost layers of the Cocos Ridge crust may contain some fluids, e.g. in the thin sedimentary cover, it can be expected that the deeper crust and mantle are not strongly serpentinized due to the thickness of the overlying crust and the absence of bending-related faults [von Huene et al., 2000, Ranero et al., 2005], which are abundant in the smooth segment offshore northern Costa Rica and Nicaragua [see, for example, Grevemeyer et al., 2007, Dinc, 2008, Ivandic, 2008, Ivandic et al., 2008, Lefeldt, 2008]. The fluids would then probably be released at shallower depths, where flux-induced mantle melting might not occur.

Some indications that the water content of the Cocos Ridge crust is indeed low come from active seismic profiles across the Cocos Ridge, which show elevated crustal thickness, but no sign of reduced crustal or mantle velocities as observed offshore Nicaragua (compare results by Bialas et al. [1999], Stavenhagen et al. [1998] with "standard" velocities of oceanic crust older than 10 Ma by Grevemeyer and Weigel [1996], Carlson [1998]).

The hypothesis that less fluids are carried down the south Costa Rican subduction zone is consistent with geochemical signatures of Central American arc lavas, which show a strong slab fluid signal in Nicaragua, weakening towards the south-east [Ruepke et al., 2002]. On the other hand, Hoernle et al. [2008] observe a southwards-increasing slab melt component. If this is derived from the Cocos Ridge itself, at least some melting must take place in this region; alternatively, these observations can be explained by the presence of a slab window.

If we assume that the subducting slab is not strongly hydrated at mantle depths, so no significant amount of fluids is released into the mantle wedge, the mantle wedge velocity is higher than the 7.6 km/s assumed in the modelling studies. However, it is the velocity contrasts that are imaged in receiver functions, and we can still expect the subducting slab to appear as a high-velocity feature. Indeed, modelling studies using higher mantle velocities have been performed and do not significantly differ from those shown above.

Absence of intermediate/deep seismicity

The hypothesis of little hydrous alteration of the subducting Cocos Plate under south-eastern Costa Rica would also offer an explanation for the surprisingly small seismicity of the WBZ at intermediate and large depths underneath the Talamanca Range. Several studies [Kirby, 1995, Kirby et al., 1995, Peacock, 2001, Hacker et al., 2003] propose that intermediate and deep earthquakes in subduction zones are caused by dehydration reactions in the subducting oceanic crust and mantle. If the incoming Cocos plate is not sufficiently hydrated, no dehydration will occur at depth, so neither volcanism nor intermediate/deep earthquakes will be observed. A similar argumentation was made by Ranero et al. [2005].

Seismicity is furthermore influenced by the thermal regime in the subducting slab, and the high temperatures may also play a part in preventing significant intermediate and deep seismicity. In particular, it has been argued that young plates may contain less water than old plates because of the shallower depth of the 600°C isotherm which limits serpentinization [Rüpke et al., 2004].

Uplift

While a scenario invoking higher slab temperature and a considerably smaller amount of fluids carried into the subduction zone may explain the absence of deep seismicity and volcanism, it does not account for uplift of the Cordillera de Talamanca. In fact, the strongest uplift is concentrated on Osa Península [Gardner et al., 1992], which may indeed be caused by the buoyant Cocos Ridge underlying the coastal areas. While the crust is still close to the surface, it could uplift the overlying crust because it resists bending more than "standard" oceanic crust does. At slightly deeper levels, the temperature of the slab may still be high enough to allow for bending towards steeper subduction angles.

Although the questions concerning uplift, the cessation of active volcanism and the absence of deep seismicity can at present only be answered in a speculative way, it has become clear that the simple underplating model assumed so far cannot satisfactorily explain the new observations. More factors than just the subducting ridge certainly play a role. MacMillan et al. [2004] argued that it was *not* the onset of Cocos Ridge subduction, but the action of the triple junction and Coiba ridge that quenched volcanism. Altough their argument relied mainly on the supposed onset time of ridge collision, which is not well constrained so far, the action of the Panama Fracture Zone and Coiba ridge and the vicinity of the North Panama Deformed Belt and Central Costa Rica Deformed Belt certainly complicate the regional tectonic situation.

Most probably, all these factors come into play and interact. The reginal tectonics, with the subducting Cocos Plate and the underthrusting Caribbean Plate, and the effect of the thick Cocos Ridge will produce a compressional regime and may also create uplift. The mantle flow pattern will be influenced by the vicinity of the Panama Fracture Zone, where the existence of a slab tear/slab window is at present unclear. At the same time, the subducting slab is characterized by thickened crust with little faulting, which can be argued to allow for little fluid infiltration, and is younger and hotter than the Cocos Plate to the north. In addition to the temperature effect, less fluids are available in the subducting slab, so the subduction zone will be influenced by the complex interplay of the complicated tectonic geometry and the fluid budget. Investigations of the mantle underlying the Cocos Ridge, the ridge crest and southern ridge flank, and modelling studies concerning the temperature and flexibility of the slab may in the future be able to better resolve these problems.

7.5   Combined Models of Cocos Ridge Subduction and Underplating?

While the presence of a dipping structure under the Cordillera de Talamanca appears plausible, the actual scenario may be more complicated. Figure 7.4 presents two possible "hybrid" models which involve both a dipping slab feature and underplating.
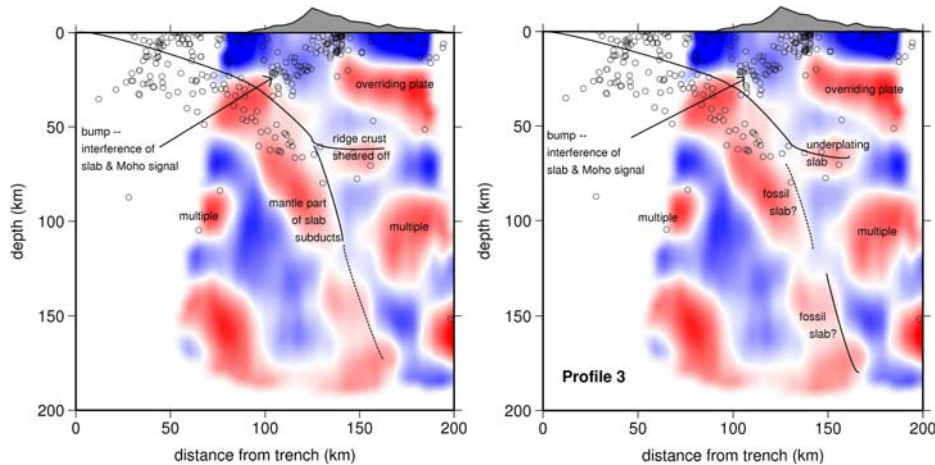
Figure 7.4: *Low-frequency receiver function profile 3 (centre profile), annotated for alternative scenario involving dipping slab and underplating. Left: model a, right: model b*

- **Model a:**

  It is possible that the buoyant Cocos Ridge crust is sheared off from the slab and underplates beneath the Cordillera de Talamanca crust, while the mantle part of the slab subducts normally. While this mechanism has been proposed for subducting continental crust [Chemenda et al., 2000], it needs to be investigated if it is possible for the oceanic crust to separate from the underlying mantle and underplate horizontally. If this were to happen, the Cocos Ridge crust would probably be compressed and deformed, causing the disrupted, hard to interprete features observed at the tip of the mantle wedge and underneath the overriding plate Moho.

- **Model b:**

  As a second possibility, it may be argued that the Cocos Plate is presently underplating beneath the Cordillera de Talamanca, in agreement with the usual model. The dipping feature seen in receiver functions is then identified with a fossil subducting slab, which has torn off the present slab and is now stuck in the subduction zone [Conrad et al., 2004].

  The main problem with this latter scenario is that the dipping signal is continuous down to about 120 km depth. Even if a tear in the slab may be present below this depth – the disruption in the slab signal could be caused by this, or may be explained by the interference with multiples – one would intuitively rather expect a slab tear directly underneath the region where the slab is at present underplating, i.e. around 60 km depth. Here, however, no such thing is observed. Still, this solution cannot be excluded since scattering effects

from the edge of the slab could come into play [Morozov, 2004, Morozov and Zheng, 2006]. Therefore, receiver functions would not be able to exactly image where the slab ends, since the diffraction might extend some way further downdip. While scattering cannot account for the dipping feature itself, its extent cannot be clearly seen from the receiver functions if scattering effects are dominant.

Both models involving underplating have the advantage that the absence of deep seismicity and the cessation of active volcanism are explained along the same lines as in the "standard" underplating model, while still allowing for the existence of a dipping feature as observed in receiver functions.

On the other hand, we should be aware that to explain the receiver functions along the lines of an underplating model would be expanding the observations strongly in an attempt to match our expectations, and does not appear intuitively likely[1]. If we were not expecting underplating, we certainly would not believe to see it in the migrated receiver function profiles. Although the image quality cannot be compared with what can be achieved by, e.g., active seismic methods, the data quality is reasonably good; receiver function images are rarely any clearer than these. The changes in crustal structure and subducting slab from north to south along the trench are minor and do not indicate that the slab – which subducts normally in the north as confirmed by tomography and seismicity studies – should tear and cease to subduct in the south. A steeply subducting slab is furthermore consistent with gravimetric modelling performed by the A2/A6 subproject (Giszas, personal communication – see Section 5.4).

Since none of the models presented so far is completely satisfactory in its attempt to explain the observations in the receiver function analysis and the tectonic/geophysical/geochemical characteristics of the study region, a final model is proposed which tries to explain our observations with a different approach:

7.6 A Transitional State in the Formation of a Flat-Slab Segment?

If we follow the analysis by Espurt et al. [2008] that several million years elapse between the onset of ridge subduction at the trench and the development of a flat-slab segment, the SE Costa Rican subduction zone might at the present be undergoing a reconfiguration in subduction style. It is still disputed when the Cocos Ridge arrived at the Middle-American trench, with estimates ranging from 1 Ma to 6 Ma ago (Chapter 2). The same argument has been applied to the Carnegie Ridge, which might also be causing a transition to flat-slab subduction, broadening arc volcanism while still subducting with a moderately steep angle. In the case of the Cocos Ridge, the cessation of arc volcanism suggests that the transition to flat subduction has already proceeded farther, but it may not be completed yet.

A second argument in favour of this hypothesis is that uplift, which is generally concentrated above the tip of the propagating flat-slab segment and moves away from the trench as the flat-slab region grows, is strongest at Osa Peninsula, that is very close to the trench. This might be an indication that flat subduction is only in its early phase of development at the present time, and has not yet created a significant flat-slab area.

---

[1] It certainly conflicts with Occam's razor.

This model is, of course, speculative, but hardly more so than the proposed hybrid subduction/underplating models are. Its beauty lies in the fact that no new explanation for the volcanic gap and absence of intermediate/deep seismicity is needed, uplift is predicted and the expectations concerning flat subduction of an aseismic ridge are fulfilled; while at the same time the receiver function results imaging a steeply dipping feature are incorporated in the model.

Unfortunately, we cannot come back to repeat the observations in a few million years' time, and the receiver function image cannot resolve clearly if there is an underplating feature – of crustal or slab thickness – beneath the overriding crust. As already mentioned above (section 7.3, this is mainly due to the fact that the signals at this depth are dominated by multiples, so any horizontal signal underlying the Moho cannot be clearly identified. On the other hand, it has been argued that the receiver functions indicate that some dipping structure underlies the subduction zone, contrary to previous expectations. Whether this is the dipping slab or just part of the slab cannot at present be decided.

Chapter 8

Conclusions and Outlook

This study indicates for the first time that a dipping structure is present underneath the volcanic gap in the Cordillera de Talamanca. Neither shallow underplating of the Cocos Plate nor a slab window can be seen in the studied profiles. Instead, a dipping feature is well imaged as a positive conversion, subducting steeply to about 170 km depth at an angle of approx. 60°. This feature is consistent with the lower end of the subducting slab imaged in refraction seismics [Stavenhagen, 1998] and with the slab observed by tomography [Dinc, 2008].

The steeply dipping structure, interpreted as the subducting Cocos Plate, is in disagreement with expectations based on previous studies and has major impact on the tectonic settings of the region. If this structure is the steeply subducting Cocos Plate, a new explanation is needed for the cessation of active volcanism in the Cordillera de Talamanca. This may involve compressional forces preventing the ascent of magmas/fluids. Alternatively, the Cocos Ridge crust may be nearly anhydrous, so that no mantle wedge melting may occur. A different interpretation would be that the slab may be split or torn off so that underplating indeed explains the gap in active volcanism and absence of intermediate/deep seismicity, while the dipping feature is either part of the subducting slab or a fossil remnant of earlier subduction. Finally, the subducting slab imaged at present may be a transitional state within a subduction zone that is presently undergoing a transition to flat-slab subduction.

The Moho of the overriding plate is observed at 35-40 km depth, and a crustal discontinuity occurs around 15-20 km depth, with slight lateral variations. These results are consistent with active seismic studies by Stavenhagen [1998].

The modelling studies point to the existence of anisotropy caused by corner flow. This is consistent with the expectations for the "standard" subduction zone scenario, if the mantle is dominated by A-type/C-type olivine. The presence of significant amounts of water in the mantle wedge would entail B-type olivine configuration and resulting trench-parallel anisotropy if the flow pattern is dominated by corner flow. However, the models assuming only trench-parallel anisotropy in the mantle wedge are not in agreement with the observations, indicating corner flow in a comparatively dry mantle wedge below the Cordillera de Talamanca.

In spite of the good agreement of the simple corner-flow model with the observed receiver functions, complicated flow patterns may be present beneath the Talamanca. A slab window as proposed by Johnston and Thorkelson [1997] and Abratis and Wörner [2001] is not seen in the receiver functions, but might occur at greater depth or further to the south, possibly giving rise to

149

trench-parallel flow in addition to the (probably dominant) corner-flow.

While these studies have yielded new insights into the tectonic setting of southern Costa Rica, several questions remain unanswered. Although doubts are cast on the "standard" underplating model of the Cocos Ridge as a cause for the cessation of active volcanism in the Cordillera de Talamanca, the real cause remains unknown.

Outlook

The next step in the analysis of the receiver functions should be a 3-d migration approach. In this study, migration was performed in 3-d, but based on a 1-d velocity model with horizontal layering. Besides being the "standard" migration method usually (and successfully) applied in receiver function imaging [e.g., Kosarev et al., 1999, Gossler et al., 1999, Yuan et al., 2000, Ramesh et al., 2005], this method was chosen because no 3-d model was available and anyway horizontal underplating of the Cocos Ridge was expected. The modelling study shows that in spite of the 1-d velocity model used in the migration, a dipping structures could be imaged with an angle close to the real dip angle. Even so, the image quality can be improved by a real 3-d migration, which could iteratively lead to a more realistic velocity model.

The hypothesized presence of an underplating slab or crustal part of the slab beneath the Cordillera de Talamanca could be resolved by obtaining better velocity models at depths below 35 km. Gravity modelling may also be able to find out if a buoyant structure underlies the overriding plate crust.

The question concerning the presence/absence of fluids/magmas could be tackled with an absorption analysis. Knowledge of the hydration state of the mantle wedge would also help decide which olivine fabric can be expected here. If the fabric was known, anisotropy patterns could be directly translated into mantle flow patterns.

Shear-wave splitting analyses might provide a further independent means to investigate the anisotropy scenario. Depth resolution would suffer from the lack of deep/intermediate seismicity, which would reduce the analysis to SKS phases; but possibly surface wave dispersion studies could be combined with the shear-wave splitting measurements to yield insight into the depth distribution of anisotropy.

Finally, a study of the geometry of the subduction zone further to the south would be able to resolve the question whether the Cocos Ridge crest subducts at a similarly steep angle as its northern flank observed in this study, and if there is a slab tear/slab window underneath the Costa Rican-Panamanian border or underneath northern Panama. The continuation of the subduction zone into Panama, still within the volcanic gap, and the southern edge of the gap in active volcanism would be very interesting research sites and provide valuable insight into the processes acting in this region and their relation to the subduction geometry and fluid processes.

Thank you

Wolfgang. When the truck was coming after us, I would never have stayed with the steering wheel if you hadn't been at my side. The same thing applies to this thesis. If nothing works, you motivate people just by listening to your ideas and feeling you are confident they can do it. Thanks so much for three years of guidance, help, patience and enthousiasm.

Ernst. I will miss the nightshifts on the ship with you. Thanks for agreeing to co-referee this thesis, for sharing your experience, and the sunrise.

Heidrun. Thanks for so much empathy when I was trying to finish everything on time and losing my head over it.

Martin. I know I can be a nuisance, thanks for putting up with me. Whether you were next door or an ocean away, you were always there for my problems, and complaints, and doubts.

Mike. You were a constant source of encouragement and friendship. The Solar System wouldn't be the same without you.

Laura, Albert, Diannita y Valeria, Liz y Stephanie. El primer día que llegué en Costa Rica para quedarme medio ano, se me robó mi bulto, con todo lo que tenía de valor. Pensaba que era mala suerte, pero hoy sé que es lo mejor que me hubiera podido pasar, porque me hizo quedarme en su casa. Allí encontré un hogar, y otra familia lejos de mi casa. Extrano las conversaciones, el desayuno, la cena y la soda juntos. Ahora sé cómo es tener hermanas. No hay cosa mejor que llegar tarde del campo y saber que hay una luz encendida, alguien esperando. Su confianza en mí y lo que estaba haciendo me daban fuerza. Gracias por su amor. Siempre tendrán el mío.

Waldo. Cuando estaba en Alemania y expliqué a mi familia que iba a ir a Costa Rica medio año − sola − se preocupaban, y les dije, "pero allí está Waldo, todo está bien". Eras mi último recurso cuando había problemas, y muchos problemas las resolviste antes de que se presentaran. Pero más que mi plan de emergencia, eres un amigo querido. Te echo mucho de menos a vos y a tu familia.

Mauricio and Memo. You made all of this possible. You were behind the scenes when it came to going into the field, dealing with customs, bureaucracy, anything that had gone wrong. Thanks so much. And thank you, Mau, for your help when I was without money, credit card, passport, flight ticket, and place to stay.

Ricardo y Chico. No lo habriá podido hacer sin vos. Gracias por siempre estar allí cuando necesitaba ayuda, por todos los favores, por las noches de karaoke y baile a pesar de las madrugadas en el campo. Por tener siempre buen humor, incluso en la lluvia de Río Orosi y los mosquitos de Pejibaye y Guayabo Arriba. Os quiero mucho.

Gato. Sé que era difícil encontrar tiempo para salir al campo conmigo. Gracias. Y gracias por enseñarme el platanillo, contarme del níspero y de todas las otras plantas y frutas deliciosas.

Comandante Rodrigo Peralta. Muchísimas gracias por organizar las operaciones con el barco de guardacostas. Era un placer trabajar con usted.

The German Embassy in San José helped with the coastguard operations, customs and my stolen passport. Thank you to Bettina Kitzing. I wish I could thank Bettina Sassen. We all miss her.

Don Timoteo y don Silverio, por darme la bienvenida en la reserva bribrí, y pasar aquella noche contándome leyendas indígenas de terremotos y huracanes.

Marlis und Paul. Danke für 28 Jahre. Ich liebe euch.

Acknowledgements

Doy las gracias a toda la gente que nos prestaban su jardín o prado o campo – o incluso su casa – para instalar los sismómetros, y que muchas veces durante el trabajo nos acompañaban, nos ayudaron o nos sorprendieron con bebidas y comida, servidas en plena naturaleza.

Bibliography

G. A. Abers. Seismic low-velocity layer at the top of subducting slabs: observations, predictions, and systematics. *Phys. Earth Planet. Int.*, 149:7–29, 2005.

M. Abratis and G. Wörner. Ridge collision, slab-window formation, and the flux of Pacific asthenosphere into the Caribbean realm. *Geology*, 29(2):127–130, February 2001.

S. Adamek, C. Frohlich, and W. D. Pennington. Seismicity of the Caribbean-Nazca Plate Boundary: Constraints on Microplate Tectonics of the Panama Region. *J. Geophys. Res.*, 93(B3):2053–2075, March 1988.

K. Aki and P. G. Richards. *Quantitative Seismology*. University Science Books, 2 edition, 2002.

Ch. J. Ammon. The isolation of receiver effects from teleseismic P waveforms. *Bull. Seis. Soc. Am.*, 81(6):2504–2510, December 1991.

Ch. J. Ammon. Receiver Function Overview. http://www.eqseis.geosc.psu.edu/ cammon/HTML/RftnDocs/rftn01.html, 1997.

I. Arroyo. *Local earthquake tomography at the Central Pacific Margin of Costa Rica*. PhD thesis, Christian-Albrechts Universität zu Kiel, Germany, 2008.

I. G. Arroyo H. Sismicidad y Neotectónica en la región de influencia del proyecto Boruca: hacia una mejor definición sismogénica del Sureste de Costa Rica. Master's thesis, Escuela Centroamericana de Geología, Universidad de Costa Rica, 2001.

E. Audoine, M. K. Savage, and K. Gledhill. Anisotropic structure under a back arc spreading region, the Taupo Volcanic Zone, New Zealand. *J. Geophys. Res.*, 109(B11305), 2004.

J. Bialas, E. R. Flueh, and G. Bohrmann. FS Sonne Cruise Report SO144/1&2 PAGANINI (PAnama basin and GAlapagos plume – New INvestigations of Intraplate magmatism). In *Geomar Report 94*, page 122 ff. GEOMAR Research Center for Marine Geosciences, Kiel, Alemania, 1999.

P. Bird. An updated digital model of plate boundaries. *Geochem. Geophys. Geosys.*, 4(3):1027, 2003.

D. K. Blackman. Use of mineral physics, with geodynamic modelling and seismology, to investigate flow in the Earth's mantle. *Reports on Progress in Physics*, 70:659–689, 2007.

T. Bohlen. Parallel 3-D viscoelastic finite-difference seismic modelling. *Computers @ Geosciences*, 28(8):887–889, 2002.

M. G. Bostock. Anisotropic upper-mantle stratigraphy and architecture of the Slave craton. *Nature*, 390:392–395, 1997.

M. G. Bostock and S. Rondenay. Migration of scattered teleseismic body waves. *Geophys. J. Int.*, 137:732–746, 1999.

M. G. Bostock and M. D. Sacchi. Deconvolution of teleseismic recordings for mantle structure. *Geophys. J. Int.*, 129:143–152, 1997.

British Geological Survey. British Geological Survey Timechart. http://www.bgs.ac.uk/education/britstrat/home.html.

M. Budweg. *Der obere Mantel in der Eifel-Region untersucht mit der Receiver Function Methode.* PhD thesis, Universität Potsdam, Germany, 2003.

L. J. Burdick and Ch. L. Langston. Modelling crustal structure through the use of converted phases in teleseismic body-wave forms. *Bull. Seismol. Soc. Am.*, 67:677–691, 1977.

K. Burke. Tectonic evolution of the Caribbean. *Ann. Rev. Earth Planet. Sci.*, 16:210–230, 1988.

M. Bystricky, K Kunze, L. Burlini, and J.-P. Burg. High Shear Strain of Olivine Aggregates: Rheological and Seismic Consequences. *Science*, 290:1564–1567, November 2000.

R. L. Carlson. Seismic velocities in the uppermost oceanic crust: Age dependence and the fate of layer 2A. *J. Geophys. Res.*, 103(B4):7069–7077, 1998.

R. L. Carlson and D. J. Miller. Mantle wedge water contents estimated from seismic velocities in partially serpentinized peridotites. *Geophys. Res. Lett.*, 30(5):1250, 2003.

M. J. Carr. Symmetrical and segmented variation of physical and geochemical characteristics of the Central American volcanis front. *J. Volcanol. Geotherm. Res.*, 20:231–252, 1984.

M. J. Carr and R. E. Stoiber. Volcanism (Chapter 14). In G. Dengo and J. E. Case, editors, *The Geology of North America*, volume H. "The Caribbean region", pages 375–391, 1990.

M. J. Carr, M. D. Feigenson, and E. A. Bennett. Incompatible element and isotopic evidence for tectonic control of source mixing and melt extraction along the Central American arc. *Contrib. Mineral. Petrol.*, 105:369–380, 1990.

A. I. Chemenda, J.-P. Burg, and M. Mattauer. Evolutionary model of the Himalaya-Tibet system: geopoem based on new modelling, geological and geophysical data. *Earth Planet. Sci. Lett.*, 174:397–409, 2000.

N. I. Christensen. The magnitude, symmetry and origin of upper mantle anisotropy based on fabric analyses of ultramafic tectonites. *Geophys. J. Royal Astron. Soc.*, 76:89–111, 1984.

R. W. Clayton and R. A. Wiggins. Source shape estimation and deconvolution of teleseismic bodywaves. *Geophys. J. R. Astron. Soc.*, 47:151–177, 1976.

M. Cloos. Lithospheric buoyancy and collisional orogenesis: Subduction of oceanic plateaus, continental margins, island arcs, spreading ridges, and seamounts. *Geol. Soc. Am. Bull.*, 105:715–737, June 1993.

L. S. Collins, A. G. Coates, J. B. C. Jackson, and J. A. Obando. Timing and rates of emergence of the Limón and Bocas del Toro basins: Caribbean effects of Cocos Ridge subduction. In P. Mann, editor, *Geologic and Tectonic Development of the Caribbean Plate Boundary in Southern Central America*, number 295 in Geol. Soc. Am. Spec. Papers, pages 263–289. Boulder, Colorado, 1995.

C. P. Conrad, S. Bilek, and C. Lithgow-Bertelloni. Great earthquakes and slab pull: interaction between seismic coupling and plate-slab coupling. *Earth Planet. Sci. Lett.*, 218:109–122, 2004.

T. Damm and H.-J. Götze. Modern geodata management – application of interdisciplinary interpretation and visualization in Central America. *Int. J. Geophys., under revision.*

J. Z. de Boer, M. S. Drummond, M. J. Bordelong, M. J. Defant, H. Bellon, and R. C. Maury. Cenozoic magmatic phases of the Costa Rican island arc (Cordillera de Talamanca). In P. Mann, editor, *Geologic and Tectonic Development of the Caribbean Plate Boundary in Southern Central America*, number 295 in Geol. Soc. Am. Spec. Papers, pages 35–55. Boulder, Colorado, 1995.

C. DeMets, R. G. Gordon, D. F. Argus, and S. Stein. Current plate motions. *Geophys. J. Int.*, 101:425–478, 1990.

P. Denyer, W. Montero, and G. E. Alvarado. *Atlas tectónico de Costa Rica.* Editorial de la Universidad de Costa Rica, 2003.

H. R. DeShon, S. Y. Schwartz, S. L. Bilek, L. M. Dorman, V. Gonzalez, J. M. Protti, E. R. Flueh, and T. H. Dixon. Seismogenic zone structure of the southern Middle America Trench, Costa Rica. *J. Geophys. Res.*, 108(B10):2491, 2003.

J. B. Diebold. Three-dimensional traveltime equation for dipping layers. *Geophysics*, 52(11): 1492–1500, November 1987.

A. N. Dinc. *Local Earthquake Tomography of Central America: Structural Variations and Fluid Transport in the Nicaragua-Costa Rica Subduction Zone.* PhD thesis, Christian-Albrechts Universität zu Kiel, Germany, 2008.

A. N. Dinc, I. Koulakov, M. Thorwart, W. Rabbel, E. Flueh, I. Arroyo, W. Taylor, and Alvarado G. Local Earthquake Tomography of Central Costa Rica: Transition from seamount to ridge subduction. *Geophys. J. Int.*, accepted, 2008.

B. Efron and R. Tibshirani. Bootstrap methods for standard errors, confidence intervals, and other measured of statistical accuracy. *Stat. sci.*, 1:54–77, 1986.

G. Escalante. The geology of southern Central America and western Colombia (Chapter 8). In G. Dengo and J. E. Case, editors, *The Geology of North America*, volume H. "The Caribbean region", pages 201–228, 1990.

N. Espurt, F. Funiciello, J. Martinod, B. Guillaume, V. Regard, C. Faccenna, and S. Brusset. Flat subduction dynamics and deformation of the South American plate: Insights from analog modelling. *Tectonics*, 27, 2008.

M. D. Feigenson and M. J. Carr. The source of Central American lavas: inferences from geochemical inverse modeling. *Contrib. Mineral. Petrol.*, 113:226–235, 1993.

A. Ferris, G. A. Abers, D. H. Christensen, and E. Veenstra. High resolution image of the subducted Pacific (?) plate beneath central Alaska, 50-150 km depth. *Earth Planet. Sci. Lett.*, 214(3-4): 575–588, September 2003.

K. M. Fisher, M. J. Fouch, D. A. Wiens, and M. S. Boettcher. Anisotropy and Flow in Pacific Subduction Zone Back-Arcs. *Pure Appl. Geophys.*, 151:463–475, 1998.

M. J. Fouch and K. M. Fisher. Mantle anisotropy beneath northwest Pacific subduction zones. *J. Geophys. Res.*, 101(B7):15987–16002, July 1996.

A. W. Frederiksen and M. G. Bostock. Modelling teleseismic waves in dipping anisotropic structures. *Geophys. J. Int.*, 141:401–412, 2000.

T. W. Gardner, D. Verdonck, N. M. Pinter, R. Slingerland, K. P. Furlong, T. F. Bullard, and S. G. Wells. Quaternary uplift astride the aseismic Cocos Ridge, Pacific coast, Costa Rica. *Geol. Soc. Am. Bull.*, 104:219–232, February 1992.

J. Gossler, R. Kind, S. V. Sobolev, H. Kämpf, K. Wylegalla, M. Stiller, and TOR Working Group. Major crustal features between the Harz Mountains and the Baltic Shield derived from receiver functions. *Tectonophysics*, 314:321–333, 1999.

K. Gräfe. *Exhumation and Thermal Evolution of the Cordillera de Talamanca (Costa Rica): Constraints from Fission Track Analysis,* $^{40}Ar - ^{39}Ar$ *and* $^{87}Rb - ^{87}Sr$ *Chronology.* PhD thesis, Tübinger Geowiss. Arbeiten (TGA) A39, 1998.

I. Grevemeyer and W. Weigel. Seismic velocities of the uppermost igneous crust versus age. *Geopys. J. Int.*, 124:631–635, 1996.

I. Grevemeyer, C. R. Ranero, E. R. Flueh, D. Kläschen, and J. Bialas. Passive and active seismological study of bending-related faulting and mantle serpentinization at the Middle America trench. *Earth Planet. Sci. Lett.*, 258:528–542, 2007.

B. Guillier, J.-L. Chatelain, É. Jaillard, H. Yepes, G. Poupinet, and J.-F. Fels. Seismological evidence on the geometry of the orogenic system in central-northern Ecuador (South America). *Geophys. Res. Lett.*, 28(19):3749–3752, 2001.

M.-A. Gutscher, J. Malavieille, S. Lallemand, and J.-Y. Collot. Tectonic segmentation of the North Andean margin: impact of the Carnegie Ridge collision. *Earth Planet. Sci. Lett.*, 168:225–270, 1999.

M.-A. Gutscher, R. Maury, J.-Ph. Eissen, and E. Bourdon. Can slab melting be caused by flat subduction? *Geology*, 28(6):535–538, June 2000a.

M.-A. Gutscher, W. Spakman, H. Bijwaard, and E. R. Engdahl. Geodynamics of flat subduction: Seismicity and tomographic constraints from the Andean margin. *Tectonics*, 19(5):814–833, 2000b.

B. R. Hacker, S. M. Peacock, G. A. Abers, and S. D. Holloway. Subduction factory 2. Are intermediate-depth earthquakes in subducting slabs linked to metamorphic dehydration reactions? *J. Geophys. Res.*, 108(B1):2030, 2003.

A. Hampel. The migration history of the Nazca Ridge along the Peruvian active margin: A re-evaluation. *Earth Planet. Sci. Lett.*, 203:665–679, 2002.

A. Hampel, N. Kukowski, J. Bialas, Ch. Huebscher, and R. Heinbockel. Ridge subduction at an erosive margin: The collision zone of the Nazca Ridge in southern Peru. *J. Geophys. Res.*, 109, 2004.

G. Helffrich. Subducted Lithospheric Slab Velocity Structure: Observations and Mineralogical Inferences. In G. E. Bebout, D. W. Scholl, S. H. Kirby, and J. P. Platt, editors, *Subduction: Top to Bottom*, number 96 in Geophysical Monograph, pages 215–222. American Geophysical Union, 1995.

R. Hey. Tectonic evolution of the Cocos-Nazca spreading center. *Geol. Soc. Am. Bull.*, 88:1404–1420, December 1977.

K. Hoernle, P. van den Bogaard, R. Werner, B. Lissinna, F. Hauff, G. Alvarado, and D. Garbe-Schönberg. Missing history (16-71 Ma) of the Galápagos hotspot: Implications for the tectonic and biological evolution of the Americas. *Geology*, 30(9):795–798, September 2002.

K. Hoernle, D. L. Abt, K. M. Fischer, H. Nichols, F. Hauff, G. A. Abers, P. van den Bogaard, K. Heydolph, G. Alvarado, M. Protti, and W. Strauch. Arc-parallel flow in the mantle wedge beneath Costa Rica and Nicaragua. *Nature*, 541:1094–1097, January 2008.

H. Hoffmann, J. Boelsche, W. Horst, W. Lange, F. Palesch, V. Pomeranceva, and K. Wruck. Tiefen-seismische Untersuchungen in der DDR durch den VEB Geophysik – Stand und Ergebnisse. *Z. angew. Geol.*, 35:308–314, 1989.

B. K. Holtzmann, D. L. Kohlstedt, M. E. Zimmerman, F. Heidelbach, R. Hiraga, and J. Hustoft. Melt Segregation and Strain Partitioning: Implications for Seismic Anisotropy and Mantle Flow. *Science*, 301:1227–1230, August 2003.

S. Husen, R. Quintero, E. Kissling, and B. Hacker. Subduction-zone structure and magmatic processes beneath Costa Rica constrained by local earthquake tomography and petrological modelling. *Geophys. J. Int.*, 155:11–32, 2003.

M. Ivandic. *Impact of bending related faulting on the seismic properties of the incoming oceanic lithosphere of Nicaragua.* PhD thesis, Christian-Albrechts Universität zu Kiel, Germany, 2008.

M. Ivandic, I. Grevemeyer, A. Berhorst, E. R. Flueh, and K. McIntosh. Impact of bending related faulting on the seismic properties of the incoming oceanic plate offshore of Nicaragua. *J. Geophys. Res.*, 113, 2008.

S. T. Johnston and D. J. Thorkelson. Cocos-Nazca slab window beneath Central America. *Earth Planet. Sci. Lett.*, 146:465–474, 1997.

C. H. Jones and R. A. Phinney. Seismic structure of the lithosphere from teleseismic converted arrivals observed at small arrays in the southern Sierra Nevada and vicinity. *J. Geophys. Res.*, 103:10065–10090, 1998.

H. Jung and S.-I. Karato. Water-Induced Fabric Transitions in Olivine. *Science*, 293:1460–1463, August 2001.

S.-I. Karato. *Deformation of Earth Materials.* Cambridge, 2008.

I. Katayama and S.-I. Karato. Effect of temperature on the B- to C-type olivine fabric transition and implication for flow pattern in subduction zones. *Phys. Earth Planet. Int.*, 157:33–45, 2006.

I. Katayama, H. Jung, and S. Karato. A new type of olivine fabric from deformation experiments at modest water content and low stress. *Geology*, 32:1045–1048, 2004.

S. M. Kay and J. M. Abbruzzi. Magmatic evidence for Neogene lithospheric evolution of the central Andean "flat-slab" between 30°S and 32°S. *Tectonophysics*, 259:15–28, 1996.

J. N. Kellogg and V. Vega. Tectonic development of Panama, Costa Rica, and the Colombian Andes: Constraints from Global Positioning System geodetic studies and gravity. In P. Mann, editor, *Geologic and Tectonic Development of the Caribbean Plate Boundary in Southern Central America*, number 295 in Geol. Soc. Am. Spec. Papers. Boulder, Colorado, 1995.

B. L. N. Kennett, E. R. Engdahl, and R. Buland. Constraints on seismic velocities in the Earth from travel times. *Geophys. J. Int.*, 122:108–124, 1995.

R. Kind and L. P. Vinnik. The upper-mantle discontinuities underneath the GRF array from P-to-S converted phases. *J. Geophys.*, 62:138–147, 1988.

R. Kind, G. L. Kosarev, and N. V. Petersen. Receiver functions at the stations of the German Regional Seismic Network (GRSN). *Geophys. J. Int.*, 121:191–202, 1995.

S. Kirby, E. R. Engdahl, and R. Denlinger. Intermediate-Depth Intraslab Earthquakes and Arc Volcanism as Physical Expressions of Crustal and Uppermost Mantle . In G. E. Bebout, D. W. Scholl, S. H. Kirby, and J. P. Platt, editors, *Subduction: Top to Bottom*, number 96 in Geophysical Monograph, pages 195–214. American Geophysical Union, 1995.

S. H. Kirby. Intraslab earthquakes and phase changes in subducting lithosphere. *Rev. Geophys. Suppl. US National Report to International Un. of Geodesy and Geophys. 1991-1994*, pages 287–297, 1995.

E. A. Kneller and P. E. van Keken. Trench-parallel flow and seismic anisotropy in the Mariana and Andean subduction systems. *Nature*, 450:1222–1226, December 2007.

E. A. Kneller, P. E. van Keken, S.-I. Karato, and J. Park. B-type olivine fabric in the mantle wedge: Insights from high-resolution non-Newtonian subduction zone models. *Earth Planet. Sci. Lett.*, 237:781–797, 2005.

H. Kopp, E. R. Flueh, C. Papenberg, and D. Klaeschen. Seismic investigations of the O'Higgins Seamount Group and Juan Fernández Ridge: Aseismic ridge emplacement and lithosphere hydration. *Tectonics*, 23, 2004.

G. Kosarev, R. Kind, S. V. Sobolev, X. Yuan, W. Hanka, and S. Oreshin. Seismic Evidence for a Detached Indian Lithospheric Mantle Beneath Tibet. *Science*, 283:1306–1309, February 1999.

C. A. Langston. Corvallis, Oregon, crustal and upper mantle structure from teleseismic P and S waves. *Bull. Seismol. Soc. Am.*, 67:713–724, 1977.

J. Laursen, D. W. Scholl, and R. von Huene. Neotectonic deformation of the central Chile margin: Deepwater forearc basin formation in response to hot spot ridge and seamount subduction. *Tectonics*, 21(5), 2002.

T. Lay and T. C. Wallace, editors. *Modern Global Seismology*. Number 58 in International Geophysics Series. Academic Press, 1995.

W. P. Leeman, M. J. Carr, and J. D. Morris. Boron geochemistry of the Central American Volcanic Arc: Constraints on the genesis of subduction-related magmas. *Geochim. et Cosmochim. Acta*, 58:149–168, 1994.

M. Lefeldt. *Bending-Related Faulting and Mantle Serpentinization at the Nicaraguan Subduction Zone*. PhD thesis, Christian-Albrechts Universität zu Kiel, Germany, 2008.

V. Levin and J. Park. P-SH Conversions in Layered Media with Hexagonally Symmetric Anisotropy: A CookBook. *Pure App. Geophys.*, 151:669–697, 1998.

X. Li. *A Receiver Function Study of the Northwest Pacific Subduction Zone and the Hawaiian Mantle Plume*. PhD thesis, Freie Universität Berlin, Germany, 2001.

X. Li, G. Bock, G. Vafidis, R. Kind, H.-P. Harjes, W. Hanka, K. Wylegalla, M. van der Meijde, and X. Yuan. Receiver function study of the Hellenic subduction zone: imaging crustal thickness variations and the oceanic Moho of the descending African lithosphere. *Geophys. J. Int.*, 155(2): 733, November 2003.

M. D. Long and P. G. Silver. The Subduction Zone Flow Field from Seismic Anisotropy: A Global View. *Science*, 319:315–318, January 2008.

M. D. Long and R. D. van der Hilst. Upper mantle anisotroyp beneath Japan from shear wave splitting. *Phys. Earth Planet. Int.*, 151:206–222, 2005.

P. Lonsdale and K. D. Klitgord. Structure and tectonic history of the eastern Panama Basin. *Geol. Soc. Am. Bull.*, 89:981–999, July 1978.

O. H. Lücke. Modelo tridimensional de densidades de la corteza superior en el sector Central de Costa Rica, basado en interpretación del campo gravimétrico. Master's thesis, Escuela Centroamericana de Geología, Universidad de Costa Rica, 2008.

I. MacMillan, P. B. Gans, and G. Alvarado. Middle Miocene to present plate tectonic history of the southern Central American Volcanic Arc. *Tectonophysics*, 392(1-4):325–348, 2004.

S. Mahlburg Kay and C. Mpodozis. Magmatism as a probe to the Neogene shallowing of the Nazca plate beneath the modern Chilean flat-slab. *J. South Am. Earth Sci.*, 15:39–57, 2002.

S. Mahlburg Kay, V. Maksaev, R. Moscoso, C. Mpodozis, C. Nasi, and C. E. Gordillo. Tertiary Andean magmatism in Chile and Argentina between 28°S and 33°S: Correlation of magmatic chemistry with a changing Benioff zone. *J. South Am. Earth Sci.*, 1(1):21–38, 1988.

D. Mainprice, G. Barruol, and W. Ben Ismaïl. The Seismic Anisotropy of the Earth's Mantle: From Single Crystal to Polycrystal. In S.-I. Karato, A. M. Forte, R. C. Liebermann, G. Masters, and L. Stixrude, editors, *Earth's Deep Interior: Mineral Physics and Tomography From the Atomic to the Global Scale*, volume 117 of *Geophysical Monograph Series*, pages 237–264, 2000.

P. Mann, R. D. Rogers, and L. Gahagan. Overview of plate tectonic history and its unresolved tectonic problems (Chapter 8). In G. Alvarado and J. Buntschuh, editors, *Central America: Geology, Resources and Hazards*, volume 1, page 201, 2007.

J. S. Marshall, D. M. Fisher, and T. W. Gardner. Central Costa Rica deformed belt: Kinematics of diffuse faulting across the western Panama block. *Tectonics*, 19(3):468–492, June 2000.

J. Martinod, F. Funiciello, C. Faccenna, S. Labanieh, and V. Regard. Dynamical effects of subducting ridges: insights from 3-D laboratory models. *Geophys. J. Int.*, 163:1137–1150, 2005.

S. McGeary, A. Nur, and Z. Ben-Avraham. Spatial gaps in arc volcanism: the effect of collision or subduction of oceanic plateaus. *Tectonophysics*, 119:195–221, 1985.

B. McNulty and D. Farber. Active detachment faulting above the Peruvian flat slab. *Geology*, 30(6):567–570, June 2002.

M. Meschede. The impossible Galapagos connections: geometric constraints for a near-American origin of the Caribbean plate. *Geol. Rundschau*, 87:200–205, 1998.

M. Meschede and U. Barckhausen. Plate tectonic evolution of the Cocos-Nazca spreading center. In E. A. Silver, G. Kimura, and T. H. Shipley, editors, *Proceedings of the Ocean Drilling Programm, Scientific Results*, volume 170, 2000.

M. Meschede and U. Barckhausen. The relationship of the Cocos and Carnegie ridges: age constraints from paleogeographic reconstructions. *Int. J. Earth Sciences (Geol. Rundschau)*, 90: 386–392, 2001.

M. Meschede and W. Frisch. A plate-tectonic model for the Mesozoic and Early Cenozoic history of the Caribbean plate. *Tectonophysics*, 296:269–291, 1998.

M. Meschede, U. Barckhausen, and H. U. Worm. Extinct spreading on the Cocos Ridge. *Terra Nova*, 10:211–216, 1998.

W. Montero. Neotectónica de la región central de Costa Rica: Frontera oeste de la microplaca de Panamá. *Revista Geológica de América Central*, 24:29–56, 2001.

I. B. Morozov. Crustal Scattering and Some Artifacts in Receiver Function Images. *Bull. Seis. Soc. Am.*, 94(4):1492–1499, August 2004.

I. B. Morozov and K. G. Dueker. Signal-to-noise ratios of teleseismic receiver functions and effectiveness of stacking for their enhancement. *J. Geophys. Res.*, 108(B2):2106, 2003.

I. B. Morozov and H. Zheng. Effects of trench-zone scattering on receiver functions over a subduction zone: A 3-D finite-difference modelling study. *Tectonophysics*, 420:317–332, 2006.

J. Nakajima and A. Hasegawa. Shear-wave polarization anisotropy and subduction-induced flow in the mantle wedge of northeastern Japan. *Earth Planet. Sci. Lett.*, 225:365–377, 2004.

J. Nakajima, J. Shimizu, S. Hori, and A. Hasegawa. Shear-wave splitting beneath the southwestern Kurile arc and northeastern Japan arc: A new insight into mantle return flow. *Geophys. Res. Lett.*, 33, 2006.

A. Nur and Z. Ben-Avraham. Volcanic gaps due to oblique consumption of aseismic ridges. *Tectonophysics*, 99:355–362, 1983.

T. J. Owens and G. Zandt. The response of the continental crust-mantle boundary observed in broadband teleseismic receiver functions. *Geophys. Res. Lett.*, 12:705–708, 1985.

T. J. Owens, G. Zandt, and S. R. Taylor. Seismic evidence for an ancient rift beneath the Cumberland plateau, Tennessee: a detailed analysis of broadband teleseismic P waveforms. *J. Geophys. Res.*, 89:7783–7795, 1984.

M Pardo, D. Comte, and T. Monfret. Seismotectonic and stress distribution in the central Chile subduction zone. *J. South Am. Earth Sci.*, 15:11–22, 2002.

J. Park and Y. Yu. Anisotropy and coupled free oscillations: simplified models and surface wave observations. *Geophys. J. Int.*, 110(3):401–420, September 1992.

S. M. Peacock. Are the lower planes of double seismic zones caused by serpentine dehydration in subducting oceanic mantle. *Geology*, 29(4):299–302, April 2001.

M. Pérez-Gussinyé, A. R. Lowry, J. Phipps Morgan, and A. Tassara. Effective elastic thickness variations along the Andean margin and their relationship to subduction geometry. *Geochem. Geophys. Geosys.*, 9(2), February 2008.

J. Peterson. *Observations and modeling of seismic background noise*, pages 93–322. US Geological Survey, Albuquerque, NM, 1993.

R. A. Phinney. Structure of the Earth's crust from spectral behavious of long-period body waves. *J. Geophys. Res.*, 69(14):2997–3017, July 1964.

R. H. Pilger. Plate reconstructions, aseismic ridges, and low-angle subduction beneath the Andes. *Geol. Soc. Am. Bull.*, 92:448–456, July 1981.

J. L. Pindell, Cande. S. C., W. C. Pitman, III, D. B. Rowley, J. F. Dewey, J. Labreque, and W. Haxby. A plate-kinematic framework for models of Caribbean evolution. *Tectonophysics*, 155:121–138, 1988.

I. V. Pomeranceva, A. N. Mozzenko, Ch. Junge, and W. Lange. Die Methode 'Zemlja'-Ein neues Verfahren zur regionalen Untersuchung des Krustenbaues. *Z. Geologie*, 19(2):125–136, 1970.

M. Protti, F. Gündel, and K. McNally. The geometry of the Wadati-Benioff zone under southern Central America and its tectonic significance: results from a high-resolution local seismographic network. *Phys. Earth Planet. Int.*, 84:271–287, 1994.

M. Protti, F. Güendel, and K. McNally. Correlation between the age of the subducting Cocos plate and the geometry of the Wadati-Benioff zone under Nicaragua and Costa Rica. In P. Mann, editor, *Geologic and Tectonic Development of the Caribbean Plate Boundary in Southern Central America*, number 295 in Geol. Soc. Am. Spec. Papers, pages 309–326. Boulder, Colorado, 1995.

R. Quintero and E. Kissling. An improved P-wave velocity reference model for Costa Rica. *Geofis. Int.*, 40:3–19, 2001.

D. S. Ramesh, H. Kawakatsu, S. Watada, and X. Yuan. Receiver function images of the Central Chugoku region in the Japanese islands using Hi-net data. *Earth Planets Space*, 57:271–280, 2005.

V. A. Ramos, E. O. Cristallini, and D. J. Pérez. The Pampean flat-slab of the Central Andes. *J. South Am. Earth Sci.*, 15:59–78, 2002.

C. R. Ranero and R. von Huene. Subduction erosion along the Middle America convergent margin. *Nature*, 404:748–752, April 2000.

C. R. Ranero, A. Villaseñor, J. Phipps Morgan, and W. Weinrebe. Relationship between bend-faulting at trenches and intermediate-depth seismicity. *Geochem. Geophys. Geosys.*, 6(12), 2005.

G. Rosenbaum, D. Giles, M. Saxon, P. G. Betts, R. F. Weinberg, and C. Duboz. Subduction of the Nazca Ridge and the Inca Plateau: Insights into the formation of ore deposits in Peru. *Earth Planet Sci. Lett.*, 239:18–32, 2005.

L. H. Ruepke, J. Phipps Morgan, M. Hort, and J. A. D. Connolly. Are the regional variations in Central American arc lavas due to different basaltic versus peridotitic slab sources of fluids? *Geology*, 30(11):1035–1038, November 2002.

L. H. Rüpke, J. Phipps Morgan, M. Hort, and J. A. D. Connolly. Serpentine and the subduction zone water cycle. *Earth Planet. Sci. Lett.*, 223:17–34, 2004.

R. M. Russo and P. G. Silver. Trench-Parallel Flow Beneath the Nazca Plate from Seismic Anisotropy. *Science*, 263:1105–1111, February 1994.

T. Ryberg and M. Weber. Receiver function arrays: a reflection seismic approach. *Geophys. J. Int.*, 141:1–11, 2000.

V. Sallarès, Ph. Charvis, E. R. Flueh, and J. Bialas. Seismic structure of Cocos and Malpelo Volcanic Ridges and implications for hot spot-ridge interactions. *J. Geophys. Res.*, 108(B12): 2564, 2003.

M. K. Savage. Seismic anisotropy and mantle deformation: What have we learned from shear wave splitting? *Reviews Geophys.*, 37(1):65–106, February 1999.

SFB 574 Progress Report (Phase 1). *SFB574 Progress Report (Phase 1)*, 2003.

L. L. Siame, O. Bellier, M. Sébrier, and M. Araujo. Deformation partitioning in flat subduction setting: Case of the Andean foreland of western Argentina (28°S-33°S). *Tectonics*, 24, 2005.

F. Sodoudi. *Lithospheric structure of the Aegean obtained from P and S receiver functions.* PhD thesis, Freie Universität Berlin, Germany, 2005.

K. Stammler, R. Kind, N. Petersen, G. Kosarev, L. Vinnik, and Q. Liu. The upper mantle discontinuities: Correlated or anticorrelated? *Geophys. Res. Lett.*, 19:1563–1566, 1992.

A. U. Stavenhagen. *Refraktionsseismische Untersuchungen on- und offshore Costa Rica.* PhD thesis, Christian-Albrechts-Universität zu Kiel, Germany, 1998.

A. U. Stavenhagen, E. R. Flueh, C. Ranero, K. D. McIntosh, T. Shipley, G. Leandro, A. Schulze, and J. J. Dañobeitia. Seismic wide-angle investigations in Costa Rica – a crustal velocity model from the Pacific to the Caribbean coast. *Zbl. Geol. Paläont Teil I*, 3-6:393–408, September 1998.

G. Suárez, M. Pardo, J. Domínguez, L. Ponce, W. Montero, I. Boschini, and W. Rojas. The Limón, Costa Rica earthquake of April 22, 1991: Back-arc thrusting and col'lisional tectonics in a subduction environment. *Tectonics*, 14(2):518–530, April 1995.

A. Tassara, H.-J. Götze, S. Schmidt, and R. Hackney. Three-dimensional density model of the Nazca plate and the Andean continental margin. *J. Geophys. Res.*, 111, 2006.

J. van Hunen, A. P. van den Berg, and N. J. Vlaar. On the role of subducting oceanic plateaus in the development of shallow flat subduction. *Tectonophysics*, 352:317–333, 2002.

J. van Hunen, A. P. van den Berg, and N. J. Vlaar. Various mechanisms to induce present-day shallow flat subduction and implications for the younger Earth: a numerical parameter study. *Phys. Earth Planet. Int.*, 146:179–194, 2004.

P. Vannucchi, D. W. Scholl, M. Meschede, and K. McDougall-Reid. Tectonic erosion and consequent collapse of the Pacific margin of Costa Rica: Combined implications from ODP Leg 170, seismic offshore data, and regional geology of the Nicoya Peninsula. *Tectonics*, 20(5):649–668, 2001.

P. Vannucchi, C. R. Ranero, S. Galeotti, S. M. Straub, D. W. Scholl, and K. McDougall-Ried. Fast rates of subduction erosion along the Costa Rica Pacific margin: Implications for nonsteady rates of crustal recycling at subduction zones. *J. Geophys. Res.*, 108(B11), 2003.

L. P. Vinnik. Detection of waves converted from P to SV in the mantle. *Phys. Earth Planet. Int.*, 15:294–303, 1977.

P. R. Vogt. Subduction and Aseismic Ridges. *Nature*, 241:189–191, January 1973.

R. von Huene and D. W. Scholl. Observations at convergent margins concerning sediment subduction, subduction erosion, and the growth of continental crust. *Reviews of Geophysics*, 29: 279–316, 1991.

R. von Huene, C. R. Ranero, W. Weinrebe, and K. Hinz. Morphotectonics of the Pacific convergent margin of Costa Rica. In P. Mann, editor, *Geologic and Tectonic Development of the Caribbean Plate Boundary in Southern Central America*, number 295 in Geol. Soc. Am. Spec. Papers, pages 291–307. Boulder, Colorado, 1995.

R. von Huene, J. Corvalán, E. R. Flueh, K. Hinz, J. Korstgard, C. R. Ranero, W. Weinrebe, and the CONDOR Scientists. Tectonic control of the subducting Juan Fernández Ridge on the Andean margin near Valparaiso, Chile. *Tectonics*, 16(3):474–488, June 1997.

R. von Huene, C. R. Ranero, W. Weinrebe, and K. Hinz. Quaternary convergent margin tectonics of Costa Rica, segmentation of the Cocos Plate, and Central American volcanism. *Tectonics*, 19(2):314–334, 2000.

Ch. H. E. Walther. The crustal structure of the Cocos ridge of Costa Rica. *J. Geophys. Res.*, 108(B3):2136, 2003.

R. Werner, K. Hoernle, U. Barckhausen, and F. Hauff. Geodynamic evolution of the Galápagos hot spot system (Central East Pacific) over the past 20 m.y.: Constraints from morphology, geochemistry, and magnetic anomalies. *Geochem. Geophys. Geosys.*, 4(12):1108, December 2003.

R. Weyl. *Geology of Central America*. Number 15 in Beiträge zur regionalen Geologie der Erde. Borntraeger, Berlin, 1980.

I. Wölbern. *Spuren des Plumes und Strukturen des oberen Mantels unter Hawaii abgeleitet aus konvertierten Wellen*. PhD thesis, Freie Universität Berlin, Germany, Scientific Technical Report STR04/05, 2003.

G. Yañez, J. Cenbrano, M. Pardo, C. Ranero, and D. Selles. The Challenger-Juan Fernández-Maipo major tectonic transition of the Nazca-Andean subduction system 33-34°S: geodynamic evidence and implication. *J. South Am. Earth Sci.*, 15:23–38, 2002.

G. A. Yañez, C. R. Ranero, R. von Huene, and J. Díaz. Magnetic anomaly interpretation across the southern central Andes (32○-34○S): The role of the Juan Fernández Ridge in the late Tertiary evolution of the margin. *J. Geophys. Res.*, 106(B4):6325–6345, 2001.

X. Yuan. *Teleseismic Receiver Function Study and Its Application in Tibet and the Central Andes*. PhD thesis, Freie Universität Berlin, Germany, Scientific Technical Report STR00/10, 1999.

X. Yuan, R. Kind, J. Mechie, and E. Sandvol. Lithospheric and upper mantle structure of southern Tibet from seismological passive source experiment. *J. Geophys. Res.*, 102:27491–27500, 1997.

X. Yuan, S. V. Sobolev, R. Kind, O. Oncken, G. Bock, G. Asch, B. Schurr, F. Graeber, A. Rudloff, W. Hanka, K. Wylegalla, R. Tibi, C. Haberland, A. Rietbrock, P. Giese, P. Wigger, P. Röwer, G. Zandt, S. Beck, T. Wallace, M. Pardo, and D. Comte. Subduction and collision processes in the Central Andes constrained by converted seismic phases. *Nature*, 408:958–961, December 2000.

S. Zhang and S.-I. Karato. Lattice preferred orientation of olivine aggregates deformed in simple shear. *Nature*, 375:774–777, June 1995.

S. Zhang, S.-I. Karato, F. Fitz Gerald, U. H. Faul, and Y. Zhou. Simple shear deformation of olivine aggregates. *Tectonophysics*, 316(1-2):133–152, January 2000.

List of Figures

List of Tables

169

Appendix A

Station Coordinates

station nr.	station name	latitude	longitude	height [m]
crt-02	Dominical	09°15.972	−83°51.547	0
crt-03	Tres Ríos	09°17.947	−83°48.311	415
crt-04	Alto San Juan	09°20.021	−83°44.131	828
crt-05	Miravalles	09°24.946	−83°40.747	1014
crt-06	San José de Rivas	09°26.687	−83°38.189	1205
crt-07	Los Ángeles	09°27.526	−83°35.095	1479
crt-08	Río Blanco	09°29.912	−83°36.733	1758
crt-11	Pejibaye	09°47.934	−83°41.906	728
crt-13	San Antonio Arriba	09°47.846	−83°33.774	1038
crt-14	Guineal	09°50.282	−83°31.743	955
crt-15	Moravia	09°48.878	−83°27.776	1223
crt-21	Río Orosi	09°46.376	−83°47.378	1572
crt-23	Jaular	09°39.682	−83°52.000	2398
crt-25	Alaska	09°31.279	−83°39.790	1585
crt-26	Cimarrones	10°04.777	−83°25.908	225
crt-27	Tres Equis	09°57.287	−83°33.645	613
crt-31	Guápiles	10°07.100	−83°48.650	700
crt-32	Guayabo Arriba	09°59.156	−83°43.228	1602
crt-33	La Esperanza	10°14.744	−83°56.036	1000
crt-34	Virgen del Socorro	10°16.020	−84°09.930	1642
L	Limón	09°59.765	−83°05.657	29
P	Poás	10°10.504	−84°14.932	2493
Q	Quepos	09°23.512	−84°07.436	55

Table A.1: *Coordinates of the Talamanca Transect stations and ETH Zürich stations included in the analysis*

station code	latitude	longitude	height [m]
con	09°35.12	−84°03.20	1350
cts	09°30.36	−84°06.20	66
dom	09°15.94	−83°51.55	44
gua	09°20.47	−83°50.32	168
man	09°22.89	−84°08.57	41
mat	09°20.05	−83°56.32	156
nar	09°35.32	−83°56.48	1622
rse	09°34.64	−84°13.03	156
sav	09°27.48	−83°58.57	193
sbl	09°25.80	−84°03.56	65
scy	09°37.09	−84°07.72	1471
sva	09°26.51	−83°50.80	736
pro	09°33.37	−83°51.65	1828
vue	09°31.87	−84°16.78	38

Table A.2: *Coordinates of the Quepos network land-stations included in the analysis*

Appendix B

Time Corrections for Talamanca Transect Stations

crt–02
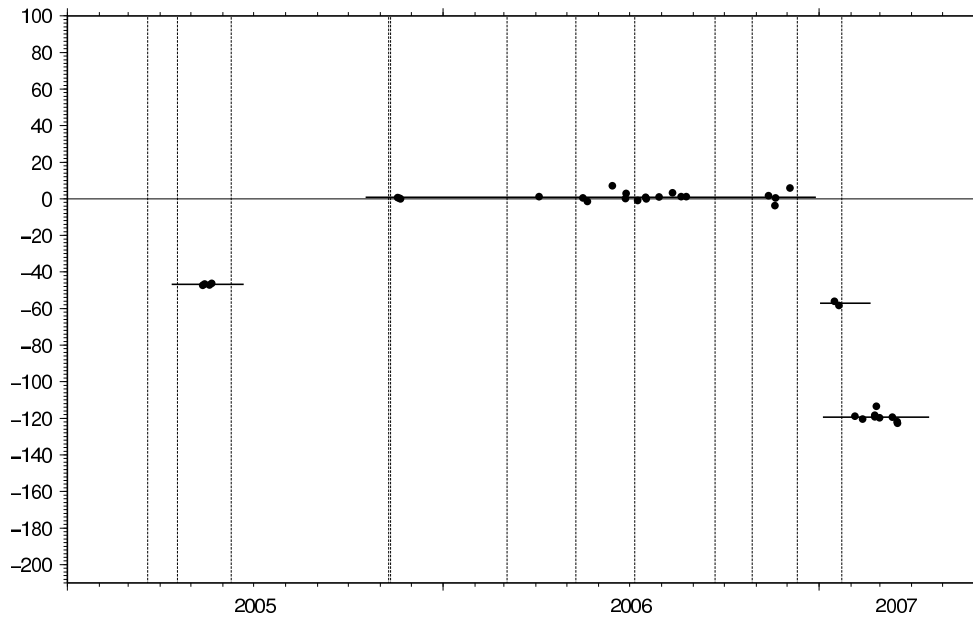
crt–07
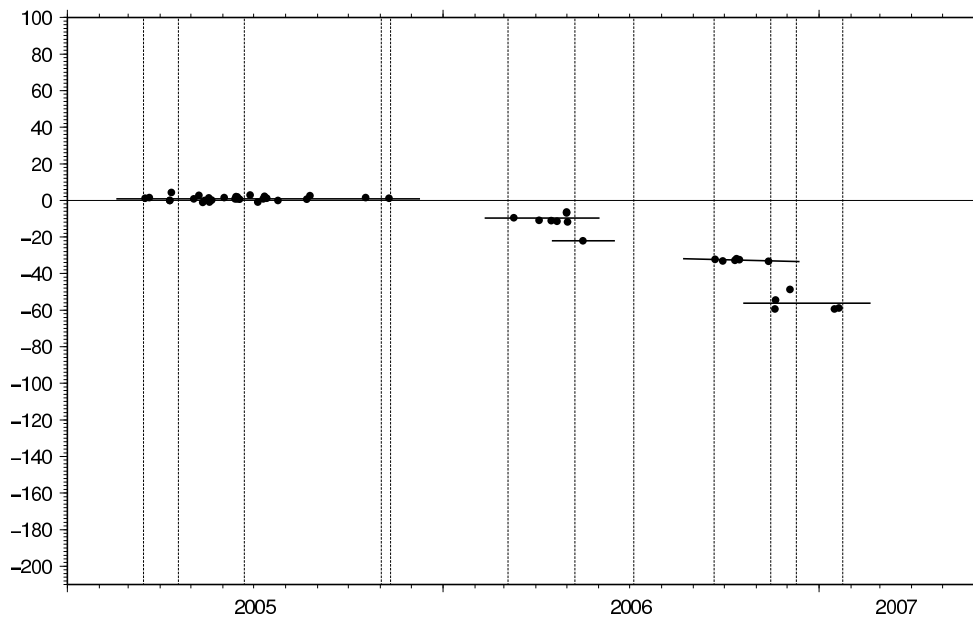
crt–08
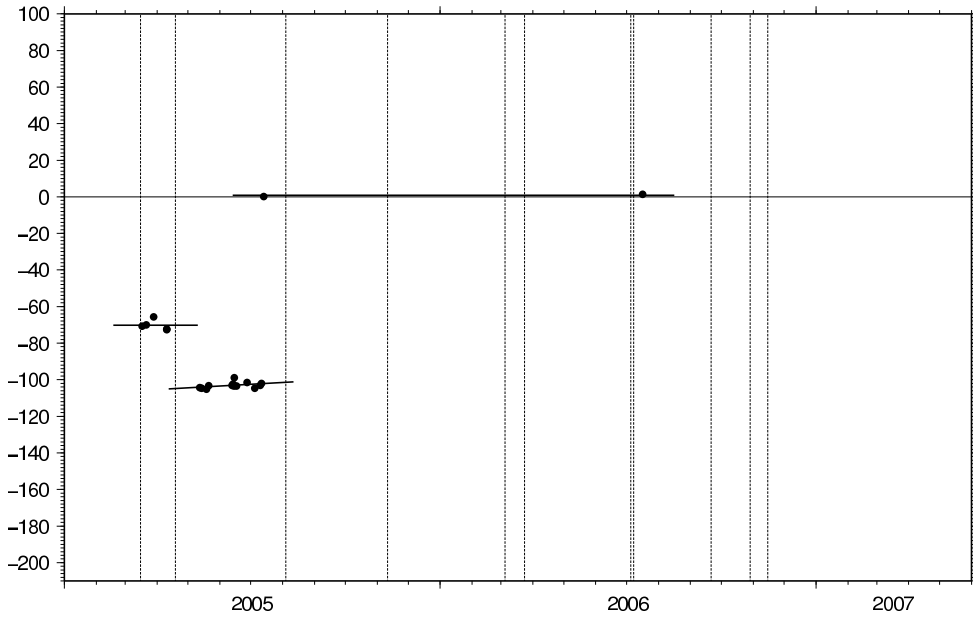
crt–13
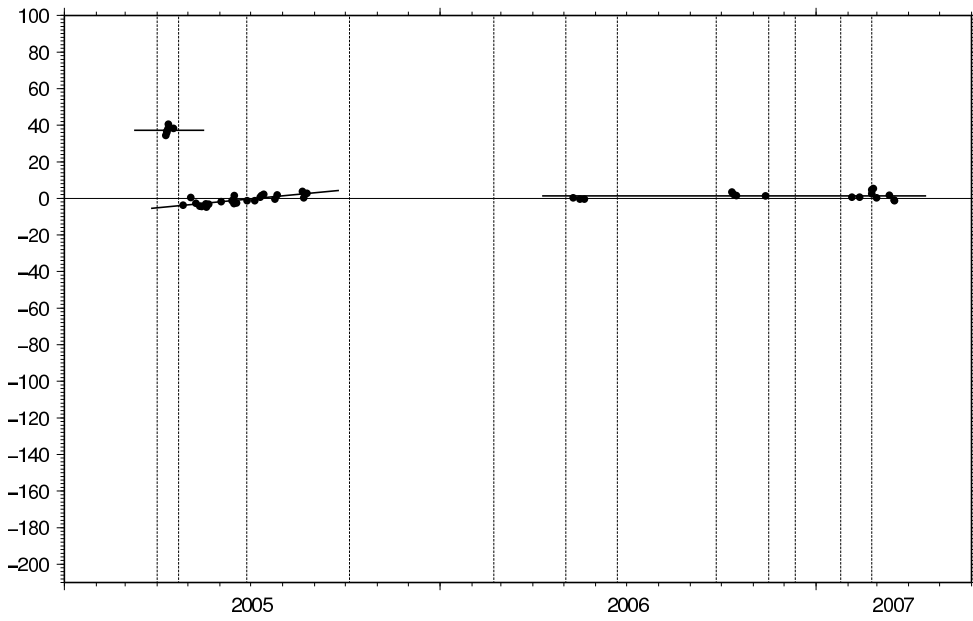
crt−15
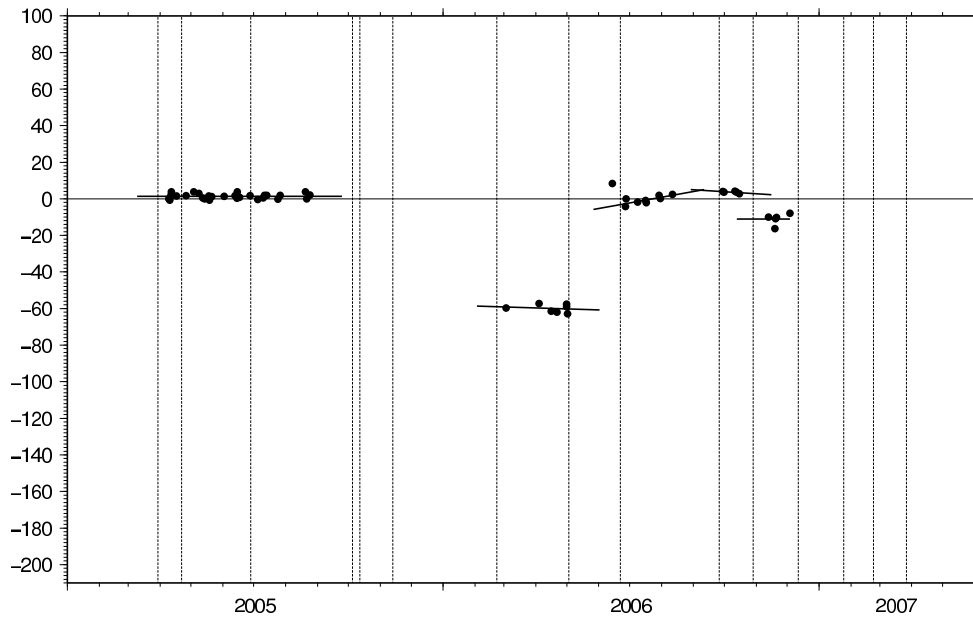
crt−21
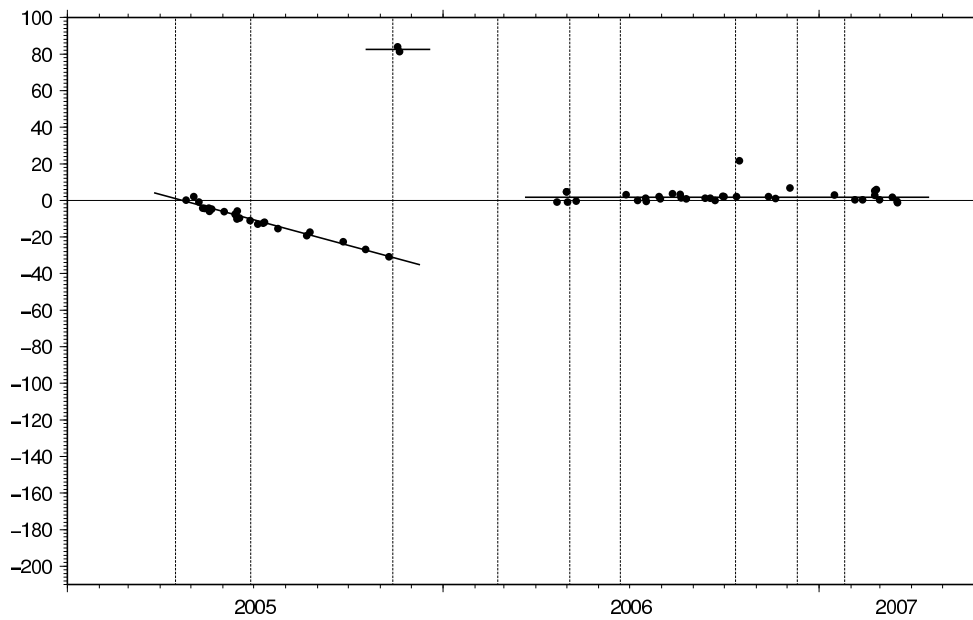
crt–23
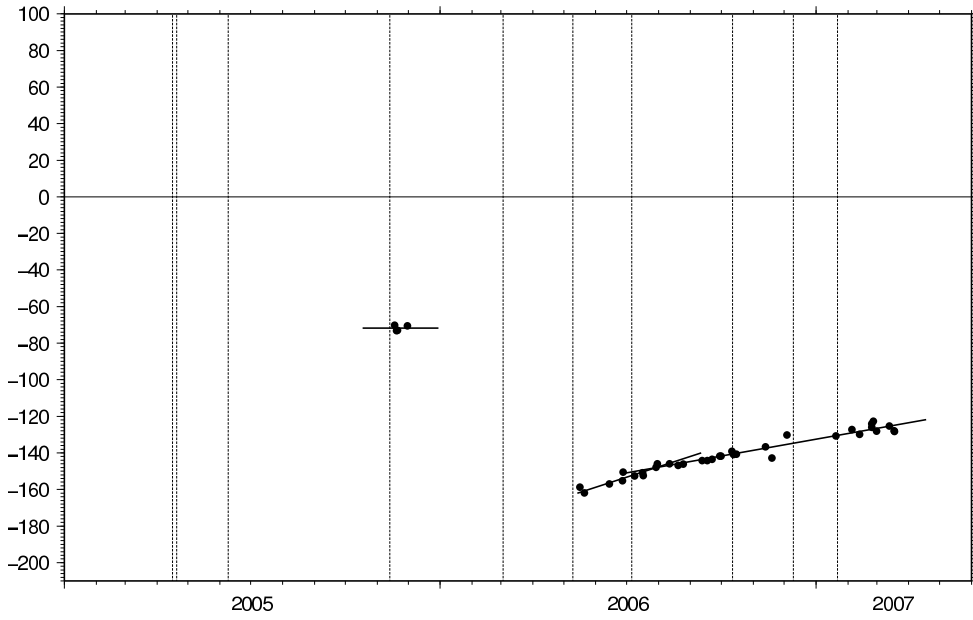
crt–25
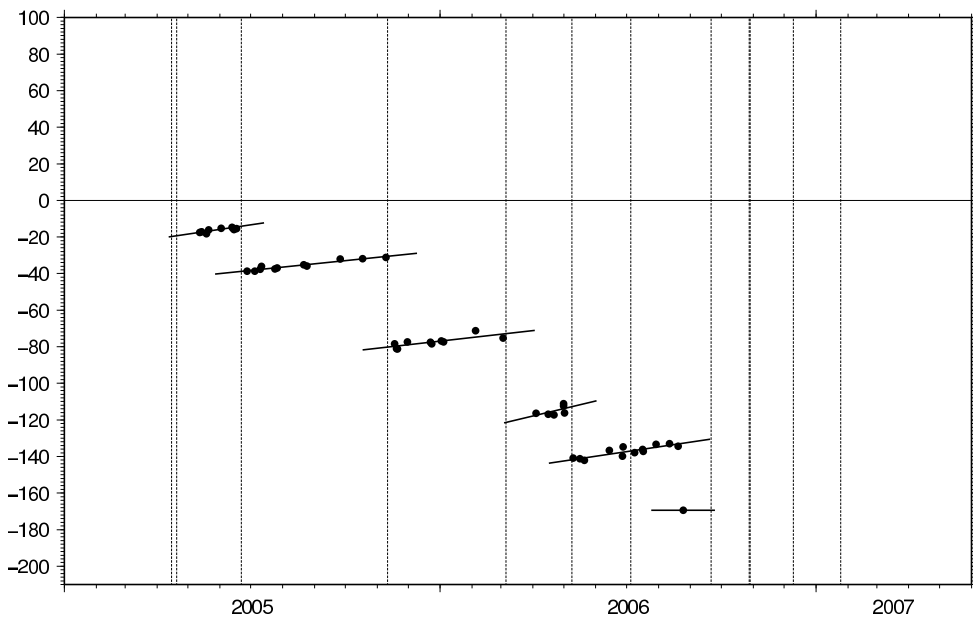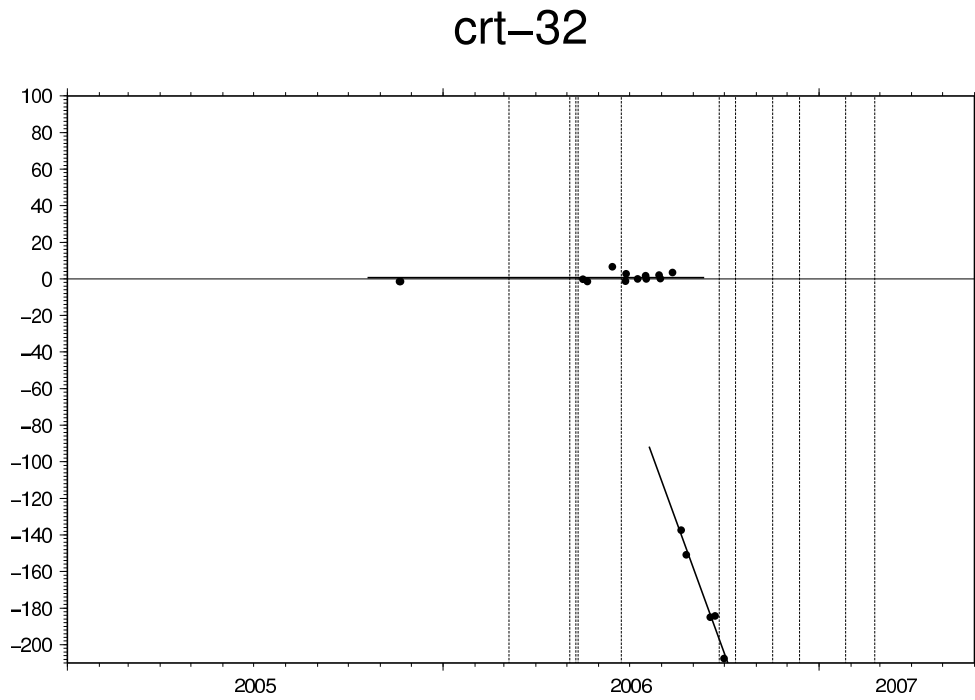
Figure B.1: *Time shifts of Talamanca Transect stations with non-negligible timing error. The time shifts (in seconds) are determined from the difference between the observed onset of a teleseismic event and its predicted onset for each given station. Vertical lines mark the dates when maintenance visits were made; the time shift is piecewise linearly interpolated in these intervals.*

Appendix C

Transverse Components – Low-frequency Migrated Profiles
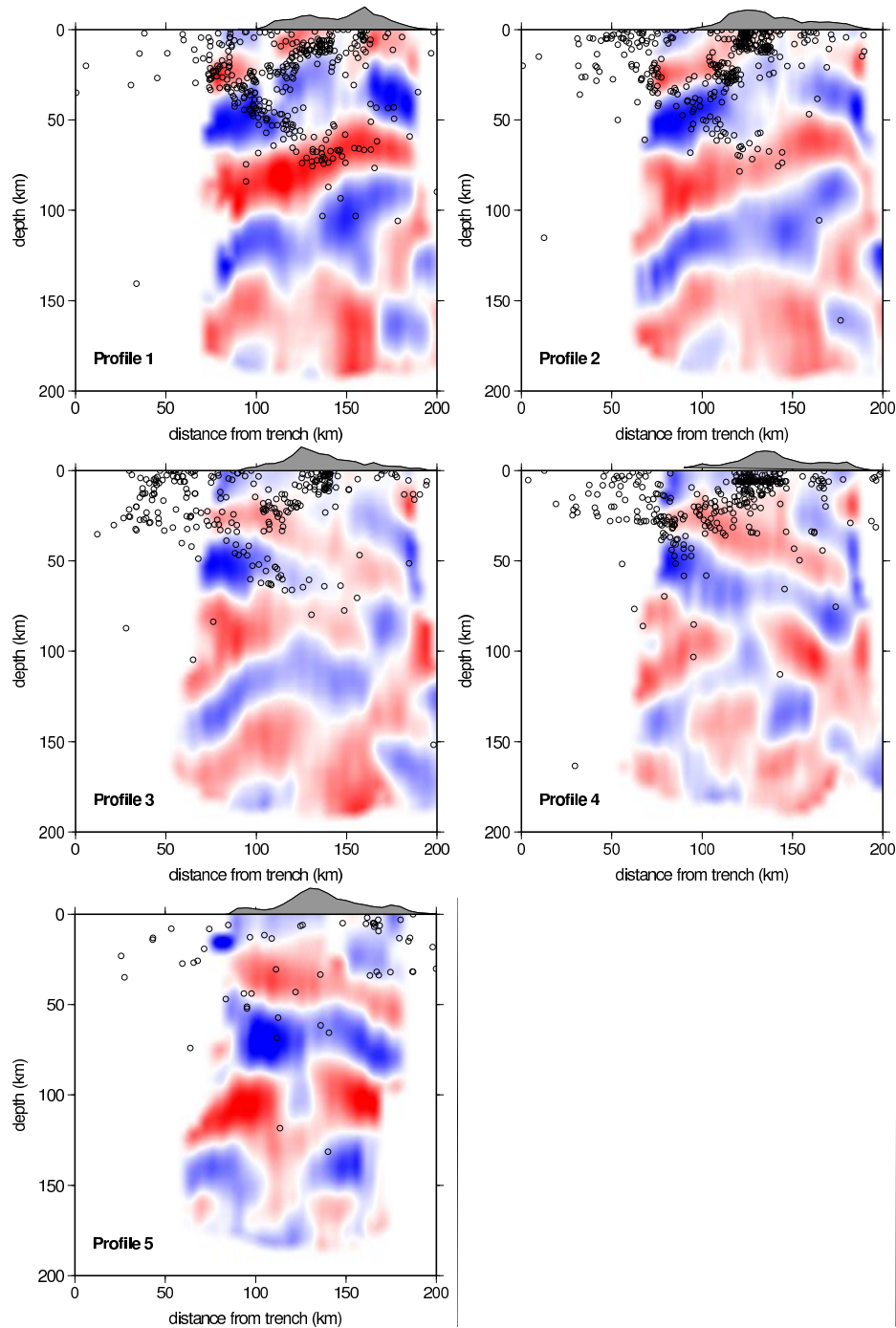
Figure C.1: *Low-frequency transverse receiver function profiles through the migration volume. Receiver functions were low-pass filtered below 5 s before migration. Red amplitudes denote positive conversion, blue amplitudes negative conversions. Upper left: profile 1 (in the north-west), lower left: profile 5 (in the south-east). The migrated section were smoothed with a 20 km Gaussian filter before plotting. The topography is overlain in grey, with an amplification factor 4. Black circles indicate earthquake epicenters observed by the Quepos network.*

Appendix D

Comparison of Earthquake Recordings for Talamanca Transect and Quepos Network

Figure D.1 compares an earthquake recorded by the Talamanca Transect station crt-02 (Dominical) with an earthquake recorded by the Quepos network station dom, at the same site. The networks were installed without temporal overlap, so different events had to be chosen:

	date	latitude	longitude	depth	magnitude
Talamanca	08 Jul 2006	51.210	-179.31	22	6.6
Quepos	07 Nov 2002	51.200	179.33	33	6.6

The difference between the recordings is mainly due to the fact that the Talamanca Transect consisted of broad-band seismometers, whereas the Quepos stations were short-period stations with a cut-off frequency of 1 Hz. Therefore, the Quepos stations cannot give a good picture of the deeper structure, because this is best resolved at long frequencies; shorter periods are strongly disrupted by noise. On the other hand, the shallow structure can be imaged by the Quepos network.

It should be kept in mind that the Quepos network was installed with the aim to observe local seismicity. For receiver functions, normally events from epicentral distances larger than 30° are used. The farther the earthquake, the more will the high-frequency content be attenuated by the passage through the earth. Therefore, we are faced with the problem that the distant earthquakes can best be observed in low frequencies, which the Quepos network is incapable of. Therefore, the number of usable events is small and the signal-to-noise ratio is low. Hence, while the Quepos stations can be used to complement the Talamanca Transect observations and better resolve the crustal structure, their quality is certainly worse than that of the Talamanca Transect data set and is only reliable where the two observations are in agreement.
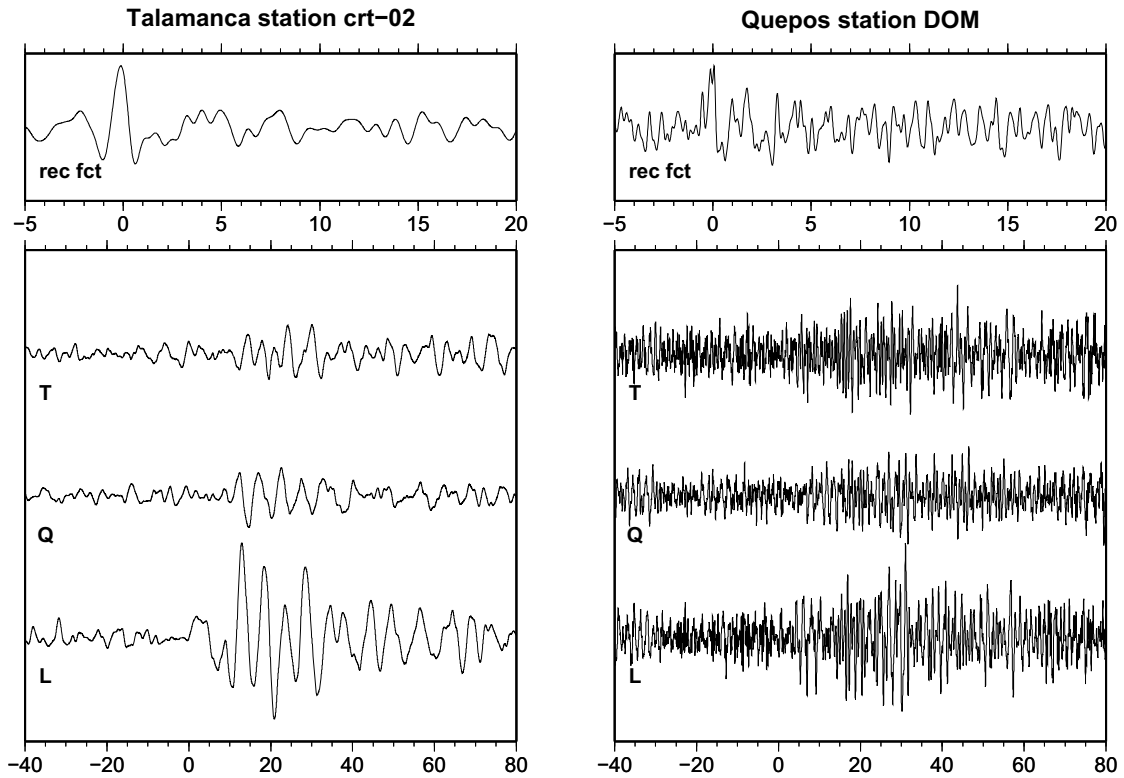
Figure D.1: *Comparison of Talamanca Transect and Quepos network recordings at station Dominical (crt-02 or dom, respectively). Lower panel: L,Q,T components after filtering, restitution and rotation. Upper panel: radial receiver function.*

Appendix E

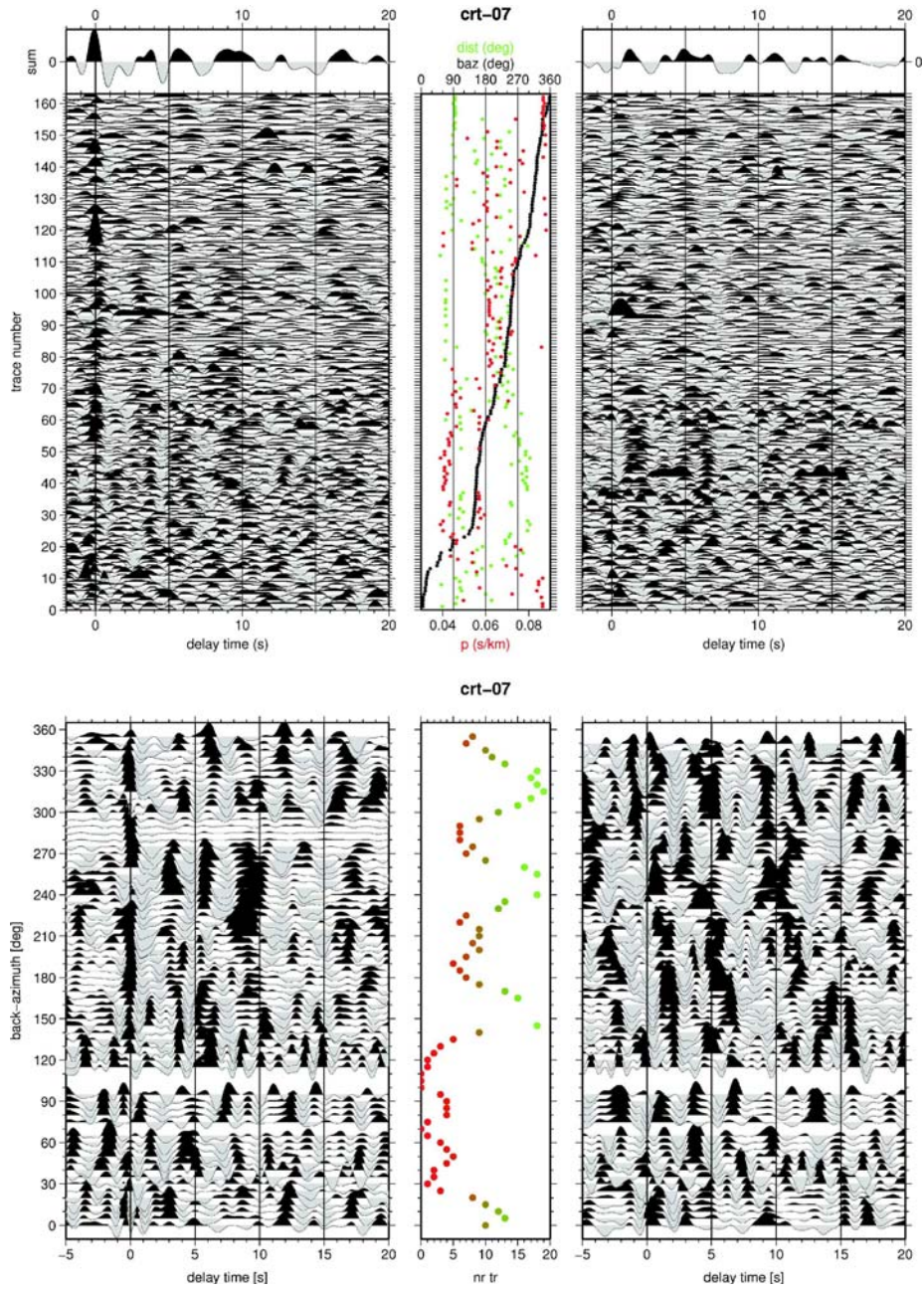# Azimuthal Behaviour of Talamanca Transect Receiver Functions

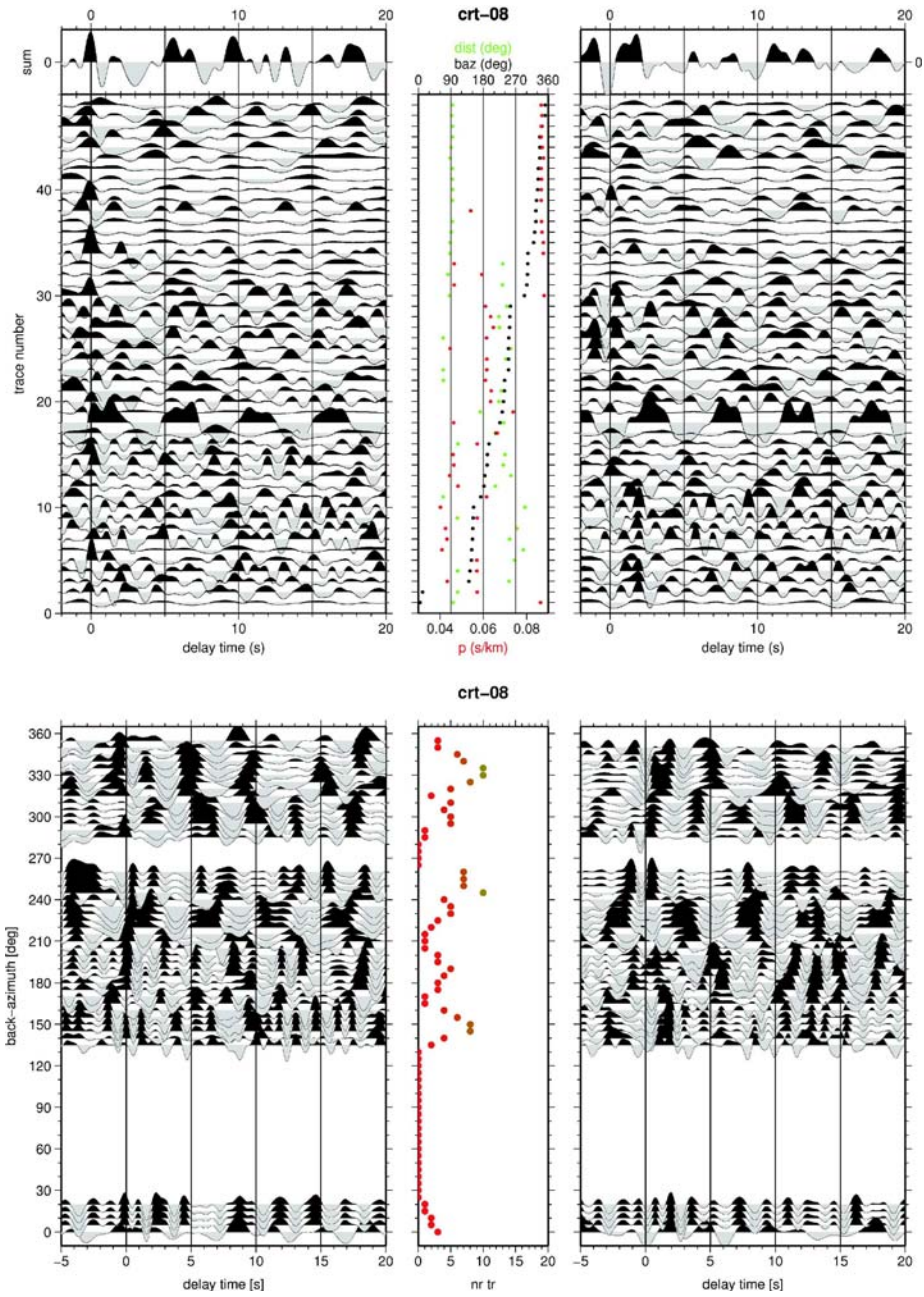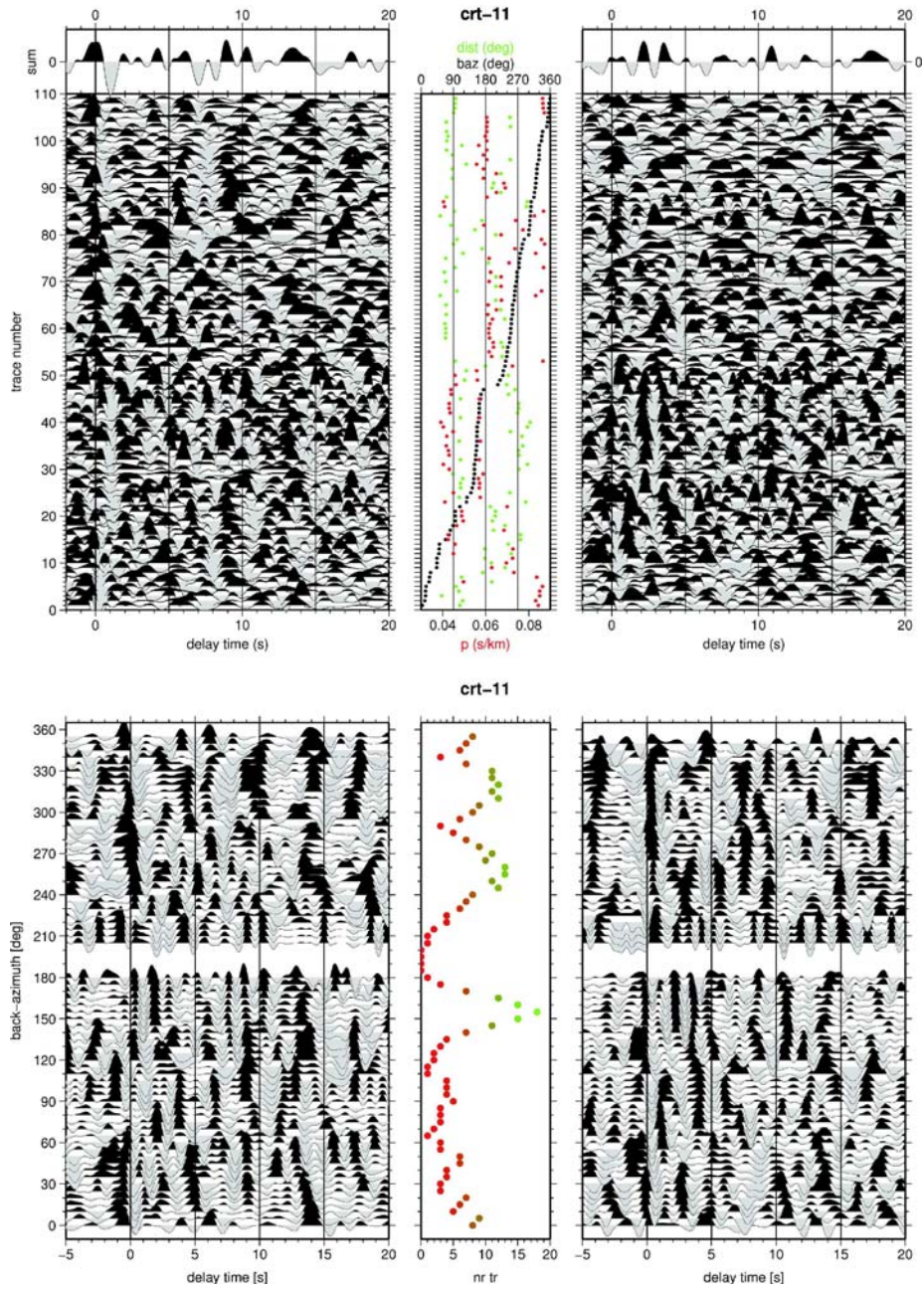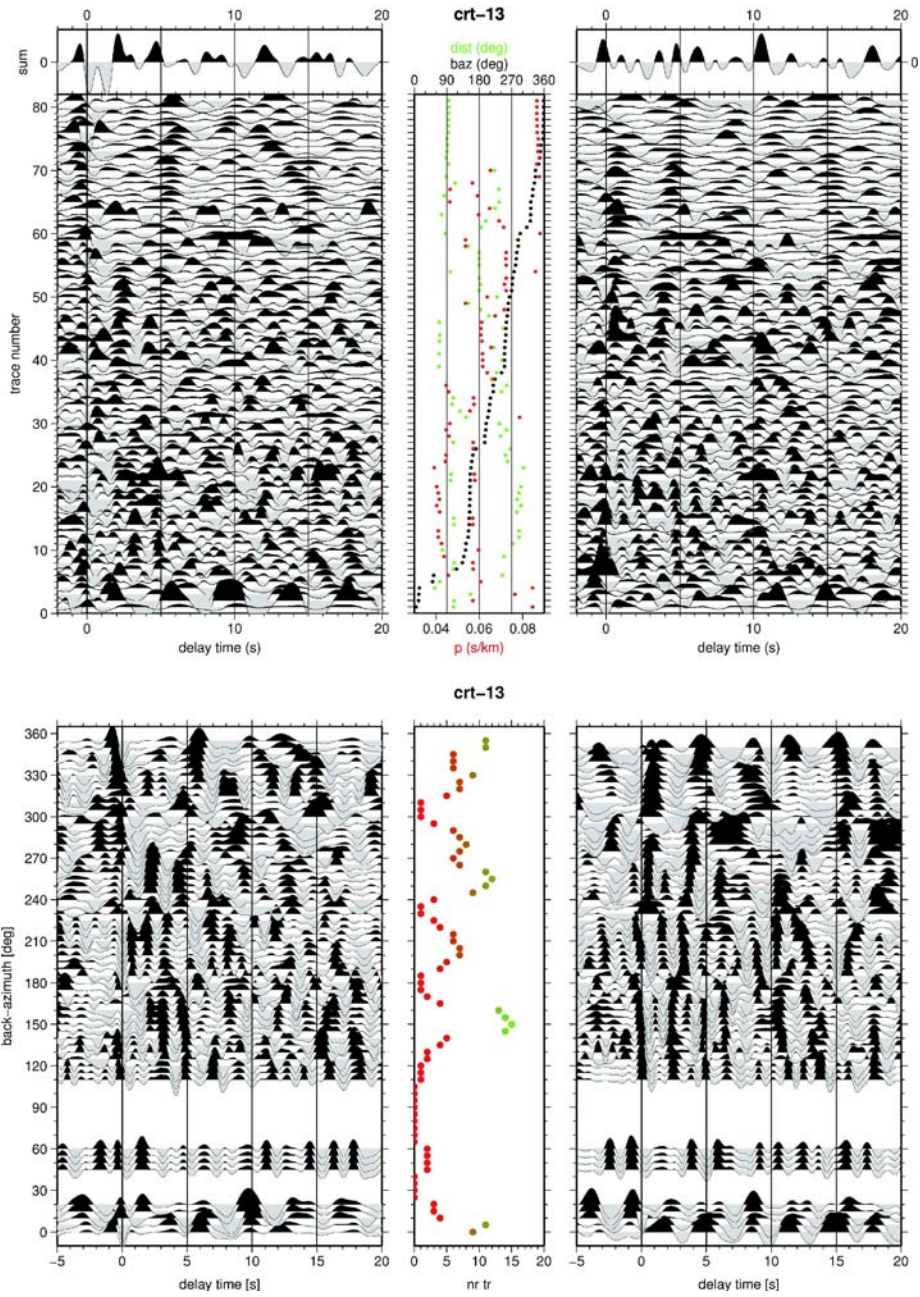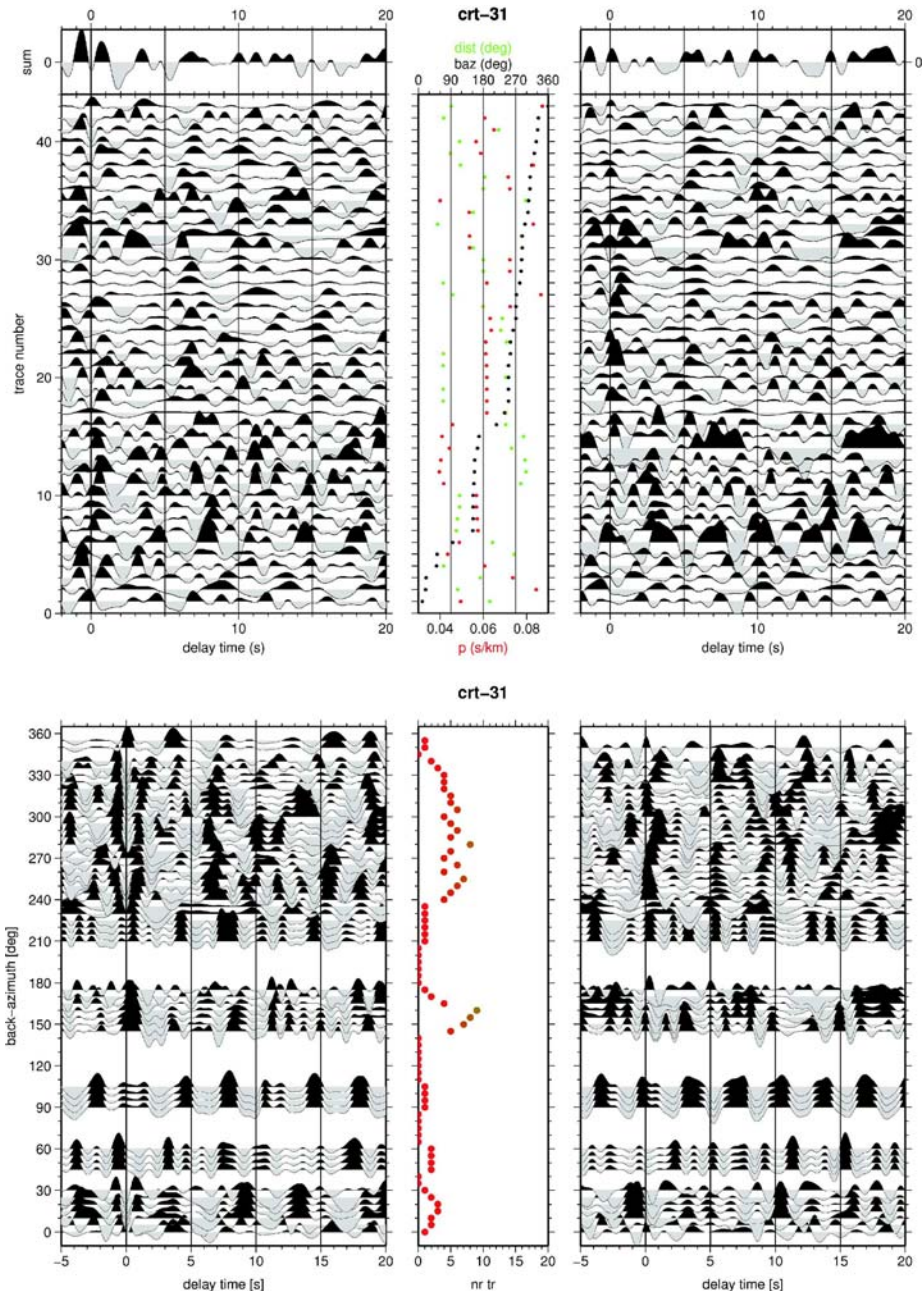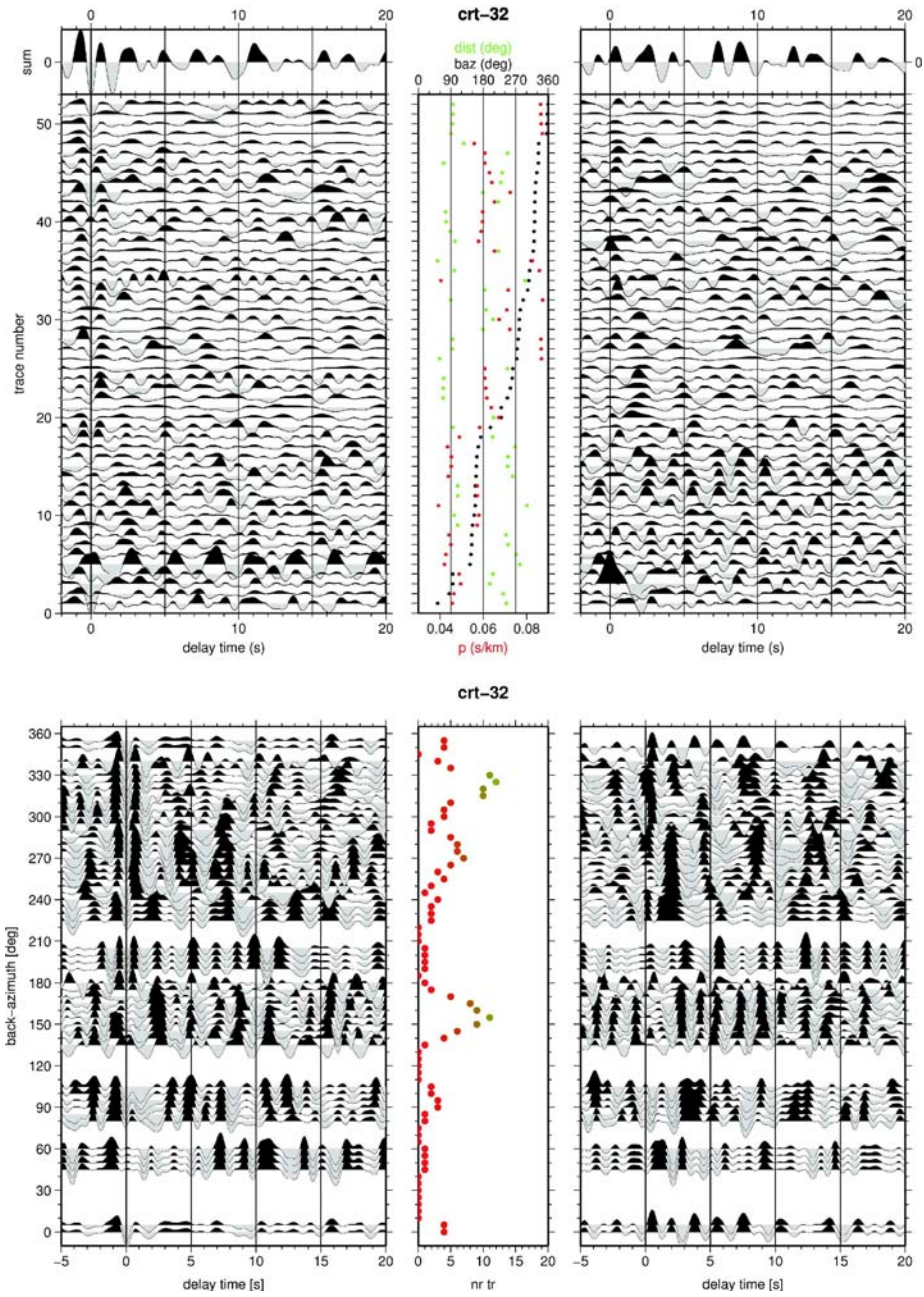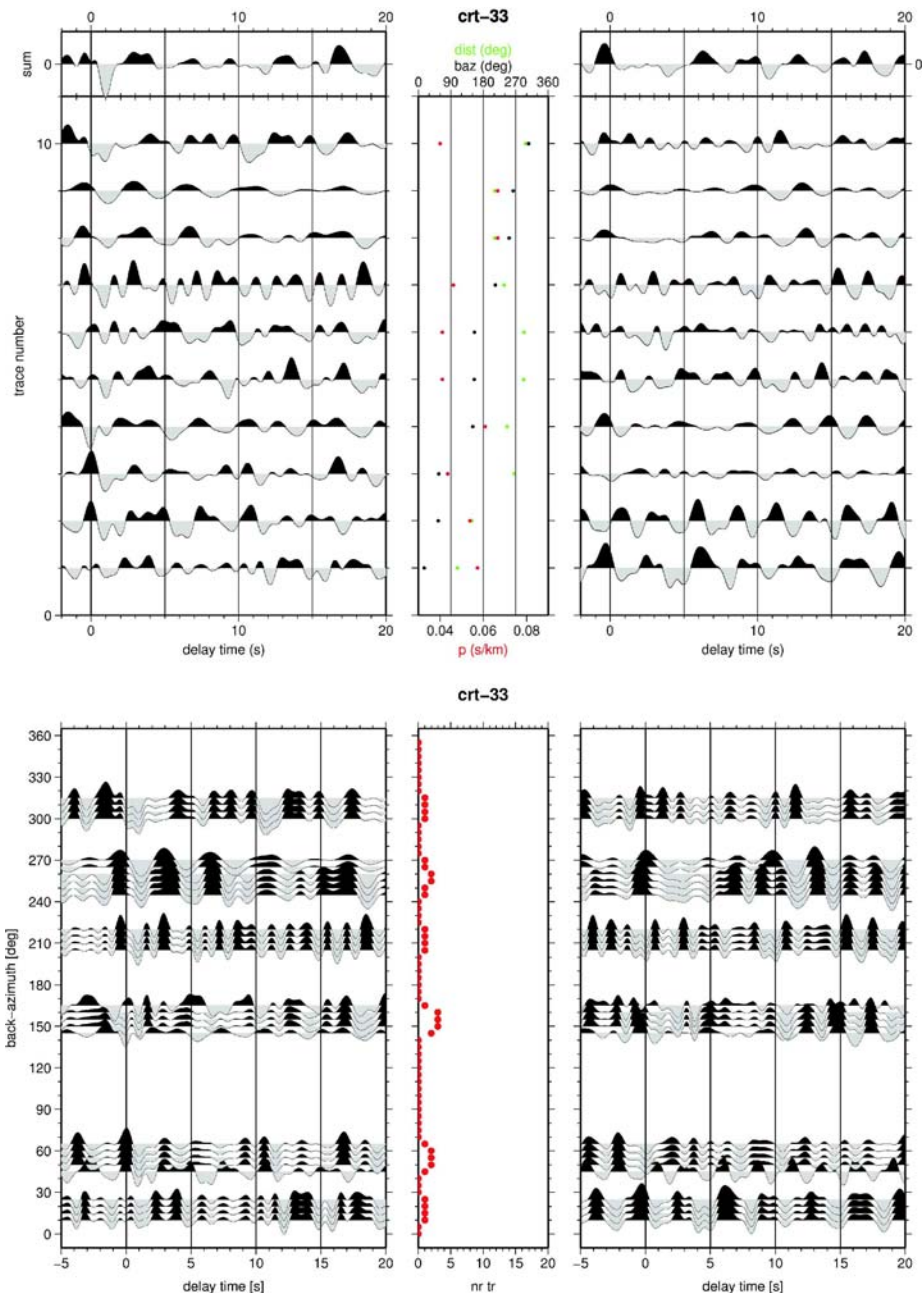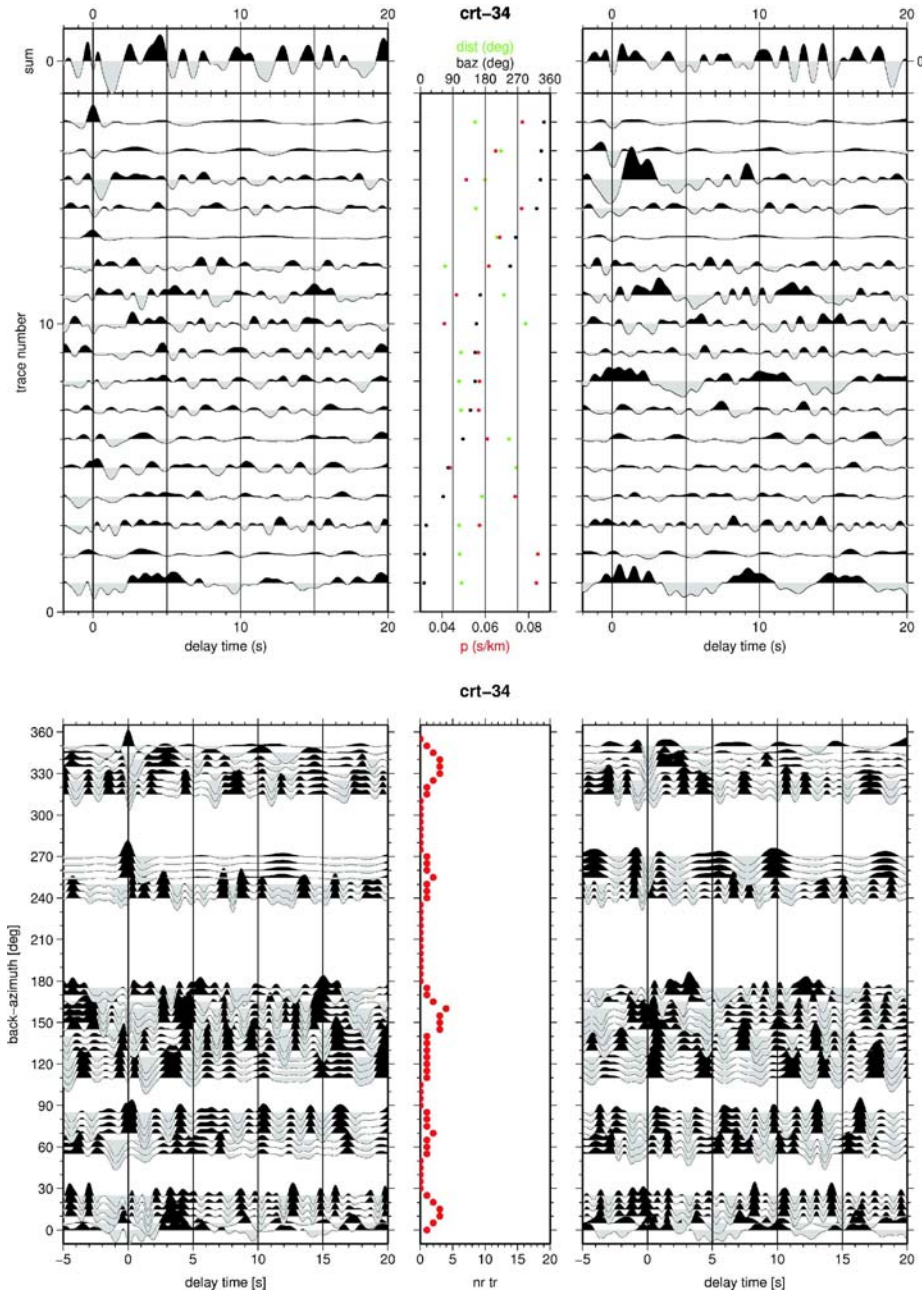crt–02

crt–02

crt–08

crt–08

crt–33

crt–33
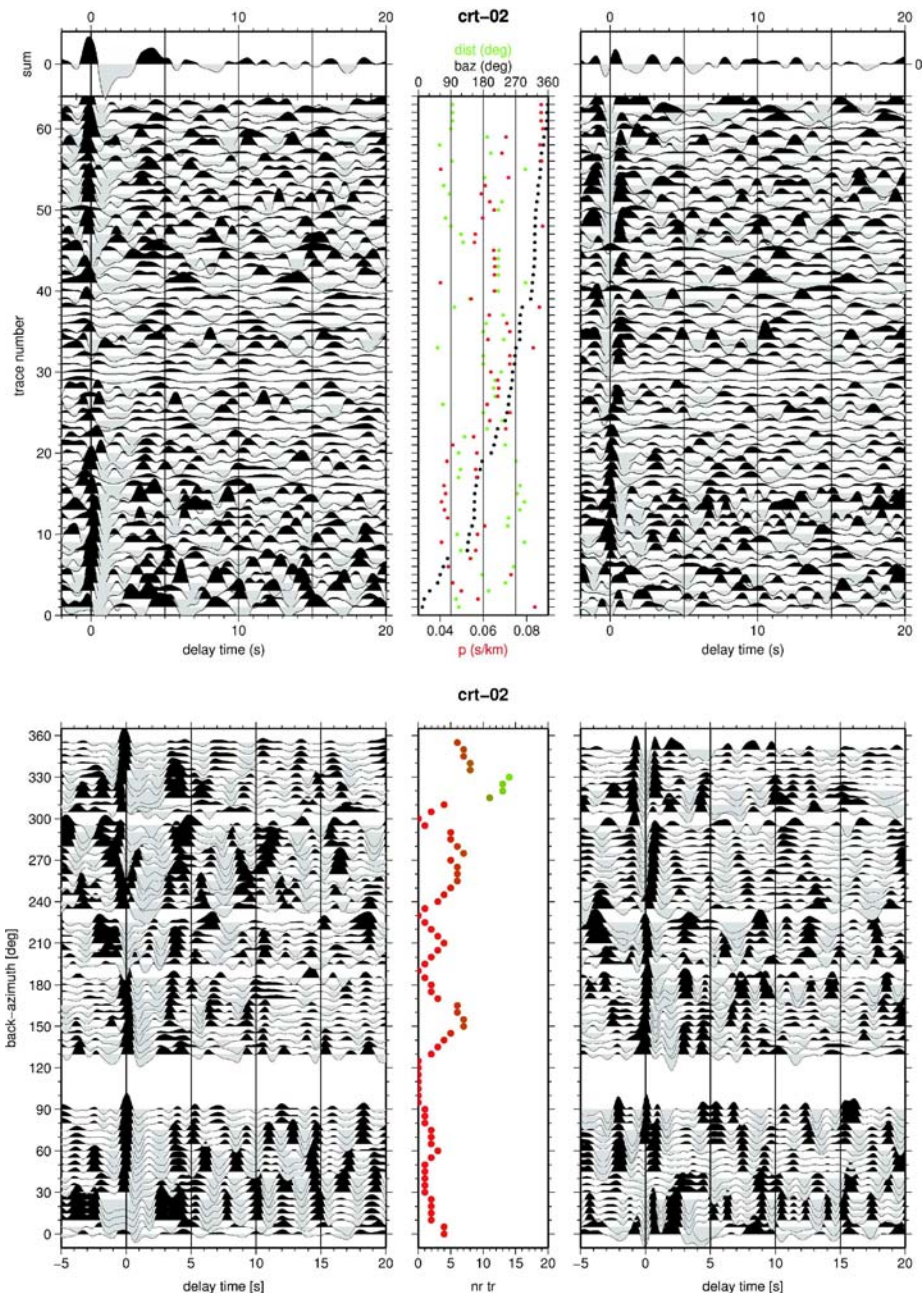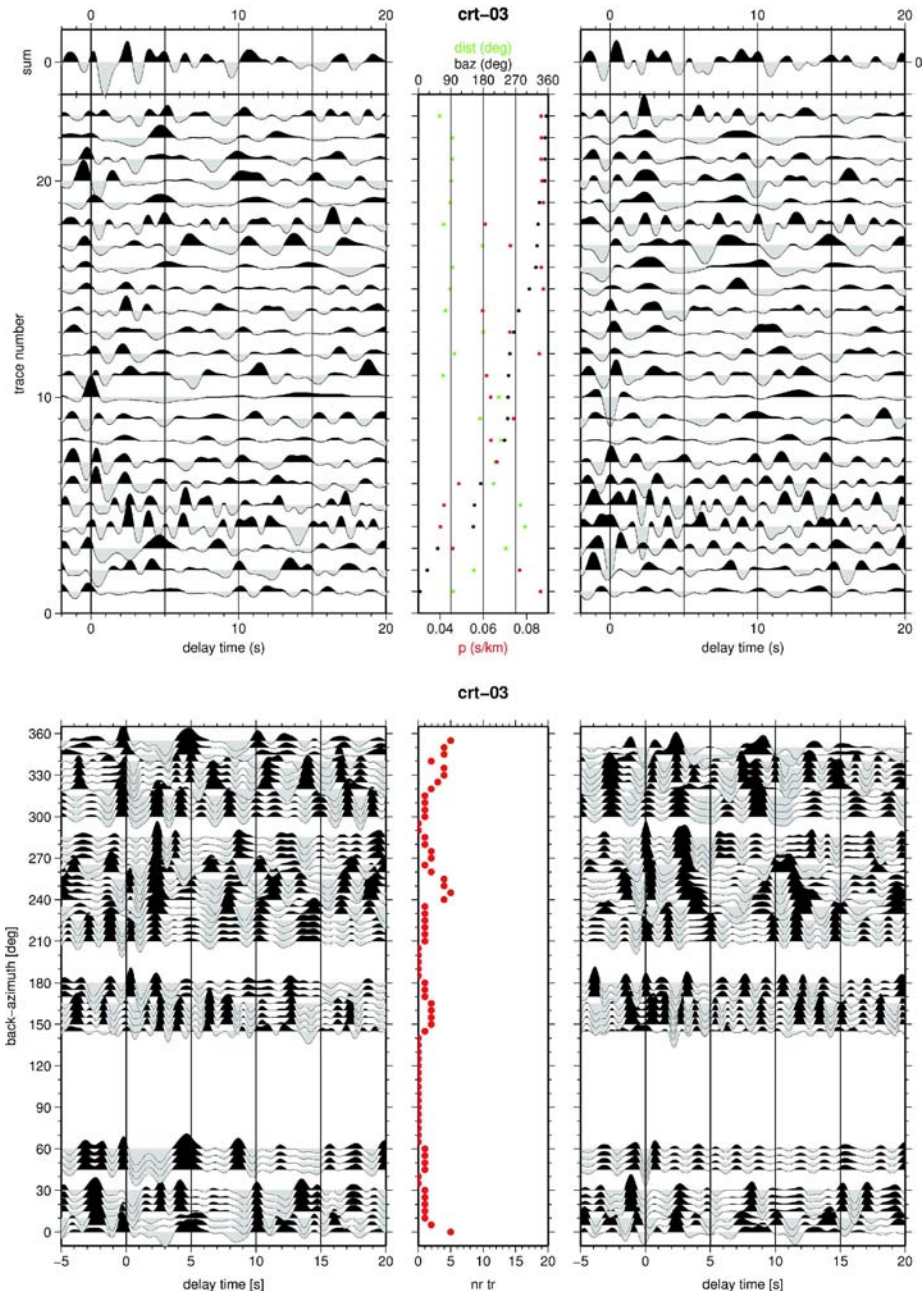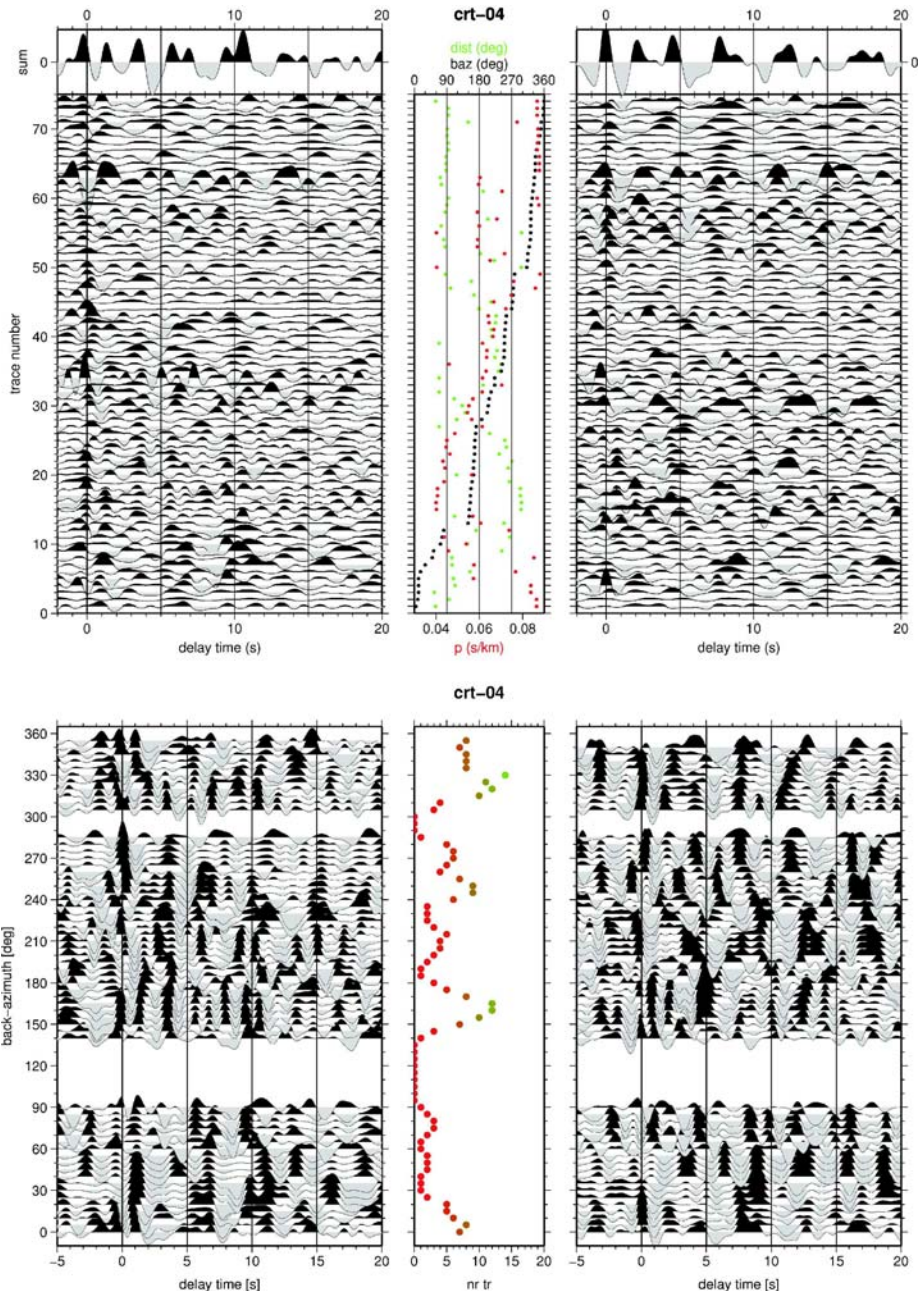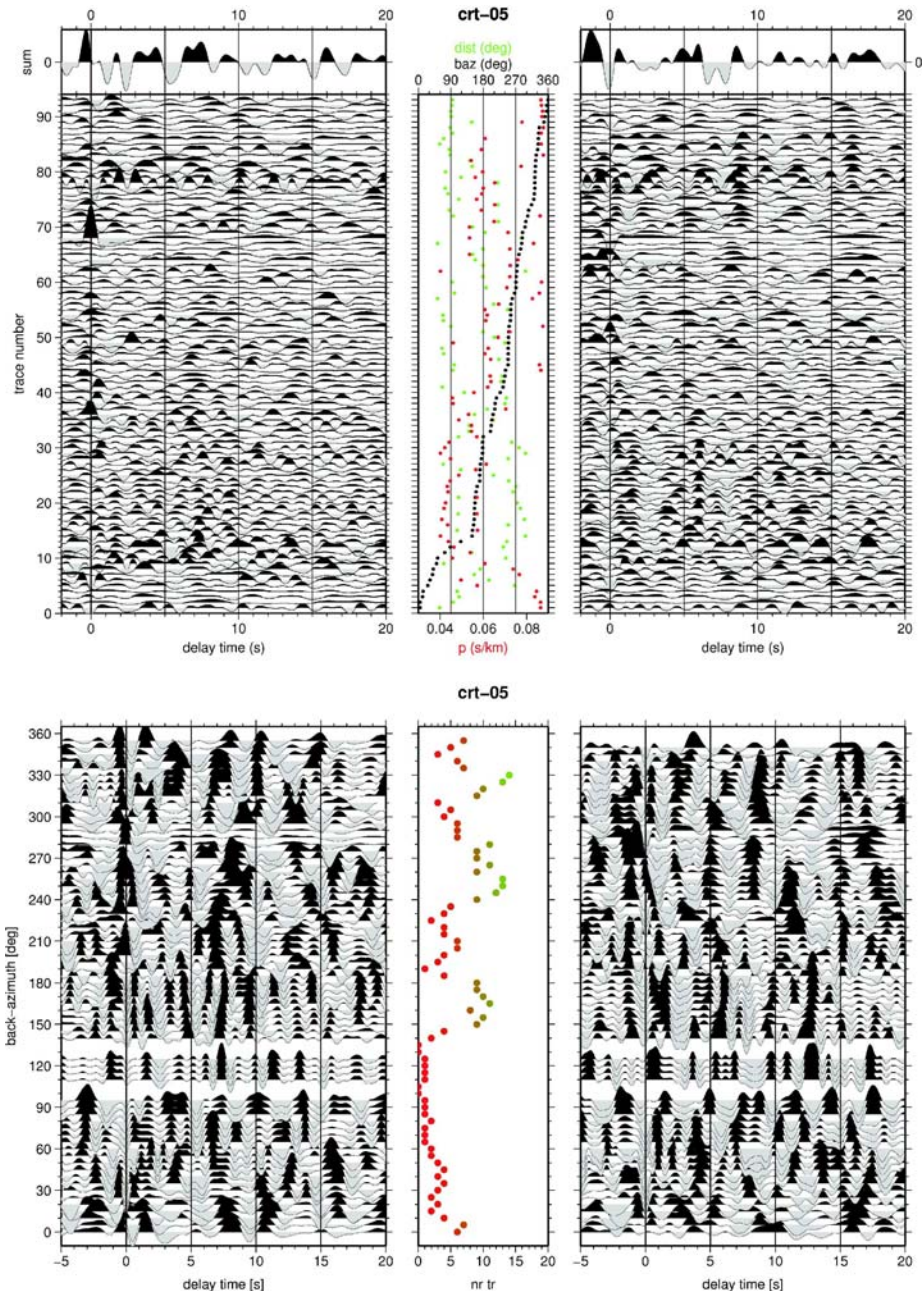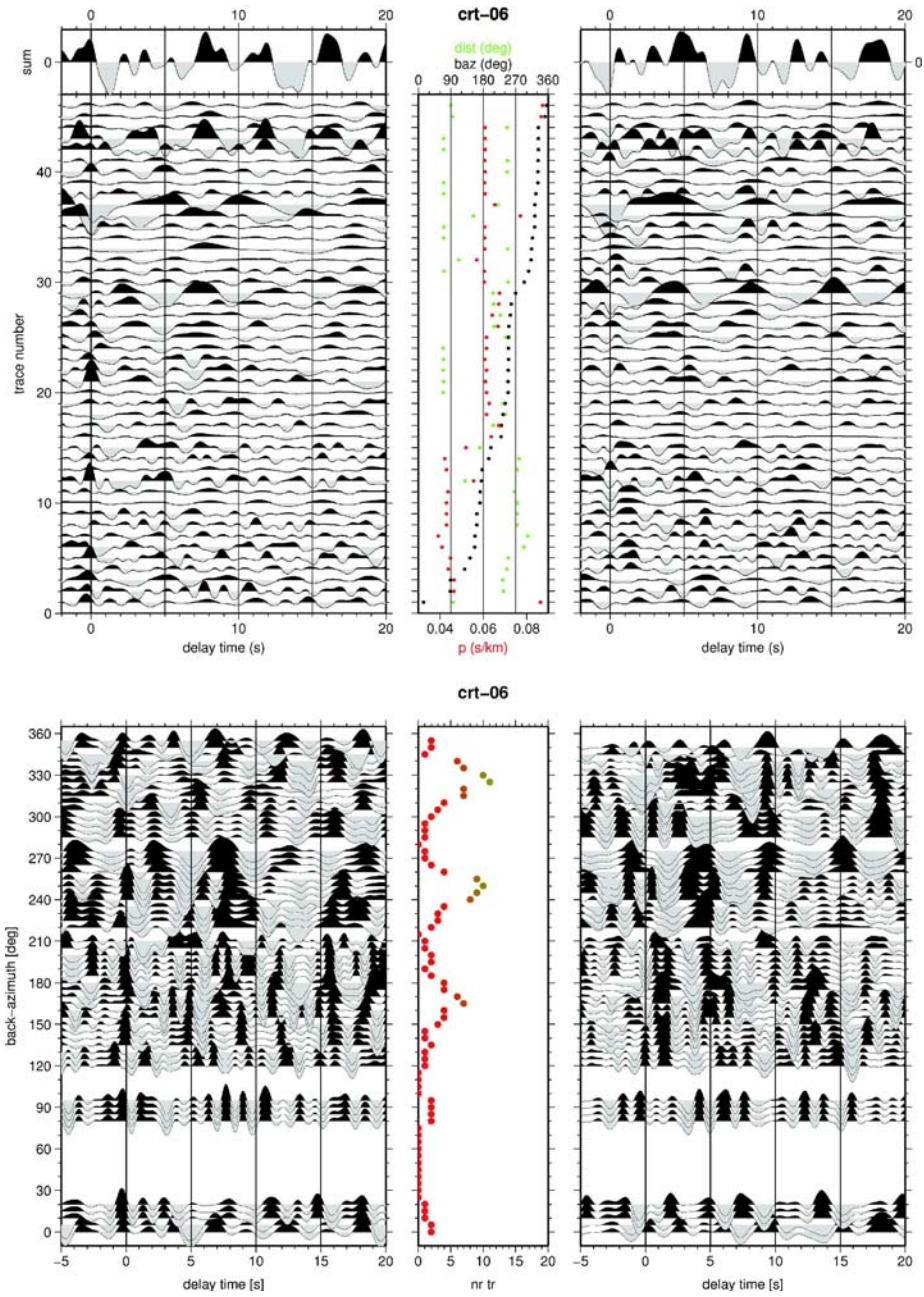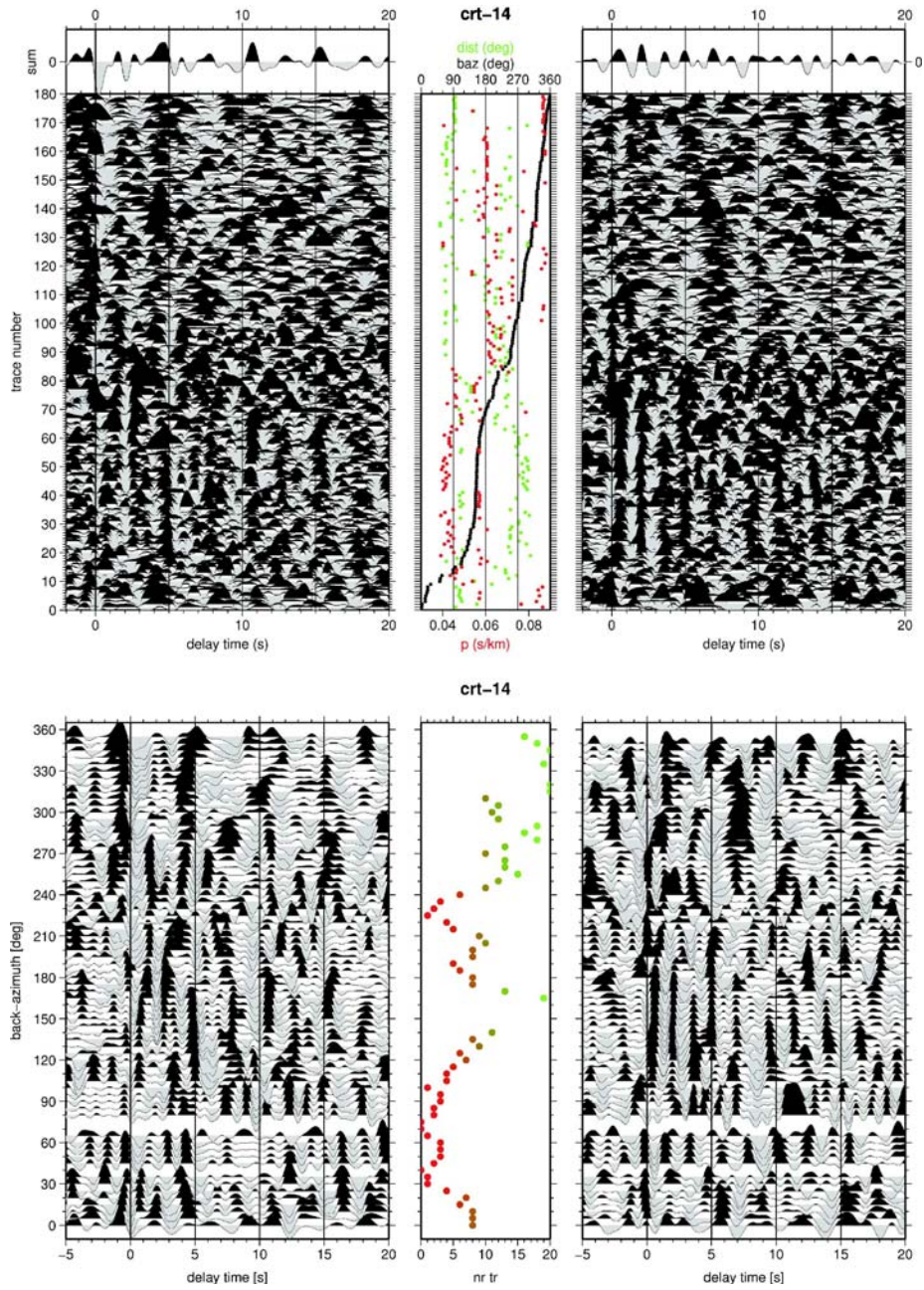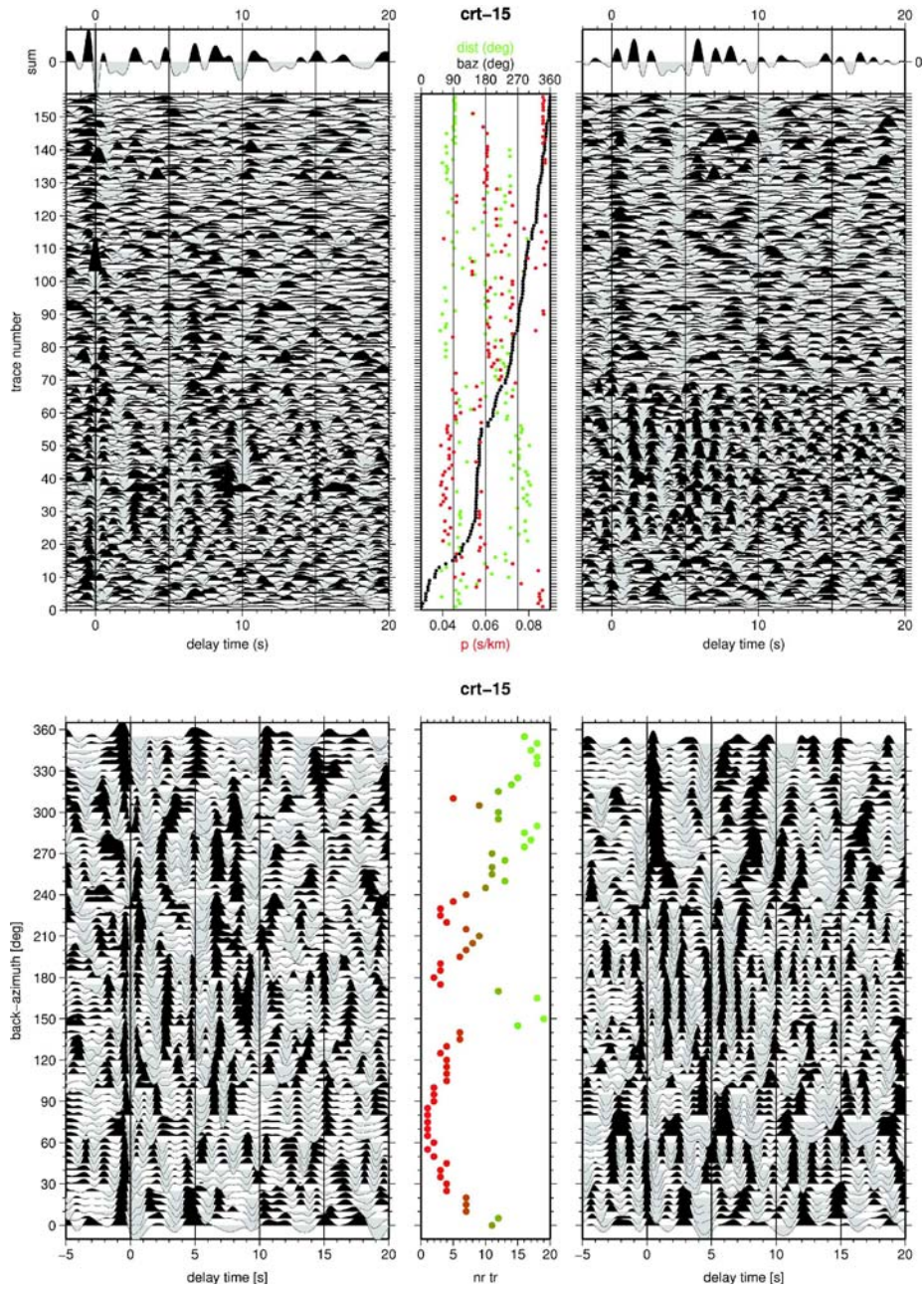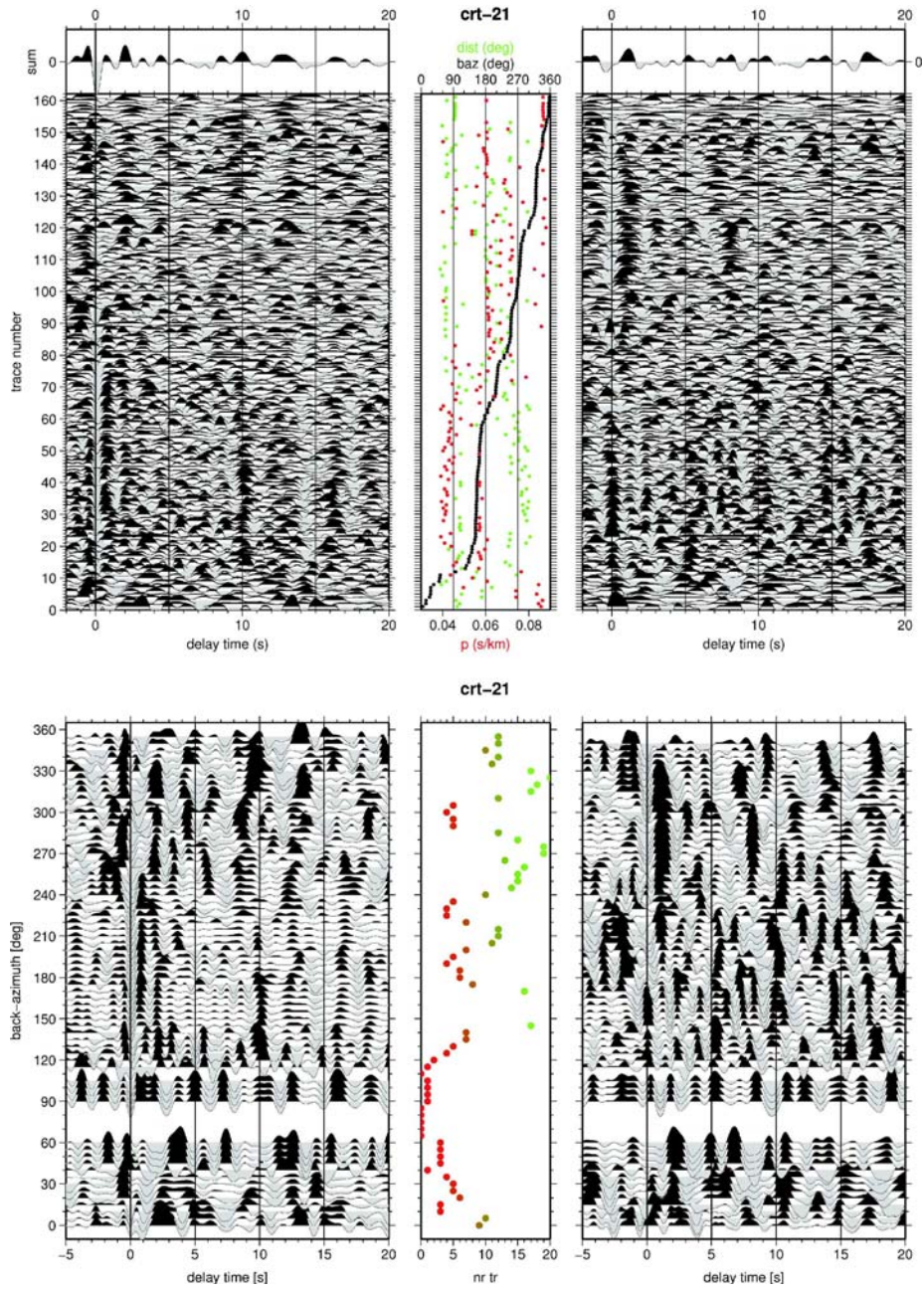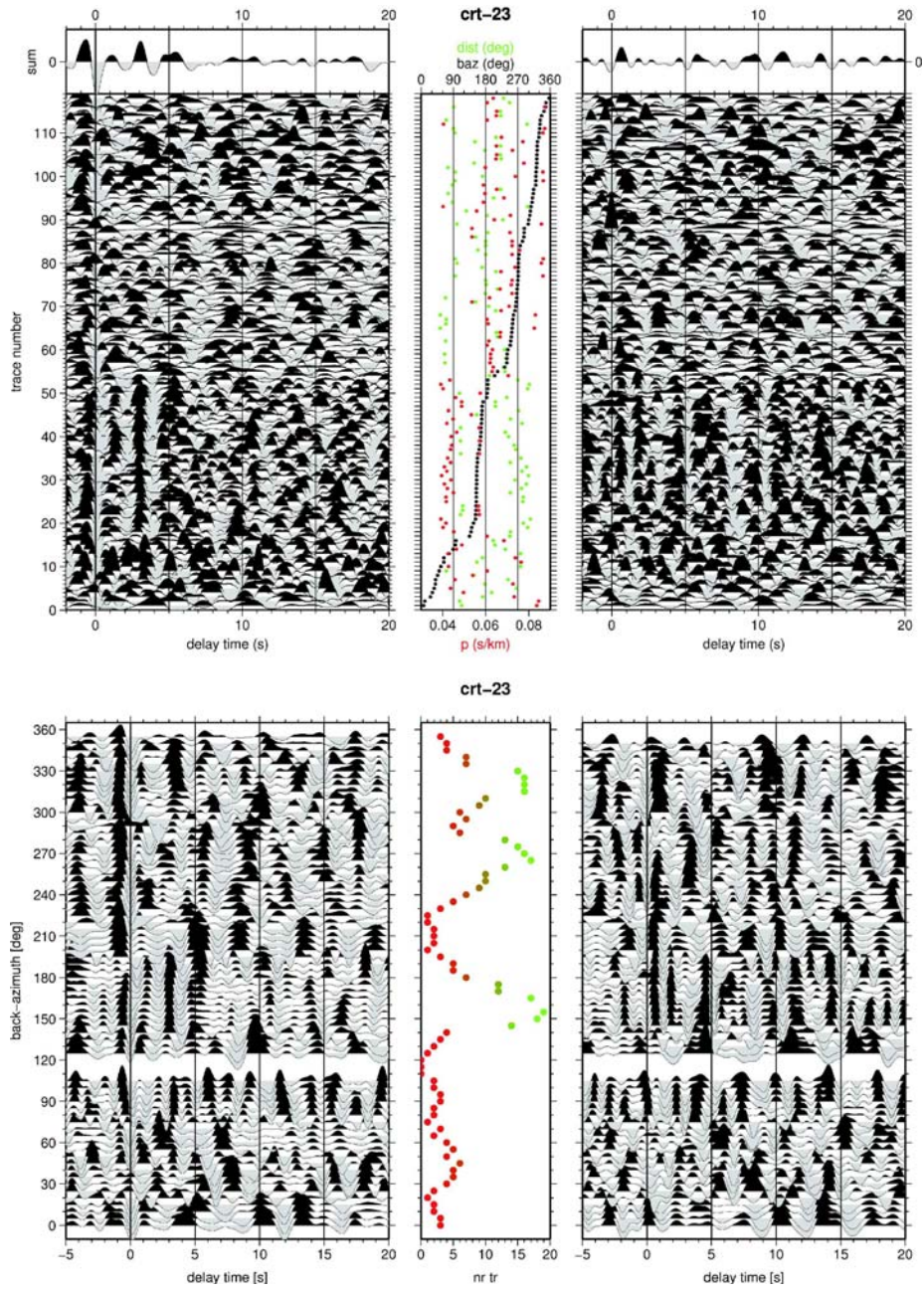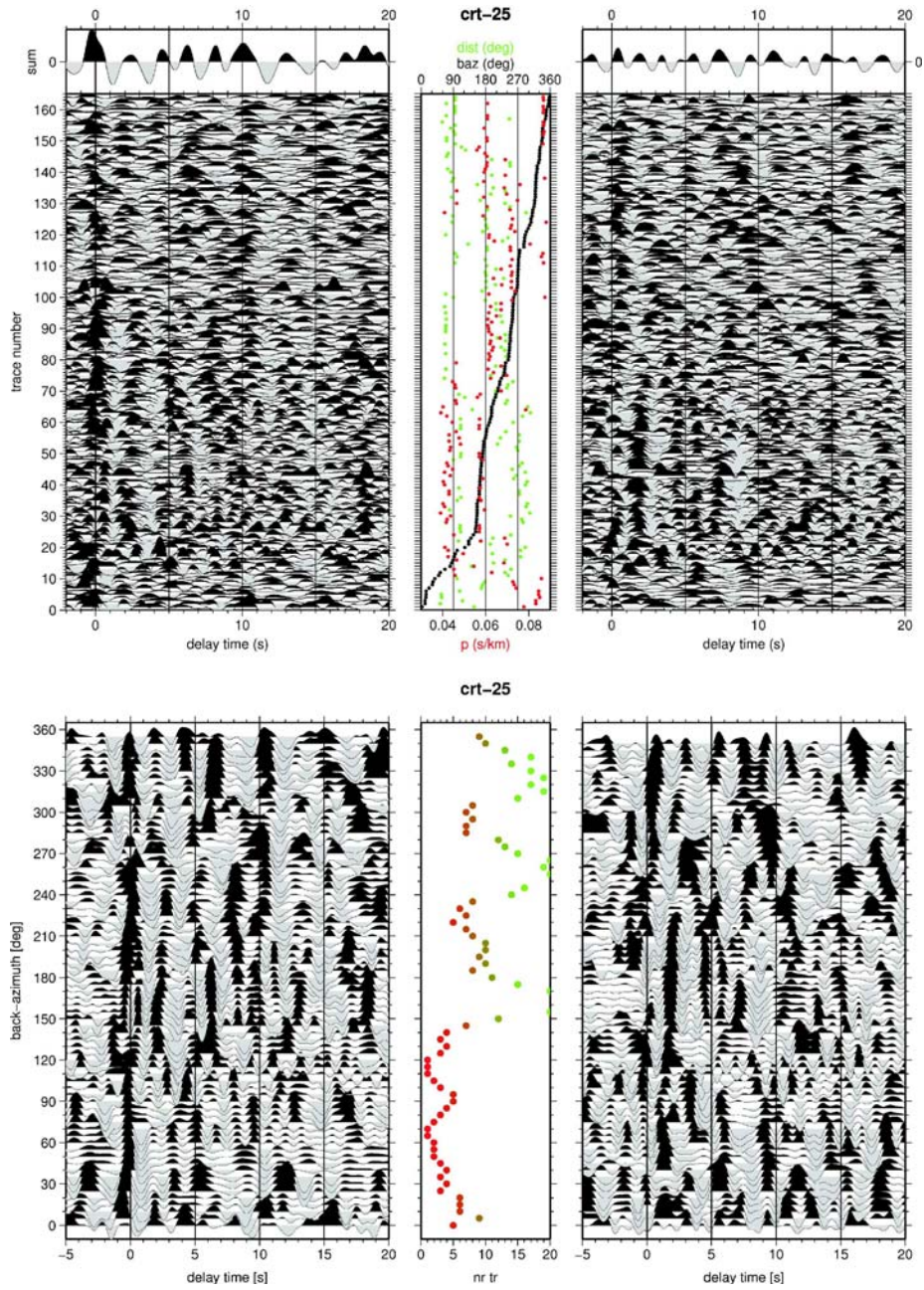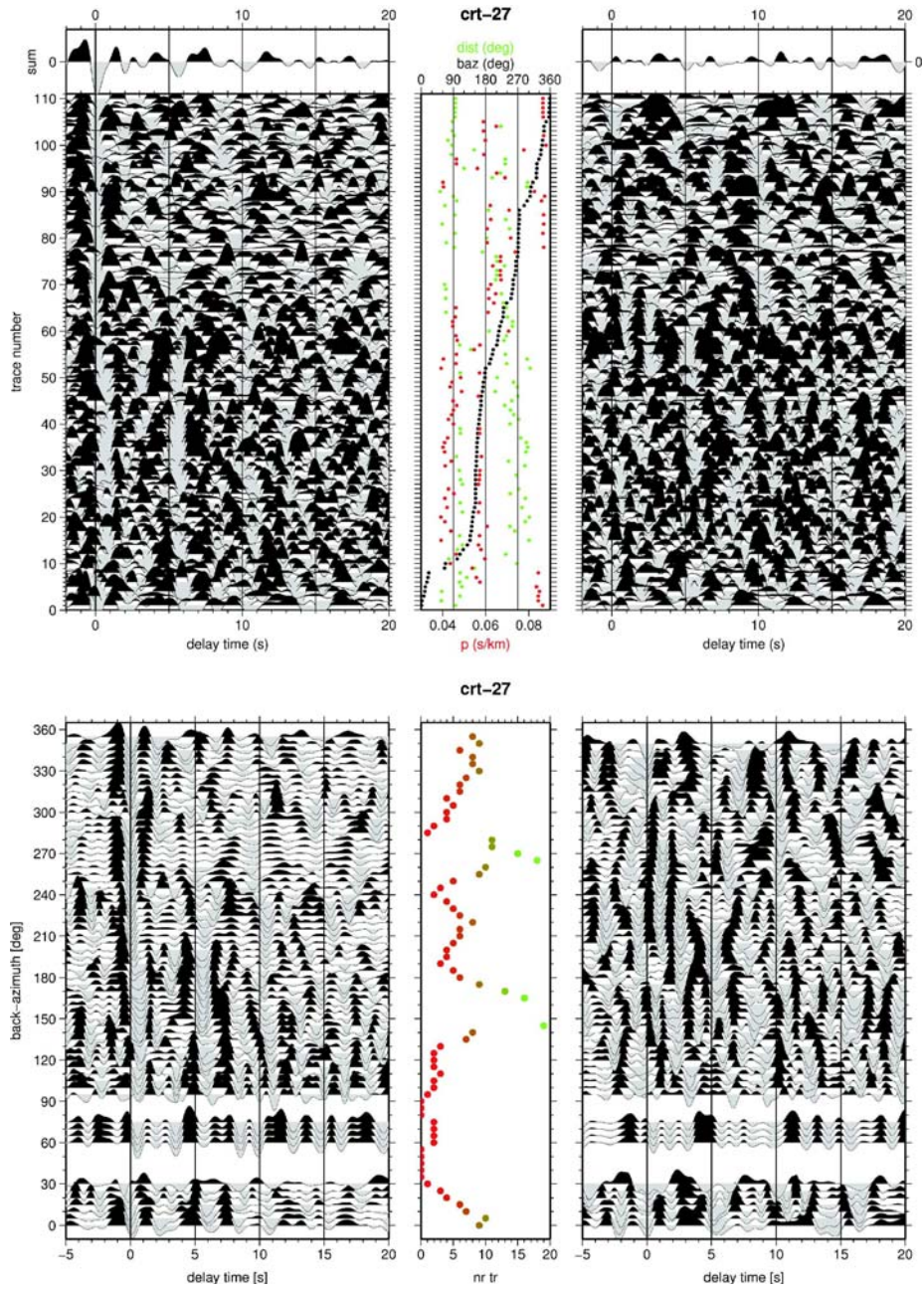
Figure E.1: *Radial (left) and transverse (right) receiver functions for the Talamanca Transect stations. Upper panel: all traces, sorted by back-azimuth. The middle panel gives back-azimuth (in degrees, black), epicentral distance (in degrees, green) and ray parameter p (s/km, red). Lower panel: Receiver functions stacked in 10° bins. The middle panel gives the number of traces in each stack (also colour-coded). Receiver functions were corrected for normal move-out for p = 6.4 s/km and filtered with a 1 Hz low-pass.*

Appendix F

Example of Migrated Profiles for Alternative Migration Algorithms

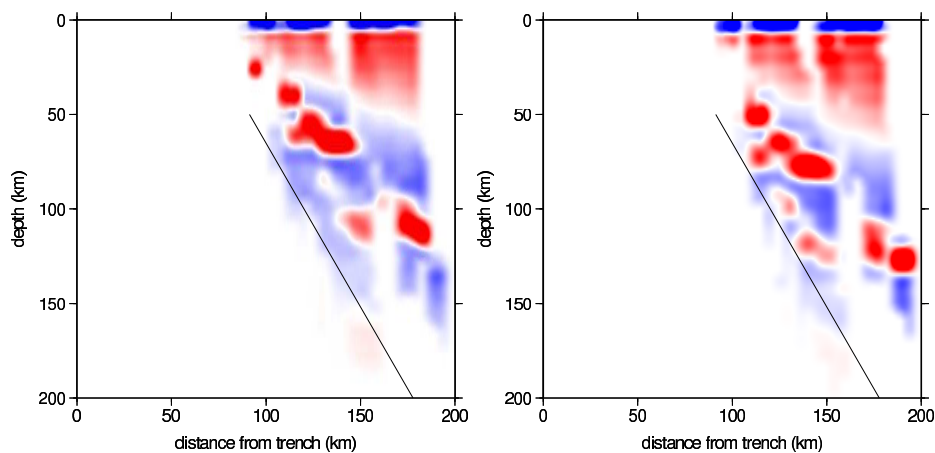## F.1 Migration Using Positive-Polarity Slab Conversions Only

Figure F.1: *Migrated profile for the 60° dipping high-velocity wedge model (for details, see Section 6.1.2). Only events from the back-azimuth range between −30° and 150° were included, which should show positive-polarity slab conversions. Left panel: Profile migrated using the Quintero and Kissling [2001] velocity model; right panel: profile migrated using the velocities from the input model (but horizontal layering). The black line traces the surface of the high-velocity dipping wedge in the input model.*

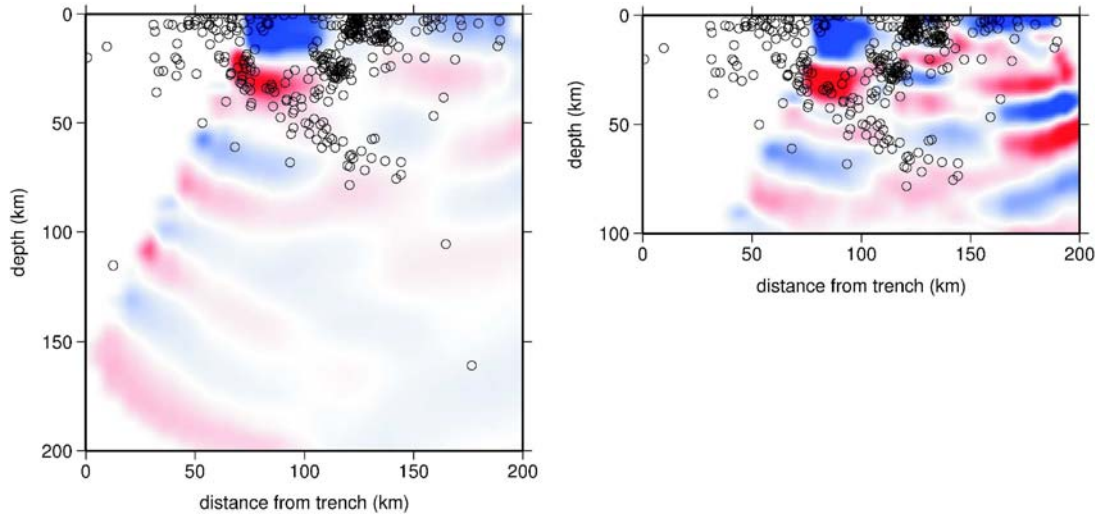## F.2   Migration into 360° Back-Azimuth Hyperbolas

Figure F.2: *Profile 3 migrated with alternative migration algorithm (for details, see Section 6.1.2). Left panel: Profile calculated for the low-frequency receiver functions (low-pass below 5 s period), right panel: profile for the high-frequency receiver function (low-pass below 1 s). While some indication of the Moho and crustal discontinuity is visible and similar to the results obtained by migration along the theoretical ray-paths (vic., Figures 5.5 and 5.6), the dipping feature is strongly disrupted by migration artefacts (prominent "smiles"). Earthquake hypocenters from the Quepos network are shown as black circles.*

Appendix G

Influence of Surface Roughness on Receiver Functions – FD Modelling results
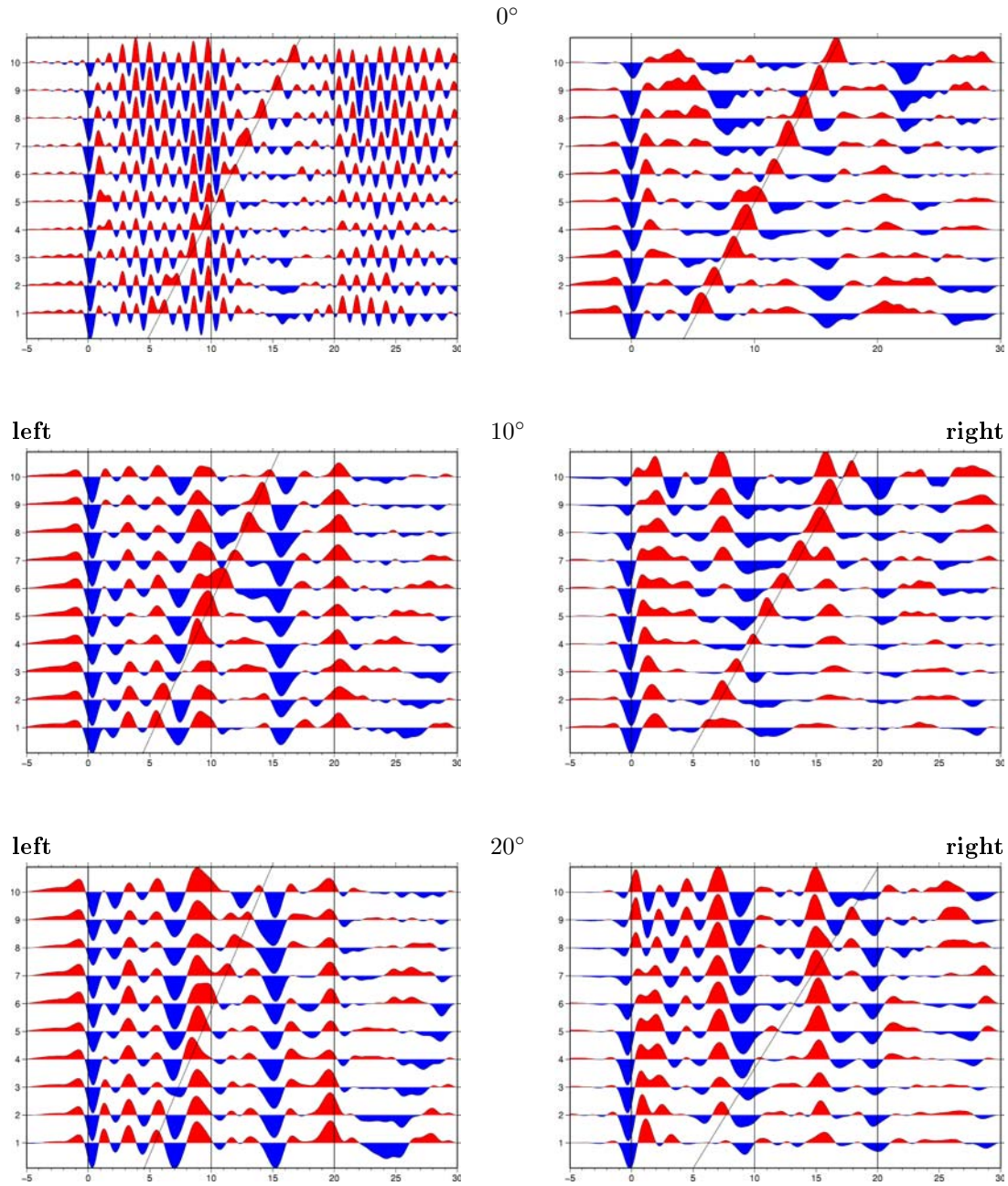
Figure G.1: *Synthetic receiver function results for FD modelling of the scenario shown in Figure 6.11, but with a 60° dipping wedge, and with a sinusoidal Moho and crustal reflector. Traces were processed and plotted like in Figure 6.14. Trace 1 is 70 km above the dipping wedge, trace 10 190 km above. Traces were NMO-corrected and scaled relative to their maximum. Upper panel, left: vertically incident plane wave, unfiltered, right: band-pass filtered below 0.5 Hz. Middle: incident plane wave propagating 10° from the vertical, lower panel: incident plane wave propagating 20° from the vertical, all low-pass filtered. Left: plane wave coming from the left (from the up-dip direction), right: plane wave coming from the right (from the down-dip direction in the model).*
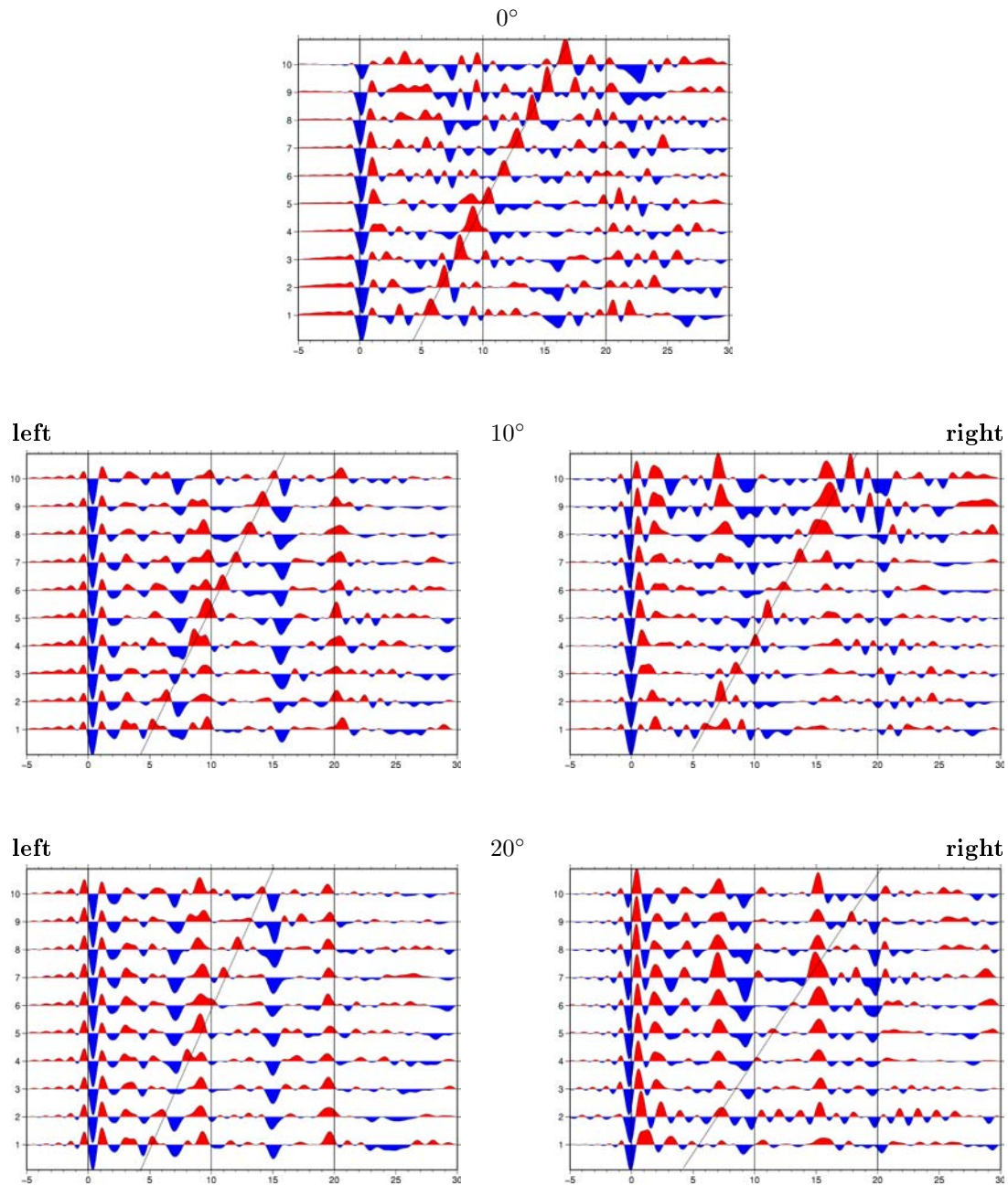
Figure G.2: *Synthetic receiver function results for FD modelling of the scenario shown in Figure 6.11, but with a 60° dipping wedge, and with random variations in Moho and crustal reflector depth. Traces were processed and plotted like in Figure 6.14. Trace 1 is 70 km above the dipping wedge, trace 10 190 km above. Traces were NMO-corrected and scaled relative to their maximum. Upper panel, left: vertically incident plane wave, unfiltered, right: band-pass filtered below 1 Hz. Middle: incident plane wave propagating 10° from the vertical, lower panel: incident plane wave propagating 20° from the vertical, all low-pass filtered. Left: plane wave coming from the left (from the up-dip direction), right: plane wave coming from the right (from the down-dip direction in the model).*
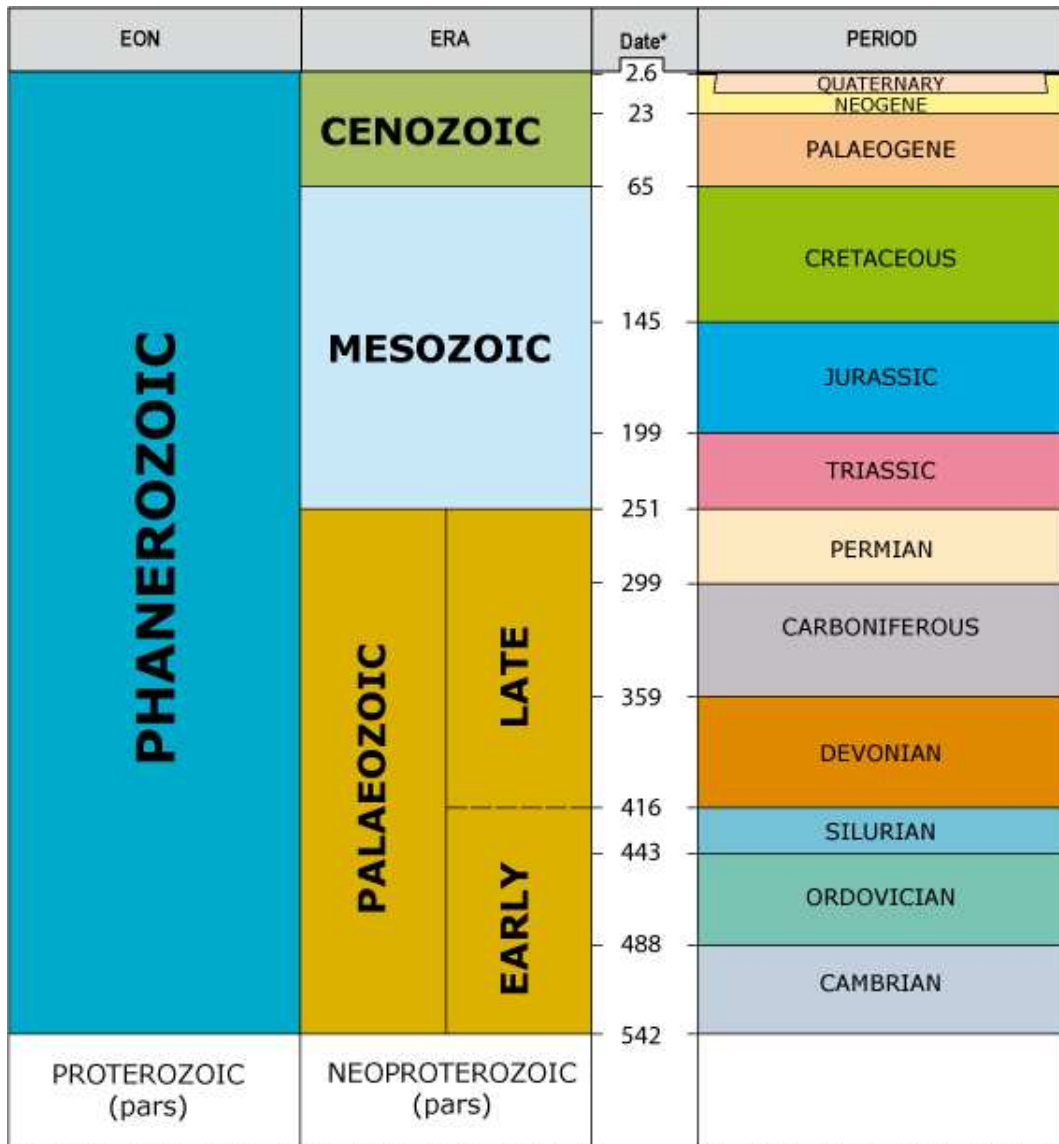
Appendix H

List of Abbreviations

baz	backazimuth
CLIP	Caribbean Large Igneous Province
CNS	Cocos-Nazca Spreading Centre
EPR	East Pacific Rise
FD	finite difference
LPO	lattice-preferred orientation
MAT	Middle American Trench
Moho	Mohorovicic Discontinuity
NMO	Normal Move-Out
OIB	Ocean Island Basalt
QSC	Quesada Sharp Contortion
SNR	signal-to-noise ratio
WBZ	Wadati-Benioff Zone

Appendix I

Geologic Time

EON	ERA		Date*	PERIOD
PHANEROZOIC	CENOZOIC		2.6	QUATERNARY
			23	NEOGENE
				PALAEOGENE
	MESOZOIC		65	CRETACEOUS
			145	JURASSIC
			199	TRIASSIC
	PALAEOZOIC	LATE	251	PERMIAN
			299	CARBONIFEROUS
			359	DEVONIAN
		EARLY	416	SILURIAN
			443	ORDOVICIAN
			488	CAMBRIAN
			542	
PROTEROZOIC (pars)	NEOPROTEROZOIC (pars)			

Figure I.1: *Geologic Time [British Geological Survey]*

Hiermit erkläre ich, dass die vorliegende Abhandlung, abgesehen von der Beratung der Betreuer nach Inhalt und Form, meine eigene Arbeit ist. Bisher ist die Arbeit noch nicht an anderer Stelle im Rahmen eines Prüfungsverfahrens vorgelegt worden.

Yvonne Dzierma

215

Curriculum Vitae

Personal Data

Name:	Yvonne Dzierma
Date and place of birth:	03 February 1980, Schwelm, Germany
Nationality:	German
Private Address:	Olshausenstr. 89 24106 Kiel

Education

1986-1990	Pestalozzi Primary School, Gevelsberg, Germany
1990-1999	Gymnasium Gevelsberg (secondary school), Germany (08.09.1996-18.12.1996 at Oswestry School, England)
1999-2002	Rheinische Friedrich-Wilhelms-Universität Bonn, Germany Physics and Mathematics
2002-2003	Universidad de Granada, Spain: Physics
2003-2005 15.07.2005	Rheinische Friedrich-Wilhelms-Universität Bonn, Germany: Physics graduation: Dipl.-Phys.
since 01.08.2005	PhD student, SFB 574 *"Volatiles and Fluids in Subduction Zones –* *Climate Feedback and Trigger Mechanisms for Natural Disasters"*, Institut für Geowissenschaften, Abteilung Geophysik, Christian-Albrechts-Universität Kiel, Germany